Modelling and Analysis of Non-Stationary Mobile Fading Channels Using Brownian Random Trajectory Models

Alireza Borhani

Modelling and Analysis of Non-Stationary Mobile Fading Channels Using Brownian Random Trajectory Models

Doctoral Dissertation for the Degree *Philosophiae Doctor (PhD)* in Information and Communication Technology

University of Agder
Faculty of Engineering and Science
2014

Doctoral Dissertations at the University of Agder 95
ISBN: 978-82-7117-780-5
ISSN: 1504-9272

Printed in the Printing Office, University of Agder
Kristiansand

To my wife, Parvaneh Sarshar,
to my parents, Davood and Shahin,
to my sister, Faranak, and to my brother, Behzad.

Preface and Acknowledgments

The research work in this dissertation was carried out at the Department of Information and Communication Technology (ICT), Mobile Communications Group (MCG) of the University of Agder (UiA) in Grimstad, Norway. The gigantic task of the completion of this dissertation would have not been possible without the supports of many individuals to whom I would like to express my deep gratitude.

I am very grateful to my supervisor Prof. Matthias Pätzold. His excellent supervision, encouragements, valuable comments, visionary ideas, and constant supports helped me a lot in moulding my efforts into favorable outcomes. I also appreciate my co-supervisor Prof. Frank Young Li for his timely supports. I am grateful to Prof. Gordon L. Stüber for hosting me at the Georgia Institute of Technology (GATECH) in Atlanta, USA. The visit from GATECH was towards the aims of S2EuNet project[1], which is a joint research project financed by the European Commission and coordinated by UiA. Moreover, I would like to express my gratitude to Associate Prof. Alenka Zajić from GATECH and Associate Prof. Svein Olav Nyberg from UiA for their useful comments and ideas.

I would like to thank the MCG secretary, Mrs. Katharina Pätzold, for her continual support. I also appreciate the timely advices of the coordinator of the PhD program at the Department of ICT, UiA, Mrs. Emma Elizabeth Horneman.

My sincere gratitude goes to my Doctoral Fellows, especially to Parvaneh Sarshar, Meisam Naderi, Nurilla Avazov, and Akmal Fayziyev. They made my stay in Grimstad very pleasant and I benefitted immensely from their knowledge and expertise.

Last but not least, my endless appreciation goes to my parents Davood and Shahin, my sister Faranak, and my brother Behzad for their encouragement, love, and continuing support throughout my life, and especially during my doctoral studies.

Alireza Borhani
June 2014
Grimstad, Norway

[1] see http://www.S2EuNet.org.

Summary

The demanding mobility features of communication technologies call for the need to advance channel models (among other needs), in which non-stationary aspects of the channel are carefully taken into consideration. Owing to the mathematical complexity imposed by mobility features of the mobile station (MS), the number of non-stationary channel models proposed in the literature is very limited. The absence of a robust trajectory model for capturing the mobility features of the MS also adds to the depth of this gap. Not only statistically non-stationary channels, but also physically non-stationary channels, such as vehicle-to-vehicle channels in the presence of moving scatterers, have been rarely investigated.

In the literature, there exist two fundamental channel modelling approaches, namely deterministic and stochastic approaches. Deterministic approaches, such as measurement-based channel modelling, are known to be accurate, but site-specific and economically expensive. The stochastic approaches, such as geometry-based channel modelling, are known to be economically inexpensive, computationally fair, but not as accurate as the deterministic approach. Among these approaches, the geometry-based stochastic approach is the best to capture the non-stationary aspects of the channel.

In this dissertation, we employ the geometry-based stochastic approach for the development of three types of channel models, namely stationary, physically non-stationary, and statistically non-stationary channel models. We geometrically track the plane waves emitted from the transmitter over the local scatterers up to the receiver, which is assumed to be in motion. Under the assumptions that the scatterers are fixed and the observation time is short enough, we develop the stationary channel models. In this regard, we propose a unified disk scattering model (UDSM), which unifies several well-established geometry-based channel models into one robust channel model. We show that the UDSM is highly flexible and outperforms several other geometric models in the sense of matching empirical data. In addition, we provide a new approach to develop stationary channel models based on delay-angle joint distribution functions.

Under the assumption that the scatterers are in motion and the observation time is again short enough, we develop a physically non-stationary channel model. In this connection, we model vehicle-to-vehicle (V2V) channels in the presence of moving scatterers. Proper distributions for explaining the speed of relatively fast and relatively slow moving scatterers are provided. The statistical properties of the proposed channel model are also derived and validated by measured channels. It is shown that relatively fast moving scatterers have a major impact on both V2V

and fixed-to-fixed (F2F) communication links, as they are significant sources of the Doppler spread. However, relatively slow moving scatterers can be neglected in V2V channels, but not in F2F channels.

Under the assumption that the scatterers are fixed and the observation time is not necessarily short anymore, we develop the statistically non-stationary channel models. To this aim, we first introduce a new approach for generating fully spatial random trajectories, which are supposed to capture the mobility features of the MS. By means of this approach, we develop a highly flexible trajectory model based on the primitives of Brownian fields (BFs). We show that the flexibility of the proposed trajectory is threefold: 1) its numerous configurations; 2) its smoothness control mechanism; and 3) its adaptivity to different speed scenarios. The statistical properties of the trajectory model are also derived and validated by data collected from empirical studies.

We then introduce a new approach to develop stochastic non-stationary channel models, the randomness of which originates from a random trajectory of the MS, rather than from the scattering area. Based on the new approach, we develop and analyze a non-stationary channel model using the aforementioned Brownian random trajectory model. We show that the channel models developed by this approach are very robust with respect to the number of scatterers, such that highly reported statistical properties can be obtained even if the propagation area is sparsely seeded with scatterers. We also show that the proposed non-stationary channel model superimposes large-scale fading and small-scale fading. Moreover, we show that the proposed model captures the path loss effect.

More traditionally, we develop and analyze two non-stationary channel models, the randomness of which originates from the position of scatterers, but not from the trajectory of the MS. Nevertheless, the travelling path of the MS is still determined by a sample function of a Brownian random trajectory. It is shown that the proposed channel models result in a twisted version of the Jakes power spectral density (PSD) that varies in time. Accordingly, it is demonstrated that non-stationarity in time is not in line with the common isotropic propagation assumption on the channel.

Contents

List of Figures

List of Tables

Abbreviations

2D	two-dimensional
ACF	autocorrelation function
AOA	angle-of-arrival
AOD	angle-of-departure
AOM	angle-of-motion
BF	Brownian field
BM	Brownian motion
BS	base station
CDF	cumulative distribution function
CLT	central limit theorem
DSRC	dedicated short-range communications
F2F	fixed-to-fixed
F2M	fixed-to-mobile
F2V	fixed-to-vehicle
GM	Gaussian mixture
GSM	global system for mobile communications
ITS	intelligent transportation system
LCR	level-crossing rate
LOS	line-of-sight
LSE	least-squares error
M2M	mobile-to-mobile
MIMO	multiple-input multiple-output
MNE	multiple negative exponential
NLOS	non-line-of-sight
PDF	probability density function
PDP	power delay profile
PSD	power spectral density
SISO	single-input single-output
SNR	signal-to-noise ratio

SOS	sum-of-sinusoids
TOA	time-of-arrival
V2V	vehicle-to-vehicle
UDSM	unified disk scattering model
UMTS	universal mobile telecommunication system
WSSUS	wide-sense stationary uncorrelated scattering

Chapter 1

Introduction

1.1 Channel Modelling: Principles and State-of-the-Art

For the development of communication systems, the accurate knowledge of the radio propagation environment is of crucial importance. This calls for the need to realistic channel models that provide sufficient insight into the radio propagation mechanisms. The mechanisms that rule plane waves in a radio propagation medium are complex and diverse. Accordingly, an important step toward the development of realistic channel models is to better understand these mechanisms. This actuates the so-called channel modelling, which has been a subject of thorough studies from the very beginning of mobile communications until today.

Standard channel models allow the designers of communication systems to evaluate the performance of different modulation schemes, coding techniques, and receiver algorithms through computer simulations. Therefore, the costly need for scenario-dependent hardware prototypes and/or field trials can be minimized [8]. In this connection, exploiting properties of channel models can be of great help for the performance analysis of the overall communication system. These properties often include the distribution of the angle-of-departure (AOD), angle-of-arrival (AOA), time-of-arrival (TOA), from which other important characteristics of the channel model, such as the power spectral density (PSD) of the Doppler frequencies, power delay profile (PDP), and time (frequency) correlation functions can be derived.

While the channel models should be accurate enough in capturing properties of real-world propagation mediums, they should also be simple enough to yield feasible implementations and reasonable short simulation times. Therefore, in the design of a channel model, the tradeoff between *accuracy* and *simplicity* should al-

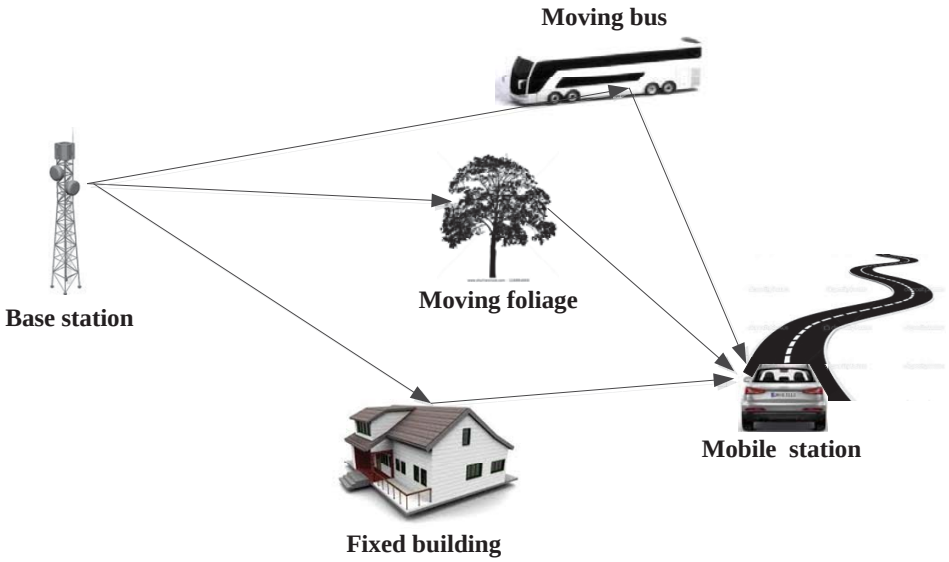

Figure 1.1: A typical propagation scenario illustrating the effect of multipath propagation in terrestrial radio environments.

ways be taken into account. In a typical propagation scenario, the transmitted signal arrives at the receiver via several paths, each of which encounters various propagation mechanisms such as reflection, scattering, and/or diffraction. Fig. 1.1 depicts a typical fixed-to-mobile (F2M) propagation scenario illustrating the effect of multipath propagation in terrestrial radio environments. In this figure, we *simplify* the illustration of the propagation mechanism, e.g., by assuming that a wave transmitted from the base station (BS) reaches the mobile station (MS) after only a single reflection by one of the scatterers. On the other hand, we boost the *accuracy* of the illustrative model by taking the effect of moving scatterers into consideration. One of the objectives of this dissertation is to show that this consideration is of great importance in some applications/frequencies.

The number of research works dealing with channel modelling is relatively high. From the investigation of time-variant linear channels [9] over the statistical theory of radio reception [10] up to spectral properties of mobile communications [11] are all preceding examples of studies on characteristics of radio fading channels. An evolution trend of channel modelling can be found, e.g., in [8, 12, 13], while a comprehensive and critical comparison among the most established channel models can be found in the assessment studies in [14] and [15]. This research line still goes forward and never stops as long as new communication technologies are demanded.

1.2 Channel Modelling: Approaches and Features

According to the literature [8, 12, 16, 17], there exist two fundamental approaches in channel modelling: the deterministic approach and the stochastic approach, each of which has several advantages/disadvantages. In what follows, we highlight the principles and the most important features of each approach.

There are two major subcategories of the deterministic approach, namely the measurement-based approach and the ray-tracing approach. Measurement-based channel models are developed by collecting empirical data from measurement campaigns carried out in real-world propagation environments. The measured channel impulses are thus very accurate, which allows us to obtain accurate channel models. The disadvantage of this approach is, however, the fact that the measured data is quite scenario-dependent. In addition, channel measurements are very costly, thus the amount of data that can be collected is very limited. The literature includes numerous measurement-based channel models, such as those developed in [2–5].

In the ray-tracing approach, a simulation tool allows us to launch and trace the propagation mechanism in an unreal propagation environment. In this approach, Maxwell's equations are often needed to be solved under some boundary conditions imposed by the underlying site-specific radio propagation environment. To develop a ray-tracing-based channel model, the topographic and electromagnetic features of the corresponding propagation area are required. Although, this approach is less costly than the measurement-based approach, it is computationally more expensive. Similar to measurement-based channel models, the channel models designed by the ray-tracing approach are very site-specific. Therefore, they cannot be readily used for extensive system-level simulations of communication systems [17]. Different ray-tracing-based channel models have been proposed in the literature, such as those proposed in [18–22].

The main idea of the stochastic approach is to generate synthetic channel responses that represent physical propagation channels with an acceptable level of accuracy. Mathematically, stochastic channel models are often less complex than deterministic ones. Nevertheless, some realistic considerations, such as the non-stationarity of the mobile radio channel, may make a stochastic channel model very complex. Different from the deterministic approach, stochastic channel models can be tuned to imitate various propagation areas, which is the main advantage of these models. The stochastic approach can be classified into two major groups, namely the correlation-based approach and the geometry-based approach.

In the correlation-based approach, the aim is to model the second-order statistics of the channel and their correlation functions. The advantage of this approach is its

computational simplicity and analytical tractability whereby it needs less input parameters as compared to the other approaches [8]. Nonetheless, the model explains only the second-order statistics of the channel, but not the physical specifications of the propagation environment. Examples of such models are [23–26] among others.

In the geometry-based approach, the stochastic channel model is developed by assuming that scatterers are randomly distributed in a standard geometric shape, such as a ring, disk, ellipse, etc. Given a certain distribution function to explain the position of local scatterers, the statistical properties of the channel model are derived and then validated by empirical data collected from measurement campaigns. These models are known to be well suited for the modelling of non-stationary mobile radio channels [17, 27, 28]. Owing to the high number of model parameters, these models can be tuned to model distinct propagation mediums. Nevertheless, optimizing the model parameters is sometimes a difficult task. Analytically, these models often benefit from a so-called *infinity assumption*, which states that the number of scatterers in the reference model tends to infinity. Accordingly, another difficulty of this approach is to find a good match between the reference model, which relies on the infinity assumption, and the simulation model, which assumes a limited number of scatterers. Numerous geometry-based stochastic channel models have been proposed in the literature, the most important ones are listed and compared in [14] and [15].

1.3 Motivations and Contributions of the Dissertation

Although, channel modelling has been the topic of thorough studies for several decades, there exists a great potential for further advancements in the field. The development of new upcoming technologies, such as vehicle-to-vehicle (V2V) communication systems, massive MIMO systems, and ad hoc networks is in immense need of robust channel models, in which further properties of real-world radio propagation channels are taken into consideration.

The non-stationarity of mobile radio channels, polarization of plane waves, and the multiple-bounce scattering effect are among those features that have rarely been considered in the channel models proposed in the literature. These features may automatically be taken into account in measurement-based channel models, but not in the models developed by means of the geometry-based stochastic approach. For instance, none of the mobile radio channel models listed in [14] has been studied under non-stationary conditions. Many empirical and analytical investigations,

e.g., [29–31], however, show that the stationary assumption for mobile radio channels is only valid for extremely short travelling distances [32]. The lack of non-stationary channel models in the literature is mainly due to the mathematical complexity imposed by mobility features of the MS. The absence of a robust trajectory model for capturing mobility features of the MS also adds to the depth of this gap. In this regard, no fully spatial trajectory model can be found in the literature.

In addition to the aforementioned lacks, the effect of moving scatterers has been studied very rarely. Nonetheless, the importance of this effect has been shown both via empirical studies [6, 17, 33] and via analytical investigations [34, 35]. Another notable lack is the fact that correlation-based channel models do not provide any physical insight to the underlying propagation area. The literature also needs a unification of a large variety of established stochastic channel models, such as those listed in [14], via a unified model.

This dissertation strives to fill these gaps by eightfold:

1. Developing a unified stationary channel model to capture the scattering effect of numerous propagation areas;

2. Proposing a new approach in channel modelling by means of which obtaining the desired statistical properties is assured, while the physical explanation of the propagation area is possible;

3. Developing a vehicle-to-vehicle channel model considering the effect of moving scatterers;

4. Proposing a new approach for the development of fully spatial trajectory models;

5. Developing a highly flexible trajectory model based on the primitives of Brownian fields (BFs) to capture the mobility features of the MS;

6. Proposing a random trajectory approach for the development of non-stationary channel models;

7. Developing several non-stationary channel models based on the random trajectory approach;

8. Superimposing large-scale fading and small-scale fading under non-stationary conditions.

1.4 Classification of the Developed Channel Models

Based on the standard classification modules in the area of channel modelling, we group the channel models developed in this dissertation in what follows.

From the channel modelling approach perspective, the main focus of this dissertation is on the *geometry-based stochastic* approach. This does not necessarily mean that the developed channel models rely on standard geometric shapes. In this dissertation, we call a channel model *geometry-based* if the wave emitted from the transmitter is geometrically (analytically) traced until its arrival at the receiver.

Another classification is based on the mobility features of the transmitter and the receiver. In this dissertation, we often provide *F2M channel models*. Nevertheless, vehicle-to-vehicle (V2V) channels, as well as fixed-to-fixed (F2F) channel models will also be designed and analyzed.

A third perspective is the frequency-selectivity of the channel models. The entire channel models provided in this dissertation are *frequency-nonselective*. In addition, we focus only on modelling single-input single-output (SISO) communication channels.

Another important perspective is the stationarity of the channel models. In this dissertation, we provide three different classes of channel models: *stationary, physically non-stationary, and statistically non-stationary* channel models, each of which is defined and discussed in the corresponding chapter. Very briefly, for the development of stationary channel models, we consider the propagation scenarios (see, e.g., Fig. 1.1) in which: 1) the presence of moving scatterers is ignored; 2) the observation time is assumed to be short enough such that the statistical properties of the channel model do not change in time.

To design physically non-stationary channel models, we consider the propagation scenarios in which: 1) the local scatterers are in motion; 2) the observation time is assumed to be short enough such that the statistical properties of the channel model do not vary in time.

To design statistically non-stationary channel models, we consider the propagation scenario in which: 1) the presence of moving scatterers is ignored; 2) the observation time is not necessarily short such that the statistical properties of the channel model may vary in time.

We remark that in real-world propagation scenarios, the radio channel may be not only statistically non-stationary, but also physically non-stationary (in the sense of local scatterers). The mathematical complexity imposed by such a combined scenario, however, does not allow us to develop the corresponding channel model. It is noteworthy that the major contribution of this dissertation is on the development

of statistically non-stationary channel models.

1.5 Organization of the Dissertation

The dissertation is organized as an assortment of *fifteen technical papers, eight of which are included* at the end of this dissertation as Appendices A–H. Those papers which focus on similar topics are combined to form a chapter. The concordance between different papers is highlighted in the chapters. The dissertation is organized as follows

- **Chapter 2** covers Papers I and II, along which we explain Contributions 1 and 2. In this chapter, we focus on the development of statistically stationary channel models. These models include: 1) a unified disk scattering model (Paper I); and 2) a channel model developed based on given joint delay-angle distributions (Paper II). Moreover, the statistical properties of the developed channel models are briefly addressed.

- **Chapter 3** covers Paper III, along which we explain Contribution 3. In this chapter, we focus on the development of a physically non-stationary channel model to capture the propagation mechanism in V2V channels in the presence of moving scatterers. Proper distribution functions for modelling the speed of moving scatterers are also given. In addition, the statistical properties of the proposed channel model are briefly discussed.

- **Chapter 4** covers Papers IV and V, along which we explain Contributions 4 and 5. In this chapter, we provide a fully spatial random trajectory model based on the primitives of BFs (Paper IV) and study its statistical properties (Paper V). Indeed, the objective of this chapter is to prepare one of the basic materials for the development of non-stationary channel models.

- **Chapter 5** covers Papers VI-VIII, along which we explain Contributions 6-8. In this chapter, we focus on the development of statistically non-stationary channel models based on the random trajectory model designed in Chapter 4. These models include: 1) a non-stationary channel model capturing different scales of fading (Paper VI); 2) a non-stationary channel model based on Brownian random paths (Paper VII); and 3) a non-stationary channel model based on drifted Brownian random paths (Paper VIII). Moreover, the statistical properties of the developed non-stationary channel models are briefly addressed.

- **Chapter 6** summarizes the dissertation and highlights some open problems pertaining to the design and development of non-stationary channel models that call for further attention.

Each chapter comprises various sections that discuss the sub-topics addressed in the chapter. The layout for each chapter has the following structure.

- The introduction provides an overview and state of the art of the main topic of the chapter.
- The section presents a joint discussion of those papers which address a similar sub-topic under the umbrella of the main topic of the chapter. Particularly,
  - Each section begins with a short introduction of the sub-topic.
  - It then presents the problem description followed by a brief discussion on the motivation behind the problem(s) of interest. Additionally, the significance of the expected outcome(s) is elucidated
  - Afterwards, the main results of the paper(s) are reviewed. The discussion includes advantages and disadvantages of the proposed method.
- The chapter summary and conclusion highlights the peculiar findings of the chapter.

Chapter 2

Stationary Channel Models

2.1 Introduction

Strictly speaking, a channel is called *stationary* if its statistical properties do not vary in time (position). In practice, this time-independency is never fulfilled in mobile radio fading channels, as the MS is in motion. Considering a very short observation time, however, allows us to assume that the channel is statistically stationary. In this case, the primary statistical properties of the corresponding channel model, such as its AOA and AOD, do not change in time. Therefore, the statistical quantities derived from those properties, such as the Doppler frequencies, also become time-independent.

The uniform ring model [36–38], uniform hollow-disk model [39, 40], uniform circular scattering model [41–46], uniform elliptical model [40, 42, 46, 47], Gaussian scattering model [48–52], conical scattering model [53], inverted-parabolic model [54], and the Rayleigh scattering model [55, 56] are the most important geometry-based channel models that have been proposed in the literature, which all benefit from the wide-sense stationary uncorrelated scattering (WSSUS) assumption.

A comprehensive comparison among all the above-mentioned geometric scattering models can be found in the assessment study in [14]. Comparing the statistical properties derived from these models with the measurement data reported in [2–5] (among others listed in [14]) reveals that none of these geometric scattering models is the best by all the selected criteria and for all considered scenarios. However, unimodal AOD PDFs seen in real-world channels are well fitted by the AOA PDF of the Gaussian scattering model, as well as that of the uniform elliptical model. It was also shown that bimodal AOD PDFs are best fitted by the AOD PDF of the uniform hollow-disk model [14]. The mathematical complexity of the models above

also plays an important role in their useability.

2.1.1 A Unified Disk Scattering Model

According to the discussion above, an important lack in the literature is a flexible scattering model that can unify several established scattering models into one robust, mathematically simple, and compact model. The motivation of Paper I is to fill this gap by adding one degree of freedom to the disk-based scattering model proposed in [57]. Paper I introduces the unified disk scattering model (UDSM) with two degrees of freedom, allowing us to unify several circularly-symmetric scattering models. The novelty of the UDSM arises from the fact that the distribution of the scatterers can be fashioned in various concentration patterns, where the shape of the concentration pattern is controlled by a so-called shape factor. By adjusting the shape factor, one can gradually change the concentration of the local scatterers from a high concentration close to the MS via the uniform distribution inside the full disk up to a high concentration on a ring centred on the MS. Therefore, the proposed UDSM not only covers the Gaussian, uniform, hollow-disk, and ring scattering models, but also covers any continuous circularly-symmetric concentration of local scatterers between these established scattering models. Fig. 2.1 shows the effect of the shape factor on the scatter diagram obtained by distributing 1000 scatterers according to the PDF of the UDSM. It is assumed that the MS is located at the centre of the disk, while the BS is highly elevated to scattering-free levels.

In Paper I, we show that the UDSM can efficiently describe the AOD and TOA characteristics of several different propagation areas including rural, suburban, and urban areas. To validate the UDSM, we compare its statistical properties with both unimodal and non-unimodal empirical data sets collected from distinct measurement campaigns [2–5]. It turns out that the UDSM is highly flexible and outperforms several other geometric models proposed in the literature. It is shown that the UDSM competes closely with the uniform elliptical model for providing the best curve-fitting to the unimodal empirical data sets. However, the UDSM outperforms considerably the uniform elliptical model in the sense of matching bimodal empirical data sets. An interesting feature of the UDSM is that by calibrating the shape factor, its AOD (TOA) PDF changes to a bimodal shape with two smooth peaks, while its mathematical expression is always unimodal. This smooth bimodal curve fits better to the non-unimodal empirical data set than the best already proposed model, i.e., the uniform hollow-disk model, which gives a biomodal shape with two sharp peaks. The UDSM is mathematically presented by a joint PDF in polar coordinates. Nevertheless, the Cartesian representation of the UDSM is also provided

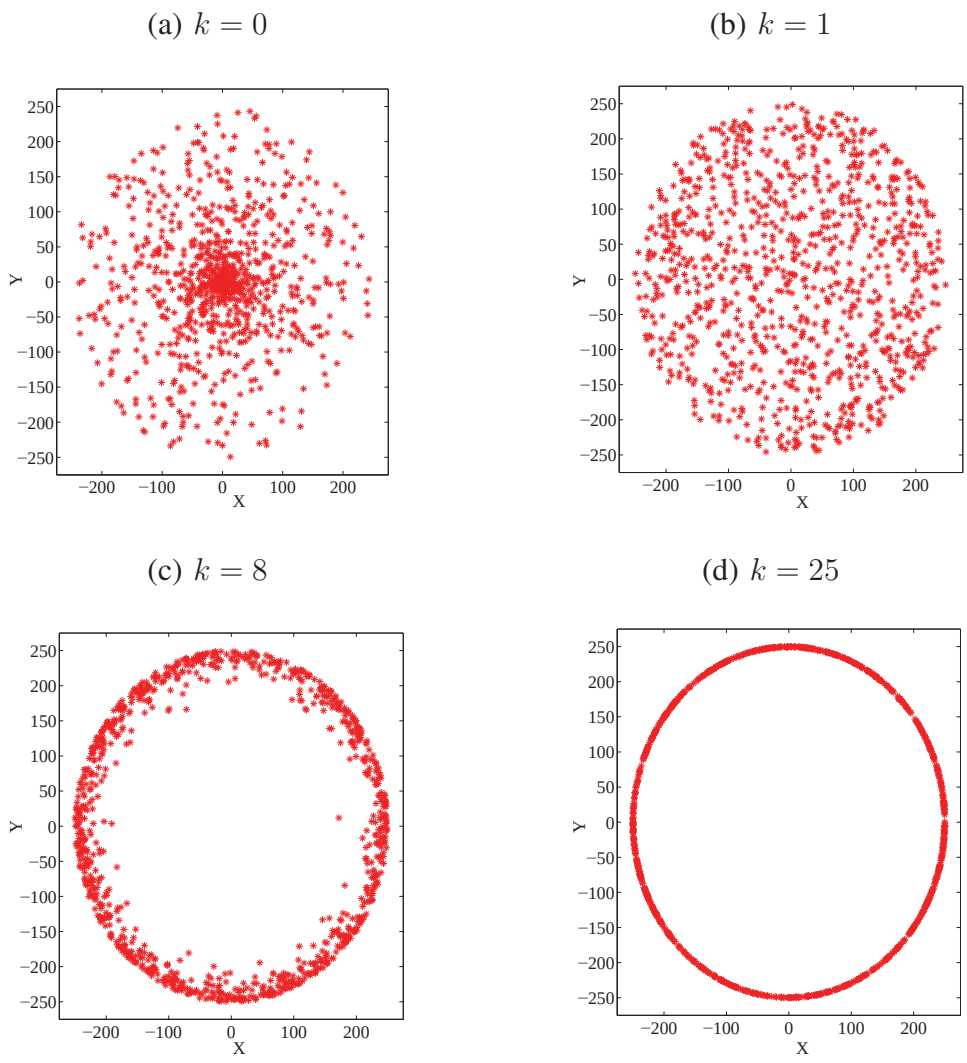

Figure 2.1: Scatter diagram illustrating 1000 randomly distributed scatterers (*) generated by using the unified disk scattering PDF with different shape factors: (a) $k = 0$, (b) $k = 1$, (c) $k = 8$, and (d) $k = 25$.

in Paper I. The polar representation of the PDF associated with the UDSM allows a mathematically simple geometry-based channel model, whereas other standard models are often more complex.

From the UDSM, one can derive stochastic and deterministic channel simulators by using the generalized principle of deterministic channel modelling [58, Sec. 8.1]. The designed channel simulator can then be used for the test, the parameter optimization, and the performance analysis of communication systems under different propagation conditions.

2.1.2 A Channel Model Based on Delay-Angle Joint Distributions

To verify a geometry-based stochastic channel model, its statistical characteristics need to be compared to empirical data collected from measured channels. A good match cannot necessarily be found, as the proposed scattering model might be oversimplified (overrestricted). As an example, many measurement campaigns (see, e.g., [3–5]) and specified channel models (see, e.g., [1]) show that the TOA PDF often follows a multiple negative exponential function (abbreviated by MNE TOA PDF). However, none of the scattering models studied in Paper I (including the UDSM itself) results in an MNE TOA PDF. The same disagreement might also arise by comparing measured AOA PDFs with the ones obtained from predefined scattering models.

To cope with this issue, Paper II proposes a new approach to the design of stationary channel models, via which obtaining the desired TOA (AOA) PDF is assured. Different from the original geometry-based channel modelling approach, the starting point of the new approach is not a predefined scattering model. Instead, we start from a given joint PDF of the TOA and AOA, from which the distribution of the local scatterers is derived. The given joint (marginal) PDF of the TOA and AOA can originate from either measured channels or channel specifications. In this way, we develop a channel model in which a perfect match between the statistical properties of the channel model and those of the measured (specified) channels is guaranteed. This approach also allows the physical explanation of the propagation area, which is not possible when using the correlation-based channel modelling approach [8] (see Chapter 1). In this approach, the obtained scattering area is not confined by firm geometric constraints, which often restrict geometry-based stochastic channel models proposed in the literature (see [14]).

In Paper II, we derive a mathematical representation for the scatterer distribution for given joint PDFs of the TOA and AOA. The result is presented in both polar and

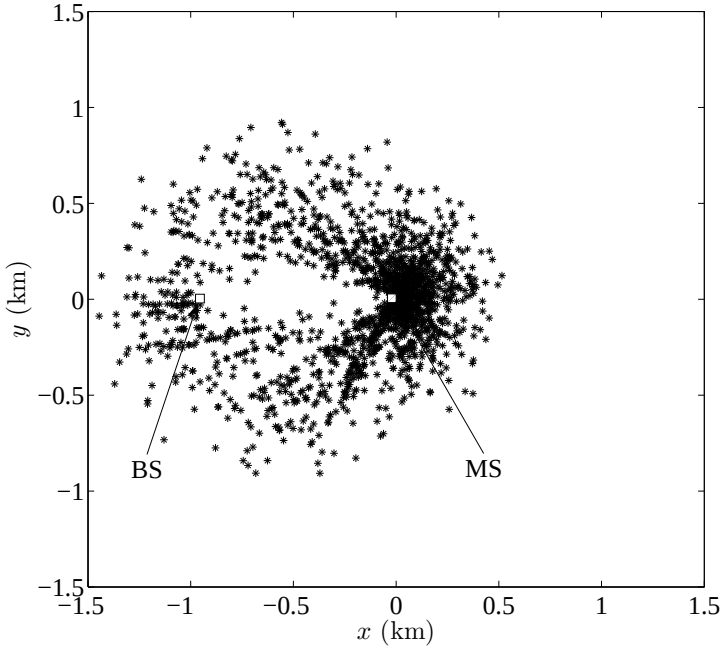

Figure 2.2: Scatter diagram for the typical urban channel with the TOA PDF specified in [1] and uniformly distributed AOAs.

Cartesian coordinates. As an exemplary application, the MNE TOA PDF specified in COST 207 is employed to derive the distribution of the local scatterers where the AOA is uniformly distributed around the MS and is independent of the TOA. The distribution of the scatterers in the propagation area is then illustrated in scatter diagrams (see, e.g., Fig. 2.2). Moreover, the marginal PDF of the distance from the scatterers to the MS is derived, displayed, and compared with simulation results. An excellent match between the analytical and simulation results is observed. It is shown that for the MNE TOA PDF, the local scatterers are not symmetrically distributed around the MS, which is in contrast with the circularly symmetric scattering assumption that is often made in the literature (see Paper I). In Paper II, we show that a typical urban area might be modelled by a disk centred on the BS-to-MS connecting line, while complicated urban environments [1] cannot be modelled by standard geometric shapes.

2.2 Chapter Summary and Conclusion

In this chapter, the principles of the UDSM, as well as its superiority over several established geometry-based channel models have been studied (see Paper I). It has been shown that the UDSM flexibly captures scattering effects caused by differ-

ent propagation environments, such as rural, sub-urban, and urban areas. We have shown that the UDSM unifies the Gaussian, uniform, hollow-disk, and ring scattering models into one compact model. It has been demonstrated that the UDSM outperforms its competitors in the sense of matching empirical data sets, in particular non-unimodal ones.

We have also proposed a new approach to the channel modelling under stationary conditions, in which the starting point of the design is an already established statistical property, such as the exponential PDP (see Paper II). Different from the correlation-based channel modelling approach, the new approach allows the physical explanation of the propagation area. We have employed the new approach to develop a stationary channel model, from which obtaining the MNE PDP is assured. We have also demonstrated that a typical urban area might be modelled by a disk centred on the line between the BS and the MS, but not necessarily on the MS, whereas bad urban areas [1] cannot be modelled by standard geometric shapes.

Chapter 3

Physically Non-Stationary Channel Models

3.1 Introduction

In this dissertation, a channel is called *physically non-stationary* if the local scatterers are in motion. We model such channels under the assumption that the observation time is very short, thus the corresponding channel model is statistically stationary. The motivation of developing such channel models is that moving scatterers are undetachable parts of real-world radio propagation environments. Moving foliage, walking pedestrians, and passing vehicles are only a few examples of scatterers in motion. In this connection, Fig. 3.1 exhibits a typical V2V propagation scenario in the presence of moving scatterers. Owing to the non-stationary nature of V2V communication channels, considering the effect of moving scatterers is of particular importance in the corresponding channel models. It has been reported in [34] that even if the transmitter and receiver are fixed (F2F communications), the received signal may still experience the Doppler effect. This means that moving scatterers can be a significant source for the Doppler spread, especially at millimeter wavelengths [35]. This phenomenon was studied empirically in [6] and [33], as well as analytically in [34] and [35].

3.2 Modelling of V2V Channels in the Presence of Moving Scatterers

The statistical properties of V2V channels in the presence of moving scatterers with random velocities and random directions have never been investigated in the litera-

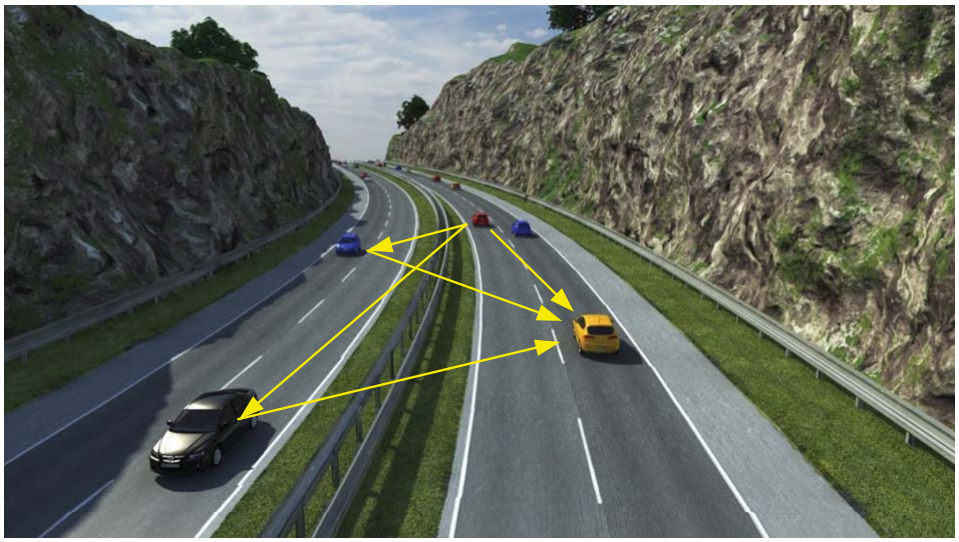

Figure 3.1: Typical V2V propagation scenario in the presence of moving scatterers (Photo from http://www.dd3d.hr).

ture. The aim of Paper III is to fill this gap by investigating the statistical properties of a narrowband V2V channel in which the local scatterers are moving with random velocities in random directions. The proposed V2V channel model does not impose any constraints on the position of the moving scatterers, thus it is somewhat different from geometry-based stochastic channel models, where local scatterers are often located on a standard geometric shape. Starting from the complex channel gain, we derive the temporal ACF and the corresponding PSD in integral form, which will then be simplified and examined under the assumption of different scatterer velocity distributions. In the area of transportation engineering, the most popular distribution models for the velocity of moving vehicles (fast moving scatterers) are the Gaussian and the Gaussian mixture (GM) models [59–64]. For the GM, exponential, and the uniform distributions of moving scatterers' velocity, the derived ACF is illustrated and compared to the classical ACF, which follows under the assumption of fixed scatterers. Moreover, the PSD of the channel is plotted and compared to the measurement data reported in [6]. These analyses are carried out at a carrier frequency of 5.9 GHz assigned to the dedicated short range communications (DSRC) standard as part of the intelligent transportation system (ITS). The results are shown for both relatively slow and relatively fast moving scatterers. The Doppler spread of the channel is also provided in closed form. It is shown that the Doppler spread of the channel model can be perfectly matched to the Doppler spread of the measured channel reported in [7].

Considering the effect of moving scatterers allows us to explain the non-zero

value of the Doppler spread obtained from F2F measurement campaigns. We remark that the non-zero value of the Doppler spread cannot be described by the channel models relying on the assumption of stationary scatterers. In Paper III, we have shown that relatively fast moving scatterers have a major impact on both V2V and F2F communication links, as they are significant sources of the Doppler spread. However, relatively slow moving scatterers can be neglected in V2V channels, but not in F2F links. It has been shown that the GM model can accurately describe the velocity distribution of relatively fast moving scatterers, while the exponential distribution can appropriately model the velocity of relatively slow moving scatterers.

The generality of the physically non-stationary channel model proposed in Paper III, allows us to derive the ACF, PSD, and the Doppler spread of the one-ring, two-ring, and elliptical model from the presented results in this paper. The proposed V2V channel model is a general model that includes the F2V and F2F channel models as special cases. Furthermore, the classical channel models, where the local scatterers are either fixed or in motion with deterministic velocities, can also be obtained as special cases of the proposed stochastic model. Paper III bridges to traffic modelling in the area of transportation engineering by employing the GM model in our analysis as a realistic distribution model describing the velocity of moving vehicles. The verification of the analytical results with measured real-world channels is another original contribution of this work.

3.3 Summary and Conclusion

In this chapter, we have discussed the concept of physically non-stationary channels, in which scatterers are moving. Particularly, we have designed a V2V channel model in which scatterers move with random velocities in random directions (see Paper III). The statistical properties of the proposed channel model have been derived and verified by empirical data obtained from measurement campaigns. We have shown that the GM and the exponential distributions are the best to explain the speed of relatively fast and relatively slow moving scatterers, respectively. It has been shown that moving objects have a major impact on many communication channels, especially those that are working in millimeter wavelengths.

Chapter 4

Trajectory Models Based on Brownian Fields

4.1 Introduction

For the development of non-stationary channel models, the MS needs to be tracked along its travelling path. Before developing non-stationary channel models, we first need to design a robust trajectory model to capture mobility patterns of the MS. The preparation of this material is the objective of the following chapter.

There are two major approaches for modelling the mobility of users: the user tracing approach and the synthetic approach [65–67]. The first approach extracts mobility patterns directly from real-world observations [68–71]. Despite the accuracy of these models, they are completely deterministic and entirely scenario dependent. Therefore, the performance of communication systems cannot easily be judged by these models. Nevertheless, there exist some trustworthy mobility models created by tracing thousands of wireless users over a long period of time [67]. The second approach develops a synthetic mobility model based on a given velocity distribution [72–74]. The physical location (trajectory) of the user is then determined by mapping given distributions of the speed and angle-of-motion (AOM) on the Euclidian space. The random walk [75, 76], random waypoint [77], Gauss-Markov [78], city section [79], and the pursue [66] mobility models are among the most important models designed by the aforementioned approach. A survey of mobility models proposed in the literature can be found in [72, 73, 80].

4.2 A Highly Flexible Trajectory Model Based on the Primitives of Brownian Fields

4.2.1 Fundamental Principles and Implementation Aspects

A fundamental drawback of synthetic mobility models is that the spatial characteristics of the path are forced to be determined by the temporal specifications of the user, such as his/her speed. A quick question that arises is, why should a physical configuration of a path be a function of the user's speed? This is in contrast to reality, where users try to adapt their speed and AOM to sideways, roads, and highways. This issue can also be extracted from [67], where the empirical user tracings reveal that the spatial characteristics of the mobility models are determined by the features of typical roads and walkways, but not by the temporal behaviour of road users.

Paper IV obviates the aforementioned drawback by providing a fully spatial trajectory model to which different speed scenarios (temporal features) can be applied. The main idea of this paper is to model the trajectory in position, but not in time. To achieve this, we need to expand the concept of stochastic processes to random fields in their very general form. We recall that stochastic processes are essentially mathematical models of random phenomena in time. On the other hand, random fields are generalized stochastic processes defined over a countable parameter, which is not necessarily time. The outcomes of random fields fall into some manifolds, multidimensional vectors, or points, which are also not necessarily measurable. Such a concept allows us to generate the random components (random vectors) of the path model in position, but not necessarily in time. The stepwise description of applying the new approach is provided in Paper IV.

In Paper IV, we employ the new approach to develop a novel random trajectory model using the primitives of Brownian fields (BFs). We design a partial random bridge from a predefined starting point to a partially random destination point, in which some drift components are employed to build targeted trajectories. The proposed trajectory model in Paper IV allows: 1) arriving at a predefined destination point if the bridge is fully established, 2) arriving at a circular boundary (target zone) with a predefined radius and centre if the bridge is partially established, 3) a totally random point in the 2D plane if the bridge is broken, and finally 4) bridging back (closed loop) to the starting point if the bridge is fully established, but the drift component does not exist. The first and the second configuration are shown in Figs. 4.1 and 4.2. More examples, as well as the description of the figures, can be found in Paper IV.

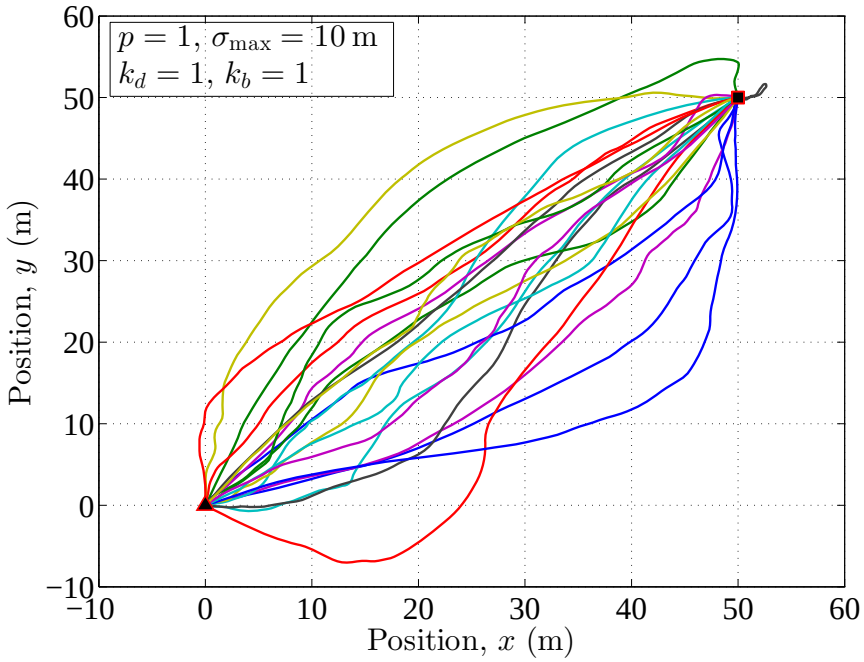

Figure 4.1: Random trajectories connecting a fixed starting point and a fixed destination point via fully random bridges based on the first primitive of BFs.

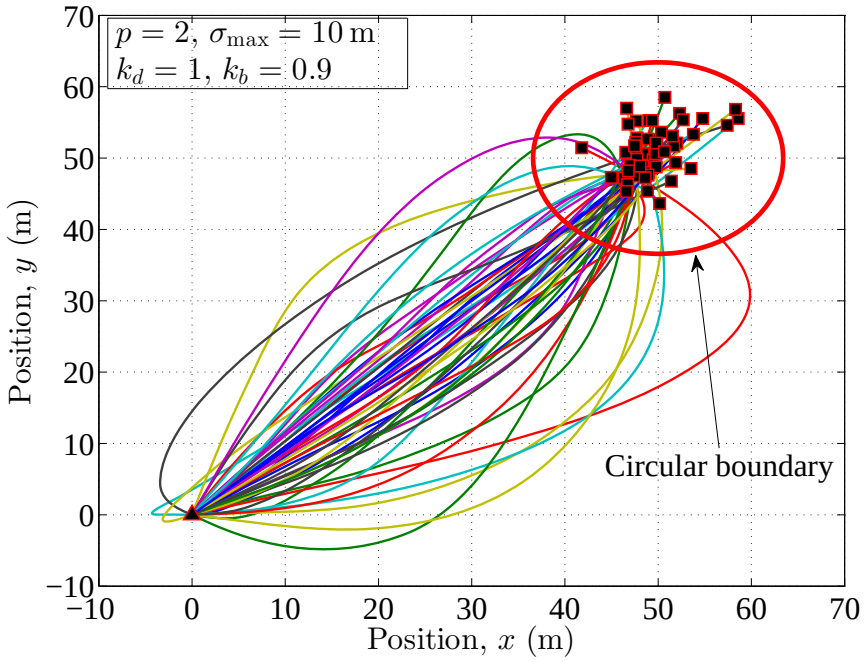

Figure 4.2: Random trajectories connecting a fixed starting point and a random destination point located in a certain target zone via partially random bridges based on the second primitive of BFs.

In this paper, we show that the proposed path model renders a great number of configurations, while the smoothness level of each path configuration can be controlled by the primitives of BFs. We also demonstrate that the proposed trajectory model can describe both targeted and non-targeted dynamics of users in motion. The resulting trajectories can be travelled with different speeds without influencing the path configuration. In addition, we show that the path model proposed in Paper IV is useful to model the trajectory of many daily life activities, such as possible trajectories of vehicles trying to perform U-turns, possible trajectories starting from the tourist information office to a historical zone, and possible trajectories from the police department to a crime scene, only to name a few. Moreover, we provide a MATLAB® code for simulating paths generated by the proposed trajectory model, showing that the code is fast and easy to implement.

4.2.2 Analysis of the Statistical Properties

To highlight the usefulness of the proposed trajectory model in Paper IV, we study its statistical properties in Paper V. It is worth mentioning that the number of mathematical studies on the spatial properties of mobility models is very limited in the literature. From this perspective, Paper V is quite unique.

Given the discussed stochastic trajectory model in Paper IV, Paper V derives its spatial mean and variance, as well as a closed-form expression for the ACF of the path process. Moreover, we introduce a complex spatial increment process, by which the AOM and the incremental travelling length processes are computed. The first-order density of these processes is presented in closed form. By summing up the incremental travelling lengths, we calculate the overall travelling length and then derive its PDF.

In Paper V, we show that the path process is in general non-stationary. Furthermore, it is shown that the AOM and the incremental travelling length processes are modelled by the phase and the envelope of a complex Gaussian process with non-identical means and variances of the quadrature components. We also demonstrate that the AOM and the incremental travelling length are in general non-stationary processes. In this connection, we prove that the AOM process does not follow the uniform distribution, which agrees with empirical traces reported in [67]. However, the uniform AOM can be obtained as a special case. In addition, we illustrate that the incremental travelling length process follows the Rice and Nakagami-q distributions as special cases. For the path based on the primitives of the standard BFs, we show that the overall travelling length follows closely the lognormal distribution, which is in line with many real-life tracing records [67, 81–83]. For the path based

on the standard BF, we prove that the overall travelling length follows the Gaussian distribution, which has been reported from empirical studies in dense urban environments [59–64, 84].

4.3 Chapter Summary and Conclusion

The spatial configuration of the path travelled by the MS has a key role in the development of non-stationary mobile fading channels. In this chapter, we have reviewed Paper IV and V, in which the fundamental principles and the statistical properties of a highly flexible trajectory model are studied, respectively.

From Paper IV, it can be concluded that the flexibility of the proposed trajectory is threefold: 1) its numerous configurations, 2) its smoothness control possibility, and 3) its adaptivity to various speed scenarios. In addition, it has been shown that the proposed model can easily be implemented in simulation environments, such as MATLAB®, NS2, and OPNET.

Among other findings reported in Paper V, we have shown that the incremental travelling length process follows the Rice and Nakagami-*q* distribution as special cases. More importantly, Paper V concludes that depending on the primitive order, the length of the total travelling path follows either the Gaussian distribution, or the lognormal distribution, both of which have been widely reported in empirical studies.

Chapter 5

Statistically Non-Stationary Channel Models

5.1 Introduction

Mobile radio channels are inherently non-stationary, meaning that their statistical properties change in time (position). Causes for this non-stationarity are manifold. In principle, any event that changes the wave propagation between the transmitter and the receiver to a significant amount regarding time, frequency or direction, causes a non-stationary change in the channel statistics [85]. Typical causes for the non-stationarity of the channel are the moving transmitter, moving receiver, and/or moving scatterers. A single moving entity is enough to have a time-varying propagation area (mechanism), which results in changes in the AOD, AOA, TOA, and AOM in time. The time-variation of these quantities is then injected to the statistical properties of the channel such as the PDP, the PSD, and the time (frequency) correlation functions.

The strength of the non-stationary changes depends heavily on the considered environment. In indoor environments, it is likely that the channel changes significantly even if the mobile moves insignificantly [85]. In outdoor scenarios, the mobile can possibly move in the order of a few tens of the wavelength of the carrier signal before the channel statistics change [86]. Many empirical and analytical investigations, e.g., [29–31] show that the stationary assumption for the channel is only valid for extremely short travelling distances [32]. In the literature, different metrics have been proposed to measure the non-stationarity of mobile radio channels. In [30], the correlation coefficient between consecutive PDPs is considered as a metric to define a local region of stationarity, namely a region where the PDP does not vary significantly. Comparing the PDPs estimated at different time instances is

another test to determine the stationarity level of the radio channel [31]. Several other metrics together with their validity tests can also be found in [87–89].

The main objective of the aforementioned metrics is to determine the region in which the channel can be assumed as WSSUS or at least quasi-WSSUS. However, real-world mobile radio channels never fulfill the stationary assumption not only in the strict sense, but also in the wide sense. In this chapter, the aim is to develop channel models that capture the non-stationarity of mobile radio channels in the strict sense. Therefore, we rely on a strict definition according to which a channel model is called *statistically non-stationary* if its statistical properties vary in time (position). This definition is in line with the one in [90]. We remark that determining the stationary region of our proposed channel models is outside of the scope of this dissertation.

The geometry-based stochastic channel modelling approach is known to be suitable for capturing the non-stationarity of mobile radio channels [17, 27, 28]. The basic idea behind the development of geometry-based non-stationary channel models is to update the channel characteristics along the travelling path of the MS. In this connection, Fig. 5.1 displays a typical F2M propagation scenario, in which the AOA at the MS and the AOM of the MS vary in position (time). By adding randomness to the position of scatterers, the model then becomes stochastic. The number of channel models proposed by this approach is very limited. A geometry-based non-stationary channel model for high-speed train communications was developed in [91]. Therein, it is assumed that the high-speed train is moving along a straight line surrounded by an infinite number of scatterers. The authors of [17] also proposed a geometry-based non-stationary channel model for V2V channels in highway environments, where it is assumed that the vehicles are moving along a straight path. A non-stationary T-junction channel model for V2V communication was also proposed in [92]. The unique geometric structure of these models, unfortunately, restricts their usability in modelling different propagation areas. In addition, the utilized path models in [17, 91, 92] are somewhat unrealistic, as the AOM of the MS cannot not change in time. This is in contrast with real-world moving scenarios in which the AOM varies along the travelling path.

The limited number of non-stationary channel models in the literature on the one hand, and some drawbacks of existing models on the other hand, call for the need to develop new, robust, and flexible non-stationary channel models. To this aim, we first introduce a new approach to develop geometry-based stochastic non-stationary channel models, the randomness of which originates from a random trajectory of the MS, rather than from the scattering area. It is shown that the channel models

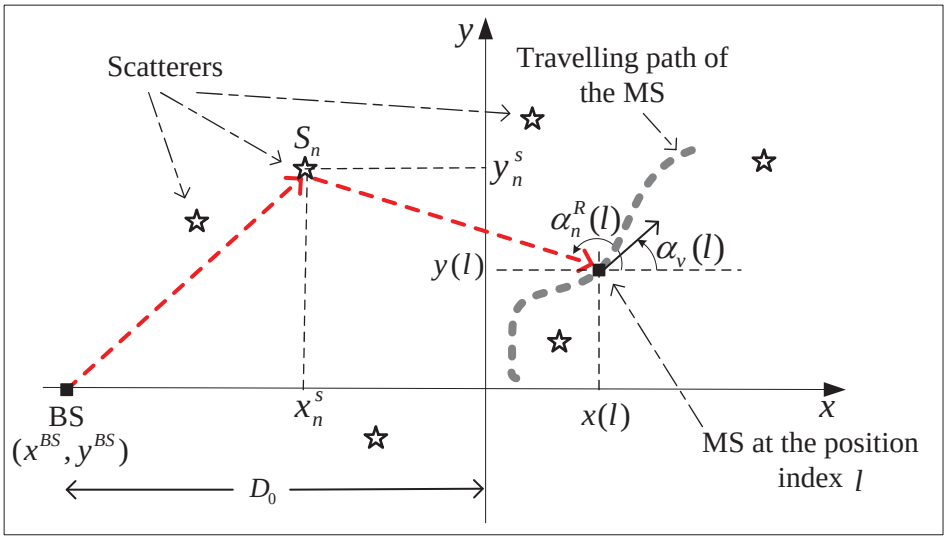

Figure 5.1: A typical F2M propagation scenario assuming single-bounce scattering.

developed by this approach have great benefits that cannot easily be obtained by the former approaches. A robust non-stationary channel model superimposing large-scale fading and small-scale fading is designed by means of the new approach. To generate the travelling path of the MS, we employ the random trajectory model proposed in Paper IV. In addition, a more traditional approach, in which the randomness of the channel model originates from the distribution of scatterers (scattering area) is also considered. This approach is utilized to develop two non-stationary channel models, in which the travelling path of the MS is a sample function (single realization) of a Brownian random path, which is assumed to be surrounded by a ring of randomly distributed scatterers.

5.2 A Random Trajectory Approach for the Development of Non-Stationary Channel Models

5.2.1 Principles of the New Approach

The traditional approach in geometry-based stochastic channel modelling is to start from a geometric pattern with randomly distributed scatterers. An example of such models is the channel model proposed in Paper I. The randomness of the scatterer positions is then injected to the characteristics of the channel model, such as its envelope, PDP, PSD, and correlation properties. One of the key factors influencing the characteristics of the channel models designed by this approach is therefore the

number of scatterers. To develop a so-called reference model, this number is assumed to tend to infinity. In this dissertation, we call this *the infinity assumption*. The infinity assumption then allows designers to apply some limit theorems, such as the central limit theorem (CLT) of Lindeberg-Lévy, to conclude that the proposed channel model behaves like a Rayleigh, Rice, or lognormal (CLT for products) fading channel. The obvious shortcoming of the reference model is that the infinity assumption does not hold in real-world propagation environments. Even if such a highly rich scattering area would exist, moving through this area would be impossible. Therefore, proposing any *mobile* radio channel model with dense scattering scenarios is mathematically convenient but physically meaningless. Another issue is the restriction of computer-based simulation environments, where applying the infinity assumption is not possible. Accordingly, designers provide a so-called simulation model, in which the infinity assumption is relaxed by reducing the number of scatterers. However, this reduction degrades the characteristics of the channel model somewhat from those of reference models.

In Paper VI, we introduce a new geometry-based stochastic channel modelling approach, the base of which is that the trajectory of the MS is random, whereas the scattering area is fixed. The positions of the scatterers are determined either by realizing any desired distribution function, or by setting them manually. Let us assume that the MS is moving along a sample trajectory generated by a random trajectory model. For a fixed scattering area, each realization of the trajectory results in different AOMs of the MS, different AOAs at the MS, as well as different travelling distances of the plane wave emitted from the transmitter. Therefore, the randomness of the trajectory model makes the characteristics of the corresponding channel model random. It follows that we provide a geometry-based non-stationary channel model, the randomness of which originates from the trajectory of the MS, rather than the scattering area.

We show that applying the new approach results in very robust non-stationary channel models, in which the infinity assumption does not need to be fulfilled. In Paper VI, we also discuss how the new approach can be used for simulating/interpreting measurement campaigns, in which a certain propagation area (fixed scattering area) undergoes several measurement trials (random trajectories).

5.2.2 Employment of the New Approach

Paper VI employs the new approach by allowing the MS to move along random paths generated by a special case of the trajectory model proposed in Paper IV. This special case allows the MS to arrive at a fixed destination point via random paths.

It is also assumed that the position of scatterers (scattering area) is obtained by realizing a 2D Gaussian distribution function.

We provide an additive complex channel gain model, in which not only the Doppler frequencies, but also the propagation path delays and the propagation path gains are stochastic processes that vary in position. In our model, the path gains are determined by a negative power law applied to the total travelling distance of the plane waves, which is in line with the basic idea of any path loss model. We also formulate the AOA process and the AOM process, from which the Doppler frequency process is derived. The corresponding first-order densities are computed. Thus, we fully characterize the complex channel gain of the proposed non-stationary channel model. We then step further by deriving the first-order density of the channel gain envelope, the first-order density of the total received power, as well as the local PDP, and the local PSD processes.

Simulation results at the operating frequency 2.1 GHz of the UMTS show that the statistical properties of the proposed non-stationary channel model are very robust with respect to the number of scatterers. For instance, it is demonstrated that the envelope of the complex channel gain closely follows a Suzuki process, even if the number of scatterers is only four. It is worth mentioning that many measurement campaigns have reported that multi-scale fading channels under non-line-of-sight propagation conditions are best modelled by a Suzuki process [93, 94]. For the same number of scatterers, we show that the local received power follows the lognormal distribution, indicating that the channel model captures the shadow fading even for a very limited number of scatterers. The merit of the proposed channel model is not only its robustness with respect to the number of scatterers, but also its capability to take non-stationary aspects of the channel into account.

Moreover, it is shown that the proposed channel model in Paper VI allows two degrees of freedom to control the spread of the shadowing. Moreover, we illustrate that the spread of the shadowing is approximately independent of the position of the BS, which is in line with the empirical experiences reported, e.g., in [95–99]. In addition, it is demonstrated that the mean received power decreases by increasing the BS-to-MS distance, affirming that the model captures the path loss effect. We also show that the time-varying effect of each scatterer on the local PDP and the local PSD can perfectly be tracked if the channel is sufficiently sparse.

The proposed non-stationary channel model superimposes different levels of fading via a physically explainable multipath fading model, rather than a multiplicative one. The proposed channel model provides a physical (geometrical) insight to the theoretical studies in [100, 101]. The results provided in this paper are very

useful for the development of mobile communication systems, e.g., for the design of Rake receivers [102], power control and handoff algorithms.

5.3 A Random Scattering Approach for the Development of Non-Stationary Channel Models

In this section, we focus on a more traditional approach in which a non-stationary channel model is developed by updating the channel characteristics along the travelling path of the MS, which is surrounded by *randomly distributed scatterers*. In this regard, the travelling path of the MS can be an outcome of a random trajectory, while the propagation area can be modelled by any standard geometry-based stochastic scattering model discussed in Chapter 2. This approach is used to propose the non-stationary channel models in Paper VII and VIII, where the infinity assumption needs to be held. Thus, Papers VII and VIII differ from Paper VI not only in the utilized approach, but also in the number of scatterers.

Paper VII employs a special case of the proposed trajectory model in Paper IV to generate the travelling path of the MS. The path is a realization of the manipulated standard Brownian motion processes, via which either a random or a predefined destination point can be reached. In this regard, the straight (line) path model in [103] is obtained from the proposed model if the random components of the path along each axis are ignored, but the drift components exist, but not the random components. To capture the scattering effects of the propagation environment, we use a non-centred one-ring scattering model, in which the MS is surrounded by a ring of scatterers centred not necessarily on the MS.

In Paper VII, we track the MS along a fixed Brownian path to record the variations of the wave propagation mechanism in time. Accordingly, we derive the local AOAs, local AOMs, local PSD of the Doppler frequencies, and the ACF of the complex channel gain, showing that even for a walking speed scenario, the channel model shows non-stationary behaviors. It is proved that non-stationarity in time is not in line with the common isotropic propagation assumption on the channel. Numerical results at 2.1 GHz shows that the proposed channel model results in a twisted version of the Jakes PSD that varies in time. Furthermore, it is shown that the stationary one-ring scattering model [36–38] can be obtained as a special case of the proposed channel model.

In Paper VIII, we follow almost the same procedure. The difference is that in Paper VIII, the employed trajectory model incorporates random fluctuations only along a specific line (axis). In this connection, by increasing the slope of the drift

towards infinity, the fluctuations occur only along the vertical axis. Again, a non-centred one-ring scattering model is used to capture the scattering effect of the propagation area. The displacement of the MS from the ring's center results in a non-isotropic channel model.

In Paper VIII, we show that the proposed path model results in a non-stationary non-isotropic channel model, from which the stationary isotropic one-ring scattering model can be obtained as a special case. The statistical properties of the proposed channel model are derived and explained physically. It is shown that the AOA process is first-order non-stationary, while the PDF of the AOM is stationary. The corresponding PSD of the Doppler frequencies and ACF of the complex channel gain are also provided, showing that these characteristics are heavily time-dependent. It is shown that the proposed channel model results in a twisted Jakes PSD that changes in time, indicating that the non-stationarity in time is in contrast with the isotropic propagation assumption on the channel.

5.4 Chapter Summary and Conclusion

We have introduced two different approaches for the development of non-stationary channel models. In the first approach, the randomness of the channel model originates from the randomness of the trajectory of the MS, while in the second one, the randomness of the scattering area makes the model stochastic. The first approach is very new and renders robust non-stationary channel models. The second approach is somewhat similar to the approach used in [17, 91, 92] with the difference that in Papers VII and VIII, the AOM of the MS can change in time, while in [17, 91, 92], the AOM remains fixed.

We have shown that both approaches are very useful for the modelling of non-stationary mobile fading channels. Highly reported physical channel statistics can be obtained from the channel models developed by these approaches. We have demonstrated that in the channel models developed by the first approach, the infinity assumption does not need to be fulfilled. Even a very limited number of scatterers is sufficient to develop a non-stationary channel model resulting in a Suzuki distributed envelope of the complex channel gain (among other useful properties). To obtain the desired statistical properties by means of the second approach, the infinity assumption, however, needs to be held. It was also realized that the non-stationarity of the channel model can better be seen in the PSD as compared to the ACF of the complex channel gain.

We have also shown that Brownian processes (fields) are very useful for captur-

ing the mobility features of the MS. It can be concluded that one alternative to the development of robust non-stationary channel models in the sense of matching different propagation environments, is to employ flexible trajectory models that allow variations of the AOM.

We finish this chapter by remarking that Paper XV (not included in this dissertation) also develops a new non-stationary channel model, in which the effect of velocity variations of the mobile station is studied.

Chapter 6

Summary of Contributions and Outlook

6.1 Major Contributions

This dissertation dealt with the modelling of mobile fading channels under stationary, physically non-stationary, and statistically non-stationary conditions. The topics covered the range from providing stationary and non-stationary channel models, over analyzing the effect of moving scatterers, up to the trajectory modelling by means of Brownian fields. In the following, the contributions of this doctoral dissertation are summarized.

- A unified stationary channel model called the UDSM was proposed. The statistical properties of the UDSM were derived and validated by empirical data. It was shown that the UDSM is very flexible and robust in the sense of matching empirical data obtained from different measurement campaigns.

- A new approach for the development of stationary channel models based on desired statistical properties was proposed. It was shown that the new approach allows the physical explanation of the propagation area, while obtaining the desired statistical characteristics is assured.

- A physically non-stationary channel model for explaining V2V channels in the presence of moving scatterers was developed. The statistical properties of the channel were derived and verified by empirical data. Proper distributions for explaining the speed of relatively fast and relatively slow moving scatterers were proposed. It was shown that relatively fast moving scatterers have a major impact on both V2V and fixed-to-fixed (F2F) communication links,

whereas relatively slow moving scatterers can be neglected in V2V channels, but not in F2F channels.

- A new approach for generating fully spatial random trajectory models was proposed. A highly flexible trajectory model based on the primitives of BFs was developed. It was shown that the proposed trajectory model can explain numerous mobility patterns of the MS. The statistical properties of the trajectory model were also derived and validated by empirical data obtained from user tracings.

- A random trajectory approach for the development of non-stationary channel models was introduced. It was shown that the new approach develops very robust channel models in the sense of the number of scatterers. It was also remarked that the new approach is useful for simulating/interpreting measurement campaigns.

- A new non-stationary channel model based on the proposed Brownian random trajectory model was developed. It was shown that the proposed channel model superimposes large-scale and small-scale fading. It was demonstrated that the characteristics of the proposed channel model are in line with those of physical channels even if the scattering area is sparsely seeded.

- Two non-isotropic non-stationary channel models in which the travelling path of the MS is the outcome of a Brownian trajectory model were developed. It was shown that the proposed channel model results in a twisted Jakes PSD that changes in time, indicating the non-stationarity in time is in contrast with the isotropic propagation assumption on the channel. It was also realized that the effect of changing the mobility pattern can better be seen in the PSD as compared to the ACF of the complex channel gain.

6.2 Outlook

This dissertation was an attempt to probe into the issues related to the modeling and analysis of mobile fading channels with different levels of stationarity. There still exist problems that remain unaddressed. Some few problems are highlighted in the following.

- The entire analysis presented in this dissertation is based on the assumption that the wave emitted from the transmitter arrives at the receiver after a single

bounce by one of the local scatterers. This assumption can be extended by considering the effect of multiple-bounce scattering.

- The entire analysis presented in this dissertation is based on the assumption that the wave emitted from the transmitter is not polarized. This assumption can be relaxed such that the polarization effect of the propagation area is taken into consideration.
- The physically non-stationary channel model designed in this dissertation needs to be analyzed under statistically non-stationary conditions.
- Channel models capturing the mixture of fixed and moving scatterers need to be developed.
- The entire channel models presented in this dissertation consider a single antenna at both the transmitter and the receiver side. The models can be expanded by considering multiple antennas at the transmitter and/or the receiver.
- The approach used to develop the highly flexible trajectory model based on the primitives of the BFs may also be used to generate other spatial trajectory models.
- The non-stationary channel models relying on Brownian random trajectory models may also be developed by utilizing other trajectory models.

REFERENCES

[1] M. Failli, Ed., *COST 207: Digital Land Mobile Radio Communications*. Luxembourg: Commission of the European Communities, 1989.

[2] K. I. Pedersen, P. E. Mogensen, and B. H. Fleury, "Spatial channel characteristics in outdoor environments and their impact on BS antenna system performance," in *Proc. IEEE 48th Veh. Technol. Conf., VTC 1998,* vol. 2. Ottawa, Canada, pp. 719–723.

[3] M. D. Batariere, T. K. Blankenship, J. F. Kepler, T. P. Krauss, I. Lisica, S. Mukthavaram, J. W. Porter, T. A. Thomas, and F. W. Vook, "Wideband MIMO impulse response measurements at 3.7 GHz," in *Proc. IEEE 45th Veh. Technol. Conf., VTC 2002*, vol. 1, pp. 26–30.

[4] K. I. Pedersen, P. E. Mogensen, and B. H. Fleury, "A stochastic model of the temporal and azimuthal dispersion seen at the base station in outdoor propagation environments," *IEEE Trans. Veh. Technol.*, vol. 49, no. 2, pp. 437–447, Mar. 2000.

[5] C. Kloch, G. Liang, J. B. Andersen, G. F. Pedersen, and H. L. Bertoni, "Comparison of measured and predicted time dispersion and direction of arrival for multipath in a small cell environment," *IEEE Trans. Antennas Propag.*, vol. 49, no. 9, pp. 1245–1263, Sep. 2001.

[6] N. Naz and D. D. Falconer, "Temporal variations characterization for fixed wireless at 29.5 GHz," in *Proc. IEEE Veh. Technol. Conf., VTC 2000*. Tokyo, Japan, May 2000, pp. 2178–2182.

[7] L. Cheng, B. E. Henty, D. D. Stancil, F. Bai, and P. Mudalige, "Mobile vehicle-to-vehicle narrow-band channel measurement and characterization of the 5.9 GHz dedicated short range communication (DSRC) frequency band," *IEEE J. Select. Areas Commun.*, vol. 25, no. 8, pp. 1501–1516, Oct. 2007.

[8] C. C. Chong, F. Watanabe, K. Kitao, T. Imai, and H. Inamura, "Evolution trends of wireless MIMO channel modeling towards IMT-advanced," *IEICE Transactions*, vol. 92-B, no. 9, pp. 2773–2788, 2009.

[9] P. Bello, "Characterization of randomly time-variant linear channels," *IEEE Trans. Commun.*, vol. 11, no. 4, pp. 360–393, Dec. 1963.

[10] R. H. Clarke, "A statistical theory of mobile-radio reception," *Bell Sys. Tech. J.*, vol. 47, no. 1, pp. 957–1000, Jul. 1968.

[11] W. C. Jakes, Ed., *Microwave Mobile Communications*. Piscataway, NJ: IEEE Press, 1994.

[12] P. Almers, E. Bonek, A. Burr, N. Czink, M. Debbah, V. Degli-Esposti, H. Hofstetter, P. Kyoesti, D. Laurenson, G. Matz, A. Molisch, C. Oestges, and H. Oezcelik, "Survey of channel and radio propagation models for wireless MIMO systems," *EURASIP J. Wireless Commun. Networking*.

[13] M. Pätzold, A. F. Molisch, and C. Oestges, "Trends in mobile radio channels—modeling, analysis, and simulation," *IEEE Veh. Technol. Mag.*, vol. 6, no. 2, Jun. 2011.

[14] K. T. Wong, Y. I. Wu, and M. Abdulla, "Landmobile radiowave multipaths' DOA-distribution: Assessing geometric models by the open literature's empirical datasets," *IEEE Trans. Antennas Propag.*, vol. 58, no. 3, pp. 946–958, Mar. 2010.

[15] A. Borhani and M. Pätzold, "A unified disk scattering model and its angle-of-departure and time-of-arrival statistics," *IEEE Trans. Veh. Technol.*, vol. 62, no. 2, pp. 473–485, Feb. 2013.

[16] H. Asplund, A. A. Glazunov, A. F. Molisch, K. I. Pedersen, and M. Steinbauer, "The COST 259 directional channel model-Part II: Macrocells," *IEEE Trans. Wireless Commun.*, vol. 5, no. 12, pp. 3434–3450, Dec. 2006.

[17] J. Karedal, F. Tufvesson, N. Czink, A. Paier, C. Dumard, T. Zemen, C. F. Mecklenbräuker, and A. F. Molisch, "A geometry-based stochastic MIMO model for vehicle-to-vehicle communications," *IEEE Trans. Wireless Commun.*, vol. 8, no. 7, pp. 3646–3657, Jul. 2009.

[18] M. C. Lawton and J. P. McGeehan, "The application of a deterministic ray launching algorithm for the prediction of radio channel characteristics in small-cell environments," *IEEE Trans. Veh. Technol.*, vol. 43, no. 4, pp. 955–969, Nov. 1994.

[19] G. Liang and H. L. Bertoni, "A new approach to 3-D ray tracing for propagation prediction in cities," *Antennas and Propagation, IEEE Transactions on*, vol. 46, no. 6, pp. 853–863, Jun. 1998.

[20] K. Rizk, J.-F. Wagen, and F. Gardiol, "Influence of database accuracy on two-dimensional ray-tracing-based predictions in urban microcells," *IEEE Trans. Veh. Technol.*, vol. 49, no. 2, pp. 631–642, Mar. 2000.

[21] K. H. Ng, E. K. Tameh, A. Doufexi, M. Hunukumbure, and A. R. Nix, "Efficient multielement ray tracing with site-specific comparisons using measured MIMO channel data," *IEEE Trans. Veh. Technol.*, vol. 56, no. 3, pp. 1019–1032, May 2007.

[22] Z. Wang, E. K. Tameh, and A. R. Nix, "Joint shadowing process in urban peer-to-peer radio channels," *IEEE Trans. Veh. Technol.*, vol. 57, no. 1, pp. 52–64, Jan. 2008.

[23] J. J. Blanz and P. Jung, "A flexibly configurable spatial model for mobile radio channels," *IEEE Trans. Commun.*, vol. 46, no. 3, pp. 367–371, Mar. 1998.

[24] O. Norklit and J. B. Andersen, "Diffuse channel model and experimental results for array antennas in mobile environments," *IEEE Trans. Antennas Propag.*, vol. 46, no. 6, pp. 834–840, Jun. 1998.

[25] A. Abdi and M. Kaveh, "A space-time correlation model for multielement antenna systems in mobile fading channels," *IEEE J. Select. Areas Commun.*, vol. 20, no. 3, pp. 550–560, Apr. 2002.

[26] C. Oestges, V. Erceg, and A. J. Paulraj, "A physical scattering model for MIMO macrocellular broadband wireless channels," *IEEE J. Select. Areas Commun.*, vol. 21, no. 5, pp. 721–729, Jun. 2003.

[27] A. F. Molisch, A. Kuchar, J. Laurila, K. Hugl, and R. Schmalenberger, "Geometry-based directional model for mobile radio channels—principles and implementation," *European Transactions on Telecommunications*, vol. 14, no. 4, pp. 351–359, Jul./Aug. 2003.

[28] A. F. Molisch, "A generic channel model for MIMO wireless propagation channels in macro- and microcells," *IEEE Trans. Signal Processing*, vol. 52, no. 1, pp. 61–71, Jan. 2004.

[29] A. Ispas, G. Ascheid, C. Schneider, and R. Thomä, "Analysis of local quasi-stationarity regions in an urban macrocell scenario," in *Proc. 71th IEEE Veh. Technol. Conf., VTC 2010-Spring*. Taipei, Taiwan, May 2010.

[30] A. Gehring, M. Steinbauer, I. Gaspard, and M. Grigat, "Empirical channel stationarity in urban environments," in *Proc. 4th European Personal Mobile Communications Conference*. Vienna, Austria, Feb. 2001.

[31] D. Umansky and M. Pätzold, "Stationarity test for wireless communication channels," in *Proc. IEEE Global Communications Conference, IEEE GLOBECOM 2009*. Honolulu, Hawaii, USA, Nov./Dec. 2009.

[32] A. Paier, J. Karedal, N. Czink, C. Dumard, T. Zemen, F. Tufvesson, A. F. Molisch, and C. F. Mecklenbräucker, "Characterization of vehicle-to-vehicle radio channels from measurements at 5.2 GHz," *Wireless Personal Communications (WPC)*, vol. 50, no. 1, pp. 19–32, Jul. 2009.

[33] A. Domazetovic, L. J. Greenstein, N. B. Mandayam, and I. Seskar, "Estimating the Doppler spectrum of a short-range fixed wireless channel," *IEEE Communications Letters*, vol. 7, no. 5, pp. 227–229, May 2003.

[34] V.-H. Pham, M. H. Taieb, J. Y. Chouinard, S. Roy, and H.-T. Huynh, "On the double Doppler effect generated by scatterer motion," *REV Journal on Electronics and Communications*, vol. 1, no. 1, pp. 30–37, Jan.-Mar. 2011.

[35] S. Roy, H. T. Huynh, and P. Fortier, "Compound Doppler spread effects of subscriber motion and scatterer motion," *International Journal of Electronics and Communications*, vol. AEÜ-57, no. 4, pp. 237–246, 2003.

[36] D.-S. Shiu, G. J. Foschini, M. J. Gans, and J. M. Kahn, "Fading correlation and its effect on the capacity of multielement antenna systems," *IEEE Trans. Commun.*, vol. 48, no. 3, pp. 502–513, Mar. 2000.

[37] A. Abdi and M. Kaveh, "A space-time correlation model for multielement antenna systems in mobile fading channels," *IEEE J. Select. Areas Commun.*, vol. 20, no. 3, pp. 550–560, Apr. 2002.

[38] M. Pätzold and B. O. Hogstad, "A space-time channel simulator for MIMO channels based on the geometrical one-ring scattering model," in *Proc. 60th IEEE Veh. Technol. Conf., VTC 2004-Fall*, vol. 1. Los Angeles, CA, USA, Sep. 2004, pp. 144–149.

[39] A. Y. Olenko, K. T. Wong, and E. H. O. Ng, "Analytically derived TOA-DOA statistics of uplink/downlink wireless multipaths arisen from scatterers on an hollow-disc around the mobile," *IEEE Antennas Wireless Propag. Lett.*, vol. 2, pp. 345–348, 2003.

[40] I. Jaafar, H. Boujemaa, and M. Siala, "Angle and time of arrival statistics for hollow-disc and elliptical scattering models," in *Proc. 2nd Int. Conf. Signals, Circuits Syst., Nov. 2008*, pp. 1–4.

[41] P. C. F. Eggers, "Generation of base station DOA distributions by Jacobi transformation of scattering areas," *Electron. Lett.*, vol. 34, no. 1, pp. 24–26, Jan. 1998.

[42] R. J. Piechocki, G. V. Tsoulos, and J. P. McGeehan, "Simple general formula for PDF of angle of arrival in large cell operational environments," *Electron. Lett.*, vol. 34, no. 18, pp. 1784–1785, Sep. 1998.

[43] P. Petrus, J. H. Reed, and T. S. Rappaport, "Geometrical-based statistical macrocell channel model for mobile environments," *IEEE Trans. Commun.*, vol. 50, no. 3, pp. 507–510, Mar. 2002.

[44] D. R. Van Rheeden and S. C. Gupta, "A geometric model for fading correlation in multipath radio channels," in *IEEE Int. Conf. on Communications, ICC 1998*. Atlanta, GA, USA, Jun. 1998, pp. 1655–1659.

[45] L. Jiang and S. Y. Tan, "Simple geometrical-based AOA model for mobile communication systems," *Electron. Lett.*, vol. 40, no. 19, pp. 1203–1205, Sep. 2004.

[46] R. B. Ertel and J. H. Reed, "Angle and time of arrival statistics for circular and elliptical scattering models," *IEEE J. Select. Areas Commun.*, vol. 17, no. 11, pp. 1829–1840, Nov. 1999.

[47] J. C. Liberti and T. S. Rappaport, "A geometrically based model for line-of-sight multipath radio channels," in *Proc. IEEE Veh. Technol. Conf., VTC 1996*, Apr./May 1996, pp. 844–848.

[48] R. Janaswamy, "Angle and time of arrival statistics for Gaussian scatter density model," *IEEE Trans. Wireless Commun.*, vol. 1, no. 3, pp. 488–497, Jul. 2002.

[49] A. Andrade and D. Covarrubias, "Radio channel spatial propagation model for mobile 3G in smart antenna system," *IEICE Trans. Commun.*, vol. E86-B, no. 1, pp. 213–220, Jan. 2003.

[50] D. D. N. Bevan, V. T. Ermolayev, A. G. Flaksman, and I. M. Averin, "Gaussian channel model for mobile multipath environment," *EURASIP J. Appl. Signal Proc.*, vol. 2004, no. 9, pp. 1321–1329.

[51] S.-H. Kong, "TOA and AOD statistics for down link Gaussian scatterer distribution model," *IEEE Trans. Wireless Commun.*, vol. 8, no. 5, pp. 2609–2617, May 2009.

[52] A. H. Kazmi and N. M. Khan, "Effect of scattering around BS on the spatial statistics of mobile channel in macrocell environment," in *International Conference on Information and Emerging Technologies (ICIET), Karachi*, vol. 1, Jun. 2010, pp. 1–5.

[53] Y. I. Wu and K. T. Wong, "A geometrical model for the TOA distribution of uplink/downlink multipaths, assuming scatterers with a conical spatial density," *IEEE Antennas Propag. Mag.*, vol. 50, no. 6, pp. 196–205, Dec. 2008.

[54] A. Y. Olenko, K. T. Wong, and M. Abdulla, "Analytically derived TOA-DOA distributions of uplink/downlink wireless-cellular multipaths arisen from scatterers with an inverted-parabolic spatial distribution around the mobile," *IEEE Signal Processing Lett.*, vol. 12, no. 7, pp. 516–519, Jul. 2005.

[55] J. Laurila, A. F. Molisch, and E. Bonek, "Influence of the scatterer distribution on power delay profiles and azimuth power spectra of mobile radio channels," in *Proc. Int. Symp. Spread Spect. Tech. App.*, vol. 1, pp. 267–271.

[56] L. Jiang and S. Y. Tan, "Geometrically based statistical channel models for outdoor and indoor propagation environments," *IEEE Trans. Veh. Technol.*, vol. 56, no. 6, pp. 3587–3593, Nov. 2007.

[57] A. Borhani and M. Pätzold, "Time-of-arrival, angle-of-arrival, and angle-of-departure statistics of a novel simplistic disk channel model," in *Proc. 5th International Conference on Signal Processing and Communication Systems, ICSPCS 2011*. Honolulu, Hawaii, Dec. 2011.

[58] M. Pätzold, *Mobile Fading Channels*, 2nd ed. Chichester: John Wiley & Sons, 2011.

[59] P. P. Dey, S. Chandra, and S. Gangopadhaya, "Speed distribution curves under mixed traffic conditions," *Journal of Transportation Engineering*, vol. 132, no. 6, pp. 475–481, Jun. 2006.

[60] T. Hastie, R. Tibshirani, and J. Friedman, *The Elements of Statistical Learning: Data Mining, Inference, and Prediction*. Springer, 2001.

[61] J. Jun, "Understanding the variability of speed distributions under mixed traffic conditions caused by holiday traffic," *Transportation Research Part C: Emerging Technologies*, vol. 18, no. 4, pp. 599–610, Jun. 2010.

[62] C.-M. Hsu and F.-L. Lian, "A case study on highway flow model using 2-D Gaussian mixture modeling," in *Proc. Intelligent Transportation Systems Conference, ITSC07*. Seattle, WA, USA, Sep. 2007, pp. 790–794.

[63] N. Ueda, R. Nakano, Z. Ghahramani, and G. E. Hinton, "SMEM algorithm for mixture models," *Neural Computation*, vol. 12, no. 9, pp. 2109–2128, Sep. 2000.

[64] W. Zhu, K. Boriboonsomsin, and M. Barth, "Microscopic traffic flow quality of service from the drivers' point of view," in *Proc. Intelligent Transportation Systems Conference, ITSC'07*. Seattle, WA, USA, Sep./Oct. 2007, pp. 47–52.

[65] R. R. Roy, *Handbook of Mobile Ad Hoc Networks for Mobility Models*. Springer, 2011.

[66] M. Sánchez and P. Manzoni, "ANEJOS: a Java based simulator for ad hoc networks," *Future Generation Computer Systems*, vol. 17, no. 5, pp. 573 – 583, 2001.

[67] M. Kim, D. Kotz, and S. Kim, "Extracting a mobility model from real user traces," in *Proc. 25th IEEE International Conference on Computer Communications (INFOCOM'06)*, 2006, pp. 1–13.

[68] T. Henderson, D. Kotz, and I. Abyzov, "The changing usage of a mature campus-wide wireless network," in *Proc. The 10th Annual International Conference on Mobile Computing and Networking (MobiCom'04)*. Philadelphia, PA, USA, Feb. 2004, pp. 187–201.

[69] D. Kotz and K. Essien, "Analysis of a campus-wide wireless network," *Wireless Networks*, vol. 11, no. 1-2, pp. 115–133, Jan. 2005.

[70] A. Chaintreau, P. Hui, J. Crowcroft, C. Diot, R. Gass, and J. Scott, "Pocket switched networks: Real-world mobility and its consequences for opportunistic forwarding," in *University of Cambridge Computer Laboratory, Tech. Rep. UCAM-CL-TR-617, Feb.*, 2005.

[71] M. McNett and G. M. Voelker, "Access and mobility of wireless PDA users," in *Department of Computer Science and Engineering, University of California, San Diego, Tech. Rep. CS2004-0780, Feb.*, 2004.

[72] T. Camp, J. Boleng, and V. Davies, "A survey of mobility models for ad hoc network research," *Wireless Communications and Mobile Computing*, vol. 2, no. 5, pp. 483–502, Sep. 2002.

[73] F. Bai and A. Helmy, *A Survey of Mobility Modeling and Analysis in Wireless Adhoc Networks*. Book chapter in: Wireless Ad Hoc and Sensor Networks, Kluwer academic Publishers, 2004.

[74] F. Bai, N. Sadagopan, and A. Helmy, "The IMPORTANT framework for analyzing the impact of mobility on performance of routing protocols for adhoc networks," *Ad Hoc Networks*, vol. 1, no. 4, pp. 383 – 403, 2003.

[75] A. Einstein, "Über die von der molekularkinetischen Theorie der Wärme geforderte Bewegung von in ruhenden Flüssigkeiten suspendierten Teilchen," *Annalen der Physik*, no. 17, pp. 549–560, May 1905.

[76] K. Pearson, "The problem of the random walk," *Nature*, vol. 72, no. 1865, p. 294, 1905.

[77] D. B. Johnson and D. A. Maltz, *Dynamic Source Routing in Ad Hoc Wireless Networks*. The Kluwer International Series in Engineering and Computer Science, 1996, vol. 353.

[78] B. Liang and Z. J. Haas, "Predictive distance-based mobility management for PCS networks," in *Proc. 18th Annual Joint Conference of the IEEE Computer and Communications Societies (INFOCOM'99)*, vol. 3, 1999, pp. 1377–1384.

[79] V. A. Davis, "Evaluating mobility models within an ad hoc network," in *MS thesis, Colorado School of Mines*, 2000.

[80] J. Härri, F. Filali, and C. Bonnet, "Mobility models for vehicular ad hoc networks: a survey and taxonomy," *Communications Surveys Tutorials, IEEE*, vol. 11, no. 4, pp. 19–41, 2009.

[81] B. C. Csáji, A. Browet, V. A. Traag, J. Delvenne, E. Huens, P. V. Dooren, Z. Smoreda, and V. D. Blondel, "Exploring the mobility of mobile phone users," *Physica A: Statistical Mechanics and its Applications*, vol. 392, no. 6, pp. 1459 – 1473, 2013.

[82] T. Garske, H. Yu, Z. Peng, M. Ye, H. Zhou, X. Cheng, J. Wu, and N. Ferguson, "Travel patterns in China," *PLOS ONE*, vol. 6, no. 2, pp. 1–9, Feb. 2011.

[83] M. A. P. Taylor and Susilawati, "Modelling travel time reliability with the Burr distribution," *Procedia - Social and Behavioral Sciences*, vol. 54, pp. 75–83, 2012.

[84] S. B. Young, "Evaluation of pedestrian walking speeds in airport terminals," *Journal of the Transportation Research Board*, vol. 1674, no. 2, pp. 20–26, 1999.

[85] M. Herdin, *Non-Stationary Indoor MIMO Radio Channels*. PhD dissertation, Technical University of Wien, 2004.

[86] J. D. Parsons and A. S. Bajwa, "Wideband characterisation of fading mobile radio channels," *Communications, Radar and Signal Processing, IEE Proceedings F*, vol. 129, no. 2, pp. 95–101, Apr. 1982.

[87] G. Matz, "On non-WSSUS wireless fading channels," *IEEE Trans. Wireless Commun.*, pp. 2465–2478, Sep. 2005.

[88] L. Bernado, T. Zemen, F. Tufvesson, A. F. Molisch, and C. F. Mecklenbräuker, "The (in-) validity of the WSSUS assumption in vehicular radio channels," in *Personal Indoor and Mobile Radio Communications (PIMRC), 2012 IEEE 23rd International Symposium on*, Sep. 2012, pp. 1757–1762.

[89] I. Viering, H. Hofstetter, and W. Utschick, "Validity of spatial covariance matrices over time and frequency," in *Global Telecommunications Conference, 2002. GLOBECOM '02. IEEE*, vol. 1, Nov. 2002, pp. 851–855.

[90] A. Chelli, *Channel Modelling and System Performance Analysis of Vehicle-to-Vehicle Communication Systems*. PhD dissertation, University of Agder, 2013.

[91] A. Ghazal, C.-H. Wang, H. Haas, M. Beach, X. Lu, D. Yuan, and X. Ge, "A non-stationary MIMO channel model for high-speed train communication systems," in *Proc. 75th IEEE Veh. Technol. Conf., VTC 2012-Spring*. Yokohama, Japan, May 2012.

[92] A. Chelli and M. Pätzold, "A non-stationary MIMO vehicle-to-vehicle channel model based on the geometrical T-junction model," in *Proc. International*

Conference on Wireless Communications and Signal Processing, WCSP 2009. Nanjing, China, Nov. 2009.

[93] H. Suzuki, "A statistical model for urban radio propagation," *IEEE Trans. Commun.*, vol. 25, no. 7, pp. 673–680, Jul. 1977.

[94] F. Hansen and F. I. Meno, "Mobile fading—Rayleigh and lognormal superimposed," *IEEE Trans. Veh. Technol.*, vol. 26, no. 4, pp. 332–335, Nov. 1977.

[95] M. J. Marsan, G. C. Hess, and S. S. Gilbert, "Shadowing variability in an urban land mobile environment at 900 MHz," *Electronics Letters*, vol. 26, no. 10, pp. 646–648, May 1990.

[96] J. E. Berg, R. Bownds, and F. Lotse, "Path loss and fading models for microcells at 900 MHz," in *Proc. 42nd IEEE Veh. Technol. Conf., VTC 1992*, May 1992, pp. 666–671.

[97] S. Mockford, A. M. D. Turkmani, and J. D. Parsons, "Local mean signal variability in rural areas at 900 MHz," in *Proc. 40th IEEE Veh. Technol. Conf., VTC 1990*, May 1990, pp. 610–615.

[98] A. Mawira, "Models for the spatial correlation functions of the (log)-normal component of the variability of VHF/UHF field strength in urban environment," in *Third IEEE Int. Symp. on Personal, Indoor and Mobile Radio Communications, PIMRC '92.*, Oct. 1992, pp. 436–440.

[99] S. Kozono and K. Watanabe, "Influence of environmental buildings on UHF land mobile radio propagation," *IEEE Trans. Commun.*, vol. 25, no. 10, pp. 1133–1143, Oct. 1977.

[100] J. Salo, L. Vuokko, H. M. El-Sallabi, and P. Vainikainen, "An additive model as a physical basis for shadow fading," *IEEE Trans. Veh. Technol.*, vol. 56, no. 1, pp. 13–26, Jan 2007.

[101] N. B. Mehta, J. Wu, A. F. Molisch, and J. Zhang, "Approximating a sum of random variables with a lognormal," *IEEE Trans. Wireless Commun.*, vol. 6, no. 7, pp. 2690–2699, Jul. 2007.

[102] A. F. Molisch, "Ultrawideband propagation channels—theory, measurement, and modeling," *IEEE Trans. Veh. Technol.*, vol. 54, no. 5, Sep. 2005.

[103] A. Borhani and M. Pätzold, “A non-stationary one-ring scattering model,” in *Proc. IEEE Wireless Commun. and Net. Conf. (WCNC’13)*. Shanghai, China, Apr. 2013.

Appendices A–H

List of Publications

The purpose of this preface is to record all the articles published by the author of this dissertation.

The list of publications consists of submitted and already published papers. Firstly, the articles that are briefly discussed in Chapters 2–5 of this dissertation and are replicated in Appendices A–H are listed. Thereafter, the papers that are published within the framework of this doctoral thesis, but not included in this dissertation, are catalogued.

Articles Included in this Dissertation

The followings are the journal papers that are included in Appendices A–H of this dissertation:

Paper I A. Borhani and M. Pätzold, "A unified disk scattering model and its angle-of-departure and time-of-arrival statistics," *IEEE Transactions on Vehicular Technology*, vol. 62, no. 2, pp. 473-485, Feb. 2013.

Paper II A. Borhani and M. Pätzold, "On the spatial configuration of scatterers for given delay-angle distributions," *Engineering Letters*, vol. 22, no. 1, pp. 34-38, Feb. 2014.

Paper III A. Borhani and M. Pätzold, "Correlation and spectral properties of vehicle-to-vehicle channels in the presence of moving scatterers," *IEEE Transactions on Vehicular Technology*, vol. 62, no. 9, pp. 4228-4239, Nov. 2013.

Paper IV A. Borhani and M. Pätzold, "A Highly Flexible Trajectory Model Based on the Primitives of Brownian Fields—Part I: Fundamental Principles

and Implementation Aspects," *IEEE Transactions on Wireless Communications*, to be appeared, 2014.

Paper V A. Borhani and M. Pätzold, "A Highly Flexible Trajectory Model Based on the Primitives of Brownian Fields—Part II: Analysis of the Statistical Properties," *IEEE Transactions on Wireless Communications*, under review, 2014.

Paper VI A. Borhani, G. L. Stüber, and M. Pätzold, "A Random Trajectory Approach for the Development of Non-Stationary Channel Models Capturing Different Scales of Fading," *IEEE Transactions on Wireless Communications*, under review, 2014.

Paper VII A. Borhani and M. Pätzold, "A novel non-stationary channel model utilizing Brownian random paths," *REV Journal on Electronics and Communications (JEC)*, in press, 2014.

Paper VIII A. Borhani and M. Pätzold, "A new non-stationary channel model based on drifted Brownian random paths," *Springer, Transactions on Engineering Technologies*, in press, 2014.

Articles Not Included in this Dissertation

The conference papers pointed out in the following are also published during this PhD study and carry equal importance as the ones mentioned in the previous section. However, to reduce the overlap between the articles, they are not included in this dissertation.

Paper IX A. Borhani and M. Pätzold, "Time-of-arrival, angle-of-arrival, and angle-of-departure statistics of a novel simplistic disk channel model," in *Proc. IProc. 5th International Conference on Signal Processing and Communication Systems, ICSPCS 2011*, Honolulu, Hawaii, Dec. 2011.

Paper X A. Borhani and M. Pätzold, "Modeling of vehicle-to-vehicle channels in the presence of moving scatterers," in *Proc. 76th Vehicular Technology Conference, VTC 2012-Fall*, Québec City, Canada, Sep. 2012.

Paper XI A. Borhani and M. Pätzold, "A non-stationary one-ring scattering model," in *Proc. IEEE Wireless Communications and Networking Conference, WCNC 2013*, Shanghai, China, Apr. 2013, pp. 2661-2666.

Paper XII A. Borhani and M. Pätzold, "On the distribution of scatterers for given delay-angle joint probability density functions," in *Proc. 10th IEEE Vehicular Technology Society Asia Pacific Wireless Communications Symposium, APWCS 2013*, Seoul, Korea", Aug. 2013, pp. 185-189.

Paper XIII [1] A. Borhani and M. Pätzold, "Modelling of non-stationary mobile radio channels using two-dimensional Brownian motion processes," in *Proc. 6th International Conference on Advanced Technologies for Communications, ATC 2013*, Ho Chi Minh City, Vietnam, October 1618 , 2013, pp. 241-246.

Paper XIV [2] A. Borhani and M. Pätzold, "Modelling of non-stationary mobile radio channels incorporating the Brownian mobility model with drift," in *Proc. World Congress on Engineering and Computer Science, WCECS 2013*, San Francisco, USA, 23-25 Oct., 2013, pp. 695-700.

Paper XV M. Pätzold and A. Borhani, "A non-stationary multipath fading channel model incorporating the effect of velocity variations of the mobile station," in *Proc. Wireless Communication and Network Conference, WCNC 2014*, Istanbul, Turkey, Apr. 2014, pp. 194-199.

[1] This paper received the "Best Student Paper Award" from the ATC'13 Conference.
[2] This paper received the "Certification of Merit" from the WCECS'13 Conference.

Appendix A

Paper I

Title:	A Unified Disk Scattering Model and its Angle-of-Departure and Time-of-Arrival Statistics
Authors:	**Alireza Borhani** and Matthias Pätzold
Affiliation:	University of Agder, Faculty of Engineering and Science, P. O. Box 509, NO-4898 Grimstad, Norway
Journal:	*IEEE Transactions on Vehicular Technology*, pp. 473-485, Feb. 2013.

A Unified Disk Scattering Model and its Angle-of-Departure and Time-of-Arrival Statistics

Alireza Borhani and Matthias Pätzold

***Abstract* — This paper proposes a novel probability density function (PDF) for the distribution of the local scatterers inside a disk centered on the mobile station (MS). The new scattering model is introduced as the unified disk scattering model (UDSM), as it unifies a variety of typical circularly-symmetric scattering models into one simple model. By adjusting a designated shape factor controlling the distribution of the scatterers, both the uniform circular and uniform ring scattering models can be obtained as special cases. Furthermore, the original Gaussian and uniform hollow-disk scattering models can be approximated with a high level of accuracy. Besides these established scattering models, any continuous concentrations of the local scatterers from a high density near the MS to a high density close to the outer edge of the disk can also be achieved. Under the assumption of single-bounce scattering, the joint PDF of the the angle-of-departure (AoD) and angle-of-arrival (AoA), as well as the joint PDF of the time-of-arrival (ToA) and AoA are derived. Subsequently, the corresponding marginal PDFs are provided in closed form. Finally, the UDSM is validated by several measured channels, showing that the UDSM outperforms several other geometric models proposed in the literature. The proposed model is useful for the designers of cutting-edge vehicular communication technologies to study the system performance under different scattering conditions.**

***Index terms* — Unified disk scattering model, geometric model, angle-of-departure, time-of-arrival, single-bounce scattering**

Manuscript received February 16, 2012; revised July 29, 2012 and October 18, 2012; accepted October 19, 2012. Date of publication January 25, 2013; date of current version February 12, 2013. The review of this paper was coordinated by Dr. K. T. Wong.

A. Borhani and M. Pätzold are with the Faculty of Engineering and Science, University of Agder, 4898 Grimstad, Norway (e-mails: {alireza.borhani, matthias.paetzold}@uia.no).

Color versions of one or more of the figures in this paper are available online at http://ieeexplore.ieee.org

Digital Object Identifier 10.1109/TVT.2012.2227859

I. INTRODUCTION

In radio communication systems, the temporal and spatial statistical properties of the received multipath signal play an important role in the performance analysis. For instance, for the development of transmit-beamforming schemes and antenna array systems, the information on the distribution of the AoD is of primary importance. In wideband communication systems, it is essential to know the ToA statistics in order to perform the delay analysis of the overall system in terms of the average delay and the delay spread. Consequently, for mobile communication systems, a rigorous analysis and performance evaluations cannot be attained without knowing the statistical properties of the channel. The statistical properties of the disk scattering model under different distributions of the local scatterers have been investigated widely in the literature listed below.

The geometric shape of the propagation area and the distribution of the local scatterers within this area can be identified as the main aspects affecting the AoD and ToA statistics. The geometric assumptions include the position of the MS, BS, and the shape of the scattering area. Typical scattering areas have been mainly modeled by rings, disks, and ellipses. The uniform ring model, in which the local scatterers are uniformly distributed on a thin ring centered on the MS, has been the subject of thorough studies in [1–3]. The ToA and AoA PDFs of the uniform hollow-disk model have been proposed in [4] and were then further studied in [5]. The uniform circular scattering model, where the scatterers are uniformly distributed inside a full disk centered on the MS has been analyzed in [6–11]. The uniform elliptical model has been the scattering object under study in [5, 7, 11], and [12]. The Gaussian scattering model is another well-known scattering model proposed in [13–17]. The AoD and ToA PDFs of the conical scattering model were derived in [6] and [18], respectively. The inverted-parabolic model was first proposed in [19]. Finally, we mention that the Rayleigh scattering model was first presented in [20], which has been further developed in [21].

The lack of a comprehensive and critical comparison among all the above-mentioned geometric scattering models was filled by the assessment study in [22]. The comparisons with different measured channels [23–26] (among others reported in [22]) showed that none of these geometric scattering models is the best by all the selected criteria and for all considered scenarios. However, for the unimodal empirical data sets, the well-fitting geometric models are the Gaussian and the uniform elliptical models. If a closed-form AoD PDF is required, the choice falls on the uniform elliptical model [22], because a closed-form expressions for the AoD PDF of the Gaussian scattering model does not exist. Furthermore, for the bimodal empiri-

cal data sets, the uniform hollow-disk model is an appropriate geometric model [22]. It is intuitively obvious that by applying a curve-fitting algorithm on an empirical data set using a geometric model with two degrees of freedom, such as the uniform elliptical and the uniform hollow-disk models, has a higher chance of outperforming a model with only one degree of freedom, like the Gaussian, uniform circular, conical, and the inverted-parabolic models.

Despite the intensive work on geometric scattering models, the literature still lacks of a unification of a large variety of these established geometric models via a simple, compact, and unified PDF. The motivation of this paper is to fill this gap by adding one degree of freedom to the disk-based scattering model proposed in [27]. This paper introduces the UDSM with two degrees of freedom allowing to unify several circularly-symmetric scattering models. The novelty of the UDSM arises from the fact that the distribution of the scatterers can be fashioned in various concentration patterns, where the shape of the concentration patterns is controlled by a so-called shape factor. Indeed, by adjusting the shape factor, one can gradually change the concentration of the local scatterers from a high concentration close to the MS via the uniform distribution inside the full disk up to a high concentration on a ring centered on the MS. Therefore, the proposed UDSM not only covers the Gaussian, uniform, hollow-disk, and ring scattering models, but also covers any continuous circularly-symmetric concentration of the local scatterers between these original scattering models. Moreover, by introducing the UDSM in polar coordinates, we avoid the high mathematical complexity entailed by some of the aforementioned scattering models.

Given the proposed UDSM, the joint PDF of the AoD and AoA, as well as the joint PDF of the ToA and AoA are derived. Subsequently, the marginal PDFs of the AoD and ToA are provided in closed form. The correctness of the analytical expressions is then validated by simulation results. Furthermore, the marginal PDFs are compared with those of other well-known geometric models as well as with empirical data [23–26] collected in different propagation areas including rural, suburban, and urban regions. It turns out that by adjusting the shape factor, the UDSM coincide with the uniform circular scattering model and tends asymptotically to the uniform ring model. In addition, the uniform hollow-disk and the Gaussian scattering models can be approximated with a high level of accuracy. Moreover, the comparisons between our analytical results and the empirical data reported in [23–26] show that the AoD and ToA PDFs of the UDSM match the data sets better than several other geometric models. Furthermore, it will be shown that for all values of the shape factor–except those that result in the ring scattering models–the ToA

PDF follows a negative exponential-like distribution, which has often been adopted in specified channel models, such as the ones specified in [28]. It should be mentioned that the negative exponential characteristics of the propagation delays have also been confirmed by many measurement campaigns (see, e.g., [25]).

The UDSM can efficient describe the AoD and ToA characteristics of several different propagation areas including rural, suburban, and urban areas. This novel feature is attributed to from the fact that the UDSM introduces two degrees of freedom. From the unified geometric scattering model, one can derive stochastic and deterministic channel simulators by using the generalized principle of deterministic channel modelling [29, Sec. 8.1]. The designed channel simulator can then be used for the test, the parameter optimization, and the performance analysis of modern communication systems under different propagation conditions.

The remainder of this paper is organized as follows: Section II presents the geometric disk scattering model and describes the underlying assumptions. The UDSM is introduced in Section III. Section IV studies the joint PDF of the AoD and AoA, as well as the joint PDF of the ToA and AoA. Section V derives the marginal PDFs of the AoD and ToA. The verification of the analytical results with empirical data is described in Section VI. Finally, Section VII summarizes our main findings and draws the conclusions.

II. GEOMETRIC DISK SCATTERING MODEL AND ASSUMPTIONS

The geometric disk scattering model is presented in Fig. A.1. The BS and the MS presented in this figure serve as the transmitter and the receiver, respectively. The BS antenna is per definition fixed and highly elevated to scattering-free levels, while the MS antenna is moving with velocity vector $\vec{\mathrm{v}}$ in a rich scattering area. The distance between the BS and the MS is supposed to be D. Furthermore, we assume that the local scatterers are randomly and independently distributed within a disk of radius R centered on the MS. The location of each scatterer is described by polar coordinates (r, α^R), where r describes the distance of the scatterer from the MS and α^R denotes the AoA. Owing to the high path loss, we neglect the contribution from remote scatterers and assume that a wave transmitted from the BS with an AoD α^T reaches the MS after a single bounce by one of the randomly distributed scatterers located inside the disk. Notice that the upperscripts R and T in the notation used for the AoA and AoD, i.e., α^R and α^T, refer to the receiver and the transmitter, respectively.

In this paper, it is also assumed that both the BS and the MS are equipped with single omnidirectional antennas. This assumption is the same as the one in [5,

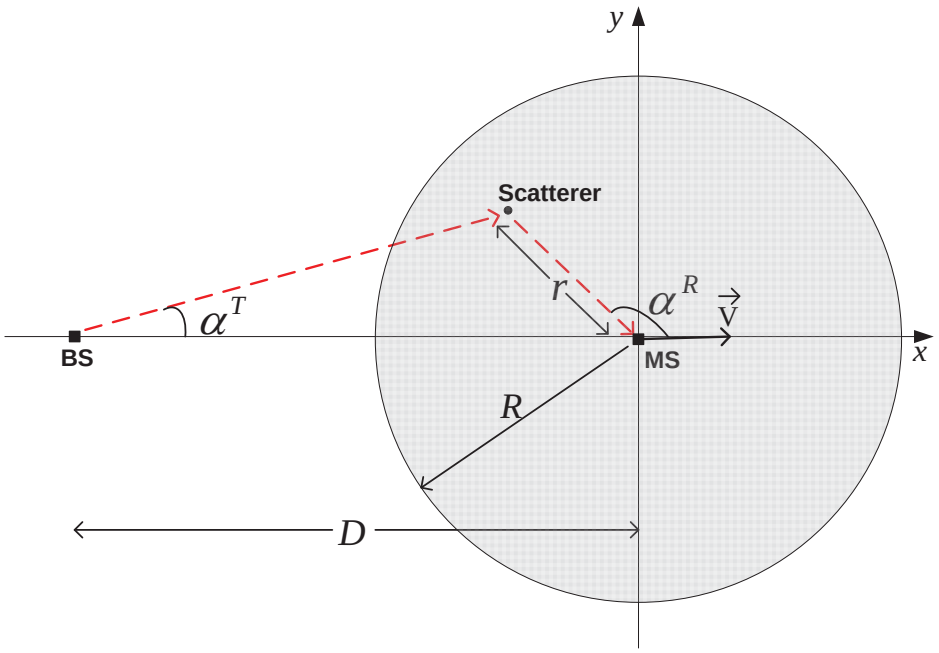

Figure A.1: The geometric disk scattering model for a single-bounce scattering scenario.

7, 11], but in contrast to [10, 30, 31], where it is assumed that the antennas are directional. In this regard, we also suppose that each of the scatterers acts as an omnidirectional lossless re-transmitter and is independent from other scatterers.

It is also assumed that the polarization effects of the transmitter antenna, scatterers, and the receiver antenna are ignored. This assumption differs from the one in [32], where the polarization effects of the aforementioned components on the emitted wave have been fully considered. Furthermore, it is assumed that the signals received at the MS antenna are plane waves travelling in the horizontal plane, and thus the AoA has only an azimuth component. This simplification is widely accepted in the literature [13–17]. However, it differs from the azimuth-elevation AoA derived from the three-dimensional scattering region proposed in [33].

III. UNIFIED DISK SCATTERING MODEL

A. Idea of the UDSM

The main idea of the UDSM is to extend the novel simplistic scattering model proposed in [27]. There, it has been assumed that the local scatterers are uniformly distributed in polar coordinates within a disk centered on the MS. Such a distribution is called the joint uniform distribution in polar coordinates. This model results

in a higher concentration of scatterers around the disk center and a lower concentration far from it. Accordingly, the joint uniform distribution in polar coordinates differs greatly from the uniform distribution of the scatterers in Cartesian coordinates (known as the uniform circular model). The proposed model in [27] has only one degree of freedom, which is the radius R of the disk. Due to the uniform distribution of the radius r within its range $[0,R]$, the PDF of the distribution of the scatterers in [27, Eq. (1)] is independent of r. The motivation of this paper is to generalize the aforementioned scattering model by adding one degree of freedom to the PDF in [27, Eq. (1)], such that the new model (UDSM) is not generally independent of r anymore. Accordingly, this paper proposes the UDSM according to which the location of the scatterers are described as follows

$$p^{(k)}_{r,\alpha^R}(r,\alpha^R) = \begin{cases} \frac{(k+1)}{2\pi R^{(k+1)}} r^k, & \text{if } 0 \le r \le R \text{ and} \\ & \pi \le \alpha^R < \pi, \\ 0, & \text{otherwise.} \end{cases} \tag{A.1}$$

In the equation above, it is also assumed that the local scatterers are randomly and independently distributed within a disk of radius R centered on the MS. In this equation, $k > -1$ is a real-valued parameter called the shape factor that controls the distribution of the scatterers within the disk presented in Fig. A.1. In fact, the shape factor k provides the additional degree of freedom, which will greatly help us to find excellent curve-fittings several established scattering models (see Section V) as well as to empirical data (see Section VI). As can be seen, the proposed UDSM described by (A.1) depends generally on r, except for $k = 0$. Notice that by setting $k = 0$, (A.1) reduces to [27, Eq. (1)], which has only one degree of freedom.

The term 2π in the denominator of (A.1) accounts for the fact that the AoA α^R is uniformly distributed between $-\pi$ and π. In other words, the UDSM is a circularly-symmetric scattering model. The other constant terms in (A.1) guarantee the unity area under (A.1). In this connection, one can show that the proposed distribution in (A.1) allows the following Cartesian representation

$$p^{(k)}_{X,Y}(x,y) = \begin{cases} \frac{(k+1)}{2\pi R^{(k+1)}} (x^2+y^2)^{\frac{k-1}{2}}, & \text{if} \\ & x^2+y^2 \le R^2, \\ 0, & \text{otherwise.} \end{cases} \tag{A.2}$$

B. Role of the Shape Factor k

The UDSM with its scattering distribution described by (A.1), or equivalently in (A.2), has two degrees of freedom, namely the radius R and the shape factor

k. The first degree of freedom, R, is common between several geometric models, such as the uniform circular, conical, inverted-parabolic, and the model in [27]. The second degree-of-freedom, k, has never been proposed fore in the literature. Indeed, k is a concentration control factor that allows to shape continuously the distribution of the local scatterer around the MS. For a given radius R, a chosen value of k from $(-1,1)$ will primarily include only scatterers near the MS, which is useful for modelling of urban and suburban propagation areas. A purely uniform distribution of the scatterers within a disk around the MS is obtained by choosing $k=0$. By increasing k, the scatterers will be concentrated on a hollow-disk centered on the MS, which provides a reasonable propagation model for rural areas. In what follows, we describe the influence and significance of this key parameter in more depth.

Let us assume that k is chosen from the range $(-1,1)$. This means that the term (x^2+y^2) appears in the denominator of (A.2). Accordingly, the UDSM distributes the local scatterers such that one can find a high concentration of scatterers close to the disk center and a low concentration at the edge of the disk. In this paper, we use the term *Gaussian-like* to address such a kind of distribution in a simple manner. Although, several other distributions can also lead to a similar non-uniform distribution of the scatterers with a higher density around the center, we use the term Gaussian-like in absence of any other proper terminology. A second reason is that the UDSM is also able to approximate the AoD and the ToA PDFs of the Gaussian model (see Section V).

For the simple special case within this range, $k=0$, the joint distribution in (A.1) reduces to the joint uniform distribution in polar coordinates [27, Eq. (1)], i.e.,

$$p^{(0)}_{r,\alpha^R}(r,\alpha^R)=\begin{cases}\frac{1}{2\pi R}, & \text{if } 0\le r\le R \text{ and}\\ & \pi\le\alpha^R<\pi,\\ 0, & \text{otherwise.}\end{cases} \tag{A.3}$$

To provide a better visualization, we present several scatter diagrams in Fig. A.2. Using the PDF in (A.1), a number of 1000 scatterers have randomly be distributed around the origin. We have repeated this procedure for four different values of the shape factor k. Figure A.2(a) demonstrates the distribution of the random scatterers generated by using the special case of (A.3), where the shape factor k is set to 0. As expected, a Gaussian-like distribution of the local scatterers inside a limited area can be observed. Referring to [27], the PDF presented in (A.3) can be considered as an approximation of the original Gaussian scattering model studied in [13–17]. In this paper, we widen the scope of (A.3) by considering the general form of the PDF

in (A.1). This means that we do not focus solely on the special case of $k = 0$. In turn, we search over a wider range of k to achieve the maximum similarity between the UDSM and the Gaussian scattering model in terms of the AoD and ToA PDFs. This can be done, e.g., by optimizing the model parameters, R and k, by minimizing the least-squares error (LSE) between the AoD (ToA) PDFs of the two models. Section V deals with this issue in more details.

Now, let us assume that the shape factor k equals 1. By substituting this in (A.1) and (A.2), the UDSM reduces to the special cases

$$p^{(1)}_{r,\alpha^R}(r,\alpha^R) = \begin{cases} \frac{1}{\pi R^2} r, & \text{if } 0 \le r \le R \text{ and} \\ & \pi \le \alpha^R < \pi, \\ 0, & \text{otherwise,} \end{cases} \tag{A.4}$$

and

$$p^{(1)}_{X,Y}(x,y) = \begin{cases} \frac{1}{\pi R^2}, & \text{if } x^2+y^2 \le R^2, \\ 0, & \text{otherwise,} \end{cases} \tag{A.5}$$

respectively. Notice that the radius r in the nominator of (A.4) can be identified as the Jacobian-inverse of the transformation of (A.5) to (A.4). In this case, (A.5) (or equivalently (A.4)) represents the uniform circular scattering model, which has been explored widely in the literature (see, e.g., [6–11]). Figure A.2(b) shows the location of the scatterers distributed by using (A.4). Notice that the joint PDF in (A.4) is completely different from the joint uniform PDF in polar coordinates presented in (A.3).

So far, we have observed that by changing the shape factor k from -1 to 1, the concentration of the local scatterers varies from a high concentration around the disk center to the uniform distribution inside the disk. In the same vein, by increasing the shape factor from 1 towards higher values $k \gg 1$, we expect to observe that the concentration of the local scatterers changes from the uniform distribution inside the full disk to a high concentration at the edge of the disk, and thus forming a ring of scatterers if $k \to \infty$.

In this regard, Fig. A.2(c) demonstrates the distribution of the local scatterers generated by using (A.1), in which the shape factor is set to $k = 8$. As can be seen in Fig. A.2(c), for medium values of the shape factor k, the UDSM joint distribution in (A.1) can be considered as an approximation of the uniform hollow-disk model, which has been studied in [4] and developed further in [5]. For large values of the shape factor k (e.g., $k = 25$), the well-known uniform ring model studied in [1–3] can be well approximated. If the shape factor k tends to infinity, the proposed PDF

in (A.1) behaves like a shifted and scaled delta function of the form $\delta(r-R)/2\pi$, which equals the polar representation of the uniform distribution of the scatterer placed on a ring of radius R shown in Fig. A.2(d). This means that the UDSM results asymptotically in the uniform ring scattering model if $k \to \infty$.

In brief, the proposed UDSM distribution in (A.1) provides: a Gaussian-like distribution of the local scatterers inside the full disk if the shape factor k is chosen from the range $(-1,1)$; the uniform circular distribution within a full disk if $k = 1$; the hollow-disk model if k is chosen moderately, e.g., $k = 8$; and the uniform ring model if $k \to \infty$ [see Fig. A.2(a)-(d)]. It is worth mentioning that since k is a continuous variable within its range, any continuous concentration of the local scatterers that emerges between the aforementioned original scattering models can also be generated. As we will see in Section VI-D, this novel feature fills the gap of need for a flexible scattering model linking two established models.

IV. JOINT PROBABILITY DENSITY FUNCTIONS

In this section, we investigate the statistical properties of the proposed model, such as the joint PDF of the AoD and AoA, as well as the joint PDF of the ToA and AoA.

A. Joint PDF of the AoD and AoA

Referring to the geometric disk model in Fig. A.1 and using the law of sines, one can write

$$\alpha^T(r,\alpha^R) = \arctan\Big(\frac{r\sin(\alpha^R)}{D+r\cos(\alpha^R)}\Big). \tag{A.6}$$

By considering the auxiliary function $A(r,\alpha^R) = \alpha^R$, we have the following roots

$$r = \frac{D\sin(\alpha^T)}{\sin(\alpha^R-\alpha^T)} \text{ and } \alpha^R = A. \tag{A.7}$$

By applying the concept of transformation of random variables [34, p. 130], we reach the joint PDF of the AoD and AoA

$$p_{\alpha^T,\alpha^R}(\alpha^T,\alpha^R) = |J|^{-1} p_{r,\alpha^R}\Big(\frac{D\sin(\alpha^T)}{\sin(\alpha^R-\alpha^T)},\alpha^R\Big), \tag{A.8}$$

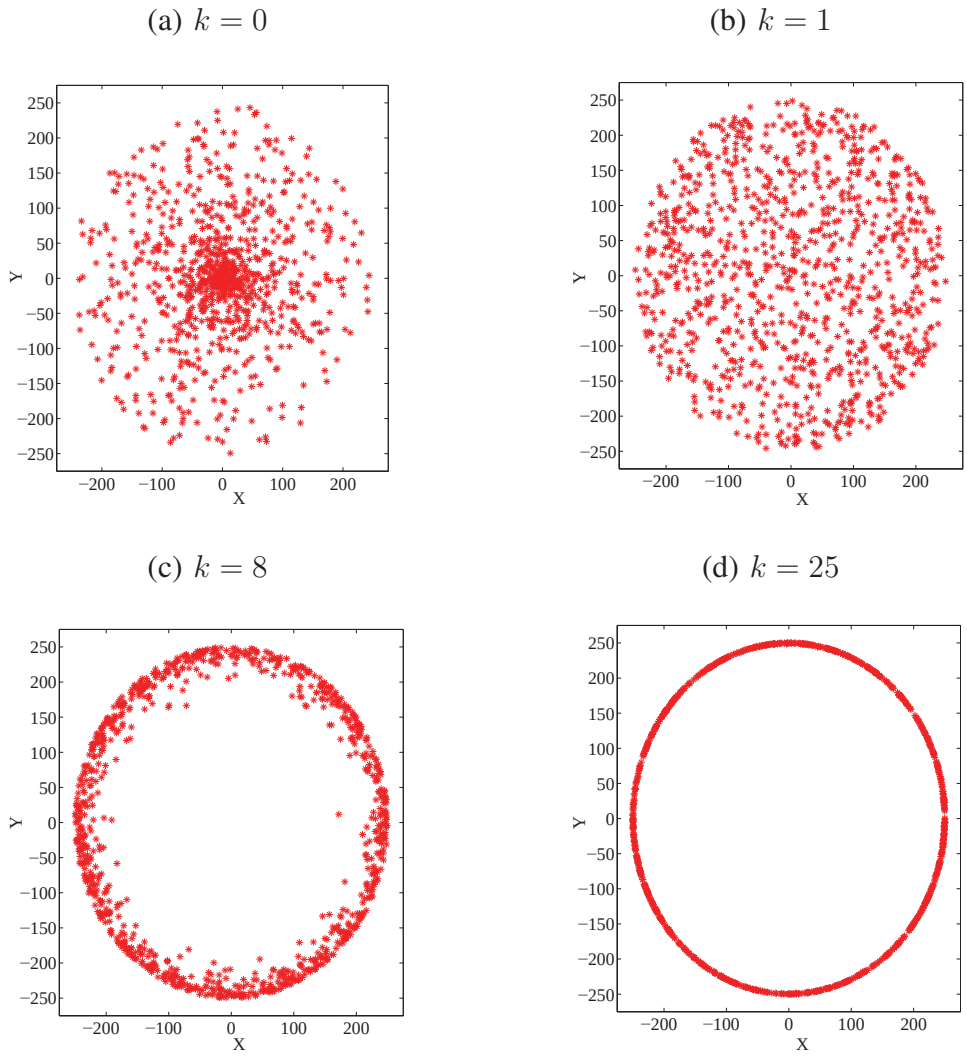

Figure A.2: Scatter diagram illustrating 1000 randomly distributed scatterers (*) generated by using the unified disk PDF [see (A.1)] with different shape factors: (a) $k = 0$, (b) $k = 1$, (c) $k = 8$, and (d) $k = 25$. The disk radius R has been set to 250 m in all cases.

where $|J|$ denotes the Jacobian of the transformation, which is determined by the following determinant

$$|J| = \begin{vmatrix} \frac{\partial r}{\partial \alpha^T} & \frac{\partial r}{\partial \alpha^R} \\ \frac{\partial \alpha^R}{\partial \alpha^T} & \frac{\partial \alpha^R}{\partial \alpha^R} \end{vmatrix}^{-1} \tag{A.9}$$

Noting that $|J|$ can be readily simplified to $|\partial r/\partial \alpha^T|^{-1}$ and recalling the general form of the UDSM distribution in (A.1), it follows that the joint PDF $p_{\alpha^T,\alpha^R}(\alpha^T,\alpha^R)$ of α^T and α^R can finally be written in closed form given by

$$p^{(k)}_{\alpha^T,\alpha^R}(\alpha^T,\alpha^R)=\begin{cases} D^{k+1}\dfrac{(k+1)}{2\pi R^{(k+1)}}\dfrac{|\sin(\alpha^R)|\sin^k(\alpha^T)}{\sin^{k+2}(\alpha^R-\alpha^T)}, & \text{if} \\ & (\alpha^T,\alpha^R)\in\mathfrak{D}, \\ 0, & \text{otherwise}, \end{cases} \tag{A.10}$$

where $\mathfrak{D}$ denotes the region

$$\mathfrak{D}\in\left\{(\alpha^T,\alpha^R)\;\middle|\; 0\le\frac{D\sin(\alpha^T)}{\sin(\alpha^R-\alpha^T)}\le R,\alpha^R\neq\alpha^T\right\} \tag{A.11}$$

for $-\pi\le\alpha^R<\pi$ and $-\arcsin(R/D)\le\alpha^T\le\arcsin(R/D)$. It is worth mentioning that whenever $\alpha^T\cdot\alpha^R<0$, then $p^{(k)}_{\alpha^T,\alpha^R}(\alpha^T,\alpha^R)$ is zero. This is obvious, because by choosing α^R and α^T such that $\alpha^T\cdot\alpha^R<0$, it is impossible to find a scatterer in the disk scattering area shown in Fig. A.1. It can be easily shown that the two-fold integral of (A.10) over its range is one. Space limitation prevents us from illustrating the results in (A.10) here. However, in Section V, the analytical results for the marginal PDFs, which are much more important for us, are illustrated and discussed in detail.

B. Joint PDF of the ToA and AoA

By taking the single-bounce scattering mechanism into account and referring to Fig. A.1, the total path length, which an emitted plane wave travels from the BS via a scatterer to the MS, equals

$$D_s(r,\alpha^R)=r+\sqrt{r^2+D^2+2rD\cos(\alpha^R)}. \tag{A.12}$$

To derive the joint PDF of the ToA and AoA, it is advantageous to introduce the functions $\tau'(r,\alpha^R)=D_s(r,\alpha^R)/c_0$ and $A(r,\alpha^R)=\alpha^R$, where τ' denotes the ToA

$$p^{(k)}_{\tau',\alpha^R}(\tau',\alpha^R)=\begin{cases} \dfrac{(k+1)c_0}{2\pi(2R)^{(k+1)}}\dfrac{[(\tau' c_0)^2-D^2]^k}{(\tau' c_0+D\cos(\alpha^R))^{k+2}} & \text{if } \tau'_{\min}\le\tau'\le\tau'_{\max} \\ \times[(\tau' c_0)^2+2\tau' c_0 D\cos(\alpha^R)+D^2], & \text{and } -\pi\le\alpha^R<\pi, \\ 0, & \text{otherwise.} \end{cases} \quad \text{(A.16)}$$

and c_0 designates the speed of light. It can be shown that the roots of these functions are given by

$$r=\frac{(\tau' c_0)^2-D^2}{2(\tau' c_0+D\cos(\alpha^R))} \text{ and } \alpha^R=A. \quad \text{(A.13)}$$

By applying again the concept of transformation of random variables, the joint PDF of the TOA and AoA can be represented by

$$p^{(k)}_{\tau',\alpha^R}(\tau',\alpha^R)=|J|^{-1}p^{(k)}_{r,\alpha^R}\Big(\frac{(\tau' c_0)^2-D^2}{2(\tau' c_0+D\cos(\alpha^R))},\alpha^R\Big), \quad \text{(A.14)}$$

in which

$$\begin{aligned} |J| &= \begin{vmatrix} \frac{\partial r}{\partial \tau'} & \frac{\partial r}{\partial \alpha^R} \\ \frac{\partial \alpha^R}{\partial \tau'} & \frac{\partial \alpha^R}{\partial \alpha^R} \end{vmatrix}^{-1} \\ &= {c_0}^{-1}\frac{2(\tau' c_0+D\cos(\alpha^R))^2}{(\tau' c_0)^2+2\tau' c_0 D\cos(\alpha^R)+D^2}. \end{aligned} \quad \text{(A.15)}$$

Substituting this expression into (A.14) and using the general form of the UDSM distribution in (A.1), it follows that the joint PDF of the ToA and AoA can be expressed by (A.16) [see the top of the current page]. The symbols $\tau'_{\min}$ and $\tau'_{\max}$ in (A.16) denote the minimum and maximum ToA, respectively. With reference to Fig. A.1, the minimum ToA $\tau'_{\min}$ occurs if the scatterer has its minimum distance from the MS, i.e., $\tau'_{\min}=c_0^{-1}D$ if $r\to 0$. Analogously, the maximum ToA $\tau'_{\max}$ occurs if the scatterer has its maximum distance from the BS, i.e., $\tau'_{\max}=c_0^{-1}(2R+D)$ if $r\to R$ and $\alpha^R\to 0$. In this regard, the two-fold integral of (A.16) over $\tau'_{\min}\le\tau'\le\tau'_{\max}$ and $-\pi\le\alpha^R<\pi$ meets unity. Again, due to the space restriction, the analytical results for the joint PDF in (A.16) are not exemplified here. However, the marginal PDFs are illustrated and discussed in what follows.

V. MARGINAL PROBABILITY DENSITY FUNCTIONS

Next, we derive the marginal PDF of the AoD (ToA) from the joint PDF of the AoD (ToA) and AoA. This is different from the common approach, e.g., [18], where the AoD (ToA) PDF is derived from the joint PDF of the AoD and ToA. This approach may result in simpler expressions for marginal PDFs, which cannot be presented in closed form. In this regard, besides providing a closed-form expression for the AoD (ToA) PDF of the UDSM, one may derive a new integral-form solution for the AoD (ToA) PDF of the Gaussian scattering model different from the one provided in [13]. In what follows, we derive the marginal PDFs of both the AoD and the ToA in closed form. Then, the obtained analytical results are confirmed by simulation results. Subsequently, we show that the AoD (ToA) PDF of the UDSM is able to either precisely or approximately meet that of the Gaussian, uniform circular, uniform hollow-disk, and the uniform ring models. The validation of our analytical results by means of empirical data is deferred to Section VI.

A. Marginal PDF of the AoD

The marginal PDF $p^{(k)}_{\alpha^T}(\alpha^T)$ of the AoD α^T can be obtained by integrating the joint PDF $p^{(k)}_{\alpha^T,\alpha^R}(\alpha^T,\alpha^R)$ presented in (A.10) over the AoA α^R, i.e.,

$$p^{(k)}_{\alpha^T}(\alpha^T) = \frac{(k+1)\gamma^{k+1}}{2\pi}\sin^k(\alpha^T)\int\limits_{D_{\alpha^R}} \frac{|\sin(\alpha^R)|d\alpha^R}{\sin^{k+2}(\alpha^R-\alpha^T)} \tag{A.17}$$

where $-\arcsin(\gamma^{-1}) \leq \alpha^T \leq \arcsin(\gamma^{-1})$, the parameter γ denotes the ratio D/R, and D_{α^R} determines the domain of integration for a given value of the AoD α^T. This domain can be readily derived by solving (A.6) with respect to α^R. Furthermore, since $\alpha^T(r,\alpha^R)$ in (A.6) is a monotonically increasing function in r, one can set r to its maximum value R. Following this procedure, the limits of the integral in (A.17) range from $\arcsin(\gamma\sin(\alpha^T))+\alpha^T$ to $\pi-\arcsin(\gamma\sin(\alpha^T))+\alpha^T$, which determine D_{α^R}.

After solving the integral in (A.17) with due regard to D_{α^R} and some mathematical manipulations, the marginal PDF $p^{(k)}_{\alpha^T}(\alpha^T)$ of the AoD α^T is given by the closed-form[1] expression in (A.18) (see the top of the next page), in which $\alpha^T \in [-\arcsin(\gamma^{-1}),\arcsin(\gamma^{-1})]$. In this equation, $\Gamma(\cdot)$ and $\beta(\cdot;\cdot,\cdot)$ denote the gamma and incomplete beta functions [35], respectively.

[1] In the open literature, analytical expressions in terms of gamma, beta, erf, erfc, Bessel, Meijer, Appell, and hypergeometric functions, are mostly addressed as *closed-form* solutions.

$$p_{\alpha^T}^{(k)}(\alpha^T)=\begin{cases}\dfrac{(k+1)\gamma^{k+1}}{2\pi}\sin^k(\alpha^T)\cos(\alpha^T) & \\ \times\Big[\frac{\sqrt{\pi}\Gamma(-\frac{k}{2})}{\Gamma(\frac{1-k}{2})}-\beta(\gamma^2\sin^2(\alpha^T);-\frac{k}{2},\frac{1}{2})\Big], & k\neq 0,\\ \\ \frac{\gamma}{\pi}\cos(\alpha^T)\lg\Big|\frac{1+\sqrt{1-\gamma^2\sin^2(\alpha^T)}}{\gamma\sin(\alpha^T)}\Big|, & k=0,\end{cases} \tag{A.18}$$

It is noteworthy that for $k=1$, the PDF $p_{\alpha^T}^{(k)}(\alpha^T)$ in (A.18) can be simplified to

$$p_{\alpha^T}^{(1)}(\alpha^T)=\frac{2\gamma}{\pi}\cos(\alpha^T)\sqrt{1-\gamma^2\sin^2(\alpha^T)} \tag{A.19}$$

which is the same as the AoD PDF of the uniform circular scattering model studied in [6–11]. Notice that by considering the uniform distribution of the local scatterers inside a hollow-disk, in which the radius of the inner border is set to 0, the AoD PDF of the uniform hollow-disk model [4, Eq. (6)] meets also the AoD PDF of the UDSM for $k=1$, i.e., $p_{\alpha^T}^{(1)}(\alpha^T)$ in (A.19).

Figure A.3 demonstrates the PDF $p_{\alpha^T}^{(k)}(\alpha^T)$ corresponding to the UDSM for different values of the shape factor k, where the MS-to-BS distance D and the disk radius R have been set to 2 km and 250 m, respectively. To validate the closed-form expression of the AoD PDF in (A.18), a histogram is computed by generating 10^5 scatterers inside a disk of radius R using (A.1). Measuring the AoD at a distance of 2 km away from the center of the disk, creating a histogram containing 50 equally-spaced bins, and dividing the number of events in each bin by the total number of events results finally in the normalized histogram shown in Fig. A.3. We repeat this procedure for different values of the shape factor k. For all selected values of k, an excellent match between the analytical result and the normalized histogram can be observed, which validates the correctness of the AoD PDF in (A.18). As can also be seen in this figure, by setting the shape factor k to -0.5 or 0, a high density of the AoD close to the origin is obtained. In general, this behavior of the AoD PDF was expected if the shape factor k is selected from the range $-1<k<1$. This can be attributed to the fact that within this range, the UDSM distribution in (A.1) distributes the local scatterers in a Gaussian-like fashion [see Fig. A.2(a)]. On the contrary, if the shape factor k is larger than one, e.g., $k=8$ or $k=25$, a high density of the AoD close to the outer edge of the disk scattering area and a low density near the origin of the disk is achieved. This property originates from the fact that the proposed PDF in (A.1) includes an approximation of the hollow-disk model if k is moderately large, e.g., $k=8$ [see Fig. A.2(c)] and the ring model if a large

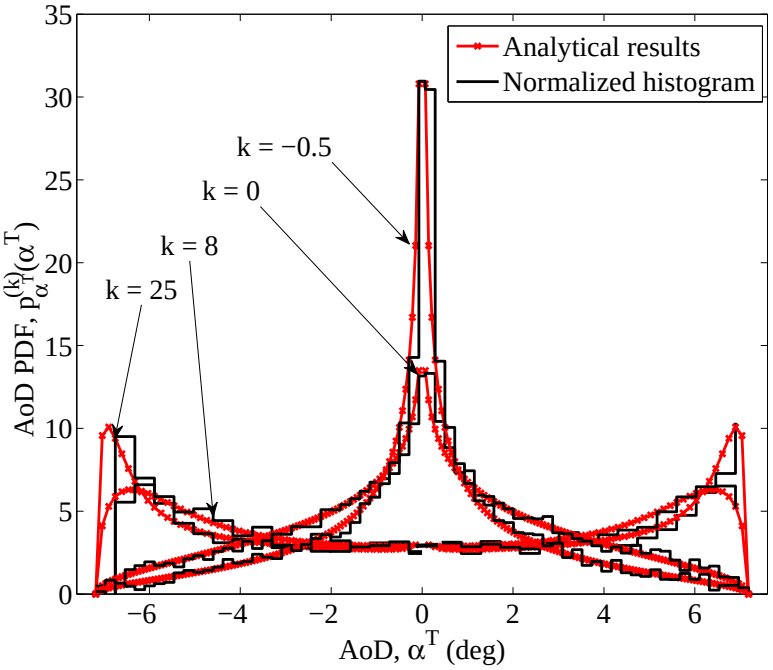

Figure A.3: PDF $p_{\alpha^T}^{(k)}(\alpha^T)$ of the AoD α^T for the proposed UDSM for different values of the shape factor k, where $\gamma = D/R = 8$.

value is chosen for k, e.g., $k = 25$ [see Fig. A.2(d)]. In addition, Fig. A.3 plots the AoD PDF $p_{\alpha^T}^{(1)}(\alpha^T)$ of the uniform circular scattering model, which is presented in (A.19). Notice that for all values of the shape factor k, the symmetrical behavior of $p_{\alpha^T}^{(k)}(\alpha^T)$ with respect to α^T implies that the mean value of α^T equals zero. Furthermore, independent of the shape factor k, the AoD has been spread between about -7 and 7 degrees. The aforementioned independency was to be expected, as the disk radius R and the distance D between the BS and the MS are the only factors affecting the limits of the AoD.

In this regard, Fig. A.4 depicts the effect of $\gamma = D/R$ on the AoD PDF $p_{\alpha^T}^{(k)}(\alpha^T)$ of the UDSM, in which the shape factor k has been set to 0. As can be seen by decreasing γ, $p_{\alpha^T}^{(0)}(\alpha^T)$ in (A.18) spreads over a wider range. Again, a high density of the AoD around the origin, implying $\alpha^T = 0$, and a low density close to the circumference of the disk, meaning $|\alpha^T| = \arcsin(\gamma^{-1})$, can be observed. This is simply due to the fact that by choosing the shape factor $k = 0$, the joint uniform PDF in polar coordinates (A.3) distributes the local scatterers in a Gaussian-like fashion.

In what follows, we try to fit the AoD PDF of the UDSM to that of the Gaussian, uniform circular, uniform hollow-disk, and the uniform ring model. First, let us stress the importance of these models. As mentioned in Section I, one of the

common assumptions on the distribution of the local scatterers is the Gaussian distribution around the MS [13–17]. It has be shown in [22] that the Gaussian model is a proper choice to describe the scatterer distribution in many propagation areas. The AoD PDF $p^{G}_{\alpha^T}(\alpha^T)$ of this model can be found in, e.g., [13, Eq. (29)]. The uniform circular model is also another well-known geometric model, which has been widely discussed in the literature [6–11]. The AoD PDF of this model has been provided in, e.g, [9, Eq. (12)]. Referring to [22], the uniform hollow-disk model [4] can provide a good fitting to bimodal empirical data sets. The corresponding AoD PDF has been derived in [4, Eq. (6)]. In this connection, the uniform ring model [1–3] is another classical scattering model, which can be interpreted as a special case of the uniform hollow disk model. The objective of the following is to show that the AoD PDF of the UDSM is able to match either precisely or approximately all those of the above-mentioned established models.

Figure A.5 shows the curve-fitting results of the AoD PDF of the UDSM and that of the established scattering models, while Table A.1 lists the corresponding LSEs. Here, the goodness-of-fit is the LSE with respect to the AoD PDF, which is denoted by $\mathrm{LSE}_{\mathrm{AoD}}$. To determine the $\mathrm{LSE}_{\mathrm{AoD}}$, the model parameters γ^{-1} and k have been optimized within their ranges. The used optimization procedure is the same as that in [22]. Choosing the parameters of the considered scattering models as listed in the second row of Table A.1, we obtained the corresponding $\mathrm{LSE}_{\mathrm{AoD}}$ to each model shown in the third row.

As can be seen in Fig. A.5 and with more details in Table A.1, the UDSM is able to match closely the established scattering models by optimizing the model parameters γ^{-1} and k. The minimum and the maximum $\mathrm{LSE}_{\mathrm{AoD}}$ belong to the uniform circular and uniform hollow-disk scattering models, respectively. Furthermore, both the uniform hollow-disk and Gaussian models lead almost to the same error ($\mathrm{LSE}_{\mathrm{AoD}} \approx 0.6$). In these cases, the curve-fitting is poor around the sharp peaks of the uniform hollow-disk model. This is due to the fact that the hollow-disk model has a bimodal AoD PDF [4, Eq. (6)], while the UDSM has a unimodal AoD PDF. Furthermore, the poor match between the UDSM and the Gaussian model in the tails of the distribution is caused by the large difference between the scatterer domains of these two models. Indeed, the UDSM has a limited scatterer domain (a disk of radius R) for scatterers, while the scatterer domain of the Gaussian model is infinite. Notice that a very close agreement ($\mathrm{LSE}_{\mathrm{AoD}} = 0.0061$) between the AoD PDF of the UDSM and that of the uniform ring model can also be observed. This agreement is theoretically perfect if $k \to \infty$ (see Section III-B). However, in our computations, we have upper-bounded the shape factor by $k = 25$, which explains

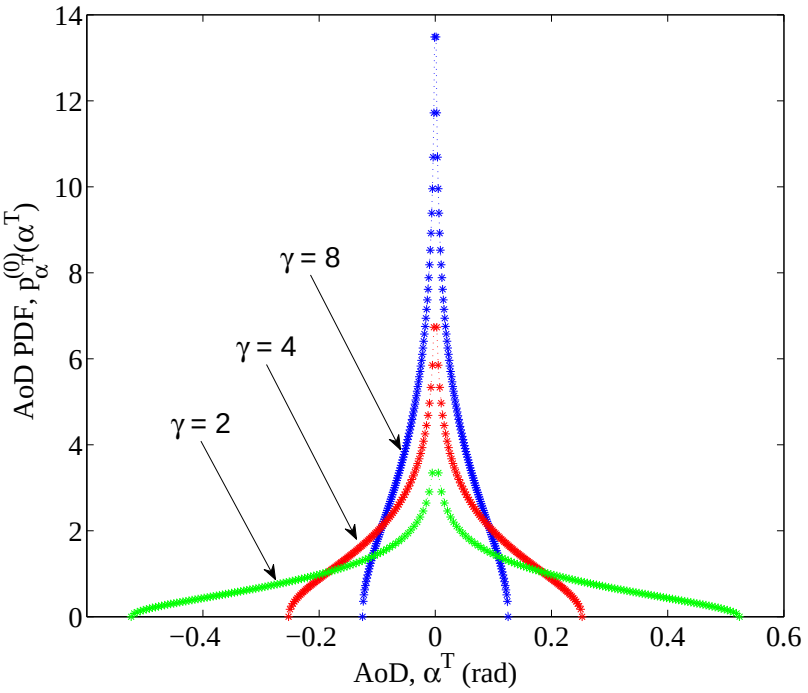

Figure A.4: PDF $p_{\alpha^T}^{(0)}(\alpha^T)$ of the AoD α^T of the unified disk scattering model for different values of $\gamma = D/R$.

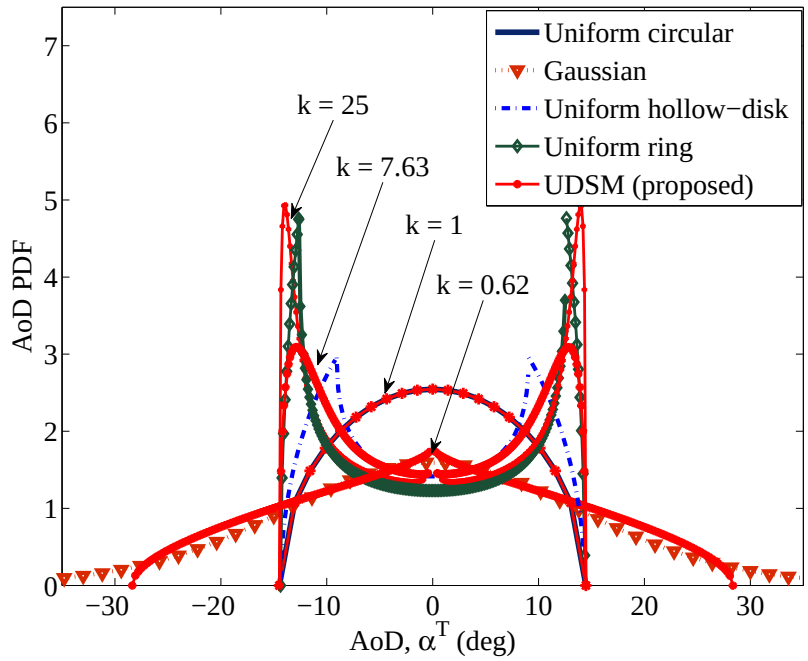

Figure A.5: Curve-fitting results after matching the AoD PDF $p_{\alpha^T}^{(k)}(\alpha^T)$ of the proposed UDSM to the AoD PDF of the uniform circular, Gaussian, uniform hollow-disk, and the uniform ring model.

the non-zero $\mathrm{LSE}_{\mathrm{AoD}}$.

B. Marginal PDF of the ToA

Starting from the joint PDF $p^{(k)}_{\tau',\alpha^R}(\tau',\alpha^R)$ in (A.16) and integrating over the AoA α^R result in the marginal PDF $p^{(k)}_{\tau'}(\tau')$ of the ToA τ', i.e.,

$$p^{(k)}_{\tau'}(\tau') = \frac{(k+1)c_0}{2\pi(2R)^{(k+1)}}[(\tau' c_0)^2 - D^2]^k \times \int\limits_{D_{\alpha^R}} \frac{[(\tau' c_0)^2 + 2\tau' c_0 D\cos(\alpha^R) + D^2]}{(\tau' c_0 + D\cos(\alpha^R))^{k+2}} d\alpha^R \tag{A.20}$$

for $\tau' \in [\tau'_{\min}, \tau'_{\max}]$. The notation D_{α^R} in the equation above denotes the domain of integration for a given value of τ'. Recalling $\tau'(r,\alpha^R) = c_0^{-1} D_s(r,\alpha^R)$ and using (A.12), it follows

$$\tau'(r,\alpha^R) = c_0^{-1}(r + \sqrt{r^2 + D^2 + 2rD\cos(\alpha^R)}). \tag{A.21}$$

Clearly, (A.21) is a monotonic increasing function in r. This means that for a given value of the AoA α^R, the ToA $\tau'(r,\alpha^R)$ takes its maximum value, denoted by $\tau'_{\max}(\alpha^R)$, if the scatterer is located on the circumference of the disk, i.e.,

$$\tau'_{\max}(\alpha^R) = c_0^{-1}(R + \sqrt{R^2 + D^2 + 2RD\cos(\alpha^R)}). \tag{A.22}$$

Similarly, $\tau'_{\max}(\alpha^R)$ takes its maximum value $\tau'_{\max} = c_0^{-1}(2R + D)$ if $\alpha^R \to 0$ [see Fig. A.1]. On the contrary, regardless of the AoA α^R, the ToA $\tau'(r,\alpha^R)$ takes its minimum value $\tau'_{\min} = c_0^{-1} D$ if the scatterer is closest to the MS, which is the case if $r \to 0$.

Now, in order to determine the domain of integration D_{α^R} in (A.20), one needs to solve (A.22) with respect to α^R. Finding the roots of this function for a given value of the ToA, say τ', it follows

$$\alpha_1^R = -\alpha_2^R = \arccos(\frac{(\tau' c_0)^2 - D^2 - 2\tau' c_0 R}{2RD}). \tag{A.23}$$

Indeed, the domain between α_1^R and α_2^R determines the integral limits in (A.20).

Geometric scattering model	**Established**	Gaussian	Uniform circular	Uniform hollow-disk	Uniform ring
	Model parameter(s)	$\sigma/D = 0.15$	$\gamma^{-1} = 0.25$	$\gamma^{-1} = 0.25$, $r/D = 0.18$	$\gamma^{-1} = 0.25$
UDSM (proposed)	$\mathrm{LSE}_{\mathrm{AoD}}$, $\mathrm{LSE}_{\mathrm{ToA}}$	0.6502, 0.9072	0, 0	0.6801, 0.7094	0.0061, 0.0014
	γ^{-1}, k	0.24, 0.62	0.25, 1	0.23, 7.63	0.24, 25

Table A.1: LSEs after matching the UDSM to established geometric scattering models

After solving the integral presented in (A.20) with due regard to the integral limits presented in (A.23), the PDF $p_{\tau'}^{(k)}(\tau')$ of the ToA τ' can be expressed by

$$p_{\tau'}^{(k)}(\tau') = \frac{c_0[(\tau' c_0)^2 - D^2]^k}{2\pi(2R)^{k+1}} \left[\frac{D\sin(\alpha^R)}{(\tau' c_0 + D\cos(\alpha^R))^{k+1}} + \int \frac{\tau' c_0 + kD\cos(\alpha^R)}{(\tau' c_0 + D\cos(\alpha^R))^{k+1}} d\alpha^R \right] \Bigg|_{\alpha^R=\alpha_2^R}^{\alpha^R=\alpha_1^R} \tag{A.24}$$

for $\tau' \in [\tau'_{\min}, \tau'_{\max}]$. It is worth mentioning that for a given shape factor k, the integral in (A.24) can be represented in terms of another integral of lower order. This statement can be supported by comparing the order of the denominator under the integral in (A.20), which is $k+2$, with that one shown in (A.24), which is $k+1$. A recursive solution for this type of integrals can be found in [36, Eq. (2.554-1)]. This means that for a given value of k, the integral part of the PDF $p_{\tau'}^{(k)}(\tau')$ presented in (A.24) can be solved in closed form. By way of example, the final expressions for the PDF $p_{\tau'}^{(k)}(\tau')$ in which the shape factor k is set to 0 and 1 are given by

$$p_{\tau'}^{(0)}(\tau') = \frac{c_0}{2\pi R} \left[\frac{D\sqrt{1-u^2}}{\tau' c_0 + Du} + \frac{2\tau' c_0}{\sqrt{(\tau' c_0)^2 - D^2}} \times \arctan\left(\sqrt{\frac{(\tau' c_0 - D)(1-u)}{(\tau' c_0 + D)(1+u)}}\right) \right] \tag{A.25}$$

and

$$p_{\tau'}^{(1)}(\tau') = \frac{c_0}{4\pi R^2}[(\tau' c_0)^2 - D^2] \left[\frac{D\sqrt{1-u^2}}{(\tau' c_0 + Du)^2} + \frac{2}{\sqrt{(\tau' c_0)^2 - D^2}} \arctan\left(\sqrt{\frac{(\tau' c_0 - D)(1-u)}{(\tau' c_0 + D)(1+u)}}\right) \right] \tag{A.26}$$

respectively, for $\tau' \in [\tau'_{\min}, \tau'_{\max}]$, where

$$u = \frac{(\tau' c_0)^2 - D^2 - 2\tau' c_0 R}{2RD}. \tag{A.27}$$

The PDF $p_{\tau'}^{(1)}(\tau')$ in (A.26) represents the distribution of the ToA in a radio propagation environment, in which the local scatterers are uniformly distributed within the disk centered on the MS. This result exactly meets the ToA PDF of the

$$p_{\tau'}^{(k)}(\tau') = \frac{c_0[(\tau' c_0)^2 - D^2]^{k-\frac{1}{2}}}{2\pi k (2R)^{(k+1)}} \left[\frac{2(k+1)\tau' c_0}{(\tau' c_0 + D\cos(\alpha^R))^k} g_1 - \frac{k((\tau' c_0)^2 - D^2)}{(\tau' c_0 + D\cos(\alpha^R))^{k+1}} g_2 \right] \Bigg|_{\alpha^R = \alpha_2^R}^{\alpha^R = \alpha_1^R} \tag{A.28}$$

where

$$g_1 = F_1\left(-k; \frac{1}{2}, \frac{1}{2}; 1-k; \frac{\tau' c_0 + D\cos(\alpha^R)}{\tau' c_0 - D}, \frac{\tau' c_0 + D\cos(\alpha^R)}{\tau' c_0 + D}\right) \tag{A.29}$$

$$g_2 = F_1\left(-k-1; \frac{1}{2}, \frac{1}{2}; -k; \frac{\tau' c_0 + D\cos(\alpha^R)}{\tau' c_0 - D}, \frac{\tau' c_0 + D\cos(\alpha^R)}{\tau' c_0 + D}\right). \tag{A.30}$$

---

uniform circular model provided, e.g., in [11, Eq. (65)].

Besides the aforementioned recursive solution in (A.24) for the ToA PDF $p_{\tau'}^{(k)}(\tau')$ of the UDSM, a general (except for $k = 0$) closed-form solution for $p_{\tau'}^{(k)}(\tau')$ can be presented by (A.28) [see the top of the current page], in which $F_1(\cdot;\cdot,\cdot;\cdot;\cdot,\cdot)$ denotes Appell's hypergeometric function [37]. Notice that for $k = 0$, the closed-form solution is given by (A.25).

Figure A.6 plots the logarithmic scale of the PDF $p_{\tau'}^{(k)}(\tau')$ of the UDSM for different values of the shape factor k, where the MS-to-BS distance D and the disk radius R have been again set to 2 km and 250 m, respectively. To validate the closed-form expression of the ToA PDF in (A.24) (or equivalently in (A.28)), the normalized histogram of the simulation results is also plotted in this figure. The procedure to obtain the normalized histogram is the same as the one discussed in Section V-A. As can be observed, for the considered values of k, there exists a good agreement between the analytical result and the normalized histogram, demonstrating that the derived ToA PDF of the UDSM is correct. Furthermore, for all given values of k, a high density of the ToA τ' around the minimum propagation delay $\tau'_{\min}$ and a low density around the maximum propagation delay $\tau'_{\max}$ can be observed. In addition, except the PDF $p_{\tau'}^{(25)}(\tau')$, all logarithmic-scaled PDFs plotted in Fig. A.6 can be approximated over a large interval by linear lines with negative slopes. This means that each of the ToA PDFs, except the aforementioned one, follows approximately a negative exponential distribution in linear scale. Such a decaying exponential behavior has often been adopted in specified channel models, such as in [28]. In this connection, it has been shown in [4, Fig. 5] that the ToA PDF of the uniform

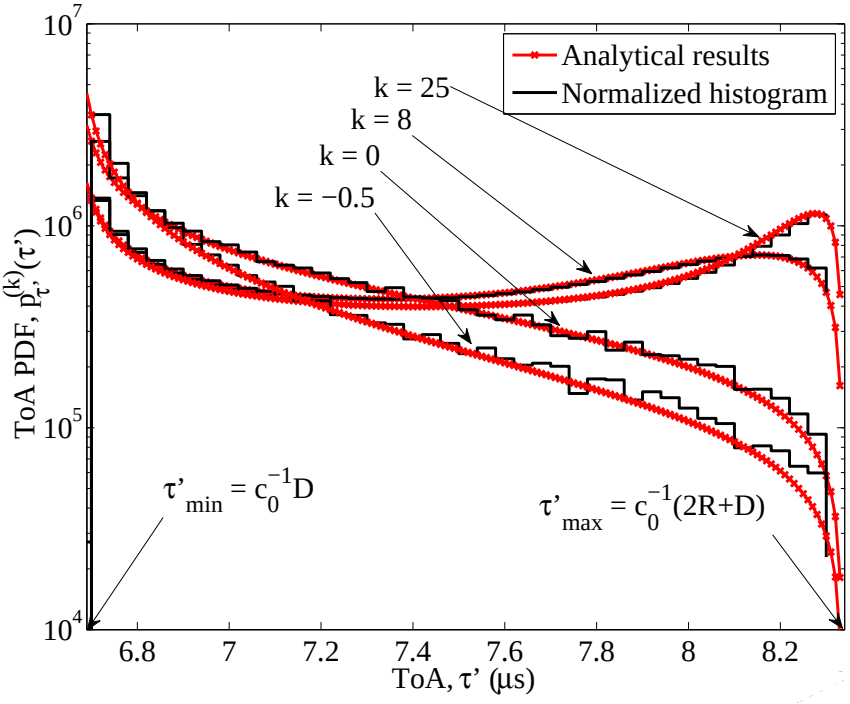

Figure A.6: PDF $p_{\tau'}^{(k)}(\tau')$ of the ToA τ' for the unified disk scattering model for different values of the shape factor k, where $\gamma = D/R = 8$.

hollow-disk model does not exhibit a decaying exponential behavior if the radius of the inner border tends to the radius of the outer one. In Fig. A.6, the changes of the curve when k increases from $k = 8$ to $k = 25$ support this statement.

Figure A.7 is devoted to show the linear scale of the PDF $p_{\tau'}^{(0)}(\tau')$ for different values of the disk radius R, where the shape factor k is set to 0, meaning that the local scatterers are distributed according to the joint uniform PDF in polar coordinates [see (A.3)]. Referring to this figure, we can observe that for an assumed value of D, an increase of R results in a higher probability of receiving signals with larger delays. This is in concert with Fig. A.4, showing that an increase of R spreads the distribution of the AoD. Figure A.7 presents clearly that the ToA τ' follows a decaying exponential-like distribution function. It should also be mentioned that the measurement results reported in [25] indicate that the propagation delays in typical urban environments can be modeled by a negative exponential function. A more detailed comparison between the analytical and empirical ToA PDFs is provided in Section VI.

In accordance with Section V-A, we try to fit the ToA PDF of the UDSM to that of the Gaussian, uniform circular, uniform hollow-disk, and the uniform ring model. The importance of these models has been discussed in Section V-B. The

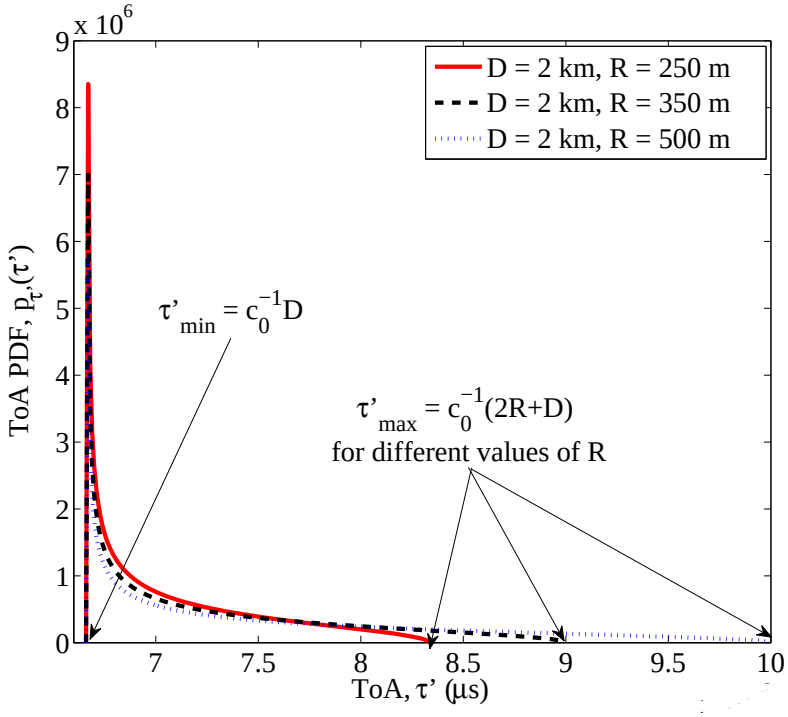

Figure A.7: PDF $p^{(0)}_{\tau'}(\tau')$ of the ToA τ' for the proposed UDSM for different values of the disk radius R, where $D = 2$ km ($c_0 = 3 \times 10^8$m/s).

ToA PDF $p^{G}_{\tau'}(\tau')$ of the Gaussian model can be found in, e.g., [13, Eq. (39)]. Notice that a drawback of the Gaussian scattering model is the lack of a closed-form solution for the ToA PDF implying that numerical integration techniques have to be invoked [13]. The ToA PDF of the uniform circular model can also be found in, e.g., [11, Eq. (65)]. Meanwhile, the ToA PDF of the uniform hollow-disk model and the uniform ring model can be found in [4, Eq. (9)].

Figure. A.8 shows the curve-fitting results of the ToA PDF of the UDSM and that of the established scattering models, while Table A.1 lists the corresponding LSEs in detail[2]. As can be observed in Fig. A.5, the ToA PDF of the UDSM agrees closely with those of the considered scattering models. Referring to Table A.1, the minimum and the maximum LSE_{ToA} belong to the uniform circular and Gaussian scattering models, respectively. Furthermore, the LSE_{ToA} corresponding to the uniform hollow-disk model is very close to that of the Gaussian model. This consents

[2]In agreement with the curve-fitting in Fig. A.5, we have used the same model parameters obtained by identifying the LSE with respect to the AoD PDF. This means that the model parameters have not been optimized again to determine the LSE with respect to the ToA PDF. Nevertheless, we still use the term LSE_{ToA} to address this error in Table A.1. This is due to the fact that determining the LSE_{ToA} results in very close values (not shown in Table A.1) of the model parameters to those listed in Table A.1, which have been optimized by identifying LSE_{AoD}.

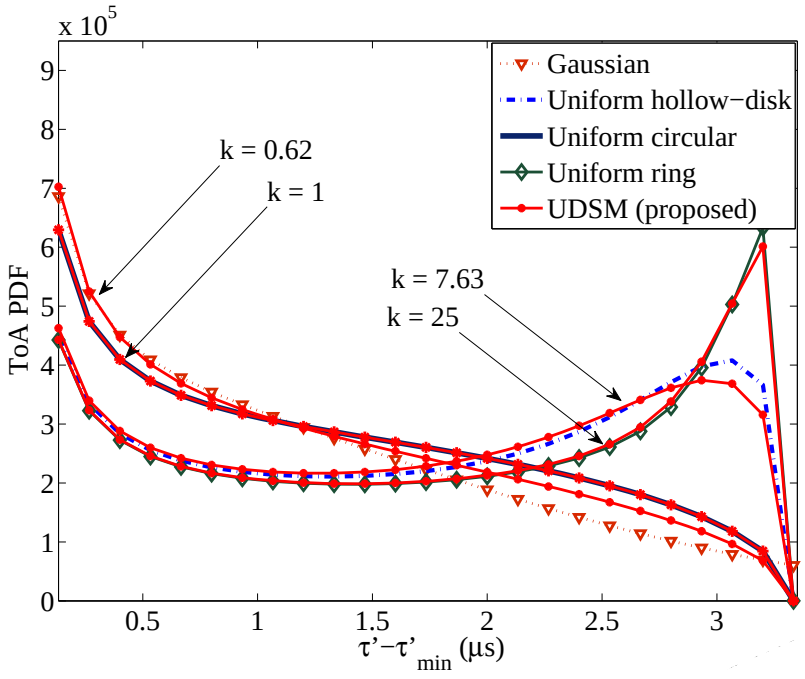

Figure A.8: Curve-fitting results after matching the ToA PDF $p_{\tau'}^{(k)}(\tau')$ of the proposed UDSM to the ToA PDF of the uniform circular, Gaussian, uniform hollow-disk, and the uniform ring model.

to the result presented in Section V-A, in which the maximum $\mathrm{LSE}_{\mathrm{AoD}}$ belongs to the uniform hollow-disk model. The curve-fitting is again poor for the tail of the Gaussian model, which is again owing to the substantial difference between the scatterer domains of the UDSM and the Gaussian model. Moreover, a very close compromise between the ToA PDFs of the UDSM and the uniform ring model can be observed. In this case, the non-zero value of the $\mathrm{LSE}_{\mathrm{ToA}}$ is again caused by upper-bounding the shape factor by $k = 25$. So far, this paper has shown that by calibrating the shape factor k in the UDSM characterized by (A.1), the Gaussian, uniform circular, uniform hollow-disk, and the uniform ring scattering model (including any continuous concentration of the local scatterers between these models) can be either precisely obtained or well approximated. This statement holds not only for the apparent shape of the disk scattering area, but also for the corresponding AoD and ToA PDFs. In this regard, Figs. A.5 and A.8, as well as Table A.1 demonstrate the effectiveness of this unification. Adding the fact that both the AoD and ToA PDFs of the UDSM have closed-form expressions, it can be concluded that the UDSM is a general robust geometric model to describe effectively the distribution of the local scatterers in different propagation areas. In what follows, the robustness of the UDSM in the sense of matching empirical data sets will be evalu-

ated as well.

VI. COMPARISON WITH MEASURED CHANNELS

The objective of the following section is to assess the validity of the UDSM by comparing the derived analytical results with several measured channels in the literature. In this connection, the goodness-of-fit of the UDSM is also compared with that of several candidate geometric models. The corresponding curve-fitting results are illustrated in Figs. A.9-A.13, while their details are listed in Table A.2.

A. Goodness-of-Fit Metric

Here, the goodness-of-fit between each candidate geometric model and an empirical data set is the LSE between the two. The first step is to normalize each empirical data set to guarantee the unity area under the data sets. Then, the calibrated parameters of each model are determined by searching over the ranges of the parameters to identify the LSE. This procedure is the same as the one used in [22, Eq. (1)]. There, the $\mathrm{LSE}_{\mathrm{AoD}}$ is the chosen metric to judge the goodness-of-fit. However, in this paper, we do not focus solely on the $\mathrm{LSE}_{\mathrm{AoD}}$. If the empirical AoD is not available (denoted by N.A.), but the corresponding ToA exists, we optimize the model parameters to determine the $\mathrm{LSE}_{\mathrm{ToA}}$ and to judge the curve-fitting results. If both the empirical AoD and ToA PDFs of a measured channel are at hand, we calibrate the model parameters by identifying the $\mathrm{LSE}_{\mathrm{AoD}}$ as the goodness-of-fit metric. The calibrated parameters will then be used to plot the corresponding ToA PDF. This means that we do not search again over the model parameters to determine the $\mathrm{LSE}_{\mathrm{ToA}}$. Nevertheless, we still use the term $\mathrm{LSE}_{\mathrm{ToA}}$ to address this error. The aforementioned procedure can fairly provide a simultaneous comparison with respect to both the AoD and ToA PDFs. Furthermore, this allows us to compare our results with the ones reported in [22].

B. Candidate Geometric Models

The candidate geometric scattering models are the uniform circular, Gaussian, inverted-parabolic, conical, uniform hollow-disk, uniform elliptical, and the proposed UDSM as listed in Table A.2. Notice that the first four models have only one degree of freedom, while the last three allow two degrees of freedom. Furthermore, all the aforementioned scattering models result in unimodal PDFs for the ToA (AoD), except the uniform hollow-disk model, which yields bimodal PDFs for both the ToA and the AoD. All the candidate models assume that the BS (served as the transmitter) is located outside of the scatterer domain, except the Gaussian model which allows an infinite scatterer domain. Notice that in all the above-mentioned

models, except the Gaussian model, the support region for the scatterers is a limited disk centered on the MS (served as the receiver).

C. Candidate Empirical Data sets

The candidate empirical data sets are the measured channels reported in [23–26]. The candidates have been chosen such that three different propagation areas including rural, suburban, and urban environments are covered (see Table A.2). Based on the classification reported in [22], the first three [23–25] measured channels have a unimodal shape of the ToA (AoD) histogram, while the last one [26] follows a bimodal shape. The environment and the BS hight corresponding to each measurement scenario consent to our first assumptions in Section II. A more compact detailed information about other characteristics of the candidate measured channels can also be found in [22].

D. Comparison Results

Starting from the measured channel in [23], the curve-fitting results of the AoD PDF of the candidate geometric models and that of the empirical data are shown in Fig. A.9. The optimized model parameters and the $\mathrm{LSE}_{\mathrm{AoD}}$ corresponding to each geometric model are listed in Table A.2. Notice that the same curve-fitting, except for the UDSM, to the same measured channel has also been provided in [22]. The calibrated model parameters and the corresponding $\mathrm{LSE}_{\mathrm{AoD}}$ in [22], are very close to those obtained in this paper. Referring to Table A.2, the uniform elliptical model leads to the minimum $\mathrm{LSE}_{\mathrm{AoD}} = 1.6601$ among the other geometric models. The UDSM also suffers a close $\mathrm{LSE}_{\mathrm{AoD}} = 1.7021$ to the minimum one and is quite far from the $\mathrm{LSE}_{\mathrm{AoD}}$ of the other models. This can also be observed in Fig. A.9, where both the uniform elliptical model and the UDSM follow the empirical data very well. In this regard, the UDSM matches around the peak of the empirical data better than the uniform elliptical model, while the uniform elliptical model provides a better fitting in the tails of the distribution. Needless to say, the most important part of a PDF corresponds to the peak of the curve. It is also noteworthy that the performance of the other geometric models is considerably less than the two aforementioned ones. We finish analyzing the third column of Table A.2 by noticing that the ToA PDF of the measured channel in [23] is not available there.

The next column of Table A.2 is devoted to the curve-fitting results shown in Fig. A.10. This figure compares the match between the ToA PDF of the candidate geometric scattering models and that of the measured channel in [24]. The delay histogram in [24, Fig. 6] has a standard deviation of $\tau'_{\mathrm{rms}} = 0.9\,\mu$s. The optimized model parameters result almost in the same τ'_{rms}, hence the data in Fig. A.10 is

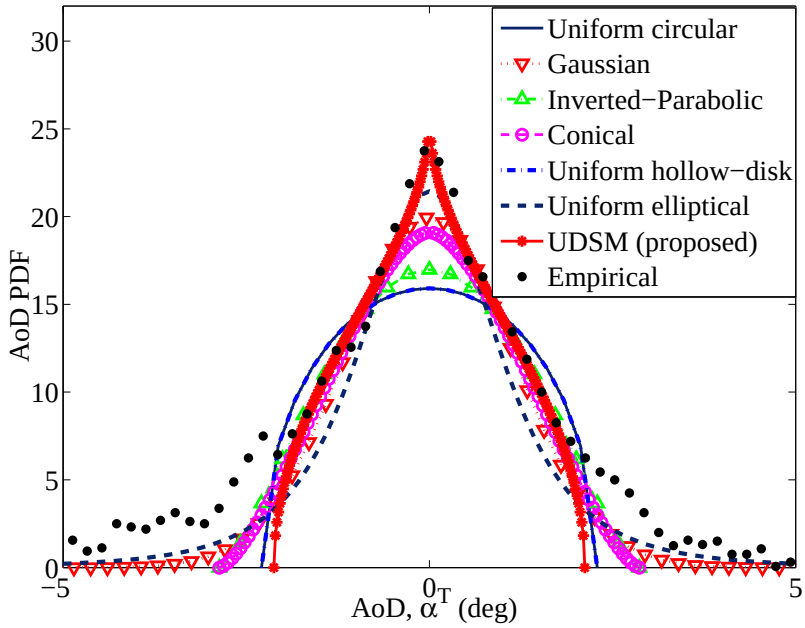

Figure A.9: Curve-fitting results after matching the various geometric models to the empirical data in [23, Fig. 1].

shown for $\tau'_{\text{rms}} p_{\tau'}(\tau')$ versus $\tau' - \tau'_{\text{min}}$. The AoD PDF of this channel has not been measured in [24], hence denoted by N.A. in Table A.2. Referring to Table A.2, the UDSM and the uniform circular models lead to the minimum and the maximum LSE_{ToA}, respectively. Besides the UDSM, the uniform elliptical and the conical models also experience a very small LSE_{ToA}. This is in concert with the results reported in [18], where it has been shown that the conical model outperforms the uniform circular and the inverted-parabolic models.

The curve-fitting results to the empirical ToA and AoD PDFs derived from the measured channel in [23] are illustrated in Figs. A.11 and A.12, respectively. The calibrated parameters in Table A.2 are obtained by identifying LSE_{AoD} of each model. These parameters are very close to those reported in [22]. We use the same calibrated parameters to plot the corresponding ToA PDFs. The delay histogram in [23, Fig. 11] has a standard deviation of $\tau'_{\text{rms}} = 0.68\,\mu\text{s}$ as reported in [13]. The calibrated model parameters result almost in the same τ'_{rms}, hence the data in Fig. A.12 is shown for $\tau'_{\text{rms}} p_{\tau'}(\tau')$ versus $\tau' - \tau'_{\text{min}}$. Referring to Table A.2, the uniform elliptical model with the minimum $\text{LSE}_{\text{AoD}} = 0.08501$ outperforms the other considered geometric models. However, this model does not provide the best fitting to the empirical ToA PDF. In this case, the UDSM with the minimum $\text{LSE}_{\text{ToA}} = 0.06283$ provides the best fitting. Meanwhile, although, the LSE_{AoD}s

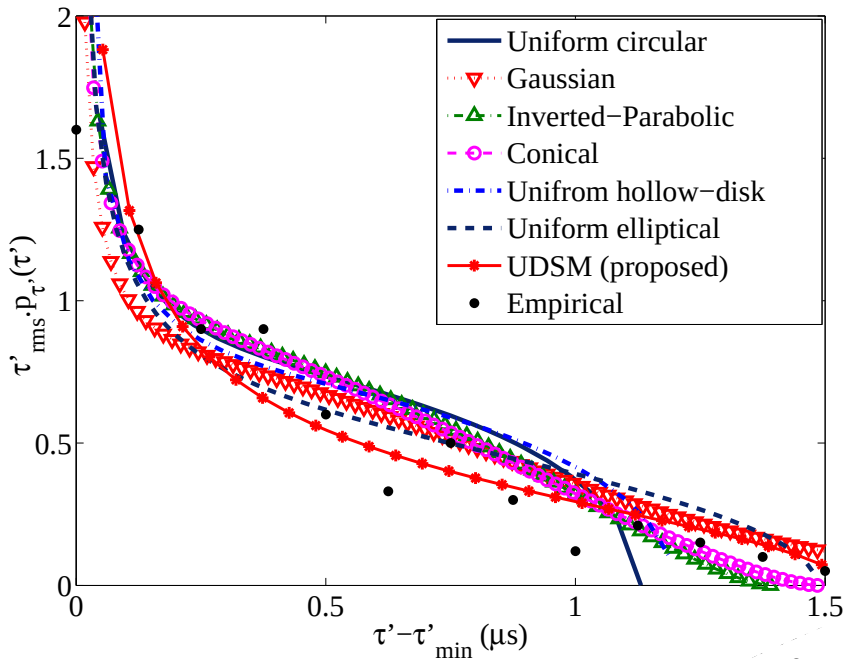

Figure A.10: Curve-fitting results after matching the various geometric models to the empirical data in [24, Fig. 6], where $\tau'_{\text{rms}} = 0.9\,\mu$s.

of the uniform elliptical and the UDSM are very close to each other, these errors have two different origins. Referring to Fig. A.11, the LSE_{AoD}s corresponding to the uniform elliptical and the UDSM originate mainly from around the peak and the tails of the curves, respectively. In addition, referring to Table A.2, the LSE_{AoD}s of the Gaussian model is considerably less than that of the uniform circular model, which agrees with the conclusion of [13].

Finally, the last column of Table A.2 lists the details of the curve-fitting illustrated in Fig. A.13. This figure depicts the curve-fitting results of the AoD PDF of the candidate geometric scattering models and that of the measured channel in [26]. The discussion on this figure show explicitly the importance of the UDSM and its novel features. In [22], it has been shown that the best two geometric models to describe the measured channel in [26] are the uniform hollow-disk and the uniform circular (Rx-inside) models, respectively. This is due to the fact that the empirical data set in [26] has indeed neither a unimodal nor a bimodel shape. It has almost a flat peak with some fluctuations, which can be fitted by both the aforementioned models. However, the uniform circular model cannot sufficiently cover the flat peak. While, the uniform hollow-disk model fits to the data through two sharp peaks. These sharp peaks are caused by the bimodality nature of the AoD PDF [4, Eq. (6)]

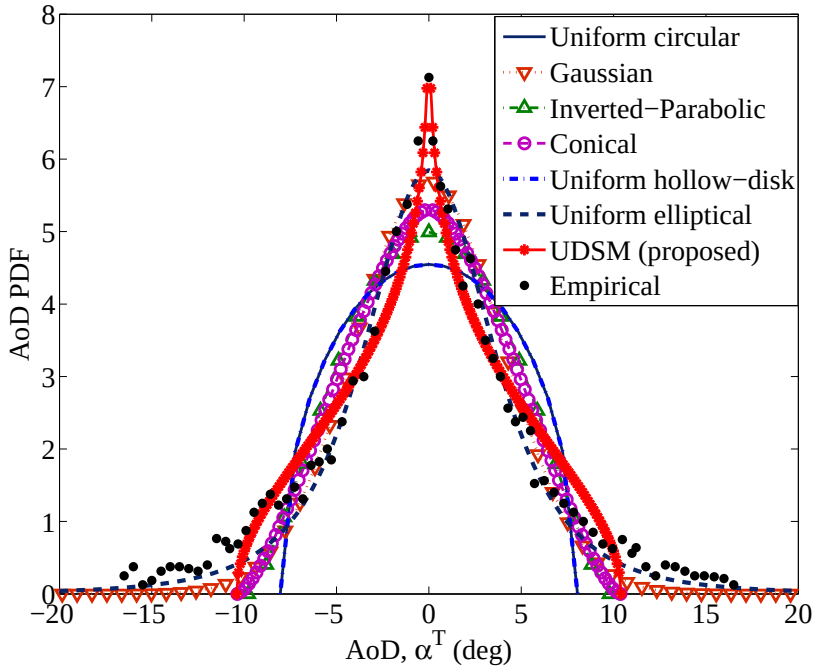

Figure A.11: Curve-fitting results after matching the various geometric models to the empirical data in [25, Fig. 4].

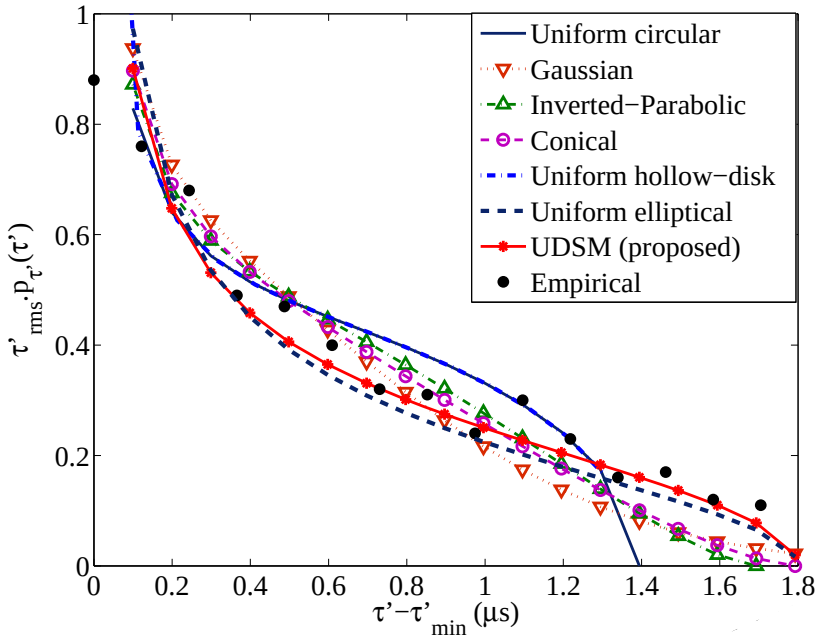

Figure A.12: Curve-fitting results after matching the various geometric models to the empirical data in [25, Fig. 11], where $\tau'_{\text{rms}} = 0.68\,\mu$s.

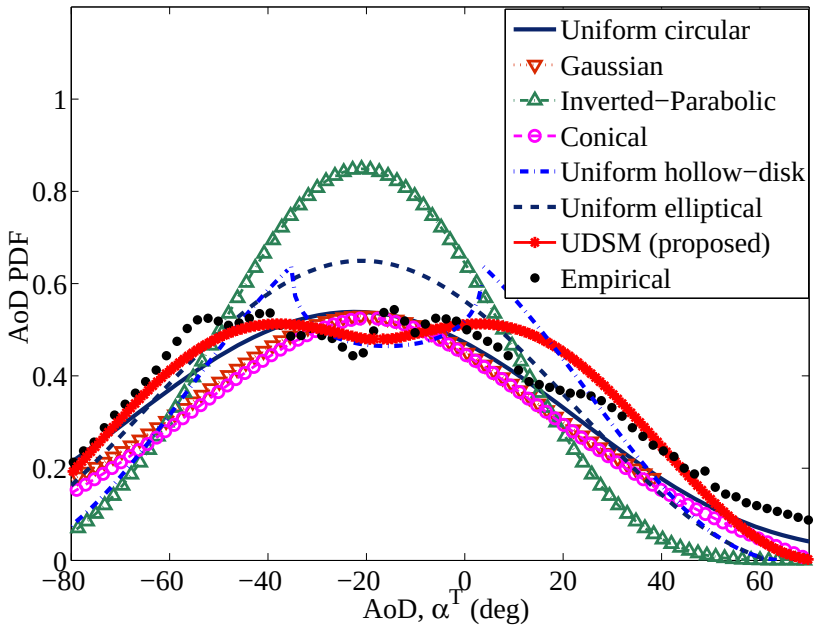

Figure A.13: Curve-fitting results after matching the various geometric models to the empirical data in [26, Fig. 6].

of this model. Now, recall from Section III-B that one of the unique features of the UDSM is to generate a flexible distribution between the uniform circular and the uniform hollow-disk models, which are quite solid geometric models. The effect of this feature can be seen in Fig. A.13, where the AoD PDF of the UDSM has a shape between those of the uniform hollow-disk and the uniform circular models. This shape is obtained by choosing $k = 2.1$ as shown in Table A.2. Notice that for $k = 1$, the UDSM results absolutely in the uniform circular model and for higher values, approximates the uniform hollow-disk model. Referring to Table A.2, the UDSM results in the minimum $\mathrm{LSE}_{\mathrm{AoD}} = 0.002109$, which is almost half of the $\mathrm{LSE}_{\mathrm{AoD}}$ corresponding to the uniform hollow-disk and the uniform circular models.

Geometric scattering model	**Reference** / **Setting area**	Pedersen [23], Fig. 1 Rural	Bataniere [24], Fig. 6 Suburban	Pedersen [25], Figs. 4 and 11 Urban	Kloch [26], Fig. 6 Urban
Uniform Circular [6–11]	LSE_{AoD}, LSE_{ToA}	9.9604, N.A.	N.A., 0.01291	0.5301, 0.5120	0.003792, N.A.
	γ^{-1}	0.04	0.25	0.15	1.14
Gaussian [13–15]	LSE_{AoD}, LSE_{ToA}	3.2211, N.A.	N.A., 0.0104	0.1944, 0.1522	0.007209, N.A.
	σ/D	0.02	0.42	0.07	0.75
Inverted-Parabolic [19]	LSE_{AoD}, LSE_{ToA}	6.2799, N.A.	N.A., 0.01121	0.3307, 0.2117	0.03586, N.A.
	γ^{-1}	0.05	0.68	0.16	1
Conical [6] and [18]	LSE_{AoD}, LSE_{ToA}	4.4103, N.A.	N.A., 0.0091	0.2501, 0.1811	0.04824, N.A.
	γ^{-1}	0.05	0.87	0.18	1
Uniform hollow-disk [4] and [5]	LSE_{AoD}, LSE_{ToA}	9.9901, N.A.	N.A., 0.01277	0.5169, 0.5281	0.003697, N.A.
	γ^{-1}, r/D	0.04, 0.0004	0.24, 0.0024	0.15, 0.0015	1, 0.35
Uniform elliptical [5, 7, 11], and [12]	LSE_{AoD}, LSE_{ToA}	1.6601, N.A.	N.A., 0.00901	0.08501, 0.07311	0.008904, N.A.
	b/a, a/D	0.04, 0.99	0.22, 0.72	0.1, 0.99	0.99, 0.99
UDSM (proposed)	LSE_{AoD}, LSE_{ToA}	1.7021, N.A.	N.A., 0.00895	0.08691, 0.06283	0.002109, N.A.
	γ^{-1}, k	0.037, 0.5	0.28, 0	0.18, 0.2	1, 2.1

Table A.2: LSEs after matching the geometric scattering models to empirical data sets

VII. CONCLUSION

Starting from a unified disk scattering model (UDSM) controlled by a shape factor to model the distribution of the local scatterers confined to a disk centered on the MS, closed-form expressions have been provided for the joint PDF of the AoD and AoA as well as the joint PDF of the ToA and AoA. From these joint PDFs, the marginal PDFs of the AoD and ToA have been also derived in closed form. The correctness of the analytical results has been confirmed by the simulation results. It has been also shown that by calibrating the shape factor, the uniform circular and the uniform ring scattering models can be obtained exactly, while the Gaussian and uniform hollow-disk models can be well approximated. The numerical results have shown that the AoD and ToA PDFs of the UDSM can either precisely or closely follow those of the Gaussian, uniform circular, uniform hollow-disk, and the uniform ring scattering models. The derived analytical results have also been validated by both the unimodal and non-unimodal empirical data sets obtained from several measured channels in the literature. The curve-fitting results have shown that the UDSM is highly flexible and outperforms several other geometric models proposed in the literature. Taking several candidate measured channels from different propagation areas into account, it has been shown that the LSE of the UDSM is always around half of that of the Gaussian model. The UDSM competes closely with the uniform elliptical model for providing the best curve-fitting to the unimodal empirical data sets. However, the UDSM outperforms considerably the uniform elliptical model in the sense of matching bimodal empirical data sets. This is due to the fact that by calibrating the shape factor, the AoD (ToA) PDF of the UDSM renders a bimodal shape with two smooth peaks, while its mathematical expression is always unimodal. This bimodal curve fits even better to the non-unimodal empirical data set than the uniform hollow-disk model, which was to date the best proposed model in this case. Further statistical characterizations devoted to, e.g., the average delay, delay spread, and correlation properties of the channel can also be a topic for further research.

ACKNOWLEDGMENT

The authors would like to thank the ten anonymous reviewers of this paper for their valuable comments, which helped us to improve the quality of the paper.

REFERENCES

[1] D.-S. Shiu, G. J. Foschini, M. J. Gans, and J. M. Kahn, "Fading correlation and its effect on the capacity of multielement antenna systems," *IEEE Trans. Commun.*, vol. 48, no. 3, pp. 502–513, Mar. 2000.

[2] A. Abdi and M. Kaveh, "A space-time correlation model for multielement antenna systems in mobile fading channels," *IEEE J. Select. Areas Commun.*, vol. 20, no. 3, pp. 550–560, Apr. 2002.

[3] M. Pätzold and B. O. Hogstad, "A space-time channel simulator for MIMO channels based on the geometrical one-ring scattering model," in *Proc. 60th IEEE Semiannual Veh. Technol. Conf., VTC 2004-Fall*, vol. 1. Los Angeles, CA, USA, Sep. 2004, pp. 144–149.

[4] A. Y. Olenko, K. T. Wong, and E. H. O. Ng, "Analytically derived TOA-DOA statistics of uplink/downlink wireless multipaths arisen from scatterers on an hollow-disc around the mobile," *IEEE Antennas Wireless Propag. Lett.*, vol. 2, pp. 345–348, 2003.

[5] I. Jaafar, H. Boujemaa, and M. Siala, "Angle and time of arrival statistics for hollow-disc and elliptical scattering models," in *Proc. 2nd Int. Conf. Signals, Circuits Syst., Nov. 2008*, pp. 1–4.

[6] P. C. F. Eggers, "Generation of base station DOA distribution by Jacobi transformation of scattering areas," *Electron. Lett.*, vol. 34, no. 1, pp. 24–26, Jan. 1998.

[7] R. J. Piechocki, G. V. Tsoulos, and J. P. McGeehan, "Simple general formula for PDF of angle of arrival in large cell operational environments," *Electron. Lett.*, vol. 34, no. 18, pp. 1784–1785, Sep. 1998.

[8] P. Petrus, J. H. Reed, and T. S. Rappaport, "Geometrically based statistical channel model for macrocellular mobile environments," in *Proc. IEEE GLOBECOM, London, UK*, vol. 2, Nov. 1996, pp. 1197–1201.

[9] D. R. Van Rheeden and S. C. Gupta, "A geometric model for fading correlation in multipath radio channels," in *IEEE Int. Conf. on Communications, ICC 1998*. Atlanta, GA, USA, Jun. 1998, pp. 1655–1659.

[10] L. Jiang and S. Y. Tan, "Simple geometrical-based AOA model for mobile communication systems," *Electron. Lett.*, vol. 40, no. 19, pp. 1203–1205, Sep. 2004.

[11] R. B. Ertel and J. H. Reed, "Angle and time of arrival statistics for circular and elliptical scattering models," *IEEE J. Select. Areas Commun.*, vol. 17, no. 11, pp. 1829–1840, Nov. 1999.

[12] J. C. Liberti and T. S. Rappaport, "A geometrically based model for line-of-sight multipath radio channels," in *Proc. IEEE Veh. Technol. Conf., VTC 1996*, Apr./May 1996, pp. 844–848.

[13] R. Janaswamy, "Angle and time of arrival statistics for Gaussian scatter density model," *IEEE Trans. Wireless Commun.*, vol. 1, no. 3, pp. 488–497, Jul. 2002.

[14] A. Andrade and D. Covarrubias, "Radio channel spatial propagation model for mobile 3G in smart antenna system," *IEICE Trans. Commun.*, vol. E86-B, no. 1, pp. 213–220, Jan. 2003.

[15] D. D. N. Bevan, V. T. Ermolayev, A. G. Flaksman, and I. M. Averin, "Gaussian channel model for mobile multipath environment," *EURASIP J. Appl. Signal Proc.*, vol. 2004, no. 9, pp. 1321–1329.

[16] S.-H. Kong, "TOA and AOD statistics for down link Gaussian scatterer distribution model," *IEEE Trans. Wireless Commun.*, vol. 8, no. 5, pp. 2609–2617, May 2009.

[17] A. H. Kazmi and N. M. Khan, "Effect of scattering around BS on the spatial statistics of mobile channel in macrocell environment," in *International Conference on Information and Emerging Technologies (ICIET), Karachi*, vol. 1, Jun. 2010, pp. 1–5.

[18] Y. I. Wu and K. T. Wong, "A geometrical model for the TOA distribution of uplink/downlink multipaths, assuming scatterers with a conical spatial density," *IEEE Antennas Propag. Mag.*, vol. 50, no. 6, pp. 196–205, Dec. 2008.

[19] A. Y. Olenko, K. T. Wong, and M. Abdulla, "Analytically derived TOA-DOA distributions of uplink/downlink wireless-cellular multipaths arisen from scatterers with an inverted-parabolic spatial distribution around the mobile," *IEEE Signal Processing Lett.*, vol. 12, no. 7, pp. 516–519, Jul. 2005.

[20] J. Laurila, A. F. Molisch, and E. Bonek, "Influence of the scatterer distribution on power delay profiles and azimuth power spectra of mobile radio channels," in *Proc. Int. Symp. Spread Spect. Tech. App.*, vol. 1, pp. 267–271.

[21] L. Jiang and S. Y. Tan, "Geometrically based statistical channel models for outdoor and indoor propagation environments," *IEEE Trans. Veh. Technol.*, vol. 56, no. 6, pp. 3587–3593, Nov. 2007.

[22] K. T. Wong, Y. I. Wu, and M. Abdulla, "Landmobile radiowave multipaths' DOA-distribution: Assessing geometric models by the open literature's empirical datasets," *IEEE Trans. Antennas Propag.*, vol. 58, no. 3, pp. 946–958, Mar. 2010.

[23] K. I. Pedersen, P. E. Mogensen, and B. H. Fleury, "Spatial channel characteristics in outdoor environments and their impact on BS antenna system performance," in *Proc. IEEE 48th Veh. Technol. Conf., VTC'98*, vol. 2. Ottawa, Canada, pp. 719–723.

[24] M. D. Batariere, T. K. Blankenship, J. F. Kepler, T. P. Krauss, I. Lisica, S. Mukthavaram, J. W. Porter, T. A. Thomas, and F. W. Vook, "Wideband MIMO impulse response measurements at 3.7 GHz," in *Proc. IEEE 45th Veh. Technol. Conf., VTC'02*, vol. 1, pp. 26–30.

[25] K. I. Pedersen, P. E. Mogensen, and B. H. Fleury, "A stochastic model of the temporal and azimuthal dispersion seen at the base station in outdoor propagation environments," *IEEE Trans. Veh. Technol.*, vol. 49, no. 2, pp. 437–447, Mar. 2000.

[26] C. Kloch, G. Liang, J. B. Andersen, G. F. Pedersen, and H. L. Bertoni, "Comparison of measured and predicted time dispersion and direction of arrival for multipath in a small cell environment," *IEEE Trans. Antennas Propag.*, vol. 49, no. 9, pp. 1245–1263, Sep. 2001.

[27] A. Borhani and M. Pätzold, "Time-of-arrival, angle-of-arrival, and angle-of-departure statistics of a novel simplistic disk channel model," in *Proc. 5th International Conference on Signal Processing and Communication Systems, ICSPCS 2011*. Honolulu, Hawaii, Dec. 2011.

[28] M. Failli, Ed., *COST 207: Digital Land Mobile Radio Communications*. Luxembourg: Commission of the European Communities, 1989.

[29] M. Pätzold, *Mobile Fading Channels*, 2nd ed. Chichester: John Wiley & Sons, 2011.

[30] L. Jiang and S. Y. Tan, "Geometrically-based channel model for mobile communication systems," *Microwave Optical Tech. Lett.*, vol. 45, no. 6, pp. 522–527, Jun. 2005.

[31] C.-L. J. Lam, K. T. Wong, and Y. I. Wu, "The TOA-distribution of multipaths between an omni-directional transceiver and a mis-oriented directional transceiver," *IEEE Trans. Commun.*, vol. 58, no. 4, pp. 1042–1047, Apr. 2010.

[32] Y. I. Wu and K. T. Wong, "Polarisation-sensitive geometric modelling of the distribution of direction-of-arrival for uplink multipaths," *IET Microwave and Antennas. Propag.*, vol. 5, no. 1, pp. 95–101, Jan. 2011.

[33] A. Y. Olenko, K. T. Wong, S. A. Qasmi, and J. Ahmadi-Shokoh, "Analytically derived uplink/downlink TOA and 2D-DOA distributions with scatterers in a 3D hemispheroid surrounding the mobile," *IEEE Trans. Antennas Propag.*, vol. 54, no. 9, pp. 2446–2454, Sep. 2006.

[34] A. Papoulis, *Probability, Random Variables, and Stochastic Processes*, 3rd ed. New York: McGraw-Hill, 1991.

[35] K. Pearson, Ed., *Tables of the Incomplete Beta-Function*, 2nd ed. Cambridge University Press, 1968.

[36] I. S. Gradshteyn and I. M. Ryzhik, *Table of Integrals, Series, and Products*. Elsevier Academic Press publications, 2007.

[37] P. Appell, *Sur Les Fonctions Hypergéométriques de Plusieurs Variables*. In Mémoir. Sci. Math. Paris: Gauthier-Villars, 1925.

Appendix B

Paper II

Title:	On the Spatial Configuration of Scatterers for Given Delay-Angle Distributions
Authors:	**Alireza Borhani** and Matthias Pätzold
Affiliation:	University of Agder, Faculty of Engineering and Science, P. O. Box 509, NO-4898 Grimstad, Norway
Journal:	*Engineering Letters*, pp. 34-38, Feb. 2014.

On the Spatial Configuration of Scatterers for Given Delay-Angle Distributions

Alireza Borhani and Matthias Pätzold

***Abstract* — This paper investigates the distribution of scatterers located around the mobile station (MS) for given delay-angle distributions. The delay-angle distribution function represents the joint probability density function (PDF) of the time-of-arrival (TOA) and angle-of-arrival (AOA). Given such a joint PDF, we first derive a general expression for the distribution of the scatterers in both polar and Cartesian coordinates. We then analyze an important special case in which the TOA and the AOA follow the multiple negative exponential (MNE) and the uniform distributions, respectively. The considered MNE PDF is the sum of several decaying exponential functions, which allows us to describe the TOA in a variety of propagation environments. For the delay profiles specified in COST 207, the scatterer distribution is simulated and visualized in scatter diagrams. The marginal PDF of the distance from the scatterers to the MS is also computed, illustrated, and confirmed by simulations. For the MNE TOA PDF, it is shown that the local scatterers are not symmetrically distributed around the MS even if the AOAs are uniformly distributed. In addition, the obtained scattering area is not confined by firm geometric constraints, which complies with real propagation environments. The importance of the work is to provide a novel approach to channel modelling, in which obtaining the desirable TOA (AOA) PDF is assured.**

***Index terms* — Channel modelling, spatial configuration, scatterer distribution, scatter diagram, delay-angle distribution, multiple negative exponential.**

A. Borhani is with the Faculty of Engineering and Science, University of Agder, 4898 Grimstad, Norway (e-mail: alireza.borhani@uia.no).

M. Pätzold is with the Faculty of Engineering and Science, University of Agder, 4898 Grimstad, Norway (e-mail: matthias.paetzold@uia.no).

I. INTRODUCTION

In the area of channel modelling, the distribution of scatterers is of crucial importance, as it allows us to study the statistical properties of the received multipath signal, such as the AOA and TOA distributions. These functions are essential for determining other characteristic quantities of the channel, like the Doppler spread, average delay, and delay spread. The spatial configuration of scatterers also plays a key role in the characterization of non-stationary channel models [1–4]. A variety of scatterer distributions have been proposed in the literature (see [5] and [6]). Among them, the unified disk scattering [6], uniform elliptical [7–9], and the Gaussian scatterer distribution model [10–14] are the most flexible ones, since they describe various propagation mediums with respect to the TOA and the angle-of-departure distributions [6].

According to the literature, the conventional approach to develop a new geometric-based channel model is to start from a given scatterer distribution and then to derive the statistical properties of the channel model, such as the AOA and TOA PDFs. To validate the proposed channel model, the obtained PDFs must then be validated by empirical data collected from measured channels. A good match, however, cannot always be found due to the restrictions of the proposed scattering model. As an example, many measurement campaigns (see, e.g., [15–17]) and specified channel models (see, e.g., [18]) show that the TOA PDF often follows a sum of negative exponential functions (acronymed by MNE TOA PDF). However, none of the scattering models studied in [5] and [6] results exactly in an MNE TOA PDF. The same disagreement might also arise by comparing measured AOA PDFs and the ones obtained from predefined scattering models.

To cope with this issue, we propose a new approach to design channel models, in which obtaining the desired TOA (AOA) PDF is incontrovertible. The starting point of our approach is not a predefined scattering model. Instead, we start from a given joint PDF of the TOA and AOA, from which the distribution of the local scatterers is derived. The given joint (marginal) PDF of the TOA and AOA can originate from either measured channels or channel specifications. In this way, we develop a channel model in which a perfect match is guaranteed between the statistical properties of the channel model and those of the measured (specified) channels. In addition, the obtained scattering area is not confined by firm geometric constraints.

Given the joint PDF of the TOA and AOA, we derive a mathematical representation for the scatterer distribution in both polar and Cartesian coordinates. As an exemplary application, the MNE TOA PDF specified in COST 207 is employed

to derive the distribution of the local scatterers on the assumption that the AOA is uniformly distributed around the MS and independent of the TOA. The distribution of the scatterers in the propagation area is then illustrated in scatter diagrams. Moreover, the marginal PDF of the distance from the scatterers to the MS is derived, displayed, and compared with simulation results. An excellent agreement between the analytical and simulation results is observed. It is shown that for the MNE TOA PDF, the local scatterers are not symmetrically distributed around the MS. Notice that circularly symmetric scattering models have often been proposed in the literature (see [5] and [6]).

The rest of this paper is organized as follows. Section II is devoted to the mathematical description of the problem, whereas its general and specific solutions are provided in Section III. The simulation results are illustrated and discussed in Section IV. Finally, the conclusions are drawn in Section V.

II. PROBLEM DESCRIPTION

Fig. B.1 demonstrates a typical propagation scenario with some local scatterers. Each plane wave arrives at the MS after a single-bounce caused by one of the scatterers. It is assumed that the base station (BS) acts as the transmitter, while the MS serves as the receiver. Furthermore, we assume that both the BS and the MS are equipped with single omnidirectional antennas. The position of each scatterer can be described by polar coordinates (r, α^R), where r denotes the distance of the scatterer from the MS, and α^R stands for the AOA seen at the MS.

With reference to Fig. B.1, the total path length that an emitted plane wave travels from the BS via a scatterer to the MS equals

$$D_s = r + \sqrt{r^2 + D^2 + 2rD\cos(\alpha^R)}. \tag{B.1}$$

The TOA τ' at the MS equals $\tau' = D_s/c_0$, where c_0 represents the speed of light. Owing to the random nature of propagation environments, the TOA τ' is a random variable, whose distribution $p_{\tau'}(\tau')$ depends on the environment. The same statement holds for the AOA α^R described by the PDF $p_{\alpha^R}(\alpha^R)$. It is worth mentioning that τ' and α^R can often be considered as independent random variables, as a certain mathematical relation between the two does not exist in most of the real propagation scenarios.

Given the joint PDF $p_{\tau'\alpha^R}(\tau', \alpha^R)$ of τ' and α^R, we are interested in finding the joint PDF $p_{r\alpha^R}(r, \alpha^R)$ of the radius r and the AOA α^R. Notice that the joint PDF $p_{r\alpha^R}(r, \alpha^R)$ represents the distribution of scatterers in polar coordinates, which is the first concern of this paper. Providing the Cartesian representation $p_{xy}(x,y)$ of

the scatterer distribution is also of interest, as it allows us to visualize the scattering area in the 2D plane. In what follows, we fulfil the main objectives of this paper by deriving $p_{r\alpha^R}(r,\alpha^R)$ and $p_{xy}(x,y)$.

III. PROBLEM SOLUTION

In this section, we first provide a general solution for the problem stated in Section II. Subsequently, a specific solution is presented under the assumptions of the MNE TOA PDF and the uniformly distributed AOAs.

A. General Solutions

By solving (B.1) with respect to r, we obtain

$$r(\tau',\alpha^R)=\frac{(\tau' c_0)^2-D^2}{2(\tau' c_0+D\cos(\alpha^R))}. \tag{B.2}$$

In the equation above, the radius r is a function of the random variables τ' and α^R. Besides this function, the auxiliary function $A(\tau',\alpha^R)=\alpha^R$ is beneficial, allowing us to derive the joint PDF of the radius r and the AOA α^R. It can be shown that the roots of these functions are given by

$$\tau'=c_0^{-1}\left(r+\sqrt{r^2+D^2+2rD\cos(\alpha^R)}\right) \text{ and } \alpha^R=A. \tag{B.3}$$

By applying the concept of transformation of two random variables [19, p. 130], the joint PDF $p_{r\alpha^R}(r,\alpha^R)$ of r and α^R is given by the following expression

$$\begin{aligned} p_{\,r\alpha^R}(r,\alpha^R) &= |J|^{-1} \\ &\times\; p_{\tau'\alpha^R}\left(c_0^{-1}(r+\sqrt{r^2+D^2+2rD\cos(\alpha^R)}),\alpha^R\right) \end{aligned} \tag{B.4}$$

in which $|J|$ stands for the Jacobian of the transformation. This quantity can be obtained by computing the following determinant

$$\begin{aligned} |J| &= \left|\begin{matrix}\frac{\partial\tau'}{\partial r} & \frac{\partial\tau'}{\partial\alpha^R}\\ \frac{\partial\alpha^R}{\partial r} & \frac{\partial\alpha^R}{\partial\alpha^R}\end{matrix}\right|^{-1} \\ &= c_0\left|1+\frac{r+D\cos(\alpha^R)}{\sqrt{r^2+D^2+2rD\cos(\alpha^R)}}\right|^{-1}. \end{aligned} \tag{B.5}$$

To derive the Cartesian representation $p_{xy}(x,y)$ of the scatterer distribution from its polar representation in (B.4), we use the following transformations $x=r\cos(\alpha^R)$

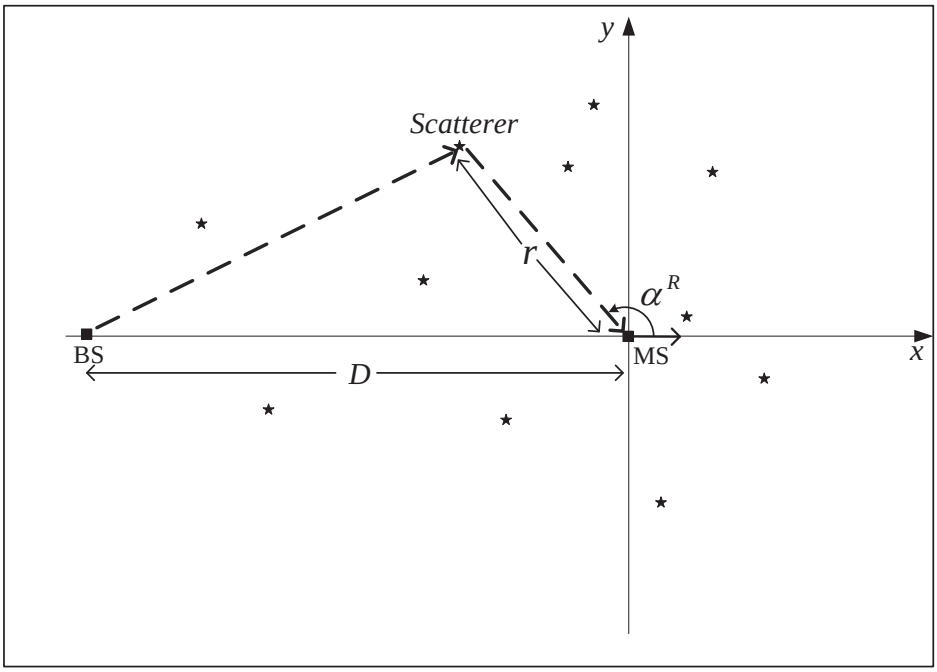

Figure B.1: A typical multipath propagation scenario with some local scatterers ($\star$).

and $y = r\sin(\alpha^R)$. Applying again the concept of transformation of random variables, we obtain

$$p_{xy}(x,y) = c_0^{-1}\left|\frac{1}{\sqrt{x^2+y^2}} + \frac{1+\frac{Dx}{x^2+y^2}}{\sqrt{(x+D)^2+y^2}}\right| \times p_{\tau'\alpha^R}\left(c_0^{-1}(\sqrt{x^2+y^2}+\sqrt{(x+D)^2+y^2}), \arctan\left(\frac{y}{x}\right)\right). \tag{B.6}$$

An important special case occurs if the TOA τ' and the AOA α^R are independent random variables. In this case, the joint PDF $p_{\tau'\alpha^R}(\cdot,\cdot)$ in (B.4) (or equivalently (B.6)) can be represented as the product of the marginal PDFs $p_{\tau'}(\cdot)$ and $p_{\alpha^R}(\cdot)$. These marginal PDFs can be obtained either from measured channels (see, e.g., [15–17]) or from specified channel models (see, e.g., COST 207 final report [18]).

The obtained PDF in (B.4) (or equivalently (B.6)) provides the statistical description of the scattering area from which obtaining $p_{\tau'\alpha^R}(\tau',\alpha^R)$ is assured. A remarkable feature of the proposed approach is that the obtained scattering area is not confined by geometric constraints (see (B.6) or (B.4)). However, most of the geometric channel models proposed in the literature are restricted by tight mathe-

matical boundaries, which might spoil the performance of the overall system.

B. Specific Solutions

One of the widely addressed TOA PDFs is the negative exponential distribution function, which has been confirmed by many measurement campaigns [15–17]. Furthermore, the COST 207 working group developed specifications for the delay distribution in different propagation areas, showing that the delay distribution can be formulated by one or two decaying exponential functions. For instance, the TOA PDF $p_{\tau'}(\tau')$ of the channel model associated with a *typical urban area* is specified by the following single negative exponential function [18]

$$p_{\tau'}(\tau') = \begin{cases} \frac{1}{1-e^{-7}} e^{\tau'/\mu s}, & \text{if } 0 \le \tau' < 7\,\mu s, \\ 0, & \text{otherwise,} \end{cases} \tag{B.7}$$

For the *bad (complicated) urban area,* $p_{\tau'}(\tau')$ is presented by the following two decaying exponential functions

$$p_{\tau'}(\tau') = \begin{cases} \frac{2}{3(1-e^{-5})} e^{\tau'/\mu s}, & \text{if } 0 \le \tau' < 5\,\mu s, \\ \frac{1}{3(1-e^{-5})} e^{-\tau'/\mu s+5}, & \text{if } 5\,\mu s \le \tau' < 10\,\mu s, \\ 0, & \text{otherwise.} \end{cases} \tag{B.8}$$

Motivated by the discussion above, we model the TOA PDF $p_{\tau'}(\tau')$ by the following sum

$$\begin{aligned} p_{\tau'}(\tau') \;&=\; \sum_{i=1}^{I} a_i e^{-\lambda_i(\tau'-\tau'_{2i-2})} \\ &\times\; \left[u(\tau'-\tau'_{2i-2}) - u(\tau'-\tau'_{2i-1})\right] \end{aligned} \tag{B.9}$$

which is called the MNE TOA PDF. In the equation above, I is the total number of exponential functions, the parameters a_i are normalizing constants to guarantee the unity area under the PDF $p_{\tau'}(\tau')$, and $u(\cdot)$ stands for the unit step function. In addition, λ_i is the decaying factor of the ith negative exponential function, which ranges from τ'_{2i-2} to τ'_{2i-1}. Accordingly, the window $u(\tau'-\tau'_{2i-2}) - u(\tau'-\tau'_{2i-1})$ is the domain of the ith exponential function.

The MNE TOA PDF in (B.9) is very useful, as it allows us to model a variety of power delay profiles by adjusting the domain and the other parameters of each negative exponential functions. All these parameters can be attained from measured (specified) TOA PDFs. For example, the representation of $p_{\tau'}(\tau')$ in (B.9) is equal to the specified TOA PDFs in (B.7) and (B.8) by choosing the model pa-

rameters listed in Table B.1. It is also worth mentioning that typical and simple propagation areas need a small number I of the exponential functions to be explained (see (B.7)), whereas atypical and complicated ones require a higher number I (see (B.8)).

To obtain a specific solution, we also assume that the AOA is uniformly distributed between $-\pi$ and π, i.e., $p_{\alpha^R}(\alpha^R) = 1/(2\pi)$ if $\alpha^R \in (-\pi, \pi]$. It is also assumed that the AOA α^R is independent of the TOA τ', allowing us to write $p_{\tau'\alpha^R}(\tau', \alpha^R) = p_{\tau'}(\tau')p_{\alpha^R}(\alpha^R)$. Using this property and substituting (B.9) and $p_{\alpha^R}(\alpha^R) = 1/(2\pi)$ in (B.4) and (B.6), the polar and Cartesian representations of the scatterer distribution are given by (B.10) and (B.11), respectively [see the bottom of this page].

IV. SIMULATION RESULTS

We assume that the MS is located at the origin of the Cartesian coordinates, while the BS is placed on the negative part of the x-axis at a distance of $D = 1\,\mathrm{km}$ from the MS (see Fig. B.1). To specify the TOA PDF presented in (B.9), we use the two sets of the model parameters listed in Table B.1, which permits us to analyze

---

$$
\begin{aligned}
p_{r\alpha^R}(r,\alpha^R) &= \frac{c_0^{-1}}{2\pi}\left|1+\frac{r+D\cos(\alpha^R)}{\sqrt{r^2+D^2+2rD\cos(\alpha^R)}}\right| \\
&\times \sum_{i=1}^{I} a_i e^{-\lambda_i(c_0^{-1}(r+\sqrt{r^2+D^2+2rD\cos(\alpha^R)})-\tau'_{2i-2})} \\
&\times \left[u\left(c_0^{-1}(r+\sqrt{r^2+D^2+2rD\cos(\alpha^R)})-\tau'_{2i-2}\right)\right. \\
&- \left. u\left(c_0^{-1}(r+\sqrt{r^2+D^2+2rD\cos(\alpha^R)})-\tau'_{2i-1}\right)\right] \qquad \text{(B.10)}
\end{aligned}
$$

$$
\begin{aligned}
p_{xy}(x,y) &= \frac{c_0^{-1}}{2\pi}\left|\frac{1}{\sqrt{x^2+y^2}}+\frac{1+\frac{Dx}{x^2+y^2}}{\sqrt{(x+D)^2+y^2}}\right| \\
&\times \sum_{i=1}^{I} a_i e^{-\lambda_i(c_0^{-1}(\sqrt{x^2+y^2}+\sqrt{(x+D)^2+y^2})-\tau'_{2i-2})} \\
&\times \left[u\left(c_0^{-1}(\sqrt{x^2+y^2}+\sqrt{(x+D)^2+y^2})-\tau'_{2i-2}\right)\right. \\
&- \left. u\left(c_0^{-1}(\sqrt{x^2+y^2}+\sqrt{(x+D)^2+y^2})-\tau'_{2i-1}\right)\right] \qquad \text{(B.11)}
\end{aligned}
$$

the distribution of the scatterers in typical and bad urban areas. For the two sets, we first display the corresponding joint PDF $p_{xy}(x,y)$ and then evaluate its correctness by the scatter diagrams obtained from simulation results. The marginal PDF $p_r(r)$ of the radius r is also plotted and verified by simulation results.

Table B.1: Model parameters according to the channel specifications reported in COST 207 [18].

COST 207 channel models	**Model parameters**								
	I	c_1	c_2	λ_1	λ_2	τ'_0	τ'_1	τ'_2	τ'_3
Typical urban	1	1.0009	-	1	-	$0\,\mu$s	$7\,\mu$s	-	-
Bad urban	2	0.6712	0.3356	1	1	$0\,\mu$s	$5\,\mu$s	$5\,\mu$s	$10\,\mu$s

Fig. B.2 shows the joint PDF $p_{xy}(x,y)$ (see (B.11)) in the logarithmic scale for a typical urban area with the delay characteristics listed in Table B.1. A higher density of scatterers can be observed close to the MS (but not exactly at $(0,0)$), while this density decreases with increasing the distance from the MS. This is in agreement with the exponential distribution of the TOA in (B.7), in which the large values of the distribution function are associated with the delays of incoming waves from nearby scatterers, whereas the tail of the function is due to far scatterers. Referring to Fig. B.2, a very low density of scatterers is observed along the BS-MS connecting line. This could be attributed to the fact that the highest value of $p_{\tau'}(\tau')$ in (B.7) belongs to the shortest path.

To confirm the analytical result shown in Fig. B.2, we have simulated the scattering area by distributing 1000 scatterers by means of the TOA PDF in (B.7). The uniform distribution between $-\pi$ and π has been considered to distribute the scatterers in azimuth. The result is shown in Fig. B.3. The scatter diagram complies with the joint PDF $p_{xy}(x,y)$ shown in Fig. B.2, as the scatterers are distributed in the same manner in both figures. Moreover, Fig. B.3 shows that this propagation area might be approximated by a disk centred on a point on the BS-MS connecting line, within which the local scatterers are non-uniformly distributed. This geometry originates from the statistical properties of the channel, but not from imposed geometric restrictions. It is also noteworthy that the BS-MS connecting line is almost free of the scatterers, which meets the result presented in Fig. B.2.

Fig. B.4 illustrates the joint PDF $p_{xy}(x,y)$ in (B.11) for the bad urban channel specified by the model parameters in the last row of Table B.1, which result in the piecewise TOA PDF $p_{\tau'}(\tau')$ in (B.8). To highlight the impact of this piecewise function on the joint PDF $p_{xy}(x,y)$, we have used two different colours in Fig. B.4. The darker (lighter) colour shows the density of the scatters associated with the

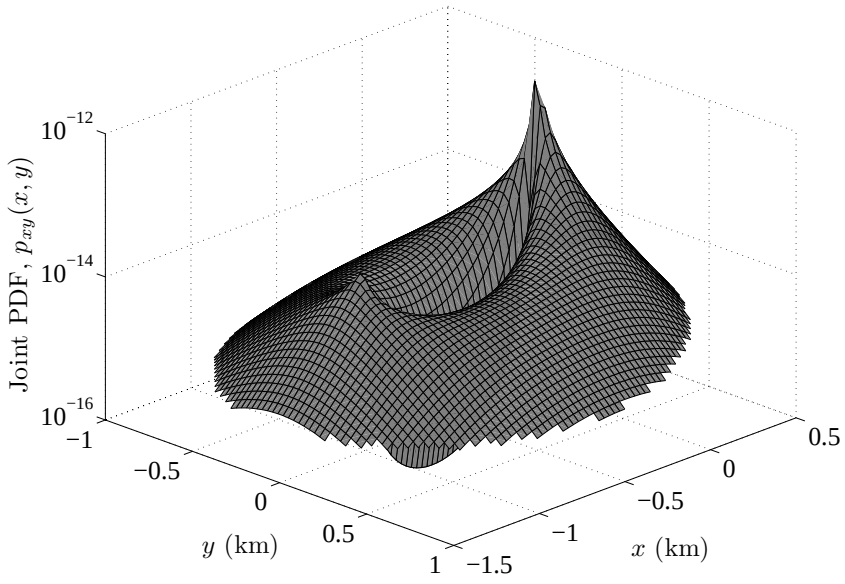

Figure B.2: The joint PDF $p_{xy}(x,y)$ (see (B.11)) for the typical urban channel with the TOA PDF in (B.7) and the uniformly distributed AOA ($D = 1$ km).

first (second) exponential function, i.e., the one ranged from 0 to 5 μs (5 to 10 μs). Referring to this figure, the darker graph is almost like the one shown in Fig. B.2, as both have been produced from almost the same delay distribution. Worth noticing is that in order to fulfill the second exponential function in (B.8), which is ranged from 5 to 10 μs, a larger scattering area is required. This can be observed by comparing the coverage area under the lighter and darker graphs.

Again, to validate the analytical result shown in Fig. B.4, we have simulated the scattering area in such a way that the TOA PDF in (B.8) is satisfied. Fig. B.5 shows the corresponding scatter diagram. A close agreement between the simulated scattering area and the joint PDF $p_{xy}(x,y)$ shown in Fig. B.4 can be observed. By increasing the distance from the MS, the density of scatterers varies in a complicated manner. Roughly, the density first decreases, then increases rapidly, and finally decreases gradually. The extent of these variations also changes with the azimuth AOA. An unexpected high density of scatterers near the BS can also be observed. Notice that the same behaviour can also be observed in Fig. B.4.

Fig. B.6 demonstrates the marginal PDF $p_r(r)$ of the radius r shown in Fig. B.1 for the two sets of parameters listed in Table B.1. This PDF can be obtained by

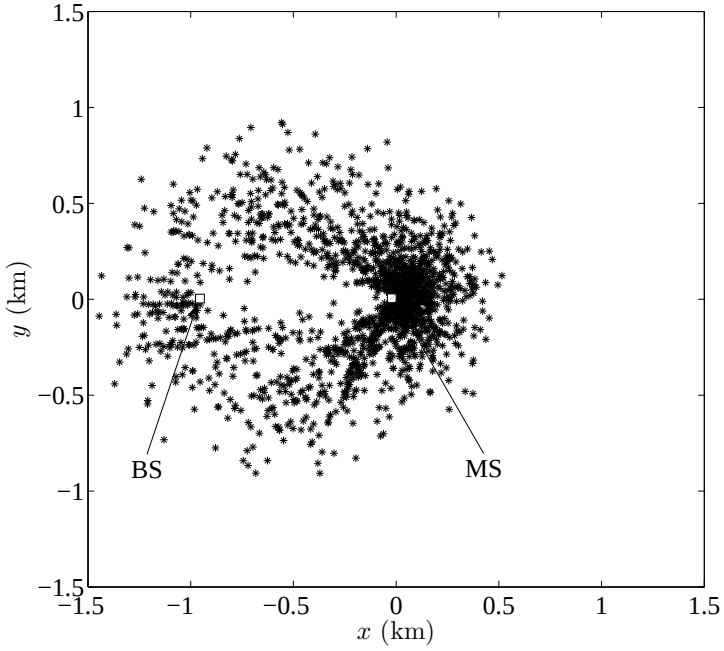

Figure B.3: The scatter diagram for the typical urban channel with the TOA PDF in (B.7) and uniformly distributed AOAs ($D = 1$ km).

integrating the joint PDF $p_{r\alpha^R}(r, \alpha^R)$ in (B.10) over the azimuth AOA α^R, i.e.,

$$p_r(r) = \int_{-\pi}^{\pi} p_{r,\alpha^R}(r, \alpha^R) d\alpha^R. \tag{B.12}$$

As can be seen from this figure, $p_r(r)$ decays gradually for both the typical and bad urban areas. However, for the bad urban channel model, a jump in $p_r(r)$ can be observed. An excellent match between the analytical and the simulation results can be seen. The characteristics of the plots are entirely in line with the simulated scattering areas shown in Figs. B.3 and B.5.

V. CONCLUSION

In this paper, we have investigated the distribution of scatterers for given delay-angle joint PDFs. Exact analytical expressions have been provided for the polar and Cartesian representation of the scatterer distribution. The proposed approach does not impose any specific geometric constraint on the propagation area. An important special case in which the TOA follows the MNE PDF and the AOA is uniformly distributed has also been analyzed. The corresponding scattering areas have been simulated, demonstrating that a typical urban area might be modelled by

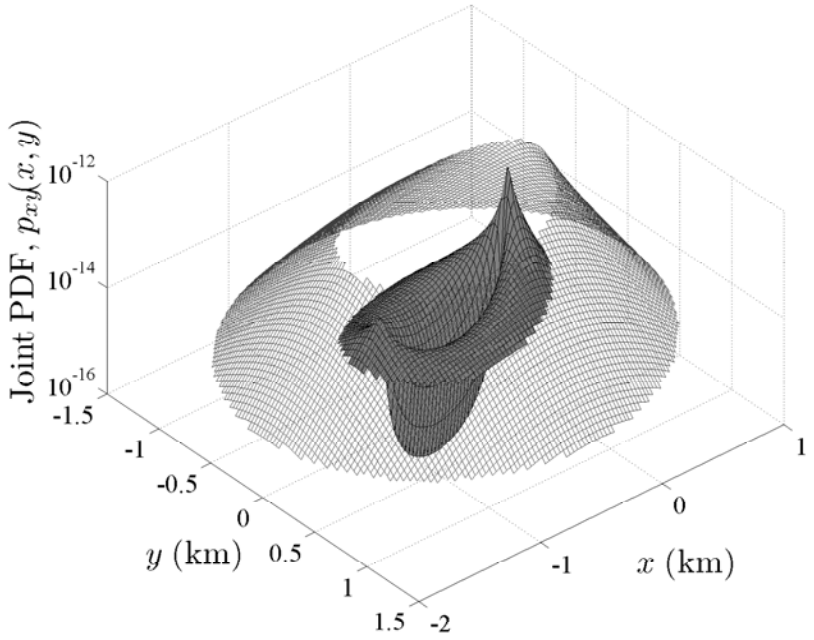

Figure B.4: The joint PDF $p_{xy}(x,y)$ (see (B.11)) for the bad urban channel with the TOA PDF in (B.8) and the uniformly distributed AOA ($D = 1$ km).

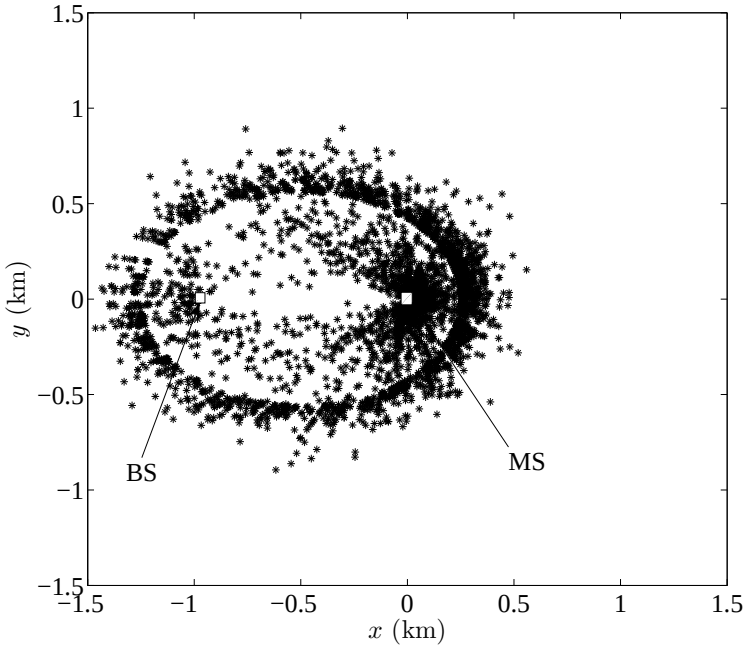

Figure B.5: The scatter diagram for the bad urban channel with the TOA PDF in (B.8) and uniformly distributed AOAs ($D = 1$ km).

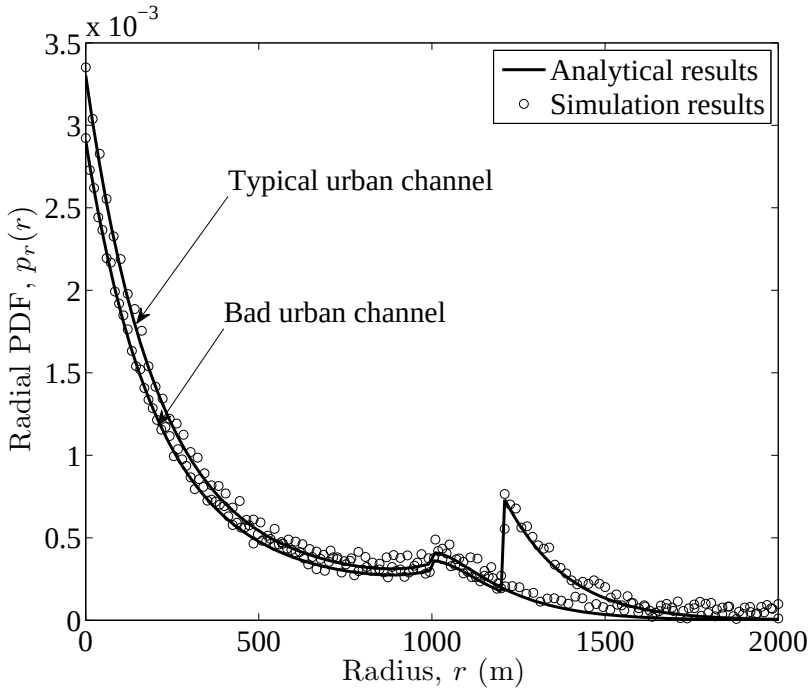

Figure B.6: The marginal PDF $p_r(r)$ (see (B.12)) for the typical and bad urban channels shown in Figs. B.2 and B.4.

a disk centred on the line between the BS and the MS. The scattering area of the bad urban channel model cannot be modelled by standard geometric shapes, as its power delay profile is mathematically complex. In such cases, the proposed approach gives a statistical representation for the scattering area. Analyzing further characteristics of the channel, such as the angle-of-departure PDF, can be investigated in future works.

REFERENCES

[1] A. Borhani and M. Pätzold, "Modelling of non-stationary mobile radio channels incorporating the Brownian mobility model with drift," in *Lecture Notes in Engineering and Computer Science: World Congress on Engineering and Computer Science, WCECS'13*, vol. 2. San Francisco, USA, Oct. 2013, pp. 695–700.

[2] A. Chelli and M. Pätzold, "A non-stationary MIMO vehicle-to-vehicle channel model based on the geometrical T-junction model," in *Proc. International*

Conference on Wireless Communications and Signal Processing, WCSP 2009. Nanjing, China, Nov. 2009.

[3] J. Karedal, F. Tufvesson, N. Czink, A. Paier, C. Dumard, T. Zemen, C. F. Mecklenbräuker, and A. F. Molisch, "A geometry-based stochastic MIMO model for vehicle-to-vehicle communications," *IEEE Trans. Wireless Commun.*, vol. 8, no. 7, pp. 3646–3657, Jul. 2009.

[4] A. F. Molisch, A. Kuchar, J. Laurila, K. Hugl, and R. Schmalenberger, "Geometry-based directional model for mobile radio channels—principles and implementation," *European Transactions on Telecommunications*, vol. 14, no. 4, pp. 351–359, Jul./Aug. 2003.

[5] K. T. Wong, Y. I. Wu, and M. Abdulla, "Landmobile radiowave multipaths' DOA-distribution: Assessing geometric models by the open literature's empirical datasets," *IEEE Trans. Antennas Propag.*, vol. 58, no. 3, pp. 946–958, Mar. 2010.

[6] A. Borhani and M. Pätzold, "A unified disk scattering model and its angle-of-departure and time-of-arrival statistics," *IEEE Trans. Veh. Technol.*, vol. 62, no. 2, pp. 473–485, Feb. 2013.

[7] I. Jaafar, H. Boujemaa, and M. Siala, "Angle and time of arrival statistics for hollow-disc and elliptical scattering models," in *Proc. 2nd Int. Conf. Signals, Circuits Syst., Nov. 2008*, pp. 1–4.

[8] R. J. Piechocki, G. V. Tsoulos, and J. P. McGeehan, "Simple general formula for PDF of angle of arrival in large cell operational environments," *Electron. Lett.*, vol. 34, no. 18, pp. 1784–1785, Sep. 1998.

[9] R. B. Ertel and J. H. Reed, "Angle and time of arrival statistics for circular and elliptical scattering models," *IEEE J. Select. Areas Commun.*, vol. 17, no. 11, pp. 1829–1840, Nov. 1999.

[10] R. Janaswamy, "Angle and time of arrival statistics for Gaussian scatter density model," *IEEE Trans. Wireless Commun.*, vol. 1, no. 3, pp. 488–497, Jul. 2002.

[11] A. Andrade and D. Covarrubias, "Radio channel spatial propagation model for mobile 3G in smart antenna system," *IEICE Trans. Commun.*, vol. E86-B, no. 1, pp. 213–220, Jan. 2003.

[12] D. D. N. Bevan, V. T. Ermolayev, A. G. Flaksman, and I. M. Averin, "Gaussian channel model for mobile multipath environment," *EURASIP J. Appl. Signal Proc.*, vol. 2004, no. 9, pp. 1321–1329.

[13] S.-H. Kong, "TOA and AOD statistics for down link Gaussian scatterer distribution model," *IEEE Trans. Wireless Commun.*, vol. 8, no. 5, pp. 2609–2617, May 2009.

[14] A. H. Kazmi and N. M. Khan, "Effect of scattering around BS on the spatial statistics of mobile channel in macrocell environment," in *International Conference on Information and Emerging Technologies (ICIET), Karachi*, vol. 1, Jun. 2010, pp. 1–5.

[15] K. I. Pedersen, P. E. Mogensen, and B. H. Fleury, "A stochastic model of the temporal and azimuthal dispersion seen at the base station in outdoor propagation environments," *IEEE Trans. Veh. Technol.*, vol. 49, no. 2, pp. 437–447, Mar. 2000.

[16] M. D. Batariere, T. K. Blankenship, and J. F. Kepler, "Wide-band MIMO impulse response measurements at 3.7 GHz," in *Proc. IEEE 45th Veh. Technol. Conf., VTC'02*, vol. 1, pp. 26–30.

[17] C. Kloch, G. Liang, J. B. Andersen, G. F. Pedersen, and H. L. Bertoni, "Comparison of measured and predicted time dispersion and direction of arrival for multipath in a small cell environment," *IEEE Trans. Antennas Propag.*, vol. 49, no. 9, pp. 1245–1263, Sep. 2001.

[18] M. Failli, Ed., *COST 207: Digital Land Mobile Radio Communications*. Luxembourg: Commission of the European Communities, 1989.

[19] A. Papoulis, *Probability, Random Variables, and Stochastic Processes*, 3rd ed. New York: McGraw-Hill, 1991.

Appendix C

Paper III

Title:	Correlation and Spectral Properties of Vehicle-to-Vehicle Channels in the Presence of Moving Scatterers
Authors:	**Alireza Borhani** and Matthias Pätzold
Affiliation(s):	University of Agder, Faculty of Engineering and Science, P. O. Box 509, NO-4898 Grimstad, Norway
Journal:	*IEEE Transactions on Vehicular Technology*, pp. 4228-4239, Nov. 2013.

Correlation and Spectral Properties of Vehicle-to-Vehicle Channels in the Presence of Moving Scatterers

Alireza Borhani and Matthias Pätzold

***Abstract* — This study derives a vehicle-to-vehicle (V2V) channel model assuming a typical propagation scenario in which the local scatterers move with random velocities in random directions. The complex channel gain of the proposed V2V channel model is provided. Subsequently, for different scatterer velocity distributions, the corresponding autocorrelation function (ACF), power spectral density (PSD), and the Doppler spread of the channel are derived, illustrated, and confirmed by the available measurement data. It is shown that the Gaussian mixture (GM) and the exponential distribution can accurately describe the velocity distribution of relatively fast and slow moving scatterers, respectively. Since the proposed V2V channel model flexibly covers several communication scenarios as special cases, including fixed-to-vehicle (F2V) and fixed-to-fixed (F2F) scenarios in the presence of both fixed and moving scatterers, it is obvious that the presented results are important for the performance analysis of cutting-edge vehicular communication systems.**

***Index terms* — Channel modeling, vehicle-to-vehicle channels, moving scatterers, autocorrelation function, power spectral density, Doppler spread**

Manuscript received September 28, 2012; revised March 12, 2013, July 26, 2013, and August 29, 2013; accepted August 31, 2013. Date of publication September 4, 2013; date of current version November 6, 2013. The review of this paper was coordinated by Prof. D. Stancil.

A. Borhani and M. Pätzold are with the Faculty of Engineering and Science, University of Agder, 4898 Grimstad, Norway (e-mails: {alireza.borhani, matthias.paetzold}@uia.no).

Color versions of one or more of the figures in this paper are available online at http://ieeexplore.ieee.org

Digital Object Identifier 10.1109/TVT.2013.2280674

I. INTRODUCTION

The drastic increase in road traffic density leads to congestion on streets and accidents, which cause immense costs in time, health, and money. V2V communication systems have emerged as a state-of-the-art technology to effectively alleviate the number of deaths, injuries, and delays caused by road accidents. In this regard, IEEE 802.11p is a promising standard for enabling wireless communication between vehicles moving under different driving conditions. For the development of future V2V communication systems and standards, a deep knowledge of the underlying fading channel characteristics is indispensable.

Different V2V channel models have been proposed in the literature. Geometry-based V2V channel models have been proposed, e.g., in [1–5]. The two-ring channel model, proposed in [4] and [5], is a typical example of a geometry-based model which allows a statistical characterization of V2V channels in urban areas. An empirical study, which reports on measured Doppler delay profiles of frequency-selective V2V channels can be found in [6]. Narrow-band channel measurements of a V2V channel and its characterization under realistic driving conditions have been reported in [7] and [8]. Other campaigns have also been conducted to measure MIMO V2V and vehicle-to-infrastructure channels [9–15]. As special cases of V2V channels, the statistical properties of F2V and F2F channels have been studied analytically, e.g., in [16–22] and empirically, e.g., in [23–28].

The majority of channel models that can be found in the literature relies on the assumption of stationary scatterers. However, moving scatterers are unavoidable in V2V communications. Moving foliage, walking pedestrians, and passing vehicles are only a few examples of scatterers in motion, which can be observed in most of the real-world radio propagation environments. Only a relatively small number of analytical studies, e.g., [29–31], have so far studied the effect of moving scatterers with random velocities and random directions on the statistical properties of the channel. Recall that in wireless communications, the frequency spread of the received signal is a result of the Doppler effect. This effect originates mainly from the moving transmitter and/or the moving receiver. However, even if the transmitter and receiver are fixed (F2F communications), the received signal can still experience the Doppler effect if the scatterers are non-stationary [29]. This means that moving scatterers can be a significant source for the Doppler spread, especially at millimeter wavelengths [30]. This phenomenon was studied empirically in [12], [25] and [26], as well as analytically in [29] and [30]. The Doppler spectrum of indoor channels in the presence of moving scatterers was also studied in [32] and [33]. In [29], the ACF and the PSD of an F2F communication link surrounded by moving scatterers

with deterministic velocities and deterministic directions were derived. There, it was shown that the velocity of moving scatterers can be modeled appropriately by a negative exponential distribution function. The authors of [29] focused solely on an F2F channel in which the moving scatterers are located on a ring centered on a fixed receiver. The effect of moving scatterers on F2V and F2F channels was also studied in [30] and [31], respectively. In addition, the impact of moving scatterers with deterministic velocities and deterministic directions on V2V links assuming the straight street model has been discussed in [34]. Accordingly, to the best of the authors' knowledge, the statistical properties of V2V channels in the presence of moving scatterers with random velocities and random directions have neither been investigated analytically nor empirically so far. Although, the authors of this paper have recently studied the effect of moving scatterers solely on the ACF of V2V fading channels in [35], further statistical characteristics of the same channel under the assumption of a realistic scatterer velocity distribution will be investigated for the first time in this paper.

This paper strives to alleviate the current lack of analytical studies on V2V channels by investigating the statistical properties of a narrowband V2V channel in which the local scatterers are moving with random velocities in random directions. The proposed V2V channel model does not impose any constraints on the position of the moving scatterers. Starting from the complex channel gain, we derive the temporal ACF and the corresponding PSD in integral form, which will then be simplified and examined under the assumption of different scatterer velocity distributions. In the transportation research area, the most popular distributions for the velocity of moving vehicles (fast moving scatterers) are the Gaussian and the GM models [36–41]. For the GM, exponential, and the uniform distributions of moving scatterers' velocity, the derived ACF is illustrated and compared with the classical ACF, which follows under the assumption of fixed scatterers. Moreover, the PSD of the channel is plotted and compared with the measurement data reported in [25]. These analyses are carried out for relatively slow and fast moving scatterers. Furthermore, the Doppler spread of the channel is provided in closed form. It is shown that the Doppler spread of the channel model can be perfectly matched to the Doppler spread of the measured channel reported in [7].

The novelty of this paper arises from the following features. First, owing to the generality of our proposed geometrical model, one is able to derive the ACF, PSD, and the Doppler spread of the one-ring, two-ring, and elliptical model from the presented results in this paper. Second, the proposed V2V channel model is a general model that includes the F2V and F2F channel models as special cases.

Furthermore, the classical channel models, where the local scatterers are either fixed or in motion with deterministic velocities, can also be obtained as special cases of the proposed stochastic model. This study bridges to traffic modeling in the area of transportation engineering by employing the GM model in our analysis as a realistic distribution model describing the velocity of moving vehicles. Utilizing the GM model for the first time in this paper, as well as analyzing further statistical properties of the channel as compared to [35] determine the main differences of this work with [35]. Herein, we also provide closed-form solutions for the analytical results, which have been presented in integral form in [35]. The verification of the analytical results with measured real-world channels is another original contribution of this work.

The remainder of this paper is organized as follows. Section II presents the propagation scenario by means of a geometrical scattering model. In Section III, we introduce several appropriate candidates for the velocity distribution of moving scatterers. The complex channel gain is presented in Section IV. Sections V and VI investigate the ACF of the V2V and F2F fading channels, respectively. The PSD of the V2V and F2F channels are presented in Sections VII and VIII, respectively. The corresponding Doppler spread is discussed in Section IX. Numerical results and verification of the analytical results by means of empirical data are provided in Section X. Finally, Section XI summarizes our main findings and draws the conclusions.

II. GEOMETRICAL SCATTERING MODEL

The geometrical scattering model, presented in Fig. C.1, is an appropriate model to describe typical propagation scenarios in urban areas, where both the transmitter and receiver vehicles are surrounded by N local scatterers denoted by S_n $(n = 1,2,...,N)$. It is assumed that the transmitter and receiver move with constant velocities v_T and v_R in the directions determined by the fixed angles α_v^T and α_v^R, respectively. Each of the local scatterers S_n $(n = 1,2,...,N)$ is in motion with a random velocity v_{S_n} in a random direction determined by $\alpha_v^{S_n}$. Owing to high path loss, we neglect the energy contribution of remote scatterers and assume that a wave emitted from the transmitter vehicle at an angle-of-departure (AOD) α_n^T reaches the receiver vehicle at an angle-of-arrival (AOA) α_n^R after a single bounce by the nth moving scatterer S_n inside the propagation area. Notice that the upperscripts R and T in the notation used for the AOA and AOD, i.e., α^R and α^T, refer to the receiver and the transmitter, respectively. Finally, we assume that both the transmitter and receiver are equipped with single omnidirectional antennas.

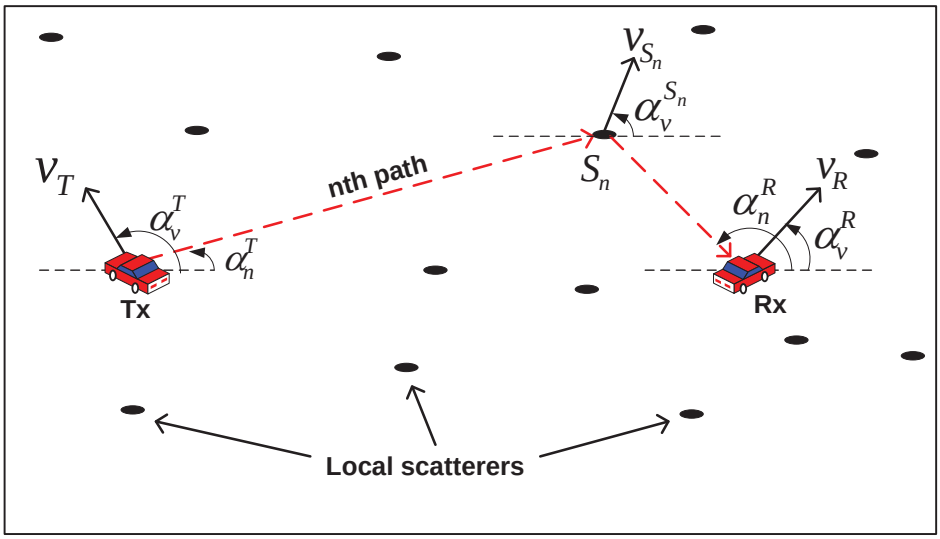

Figure C.1: Typical propagation scenario with moving transmitter (Tx) and moving receiver (Rx) illustrating the effect of single-bounce scattering in the presence of moving scatterers.

III. SCATTERER VELOCITY DISTRIBUTION CANDIDATES

In what follows, we review briefly the most important distributions that can realistically describe the velocity of moving vehicles in transportation engineering. These candidates then will be used either to derive a closed form solution or to carry out a numerical integration for the statistical characteristics of interest.

Confirmed by measurements, the classical Gaussian and the GM models are the most popular distributions for describing the velocity of vehicles moving along roads and highways [36–41]. The GM model attempts to cluster vehicles into specific groups so that the vehicles in the same group have more similarity in motion features than in other groups [41]. This random model can effectively describe the velocity of the vehicles, where the characteristics of the speed data are not homogeneous [38]. The GM distribution can be formed as follows [37]

$$p_{v_S}(v_S) = \sum_{i=1}^{I} w_i N_i(v_S; m_{iv_S}, \sigma_{iv_S}^2) \tag{C.1}$$

where $w_i \geq 0$ is the mixing proportion, which is subject to $\sum_i w_i = 1$. The number of individual Gaussian densities $N_i(\cdot;\cdot,\cdot)$ is denoted by I, where each of them has a mean m_{iv_S} and a variance $\sigma_{iv_S}^2$. As a special case, the classical Gaussian distribution can be obtained from (C.1) by setting $I = 1$. It is worth mentioning that owing to the apparent bimodality of speed distributions, the classical Gaussian model can-

not properly describe the distribution of the moving vehicles under heavy traffic congestion conditions [38]. For such cases, it was recommended in [37] to use a mixture of two different Gaussian distributions. The first mixture component representing the moderate-speed regime can be modelled as $N_1(v_S; m_{1v_S}, \sigma^2_{1v_S})$, and the second mixture component indicating the high-speed regime can be expressed by $N_2(v_S; m_{2v_S}, \sigma^2_{2v_S})$. Thus,

$$p_{v_S}(v_S) \;=\; (1-w_1)N_1(v_S; m_{1v_S}, \sigma^2_{1v_S}) + w_1 N_2(v_S; m_{2v_S}, \sigma^2_{2v_S}) \qquad \text{(C.2)}$$

exhibits the bimodal Gaussian distribution as a model for the probability that the non-stationary scatterers move with speed v_S. Notice that, setting the mixing proportion w_1 to either 0 or 1 in (C.2) results in the classical Gaussian distribution.

We have used the bimodal GM distribution to describe the velocity of relatively fast moving scatterers, while the negative exponential distribution has been chosen to model the velocity of relatively slow moving scatterers[1]. In fact, as the scatterer velocity v_S is always larger than or equal to zero, the negative tail of the Gaussian distribution excludes the use of this distribution for describing the velocity of slow moving scatterers. However, the contribution of the negative tail can be neglected if the average velocity is sufficiently large. The importance of the decaying exponential distribution to model the velocity of slow moving scatterers was comprehensively studied in [29] and [30]. For comparison reasons, the uniform distribution has also been examined in this paper.

IV. CHANNEL CHARACTERIZATION

The propagation scenario described in Section II is an extended version of the typical fixed-to-mobile scenario in the presence of fixed scatterers studied in [42, pp. 56–60]. It was shown there that the complex channel gain $\mu(t)$ of frequency-nonselective F2V channels can be modeled by a complex stochastic process representing the sum of all scattered components in the following form

$$\mu(t) = \sum_{n=1}^{N} c_n e^{j(2\pi f_n t + \theta_n)} \qquad \text{(C.3)}$$

where c_n designates the attenuation factor caused by the interaction of the emitted wave with the nth scatterer S_n, and f_n represents the Doppler frequency[2] caused by

[1] For V2V scenarios, we use the term relatively *fast* (*slow*) moving scatterers if the mean velocity m_{v_S} of the scatterers is about or greater (smaller) than the speed of the fastest (slowest) vehicle, i.e., $m_{v_S} \geq \max\{v_T, v_R\}$ ($m_{v_S} < \min\{v_T, v_R\}$).

[2] The frequency shift caused by the Doppler effect is given by $f = f_{\max}\cos(\alpha)$, where $f_{\max} = f_0 v/c_0$ denotes the maximum Doppler frequency, f_0 is the carrier frequency, c_0 denotes the speed of

the movement of the receiver. Moreover, the random variable θ_n denotes the phase shift of the nth path, which is usually assumed to be uniformly distributed between 0 and 2π [42].

The complex channel gain $\mu(t)$ in (C.3) can be used to model the propagation scenario described in Section II after taking the effects of both the moving transmitter and the moving scatterers into account. Indeed, the main differences between the proposed V2V channel in the presence of moving scatterers and the model presented in (C.3) are the additional Doppler shifts originating from the mobile transmitter and the moving scatterers. To capture the overall Doppler effect attributed to the moving vehicles and the moving scatterers, we have to replace f_n in (C.3) by

$$f_n = f_n^T + f_n^{TS} + f_n^{SR} + f_n^R. \tag{C.4}$$

In the equation above, the first frequency shift f_n^T is caused by the movement of the transmitter. The second shift f_n^{TS} is due to the fact that the transmitted signal impinges on the nth moving scatterer. The third frequency shift f_n^{SR} is the contribution which arises when the moving scatterer redirects the signal to the receiver. Finally, the last Doppler shift f_n^R is due to the movement of the receiver. In [35], it has been shown that the overall Doppler frequency f_n in (C.4) can be written in the following compact form

$$\begin{aligned} f_n \;=\; & \frac{k_0}{2\pi}\Bigg[v_T \cos\left(\alpha_v^T - \alpha_n^T\right) - v_{S_n}\Big(\cos\Big(\alpha_n^T - \alpha_v^{S_n}\Big) \\ & +\; \cos\Big(\alpha_v^{S_n} - \alpha_n^R\Big)\Big) + v_R \cos\left(\alpha_v^R - \alpha_n^R\right)\Bigg] \end{aligned} \tag{C.5}$$

where $k_0 = 2\pi f_0/c_0$ denotes the free-space wave number. Accordingly, in the presence of moving scatterers, the complex channel gain of the considered V2V channel can be modeled by (C.3) in which we replace f_n by (C.5).

It is worth mentioning that if the number of paths N tends to infinity, then one may invoke the central limit theorem, which states that the complex channel gain $\mu(t)$ in (C.3) equals a complex-valued Gaussian process with zero mean and variance $2\sigma_0^2 = \lim_{N\to\infty}\sum_{n=1}^{N} E\{c_n^2\}$ [42].

---

light, and α is the difference between the AOA and the angle of movement [43].

V. AUTOCORRELATION FUNCTION OF THE VEHICLE-TO-VEHICLE CHANNEL MODEL

The ACF $r_{\mu\mu}(\tau)$ of the complex channel gain $\mu(t)$ can be determined by using the definition $r_{\mu\mu}(\tau) := E\{\mu^*(t)\mu(t+\tau)\}$ in which $E\{\cdot\}$ denotes the expectation operator.

Under the assumption of isotropic scattering, which implies that the AOA α_n^R is uniformly distributed between 0 and 2π, and that all path gains c_n have the same size, namely $c_n = \sigma_0\sqrt{2/N}$ [42], it can be shown (see [35]) that the ACF of the underlying V2V channel model is given by (C.6) [see the top of the next page], in which $p_{\alpha_v^S}(\alpha_v^S)$ and $p_{v_S}(v_S)$ denote the distribution of the direction and the velocity distribution of the moving scatterers, respectively. Furthermore, $p_{\alpha^T\alpha^R}(\alpha^T,\alpha^R)$ describes the joint distribution of the AOD α^T and the AOA α^R.

The proposed ACF in (C.6) provides a suitable platform to study the statistical properties of different geometric channel models, such as the street, T-junction, U-turn, as well as one-ring, two-ring, and elliptical model, which are all widely used to describe typical V2V and F2F propagation areas. This is due to the fact that in the presented form of (C.6), the joint PDF $p_{\alpha^T\alpha^R}(\alpha^T,\alpha^R)$ can be optionally used to present one of the aforementioned geometric channel models. From this standpoint, the proposed formulation is widely useful and implementable in typical propagation areas. However, due to the often complex nature of $p_{\alpha^T\alpha^R}(\alpha^T,\alpha^R)$, simplifying (C.6) under the assumption of other typical geometric channel models is possible, although not mathematically tractable. In what follows, we first exemplify several possible ACFs, which can be obtained by simplifying (C.6) under specific assumptions, and then we study the proposed propagation scenario of this paper.

From (C.6), the ACF of the classical F2V scenario with fixed scatterers is obtained by setting both v_T and v_S to zero. In this case, the ACF results in $r_{\mu\mu}(\tau) = 2\sigma_0^2 J_0(k_0 v_R \tau)$, where $J_0(\cdot)$ denotes the zeroth-order Bessel function of the first kind. This model is known in the literature as the Jakes model [43].

Another special case can be obtained by substituting $p_{\alpha^T\alpha^R}(\alpha^T,\alpha^R)$ associated with the elliptical model in (C.6). This joint distribution can be derived from the exact relationship between the AOD α^T and the AOA α^R of the elliptical model presented in [44]. In this way, one can attain the ACF of the elliptical model in the presence of moving scatterers.

Let us return to the proposed V2V communication scenario and assume that the AOD α^T is uniformly distributed between 0 and 2π. The same assumption holds for $\alpha_v^{S_n}$. It is also assumed that α^T is independent of the AOA α^R. Now, if

$$r_{\mu\mu}(\tau) = 2\sigma_0^2 \int_0^{\infty}\int_0^{2\pi}\int_0^{2\pi}\int_0^{2\pi} \exp\left\{ j\left[k_0 v_T \cos\left(\alpha_v^T - \alpha^T\right) - 2k_0 v_S \cos\left(\frac{\alpha^T - \alpha^R}{2}\right) \right.\right.$$
$$\times \quad \left.\left. \cos\left(\frac{\alpha^T + \alpha^R}{2} - \alpha_v^S\right) + k_0 v_R \cos\left(\alpha_v^R - \alpha^R\right)\right] \tau \right\}$$
$$\times \quad p_{\alpha_v^S}\left(\alpha_v^S\right) p_{\alpha^T \alpha^R}\left(\alpha^T, \alpha^R\right) p_{v_S}(v_S) d\alpha_v^S d\alpha^R d\alpha^T dv_S \qquad \text{(C.6)}$$

$$r_{\mu\mu}(\tau) = \frac{\sigma_0^2}{2\pi^2} \int_0^{\infty}\int_0^{2\pi}\int_0^{2\pi} \exp\left\{ jk_0 v_T \cos\left(\alpha_v^T - \alpha^T\right) \tau \right\} J_0\left(2k_0 v_S \cos\left(\frac{\alpha^T - \alpha^R}{2}\right) \tau \right)$$
$$\times \quad \exp\left\{ jk_0 v_R \cos\left(\alpha_v^R - \alpha^R\right) \tau \right\} p_{v_S}(v_S) d\alpha^T d\alpha^R dv_S \qquad \text{(C.7)}$$

$v_S = 0$, the ACF in (C.6) results in $r_{\mu\mu}(\tau) = 2\sigma_0^2 J_0(k_0 v_T \tau) J_0(k_0 v_R \tau)$, which equals the ACF of the classical V2V channel model in the presence of fixed scatterers reported in [4, Eq. (46)] and [5, Eq. (19)]. If $v_S \neq 0$, one can integrate over the uniformly distributed random variable $\alpha_v^{S_n}$ in (C.6), which simplifies the ACF $r_{\mu\mu}(\tau)$ to (C.7) [see the top of the current page]. The result in (C.7) represents the ACF of the proposed V2V channel in the presence of moving scatterers. This presentation of the ACF has an appropriate form which needs to be examined for the different scatterer velocity distributions discussed in Section III. We depict the behavior of the ACF $r_{\mu\mu}(\tau)$ in (C.7) by means of numerical integrations in Section X-A.

VI. AUTOCORRELATION FUNCTION OF THE FIXED-TO-FIXED CHANNEL MODEL

To study the effect of moving scatterers on the ACF of the F2F channel, as a special case of the proposed V2V channel, let us consider non-moving transmitter and receiver vehicles, i.e., $v_T = v_R = 0$. Then, the ACF in (C.7) reduces to the equation

$$r_{\mu\mu}(\tau) = \frac{\sigma_0^2}{2\pi^2} \int_0^{\infty}\int_0^{2\pi}\int_0^{2\pi} J_0\left(2k_0 v_S \cos\left(\frac{\alpha^T - \alpha^R}{2}\right) \tau \right) p_{v_S}(v_S) d\alpha^T d\alpha^R dv_S \qquad \text{(C.8)}$$

which after some intricate mathematical manipulations [see Appendix A] is simplified to the following expression

$$r_{\mu\mu}(\tau) = 2\sigma_0^2 \int_0^\infty J_0^2(k_0 v_S \tau)\, p_{v_S}(v_S) dv_S. \tag{C.9}$$

In this paper, we address the ACF presented in (C.9) as the ACF of the proposed F2F channel with moving scatterers. This result allows us to study the effect of different scatterer velocity distributions $p_{v_S}(v_S)$ on the ACF $r_{\mu\mu}(\tau)$. In what follows, we present (without proof) several closed-form expressions for the ACF of the proposed F2F channel model under the assumption of different scatterer velocity distributions.

Let us first assume that the velocity v_S of the scatterers is a known constant v_{S0}, i.e., $v_S = v_{S0}$. Hence, the probability density function $p_{v_S}(x)$ of v_S is given by $p_{v_S}(v_S) = \delta(v_S - v_{S0})$. In this case, the ACF in (C.9) can be presented in the following closed-form expression

$$r_{\mu\mu}(\tau) = 2\sigma_0^2 J_0^2(k_0 v_{S0} \tau). \tag{C.10}$$

The expression above equals the ACF of V2V channels [4, Eq. (46)] in the presence of fixed scatterers if the transmitter and the receiver vehicles both move with speed v_{S0}.

If v_S follows the exponential distribution with mean m_{v_S}, then the ACF of the proposed F2F channel model is given by the expression

$$r_{\mu\mu}(\tau) = 2\sigma_0^2 \frac{{}_2F_1\left(\frac{1}{2}, \frac{1}{2}; 1; \frac{(2k_0 m_{v_S}\tau)^2}{1+(2k_0 m_{v_S}\tau)^2}\right)}{\sqrt{1+(2k_0 m_{v_S}\tau)^2}} \tag{C.11}$$

in which ${}_pF_q(a_1, ..., a_p; b_1, ..., b_q; x)$ stands for the generalized hypergeometric function [45, p. 1010].

If v_S is uniformly distributed between 0 and $2m_{v_S}$, then the ACF in (C.9) results in

$$r_{\mu\mu}(\tau) = 2\sigma_0^2\, {}_2F_3\left(\frac{1}{2}, \frac{1}{2}; 1, 1, \frac{3}{2}; -(2k_0 m_{v_S}\tau)^2\right). \tag{C.12}$$

If v_S follows the GM distribution presented in (C.1), then the ACF in (C.9) cannot be written in closed form. In this case, the following expression for the ACF

of the proposed F2F channel model in the presence of moving scatterers holds

$$r_{\mu\mu}(\tau) \;=\; 2\sigma_0^2 \sum_{i=1}^{I} w_i \int_0^{\infty} J_0^2\left(k_0 v_S \tau\right) N_i(v_S; m_{iv_S}, \sigma_{iv_S}^2) dv_S. \tag{C.13}$$

Notice that in the expression above, it is supposed that the mean velocity m_{iv_S} of each mixture component is sufficiently large, which allows us to neglect the negative tail of each Gaussian distribution.

Owing to flexibility of the proposed channel model, the ACF of the F2F one-ring model can also be derived from the general form of the ACF in (C.6). Accordingly, the ACF of the F2F one-ring model can be obtained by setting $v_T = v_R = 0$ and using the joint distribution $p_{\alpha^T\alpha^R}(\alpha^T, \alpha^R)$ of the AOD α^T and the AOA α^R of the one-ring model in (C.6). This joint distribution equals (see Appendix B)

$$p_{\alpha^T\alpha^R}(\alpha^T, \alpha^R) \;=\; \frac{1}{2\pi}\delta\left(\alpha^T - \arctan\left(\frac{\gamma^{-1}\sin(\alpha^R)}{1+\gamma^{-1}\cos(\alpha^R)}\right)\right) \tag{C.14}$$

in which $\gamma = D/R$ denotes the ratio of the distance D between the two fixed stations (transmitter, receiver) and the radius R of the one-ring model. Now, by assuming a uniform distribution between 0 and 2π for the direction of movement $\alpha_v^{S_n}$, substituting (C.14) in (C.6), and performing some mathematical manipulations, the ACF of the F2F one-ring model can finally be written as

$$\begin{aligned} r_{\mu\mu}(\tau) \;&=\; \frac{\sigma_0^2}{\pi}\int_0^{\infty}\int_0^{2\pi} J_0\left(2k_0 v_S \cos\left(\frac{\arctan\left(\frac{\gamma^{-1}\sin(\alpha^R)}{1+\gamma^{-1}\cos(\alpha^R)}\right) - \alpha^R}{2}\right)\tau\right) \\ &\times\; p_{v_S}(v_S) d\alpha^R dv_S. \end{aligned} \tag{C.15}$$

It is noteworthy that the ACF above differs from the ACF of the F2F one-ring model derived in [29, Eq. (17)]. This is due to the fact that the dependency of the AOD α^T and the AOA α^R has not been considered there. However, it can be proved that in the asymptotic case, when $\gamma \to \infty$, the ACF in (C.15) meets the one reported in [29, Eq. (17)]. Furthermore, it was shown there that the exponential distribution is the best statistical description of the velocity of relatively slow moving scatterers, but not for relatively fast moving ones, like passing vehicles. This result was obtained by comparing the Fourier transform of the ACF, namely PSD, with the measurement data reported in [25]. In Section X-E, we show that the GM distribution describes the velocity of relatively fast moving scatterers better than the exponential distribution.

VII. POWER SPECTRAL DENSITY OF THE VEHICLE-TO-VEHICLE CHANNEL MODEL

The PSD $S_{\mu\mu}(f)$ can be obtained by taking the Fourier transform of the temporal ACF $r_{\mu\mu}(\tau)$ of the complex channel gain with respect to the time difference τ. Accordingly, the Fourier transform of the ACF of the proposed V2V channel given by (C.7) results in the PSD of the considered V2V channel in the presence of moving scatterers. Generally, this PSD cannot be written in closed form. Furthermore, due to the fact that the scatterer velocity v_S is supposed to be a random variable, it follows from (C.5) that the maximum Doppler frequency $f_{\max} = \max\{f_n\} = f_0(v_T + 2v_S + v_R)/c_0$ is also a random variable. In Section X-B, we show the PSD of the V2V channel in the presence of moving scatterers by means of numerical integrations.

VIII. POWER SPECTRAL DENSITY OF THE FIXED-TO-FIXED CHANNEL MODEL

Although, finding a closed-form expression for the PSD of V2V channels is generally not possible, the PSD of several types of F2F channels can be written in closed form. In what follows, we have derived the PSD of the proposed F2F channels for different scatterer velocity distributions.

If the velocity is constant, i.e., $v_S = v_{S0}$, then the PSD $S_{\mu\mu}(f)$ of the proposed F2F channel is obtained by taking the Fourier transform of (C.10), which results in

$$S_{\mu\mu}(f) = \frac{4\sigma_0^2}{\pi k_0 v_{S0}} K\left(\sqrt{1-(\frac{\pi f}{k_0 v_{S0}})^2}\right) \tag{C.16}$$

where $K(\cdot)$ denotes the complete elliptic integral of the first kind [45, Eq. (8.110.3)]. It is worth mentioning that the expression above equals the PSD of the proposed V2V channel in the presence of fixed scatterers in [4], if the transmitter and the receiver vehicles both move with speed v_{S0}.

If v_S follows the exponential distribution, then the PSD is the Fourier transform of (C.11). It follows

$$S_{\mu\mu}(f) = \frac{2\sigma_0^2}{\pi k_0 m_{v_S}} K_0\left(\frac{\pi|f|}{2k_0 m_{v_S}}\right) \tag{C.17}$$

where $K_0(\cdot)$ represents the zeroth-order modified Bessel function of the second kind [45, Eq. (8.447.3)].

If v_S is uniformly distributed between 0 and $2m_{v_S}$, then the Fourier transform of (C.12) results in the PSD

$$S_{\mu\mu}(f) = \frac{\sigma_0^2}{2k_0 m_{v_S}} G_{3,3}^{3,0}\left(\frac{\pi^2 f^2}{(2k_0 m_{v_S})^2} \,\middle|\, \begin{matrix} \frac{1}{2}, \frac{1}{2}, 1 \\ 0, 0, 0 \end{matrix} \right) \tag{C.18}$$

where $G_{m,n}^{p,q}\left(\cdot \,\middle|\, \begin{matrix} a_1, ..., a_p \\ b_1, ..., b_p \end{matrix} \right)$ denotes the Meijer G-function [45, Eq. (9.301)].

If v_S follows the GM distribution presented in (C.1), then the PSD is obtained by taking the Fourier transform of (C.13), which can finally be simplified as

$$S_{\mu\mu}(f) \;=\; \frac{4\sigma_0^2}{\pi k_0} \sum_{i=1}^{I} w_i \int_0^{\infty} \frac{K\left(\sqrt{1 - (\frac{\pi f}{k_0 v_S})^2} \right)}{v_S} N_i(v_S; m_{iv_S}, \sigma_{iv_S}^2) dv_S. \tag{C.19}$$

We depict the PSD of the F2F channel under the assumption of the above-mentioned scatterer velocity distributions in Section X-D and show its validity in Section X-E.

IX. DOPPLER SPREAD OF THE VEHICLE-TO-VEHICLE CHANNEL MODEL

The Doppler spread $B_{\mu\mu}^{(2)}$ of the channel is defined as the square root of the second central moment of the PSD $S_{\mu\mu}(f)$. Referring to [42, p. 64], the Doppler spread $B_{\mu\mu}^{(2)}$ can be expressed in terms of the ACF $r_{\mu\mu}(\tau)$ of the complex channel gain $\mu(t)$ as follows

$$B_{\mu\mu}^{(2)} = \frac{1}{2\pi} \sqrt{ \left(\frac{\dot{r}_{\mu\mu}(0)}{r_{\mu\mu}(0)} \right)^2 - \frac{\ddot{r}_{\mu\mu}(0)}{r_{\mu\mu}(0)} } \tag{C.20}$$

where the overdot indicates the derivative with respect to the time difference τ. It can be proved that the first time derivative $\dot{r}_{\mu\mu}(\tau)$ of the ACF $r_{\mu\mu}(\tau)$ in (C.7) equals zero at the origin, i.e., $\dot{r}_{\mu\mu}(0) = 0$ [see Appendix C]. This property indicates that the PSD $S_{\mu\mu}(f)$ of the proposed channel is even and real, which is not surprising due to the isotropic scattering assumption. In Section X, we depict this property of the PSD not only for F2F channels, but also for V2V channels. Considering $\dot{r}_{\mu\mu}(0) = 0$ also simplifies $B_{\mu\mu}^{(2)}$ to

$$B_{\mu\mu}^{(2)} = \frac{\sqrt{\beta'}}{2\pi\sqrt{2}\sigma_0} \tag{C.21}$$

in which β' denotes the negative curvature of the ACF $r_{\mu\mu}(\tau)$ at the origin, i.e., $\beta' = -\ddot{r}_{\mu\mu}(0)$. Taking the second derivative of $r_{\mu\mu}(\tau)$ in (C.7) with respect to τ, then setting τ to 0, and performing some intricate mathematical manipulations, allows us to present the characteristic quantity β' in its final form

$$\beta' = k_0^2\sigma_0^2\left(v_T^2 + v_R^2 + 2\int_0^\infty v_S^2 p_{v_S}(v_S)dv_S\right) \tag{C.22}$$

which is valid for a given scatterer velocity distribution $p_{v_S}(v_S)$. In what follows, the characteristic quantity β' will be studied for different scatterer velocity distributions. If the velocity of the scatterers is a deterministic value $v_S = v_{S0}$, then

$$\beta' = k_0^2\sigma_0^2\left(v_T^2 + v_R^2 + 2v_{S0}^2\right). \tag{C.23}$$

If v_S follows the exponential distribution, then

$$\beta' = k_0^2\sigma_0^2\left(v_T^2 + v_R^2 + 4m_{v_S}^2\right). \tag{C.24}$$

If v_S is uniformly distributed between 0 and $2m_{v_S}$, then

$$\beta' = k_0^2\sigma_0^2\left(v_T^2 + v_R^2 + \frac{8}{3}m_{v_S}^2\right). \tag{C.25}$$

If v_S follows the GM distribution, then

$$\begin{aligned}\beta' \;=\; k_0^2\sigma_0^2\Bigg(& v_T^2 + v_R^2 + \sum_{i=1}^{I} w_i(\sigma_{iv_S}^2 + m_{iv_S}^2) \\ & \times\left(1 + \operatorname{erf}\left(\frac{m_{iv_S}}{\sqrt{2}\sigma_{iv_S}}\right)\right) + \frac{2m_{iv_S}\sigma_{iv_S}}{\sqrt{2\pi}} e^{-\frac{m_{iv_S}^2}{2\sigma_{iv_S}^2}}\Bigg)\end{aligned} \tag{C.26}$$

where $\operatorname{erf}(\cdot)$ stands for the error function [45, Eq. (8.250.1)].

Now, different expressions for the Doppler spread $B_{\mu\mu}^{(2)}$ of the channel can be obtained by substituting each of the characteristic quantities β' given by (C.23)–(C.26) in (C.21). These expressions can be written in the following general form

$$B_{\mu\mu}^{(2)} = \frac{1}{\sqrt{2}\lambda}\sqrt{v_T^2 + v_R^2 + v_{\text{eff}_S}^2} \tag{C.27}$$

in which $\lambda = 2\pi/k_0$ is the wavelength and v_{eff_S} stands for the effective velocity of the moving scatterers. Notice that referring to (C.23)–(C.26), v_{eff_S} *mainly* depends

on the the average velocity of the moving scatterers m_{v_S} and varies from one scatterer velocity distribution to another. In Section X-F, we show the Doppler spread of the channel for the aforementioned scatterer velocity distributions and verify its validity in Section X-G.

X. NUMERICAL RESULTS

According to the operating frequency range of the IEEE 802.11p standard, the carrier frequency $f_0 = 5.9\,\text{GHz}$ has been chosen in our numerical computations. This carrier frequency has been adopted in the dedicated short range communications (DSRC) standard being part of the intelligent transportation system (ITS) [7]. Furthermore, according to Section III, we have used the GM, negative exponential, and the uniform distribution to describe the velocity of moving scatterers. The bimodal GM parameters have been set to $m_{1v_S} = 80\,\text{km/h}$, $m_{2v_S} = 120\,\text{km/h}$, and $\sigma_{1v_S} = \sigma_{2v_S} = 20\,\text{km/h}$. Moreover, the mixing proportion w_1 varies between 0 and 1. As an example, setting $w_1 = 0$ means that the velocity of all the moving vehicles is normally distributed around the average velocity of $m_{1v_S} = 80\,\text{km/h}$ with a standard deviation of $\sigma_{1v_S} = 20\,\text{km/h}$. For a mixing proportion w_1 of 0.5, it is assumed that the velocity of half of the vehicles is normally distributed around $m_{1v_S} = 80\,\text{km/h}$, and the other half is normally distributed around $m_{2v_S} = 120\,\text{km/h}$. The directions of motion of the transmitter and the receiver are supposed to be the same and equal $\pi/3$, i.e., $\alpha_v^T = \alpha_v^R = \pi/3$. It is also assumed that the signal power $2\sigma_0^2$ has been set to 1.

A. ACF of the V2V Channel

Figs. C.2 and C.3 demonstrate the ACF $r_{\mu\mu}(\tau)$ of the proposed V2V link according to (C.7) in the presence of moving scatterers for different scatterer velocity distributions. For comparison, the classical ACF corresponding to fixed scatterers has been plotted in these figures as well. A considerable difference between the ACF of the proposed V2V channel in the presence of relatively fast moving scatterers and the ACF of the classical V2V channel with fixed scatterers can be seen in Fig. C.2. However, if the average velocity of the moving scatterers is relatively slow, this difference is not very significant as can be concluded from the results shown in Fig. C.3. Referring to Fig. C.3, the ACF $r_{\mu\mu}(\tau)$ of the V2V link in the presence of relatively slow moving scatterers follows closely that of fixed scatterers around the origin. This comparison allows us to conclude that relatively slow moving scatterers, like runners and bikers do not significantly contribute to the mean Doppler shift and the Doppler spread if both the transmitter and the receiver vehicles move relatively fast compared to the mean velocity of the scatterers. This conclusion holds

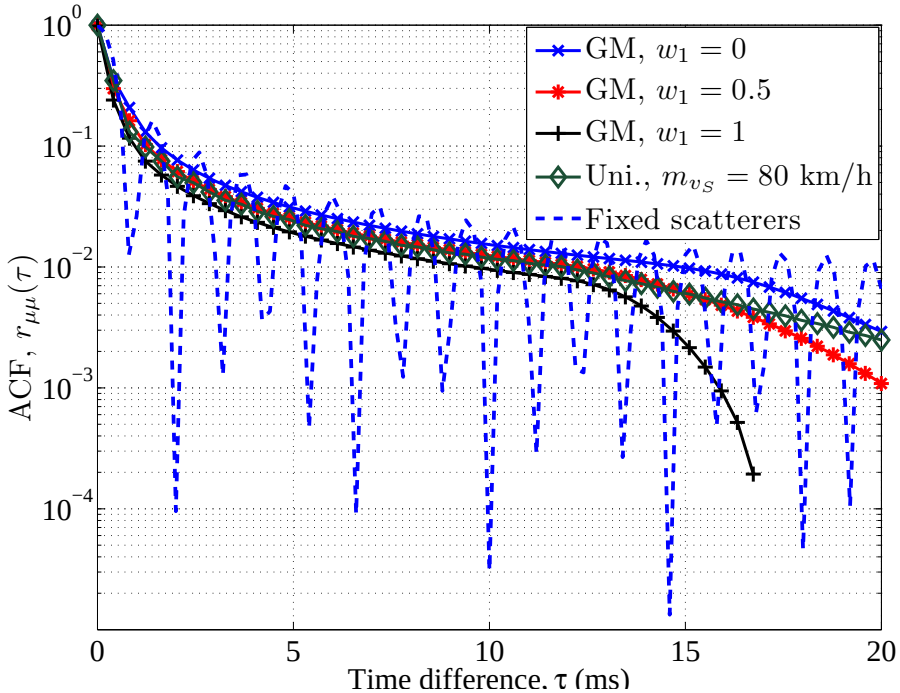

Figure C.2: The behavior of the ACF $r_{\mu\mu}(\tau)$ in (C.7) for V2V scenarios with relatively fast moving scatterers, where $v_T = v_R = 80$ km/h. The GM parameters have been set to $m_{1v_S} = 80$ km/h, $m_{2v_S} = 120$ km/h, and $\sigma_{1v_S} = \sigma_{2v_S} = 20$ km/h.

especially for very slow moving scatterers, such as foliage movements and walking pedestrians. Accordingly, their contribution to the Doppler effect can be neglected in typical V2V communication scenarios. As we will see later, this conclusion is no longer valid when we consider F2F communication scenarios. Moreover, as can be observed in both figures, different scatterer velocity distributions result in distinct curves for the ACF.

B. PSD of the V2V Channel

Figs. C.4 and C.5 depict the PSD of the channel for different scatterer velocity distributions. The results presented therein have been obtained by computing the Fourier transform of (C.7) numerically. As can be seen in Fig. C.4, by decreasing the mean velocity of the scatterers, the PSD increases around the origin and decreases in tails. This behavior approaches a delta function at the origin if the velocity of the scatterers, transmitter, and the receiver tends to zero. Furthermore, referring to Fig. C.5, it can be observed that the scatterer velocity distribution has no significant effect on the PSD of the V2V channel in the presence of relatively slow moving scatterers. This again points out that moving scatterers are not a dominant source of Doppler shifts in V2V communication channels if the transmitter and/or

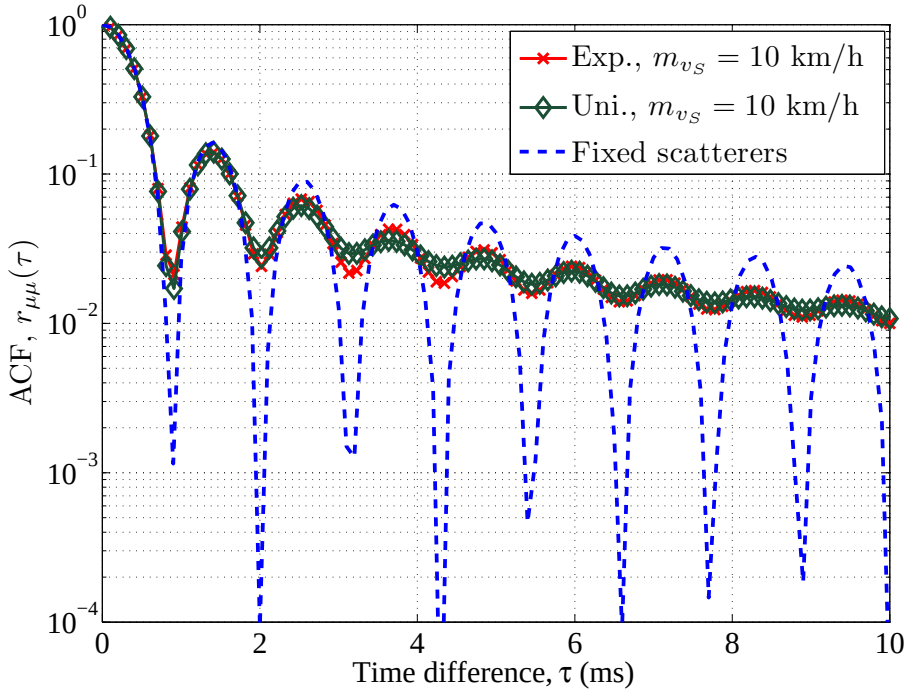

Figure C.3: The behavior of the ACF $r_{\mu\mu}(\tau)$ in (C.7) for V2V scenarios with relatively slow moving scatterers, where $v_T = v_R = 80$ km/h.

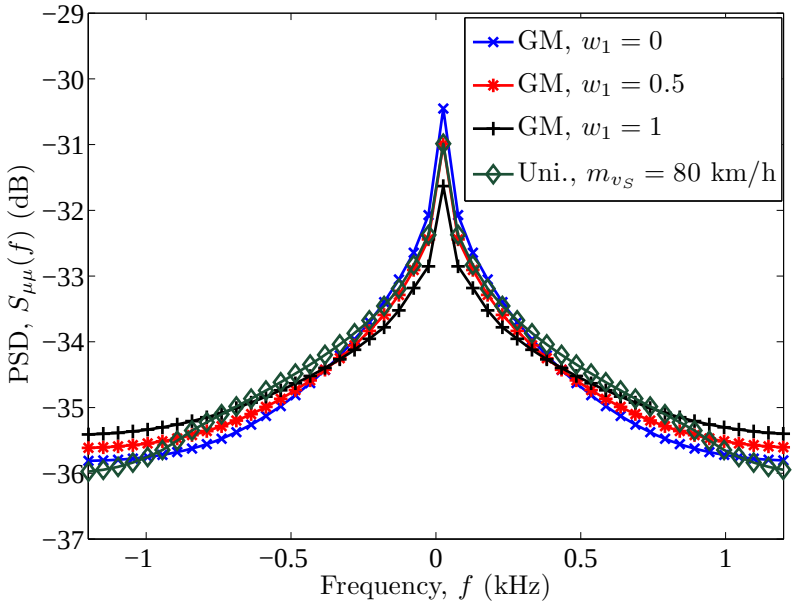

Figure C.4: The behavior of the PSD $S_{\mu\mu}(f)$ obtained by taking the Fourier transform of the ACF $r_{\mu\mu}(\tau)$ in (C.7) for V2V scenarios with relatively fast moving scatterers, where $v_T = v_R = 80$ km/h. The GM parameters have been set to $m_{1v_S} = 80$ km/h, $m_{2v_S} = 120$ km/h, and $\sigma_{1v_S} = \sigma_{2v_S} = 20$ km/h.

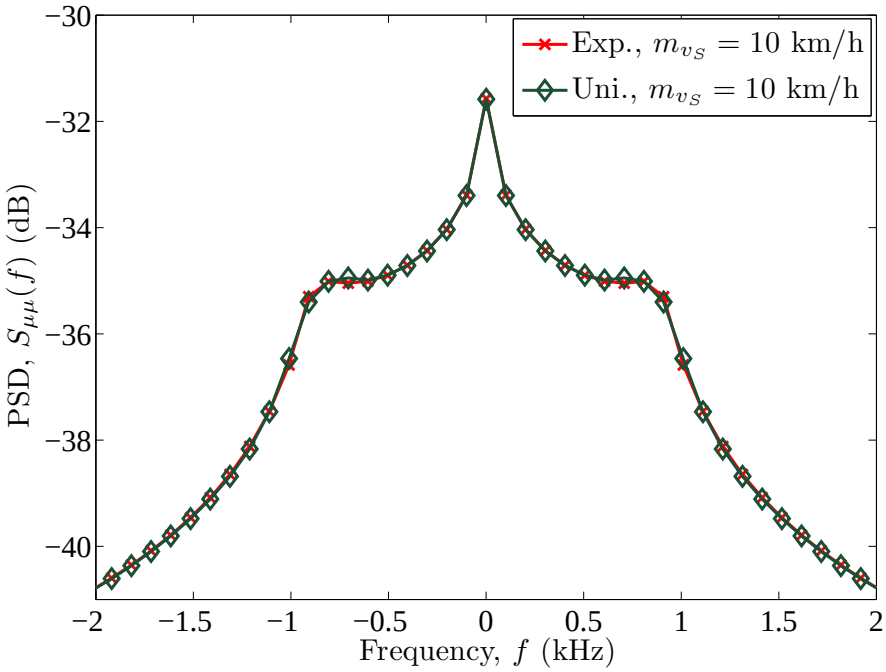

Figure C.5: The behavior of the PSD $S_{\mu\mu}(f)$ obtained by taking the Fourier transform of the ACF $r_{\mu\mu}(\tau)$ in (C.7) for V2V scenarios with relatively slow moving scatterers and $v_T = v_R = 80$ km/h.

the receiver vehicles move relatively fast relative to the average speed of scatterers. However, as mentioned before, even very slow moving scatterers are a significant source of the Doppler effect in F2F scenarios. Furthermore, according to Figs. C.4 and C.5, the PSD $S_{\mu\mu}(f)$ of the proposed channel model is even and real, which emphasizes that the ACF $r_{\mu\mu}(\tau)$ in (C.7) is also even and real.

C. ACF of the F2F Channel

Figs. C.6 and C.7 illustrate the ACF $r_{\mu\mu}(\tau)$ of the underlying F2F link according to (C.9) for various scatterer velocity distributions. In this regard, Fig. C.6 shows the effect of moving scatterers on the ACF of the channel, where the velocity v_S of the scatterers has been modeled by the GM distribution (see (C.13)) and the uniform distribution (see (C.12)). Fig. C.7 also demonstrates the impact of moving scatterers on the ACF of the F2F link, in which v_S follows either the exponential (see (C.11)) or the uniform distribution (see (C.12)). To study the impact of very slow moving scatterers, the average velocity m_{v_S} in both cases has been set to 3.6 km/h (1 m/s). To observe this effect, one just needs to compare the ACF in the presence of moving scatterers with that of fixed scatterers. Owing to triviality of the F2F channel model with fixed scatterers, we omit these results from Figs. C.6 and C.7. Indeed,

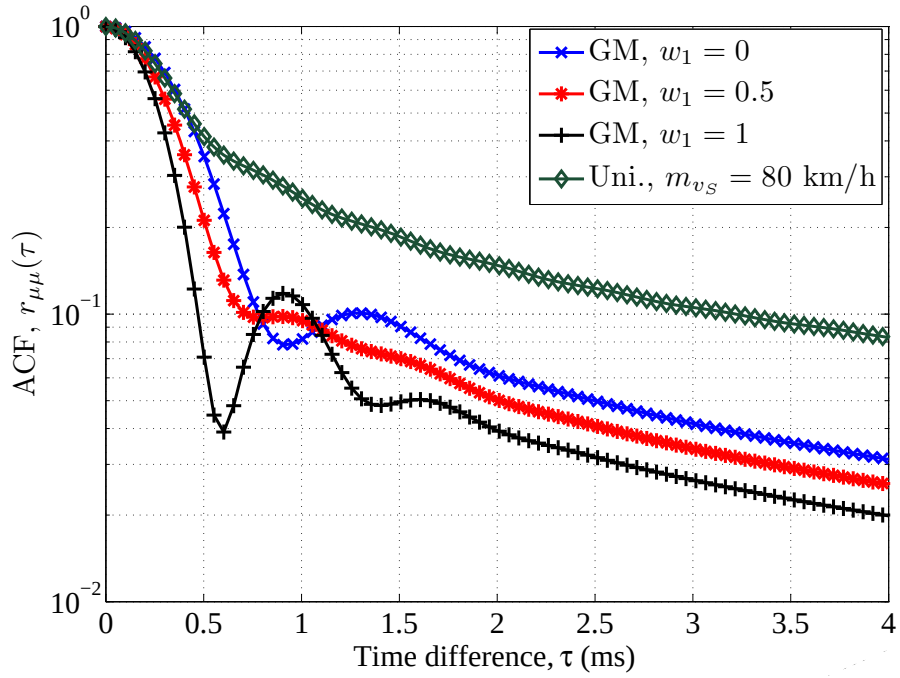

Figure C.6: The behavior of the ACF $r_{\mu\mu}(\tau)$ presented in (C.12) and (C.13) for F2F scenarios with moving scatterers. The GM parameters have been set to $m_{1v_S} = 80$ km/h, $m_{2v_S} = 120$ km/h, and $\sigma_{1v_S} = \sigma_{2v_S} = 20$ km/h.

by fixing the local scatterers, i.e., $v_S = 0$, the ACF in (C.10) results in the constant value $2\sigma_0^2$, which substantially differs from the graphs plotted in Figs. C.6 and C.7. In addition, from Fig. C.7, it can be concluded that the Doppler shifts due to even very slow moving objects, like foliage or walking pedestrians, are more important to be considered in the statistical analysis of F2F links as compared to V2V links. The importance of moving scatterers in F2F channels was extensively studied in [25, 26, 29], and [30]. It should be mentioned as well that in both F2F and V2V communication scenarios, relatively fast moving scatterers are regarded as significant sources of Doppler shifts.

D. PSD of the F2F Channel

Figs. C.8 and C.9 illustrate the PSD of the presented F2F channels for different scatterer velocity distributions. The general form of the PSD can be obtained by taking the Fourier transform of the ACF in (C.9). From Fig. C.8, as in Fig. C.4, a tendency to the delta function at the origin can be inferred if the mean velocity of the moving scatterers decreases. This behavior meets the results provided in [32] and [33]. Again, it can be seen that the PSD of the proposed channel model is even

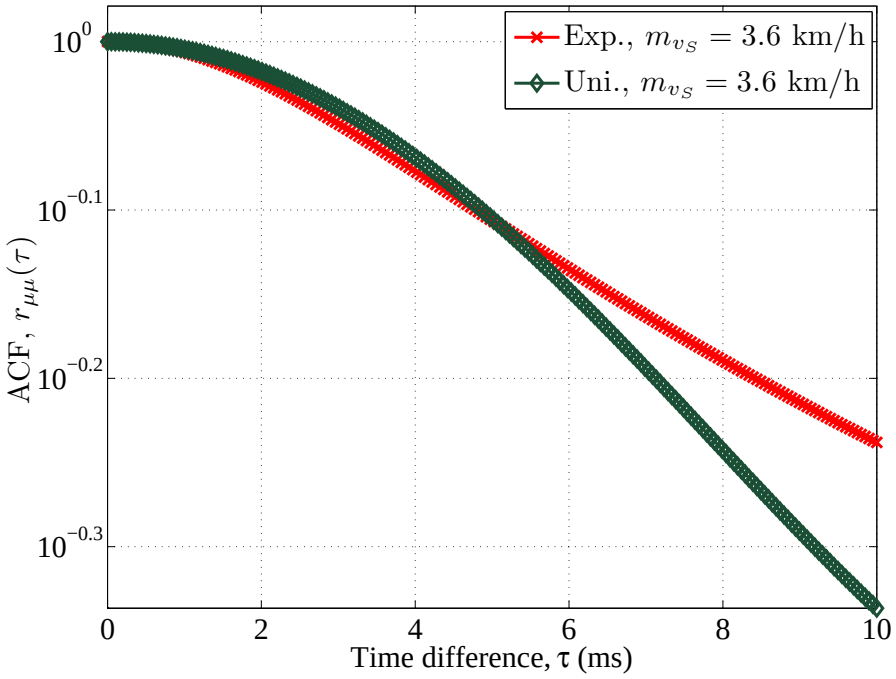

Figure C.7: The behavior of the ACF $r_{\mu\mu}(\tau)$ presented in (C.11) and (C.12) for F2F scenarios with moving scatterers.

and real. This complies with our results presented in Section IX.

E. Confirming the PSD with Empirical Data

Recall that our investigated scenarios are based on a narrowband V2V channel, in which both the transmitter and the receiver vehicles are located in an urban area surrounded by local moving scatterers. Regarding the effect of moving scatterers, the channel can be assumed as a quasi-stationary channel for a relatively short period of time. Now, to confirm the derived analytical results from such a channel by empirical data from measured channels, an appropriate measurement scenario should be considered. To the best of the authors' knowledge, there exists a lack of measurement data for V2V propagation scenarios in which the effect of moving scatterers on vehicular communications has been precisely studied. Issues that need to be addressed for a fair comparison include the stationarity and the frequency-selectivity aspects of the measured channel. Moreover, the geographic area of the measured channel is another important issue affecting the fairness of the comparison. Owing to the mismatch between the aforementioned properties of the proposed channel model of this paper and the ones reported in [6, 8, 9, 23] and [27], none of these measured channels can be used to validate the analytical results. Among the

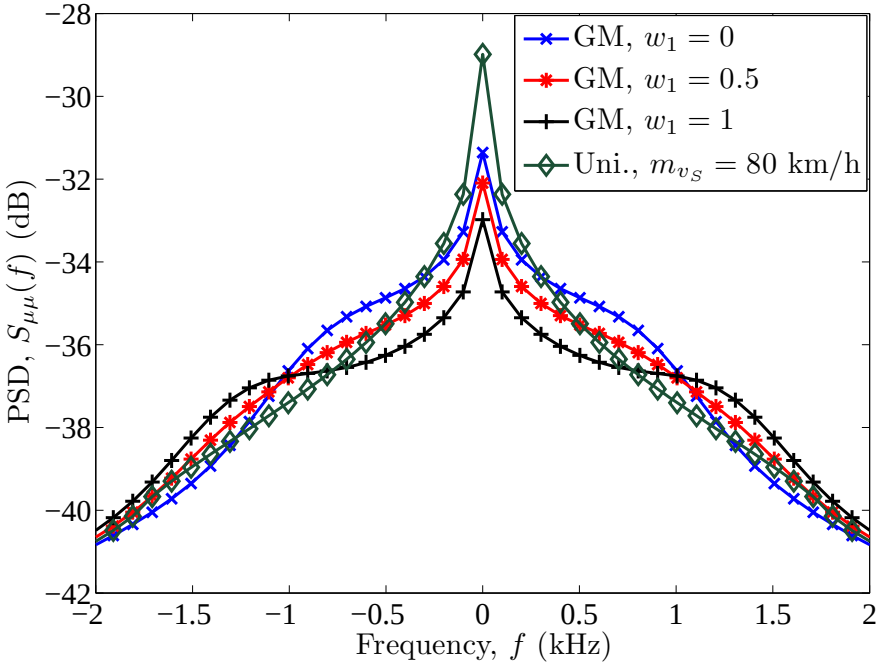

Figure C.8: The behavior of the PSD $S_{\mu\mu}(f)$ presented in (C.18) and (C.19) for F2F scenarios with moving scatterers. The GM parameters have been set to $m_{1v_S} =$ 80 km/h, $m_{2v_S} = 120$ km/h, and $\sigma_{1v_S} = \sigma_{2v_S} = 20$ km/h.

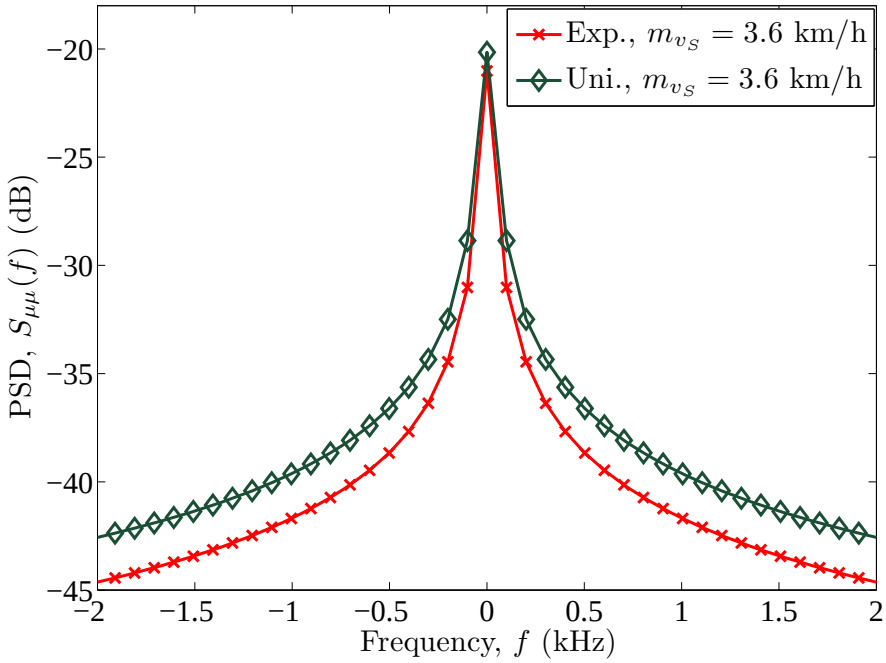

Figure C.9: The behavior of the PSD $S_{\mu\mu}(f)$ presented in (C.17) and (C.18) for F2F scenarios with moving scatterers.

measured channels studied in the literature, we focus on the empirical data reported in [7] and [25], which are taken from a flat-fading quasi-stationary channel. Notice that the validity of the stationarity and frequency-selectivity in V2V channels have been investigated, e.g., in [14] and [15].

Referring to [25], each snapshot for recording the empirical data was short enough to justify the quasi-stationary channel assumption. It is also mentioned there that the channel is frequency-nonselective. These properties comply with the features of our proposed reference channel model. Fig. C.10 shows the analytical PSD of the F2F one-ring model in comparison with the PSD that has been measured at 29.5 GHz in [25]. The analytical PSD plotted in this figure is obtained from the Fourier transform of the ACF presented in (C.15). We have used the exponential distribution to model the velocity of slow moving scatterers, like foliage movement, while the GM distribution has been used to model the velocity of fast moving scatterers, such as passing vehicles. A very close agreement between the analytical and empirical results can be observed in Fig. C.10. This close match can be seen not only for relatively slow moving scatterers, but also for relatively fast moving ones. It is also worth mentioning that this agreement is much better than the one provided in [29, Fig. 4(a,b)]. This is due to the fact that the derivation of the PSD in our proposed F2F one-ring model is based on considering the dependency of the AOD and the AOA (see (C.14)). However, the authors of [29] and [30] did not take this dependency into account. Furthermore, in those papers, the velocity of passing vehicles has been modeled by an exponential distribution, which does not accurately describe the velocity of relatively fast moving vehicles [29]. Indeed, the authors mentioned in [29] that the exponential distribution cannot precisely describe the velocity of relatively fast moving scatterers, like passing vehicles and more investigations need to be done to find an appropriate distribution in this case. For this reason, we have employed the GM distribution, which is one of the most reported distributions to statistically model the velocity of fast moving vehicles [36–41].

We finish this part by emphasizing that the system configuration reported in [25] differs from a typical V2V scenario. Indeed, channel measurements at 29.5 GHz are mostly carried out to analyze local multipoint communication systems (LMCS), which are supposed to provide multimedia services with quality of service assurance. In this regard, the acceptable match shown in Fig. C.10 acknowledges the usefulness of the proposed channel model even for such scenarios.

F. Doppler Spread of the Channel

Fig. C.11 shows the Doppler spread presented in (C.21) (or equivalently in (C.27)) versus m_{v_S} for different scatterer velocity distributions, where both the transmitter

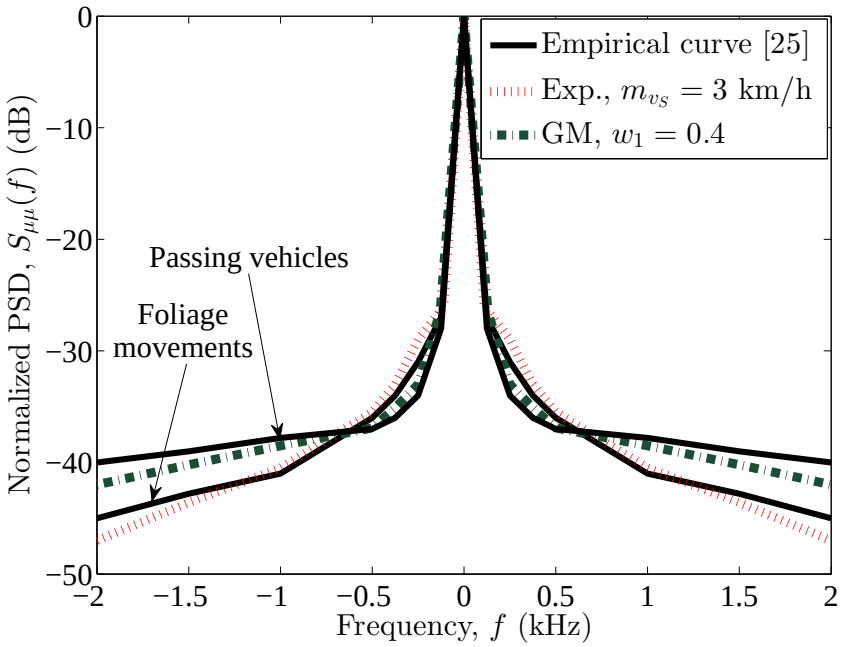

Figure C.10: Comparison between the PSD of the F2F one-ring model, i.e., the Fourier transform of the ACF in (C.15), and the measured PSD at 29.5 GHz [25]. The GM parameters have been set to $m_{1v_S} = 20$ km/h, $m_{2v_S} = 40$ km/h, and $\sigma_{1v_S} = \sigma_{2v_S} = 15$ km/h.

velocity v_T and the receiver velocity v_R have been set to 80 km/h. As it can be seen in this figure, for a given value of m_{v_S}, the exponential distribution results in a higher Doppler spread $B_{\mu\mu}^{(2)}$ as compared to the uniform and the Gaussian distributions. However, for small values of m_{v_S}, they behave almost the same. Furthermore, for a given average scatterer velocity m_{v_S}, the exponential distribution results in a higher Doppler spread $B_{\mu\mu}^{(2)}$ as compared with the uniform and Gaussian distributions.

G. Confirming the Doppler Spread with Empirical Data

To validate the derived Doppler spread, we have compared $B_{\mu\mu}^{(2)}$ with the Doppler spread measured in a suburban driving environment close to Carnegie Mellon University in Pittsburgh, PA [7, Fig. 8(b)]. The empirical data reported in [7] was obtained from a measured frequency-nonselective channel. The measurement was carried out at 5.9 GHz. It turned out that the measured Doppler spread $B_{\mu\mu}^{\star(2)}$ of the quasi-stationary channel can be expressed by the following regression line

$$B_{\mu\mu}^{\star(2)} = \frac{0.428}{\sqrt{2}\lambda} v_{\text{eff}} + 11.5 \text{ Hz} \tag{C.28}$$

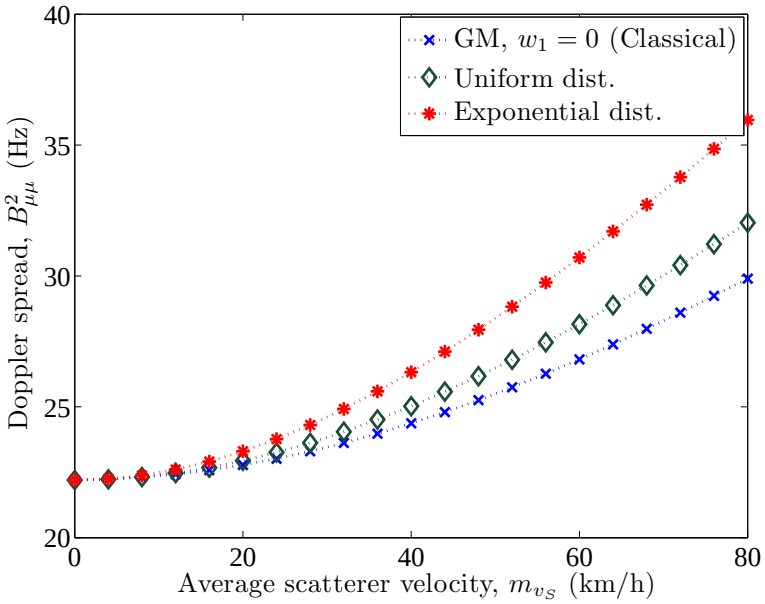

Figure C.11: The behavior of the Doppler spread $B^{(2)}_{\mu\mu}$ in (C.21) or equivalently in (C.27) for different scatterer velocity distributions. The transmitter and the receiver velocities have been set to $v_T = v_R = 80$ km/h and the GM parameters are $m_{1v_S} = 80$ km/h and $\sigma_{1v_S} = 20$ km/h.

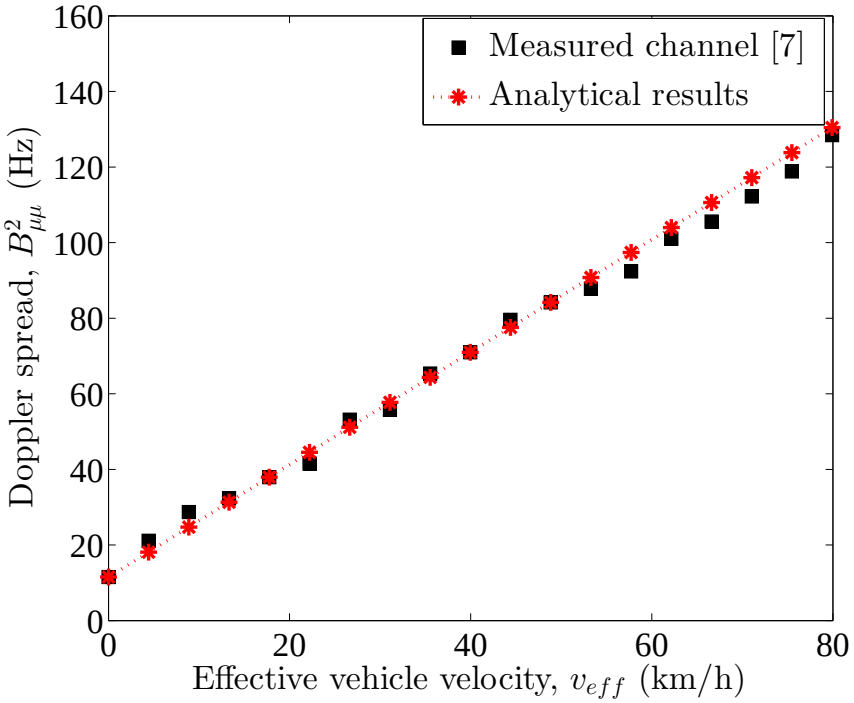

Figure C.12: Comparison between the Doppler spread $B^{(2)}_{\mu\mu}$ presented in (C.27) and the measured Doppler spread $B^{\star(2)}_{\mu\mu}$ at 5.9 GHz [7].

in which $v_{\text{eff}} = \sqrt{v_T^2 + v_R^2}$ denotes the effective velocity of the transmitter and the receiver. An interesting point in the latter equation is that the measured Doppler spread does not vanish even if both the transmitter and the receiver are fixed, i.e., $v_T = v_R = v_{\text{eff}} = 0$. The model presented in [7] cannot describe this constant shift at the origin, as the effect of moving scatterers has not been taken into account. However, our analytical model provides a clear evidence for the non-zero value of the Doppler spread even for F2F scenarios. In this regard, a close agreement between the expressions of the analytical and the empirical Doppler spread presented in (C.27) and (C.28) can be seen. This means that for a given scatterer velocity distribution, a perfect match between the regression line, presenting the Doppler spread of the channel, and the analytical one can be found by solving the equation $B_{\mu\mu}^{(2)} = B_{\mu\mu}^{\star(2)}$ for v_{eff_S}. Fig. C.12 shows an excellent match between the measured and the analytical Doppler spread of the channel under the assumption that the velocity of moving scatterers is exponentially distributed. The non-zero value of the Doppler spread at the origin, where $v_{\text{eff}} = 0$, can now be explained by the Doppler effect caused by moving scatterers located around the fixed transmitter and the fixed receiver vehicles. Notice that the non-zero value of the Doppler spread cannot be described by the channel models relying on the assumption of stationary scatterers.

XI. CONCLUSION

Starting from a typical propagation scenario, the complex channel gain of a V2V communication channel in the presence of moving scatterers has been presented. The ACF, PSD, and the Doppler spread of the V2V channel have been derived. By fixing either the transmitter or the receiver vehicles or both, the analytical results for the F2V and the F2F scenarios have been derived. Furthermore, the effect of fixing local scatterers in all above-mentioned scenarios has been studied. It has been shown that relatively fast moving scatterers have a major impact on both V2V and F2F communication links, as they are significant sources of the Doppler spread. However, relatively slow moving scatterers can be neglected in V2V channels, but not in F2F channels. Validating the analytical results with proper measurement data has been done in terms of the PSD and the Doppler spread of the channel. It has been shown that the GM model can accurately describe the velocity distribution of relatively fast moving scatterers while the exponential distribution can appropriately model the velocity of relatively slow moving scatterers. More investigations concerning other statistical properties of the channel, e.g., the coherence time, and the influence of the local distribution of the moving scatterers in specific areas, may be addressed in future works.

APPENDIX C.A

In order to obtain (C.9) from (C.8), let us start from the following reduction [46, Eq. (9-59)]

$$\int_0^T \int_0^T f(x-y)dxdy = \int_{-T}^{T} (T-|u|)\, f(u)du, \tag{C.29}$$

in which $u = x-y$ and f is an auxiliary function. If f is periodic, i.e., $f(u \pm T) = f(u)$, then the double integral above can be even more simplified to $T\int_0^T f(u)du$. Considering the fact that $J_0\left(2k_0 v_S \cos\left(\frac{\alpha^T-\alpha^R}{2}\right)\tau\right)$ in (C.8) is a periodic function with respect to $(\alpha^T-\alpha^R)/2$, and changing the random variables α^T and α^R to $2x$ and $2y$, respectively, the reduction above can be used to simplify the inner double integral (denoted by I) in (C.8) as follows

$$\begin{aligned} I &= \int_0^{2\pi}\int_0^{2\pi} J_0\left(2k_0 v_S \cos\left(\frac{\alpha^T-\alpha^R}{2}\right)\tau\right) d\alpha^T d\alpha^R \\ &= 4\int_0^{\pi}\int_0^{\pi} J_0\left(2k_0 v_S \cos(x-y)\,\tau\right) dxdy \\ &= 4\pi\int_0^{\pi} J_0\left(2k_0 v_S \cos(u)\,\tau\right) du \qquad \text{(C.30)} \\ &= 4\pi^2 J_0^2\left(k_0 v_S \tau\right) \qquad \text{(C.31)} \end{aligned}$$

where we have used $\int_0^{\pi} J_0\left(2z\cos(u)\right) du = \pi J_0^2(z)$ [45, Eq. (6.681.5)] to obtain (C.31) from (C.30). Finally, replacing the inner double integral I in (C.8) by (C.31) gives (C.9).

APPENDIX C.B

Let us assume that the mathematical relation between the AOD α^T and the AOA α^R in a given geometric channel model is presented by $\alpha^T = g(\alpha^R)$. Using the concept of [47, Eq. (3.15)], the joint PDF $p_{\alpha^T\alpha^R}(\alpha^T,\alpha^R)$ of α^T and α^R is given by

$$p_{\alpha^T\alpha^R}(\alpha^T,\alpha^R) = p_{\alpha^R}(\alpha^R)\delta\left(\alpha^T - g(\alpha^R)\right) \tag{C.32}$$

in which $\delta(\cdot)$ stands for the delta dirac function. For the classical one-ring model, the function g is given by [22, Eq. (6)]

$$\alpha^T = g(\alpha^R) = \arctan\left(\frac{\gamma^{-1}\sin(\alpha^R)}{1+\gamma^{-1}\cos(\alpha^R)}\right). \tag{C.33}$$

Substituting the function above in (C.32) and noticing the fact $p_{\alpha^R}(\alpha^R)$ equals $1/2\pi$ in the one-ring scattering model, the joint PDF $p_{\alpha^T\alpha^R}(\alpha^T,\alpha^R)$ presented in (C.14) can be attained.

APPENDIX C.C

Starting from the ACF $r_{\mu\mu}(\tau)$ in (C.7), the aim is to show $\dot{r}_{\mu\mu}(0)=0$. To ease the proof, we set

$$a = 2k_0 v_S \cos\left(\frac{\alpha^T-\alpha^R}{2}\right) \tag{C.34}$$

and

$$b = jk_0\left(v_T\cos\left(\alpha_v^T-\alpha^T\right)+v_R\cos\left(\alpha_v^R-\alpha^R\right)\right). \tag{C.35}$$

Accordingly, $r_{\mu\mu}(\tau)$ in (C.7) can be rewritten as follows

$$r_{\mu\mu}(\tau) = \frac{\sigma_0^2}{2\pi^2}\int_0^{\infty}\int_0^{2\pi}\int_0^{2\pi} J_0(a\tau)\,e^{b\tau}\,p_{v_S}(v_S)\,d\alpha^T d\alpha^R dv_S \tag{C.36}$$

where, both a and b are the functions of α^T and α^R, but not τ. The first derivative of $r_{\mu\mu}(\tau)$ with respect to the time difference τ becomes

$$\begin{aligned}\dot{r}_{\mu\mu}(\tau) &= \frac{\sigma_0^2}{2\pi^2}\int_0^{\infty}\int_0^{2\pi}\int_0^{2\pi}\left(bJ_0(a\tau)e^{b\tau}-aJ_1(a\tau)e^{b\tau}\right)\\ &\times\ p_{v_S}(v_S)\,d\alpha^T d\alpha^R dv_S\end{aligned} \tag{C.37}$$

in which we have used the following derivation rule $dJ_0(a\tau)/d\tau = aJ_{-1}(a\tau) = -aJ_1(a\tau)$. Setting $\tau=0$ in (C.37) and considering the fact that $J_0(0)=1$ and $J_1(0)=0$, we obtain

$$\dot{r}_{\mu\mu}(0) = \frac{\sigma_0^2}{2\pi^2}\int_0^{\infty}\int_0^{2\pi}\int_0^{2\pi} b\,p_{v_S}(v_S)\,d\alpha^T d\alpha^R dv_S$$

$$= \frac{\sigma_0^2}{2\pi^2} \int_0^{2\pi} \int_0^{2\pi} b \, d\alpha^T d\alpha^R. \tag{C.38}$$

Eventually, owing to the sinusoid nature of b [see (C.35)], the double integral in (C.38) over its range is zero, i.e., $\dot{r}_{\mu\mu}(0) = 0$.

REFERENCES

[1] H. Zhiyi, C. Wei, Z. Wei, M. Pätzold, and A. Chelli, "Modelling of MIMO vehicle-to-vehicle fading channels in T-junction scattering environments," in *Proc. 3rd European Conference on Antennas and Propagation, EuCAP 2009*. Berlin, Germany, Mar. 2009, pp. 652–656.

[2] A. Chelli and M. Pätzold, "A MIMO mobile-to-mobile channel model derived from a geometric street scattering model," in *Proc. 4th IEEE International Symposium on Wireless Communication Systems, ISWCS 2007*. Trondheim, Norway, Oct. 2007, pp. 792–797.

[3] X. Cheng, C. X. Wang, D. I. Laurenson, S. Salous, and A. V. Vasilakos, "An adaptive geometry-based stochastic model for non-isotropic MIMO mobile-to-mobile channels," *IEEE Trans. Wireless Commun.*, vol. 8, no. 9, pp. 4824–4835, Sep. 2009.

[4] M. Pätzold, B. O. Hogstad, and N. Youssef, "Modeling, analysis, and simulation of MIMO mobile-to-mobile fading channels," *IEEE Trans. Wireless Commun.*, vol. 7, no. 2, pp. 510–520, Feb. 2008.

[5] A. G. . Zajić and G. L. Stüber, "A new simulation model for mobile-to-mobile Rayleigh fading channels," in *Proc. IEEE Wireless Communications and Networking Conference (WCNC06)*. Las Vegas, NV, Apr. 2006, pp. 1266–1270.

[6] G. Acosta, K. Tokuda, and M. Ingram, "Measured joint Doppler-delay power profiles for vehicle-to-vehicle communications at 2.4 GHz," in *Proc. IEEE Global Communications Conference (GLOBECOM' 04)*, vol. 6. Dallas, TX, USA, Nov. 2004, pp. 3813–3817.

[7] L. Cheng, B. E. Henty, D. D. Stancil, F. Bai, and P. Mudalige, "Mobile vehicle-to-vehicle narrow-band channel measurement and characterization of the 5.9 GHz dedicated short range communication (DSRC) frequency band," *IEEE J. Select. Areas Commun.*, vol. 25, no. 8, pp. 1501–1516, Oct. 2007.

[8] J. Maurer, T. Fügen, and W. Wiesbeck, "Narrow-band measurement and analysis of the inter-vehicle transmission channel at 5.2 GHz," in *Proc. 55th IEEE Veh. Technol. Conf., VTC'02-Spring*, vol. 1. Birmingham, AL, USA, May 2002, pp. 1274–1278.

[9] A. Paier, J. Karedal, N. Czink, C. Dumard, T. Zemen, F. Tufvesson, A. F. Molisch, and C. F. Mecklenbräucker, "Characterization of vehicle-to-vehicle radio channels from measurements at 5.2 GHz," *Wireless Personal Communications (WPC)*, vol. 50, no. 1, pp. 19–32, Jul. 2009.

[10] A. Paier, J. Karedal, N. Czink, H. Hofstetter, C. Dumard, T. Zemen, F. Tufvesson, C. F. Mecklenbräucker, and A. F. Molisch, "First results from car-to-car and car-to-infrastructure radio channel measurements at 5.2 GHz," in *Proc. IEEE International Symposium on Personal, Indoor and Mobile Radio Communications, PIMRC'07*. Athens, Greece, Sep. 2007, pp. 1–5.

[11] J. Karedal, F. Tufvesson, N. Czink, A. Paier, C. Dumard, T. Zemen, C. F. Mecklenbräucker, and A. F. Molisch, "Measurement-based modeling of vehicle-to-vehicle MIMO channels," in *IEEE Int. Conf. on Communications, ICC'09*. Dresden, Germany, Jun. 2009, pp. 1–6.

[12] J. Karedal, F. Tufvesson, N. Czink, A. Paier, C. Dumard, T. Zemen, C. Mecklenbräuker, and A. Molisch, "A geometry-based stochastic MIMO model for vehicle-to-vehicle communications," *IEEE Trans. Wireless Commun.*, vol. 8, no. 7, pp. 3646–3657, Jul. 2009.

[13] A. Paier, T. Zemen, L. Bernadó, G. Matz, J. Karedal, N. Czink, C. Dumard, F. Tufvesson, A. F. Molisch, and C. F. Mecklenbräuker, "Non-WSSUS vehicular channel characterization in highway and urban scenarios at 5.2GHz using the local scattering function," in *Proc. International Workshop on Smart Antennas, WSA*. Darmstadt, Germany, 2008, pp. 9–15.

[14] O. Renaudin, V.-M. Kolmonen, P. Vainikainen, and C. Oestges, "Non-stationary narrowband MIMO inter-vehicle channel characterization in the 5-GHz band," *IEEE Trans. Veh. Technol.*, vol. 59, no. 4, pp. 2007–2015, May 2010.

[15] L. Bernadó, T. Zemen, A. Paier, G. Matz, J. Karedal, N. Czink, C. Dumard, F. Tufvesson, M. Hagenauer, A. F. Molisch, and C. F. Mecklenbräuker, "Non-WSSUS vehicular channel characterization at 5.2 GHz - spectral divergence

and time-variant coherence parameters," in *Proc. Union Radio Scientifique Internationale-URSI*. Illinois, USA, Aug. 2008.

[16] D.-S. Shiu, G. J. Foschini, M. J. Gans, and J. M. Kahn, "Fading correlation and its effect on the capacity of multielement antenna systems," *IEEE Trans. Commun.*, vol. 48, no. 3, pp. 502–513, Mar. 2000.

[17] A. Y. Olenko, K. T. Wong, and E. H. O. Ng, "Analytically derived TOA-DOA statistics of uplink/downlink wireless multipaths arisen from scatterers on an hollow-disc around the mobile," *IEEE Antennas Wireless Propag. Lett.*, vol. 2, pp. 345–348, 2003.

[18] A. Y. Olenko, K. T. Wong, and M. Abdulla, "Analytically derived TOA-DOA distributions of uplink/downlink wireless-cellular multipaths arisen from scatterers with an inverted-parabolic spatial distribution around the mobile," *IEEE Signal Processing Lett.*, vol. 12, no. 7, pp. 516–519, Jul. 2005.

[19] R. B. Ertel and J. H. Reed, "Angle and time of arrival statistics for circular and elliptical scattering models," *IEEE J. Select. Areas Commun.*, vol. 17, no. 11, pp. 1829–1840, Nov. 1999.

[20] J. C. Liberti and T. S. Rappaport, "A geometrically based model for line-of-sight multipath radio channels," in *Proc. IEEE Veh. Technol. Conf., VTC 1996*, Apr./May 1996, pp. 844–848.

[21] K. N. Le, "On angle-of-arrival and time-of-arrival statistics of geometric scattering channels," *IEEE Trans. Veh. Technol.*, vol. 58, no. 8, pp. 4257–4264, Oct. 2009.

[22] A. Borhani and M. Pätzold, "A unified disk scattering model and its angle-of-departure and time-of-arrival statistics," *IEEE Trans. Veh. Technol.*, vol. 62, no. 2, pp. 473–485, Feb. 2013.

[23] D. S. . Baum, D. Gore, R. Nabar, S. Panchanathan, K. V. S. Hari, V. Erceg, and A. J. Paulraj, "Measurement and characterization of broadband MIMO fixed wireless channels at 2.5 GHz," in *Proc. IEEE Int. Conf. Personal Wireless Communications*. Hyderabad, India, Dec. 2000, pp. 203–206.

[24] X. Zhao, J. Kivinen, and K. Skog, "Characterization of Doppler spectra for mobile communications at 5.3 GHz," *IEEE Trans. Veh. Technol.*, vol. 52, no. 1, pp. 14–23, Jan. 2003.

[25] N. Naz and D. D. Falconer, "Temporal variations characterization for fixed wireless at 29.5 GHz," in *Proc. IEEE Vehicular Technology Conference, VTC*. Tokyo, Japan, May 2000, pp. 2178–2182.

[26] A. Domazetovic, L. J. Greenstein, N. B. Mandayam, and I. Seskar, "Estimating the Doppler spectrum of a short-range fixed wireless channel," *IEEE Communications Letters*, vol. 7, no. 5, pp. 227–229, May 2003.

[27] R. P. Torres, B. Cobo, D. Mavares, F. Medina, S. Loredo, and M. Engels, "Measurement and statistical analysis of the temporal variations of a fixed wireless link at 3.5 GHz," *Wireless Personal Communications (WPC)*, vol. 37, no. 1-2, pp. 41–59, Apr. 2006.

[28] K. I. Pedersen, P. E. Mogensen, and B. H. Fleury, "A stochastic model of the temporal and azimuthal dispersion seen at the base station in outdoor propagation environments," *IEEE Trans. Veh. Technol.*, vol. 49, no. 2, pp. 437–447, Mar. 2000.

[29] V.-H. Pham, M. H. Taieb, J. Y. Chouinard, S. Roy, and H.-T. Huynh, "On the double Doppler effect generated by scatterer motion," *REV Journal on Electronics and Communications*, vol. 1, no. 1, pp. 30–37, Jan.-Mar. 2011.

[30] S. Roy, H. T. Huynh, and P. Fortier, "Compound Doppler spread effects of subscriber motion and scatterer motion," *International Journal of Electronics and Communications*, vol. AEÜ-57, no. 4, pp. 237–246, 2003.

[31] S. Thoen, L. V. der Perre, and M. Engels, "Modeling the channel time-variance for fixed wireless communications," *IEEE Communications Letters*, vol. 6, no. 8, pp. 331–333, Aug. 2002.

[32] J. B. Andersen, J. O. Nielsen, G. F. Pedersen, G. Bauch, and G. Dietl, "Doppler spectrum from moving scatterers in a random environment," *IEEE Trans. Veh. Technol.*, vol. 8, no. 6, pp. 3270–3277, Jun. 2009.

[33] P. Pagani and P. Pajusco, "Characterization and modeling of temporal variations on an ultrawideband radio link," *IEEE Trans. Antennas Propag.*, vol. 54, no. 11, pp. 3198–3206, 2006.

[34] A. Chelli and M. Pätzold, "The impact of fixed and moving scatterers on the statistics of MIMO vehicle-to-vehicle channels," in *Radio Communications*, A. Bazzi, Ed. Vienna, Austria: INTECH, Apr. 2010, ch. 3, pp. 51–63, iSBN 978-953-307-091-9.

[35] A. Borhani and M. Pätzold, "Modeling of vehicle-to-vehicle channels in the presence of moving scatterers," in *Proc. 76th IEEE Vehicular Technology Conference, VTC-Fall*. Quebec, QC, CA, Sep. 2012.

[36] P. P. Dey, S. Chandra, and S. Gangopadhaya, "Speed distribution curves under mixed traffic conditions," *Journal of Transportation Engineering*, vol. 132, no. 6, pp. 475–481, Jun. 2006.

[37] T. Hastie, R. Tibshirani, and J. Friedman, *The Elements of Statistical Learning: Data Mining, Inference, and Prediction*. Springer, 2001.

[38] J. Jun, "Understanding the variability of speed distributions under mixed traffic conditions caused by holiday traffic," *Transportation Research Part C: Emerging Technologies*, vol. 18, no. 4, pp. 599–610, Jun. 2010.

[39] C.-M. Hsu and F.-L. Lian, "A case study on highway flow model using 2-D Gaussian mixture modeling," in *Proc. Intelligent Transportation Systems Conference, ITSC07*. Seattle, WA, USA, Sep. 2007, pp. 790–794.

[40] N. Ueda, R. Nakano, Z. Ghahramani, and G. E. Hinton, "SMEM algorithm for mixture models," *Neural Computation*, vol. 12, no. 9, pp. 2109–2128, Sep. 2000.

[41] W. Zhu, K. Boriboonsomsin, and M. Barth, "Microscopic traffic flow quality of service from the drivers' point of view," in *Proc. Intelligent Transportation Systems Conference, ITSC'07*. Seattle, WA, USA, Sep./Oct. 2007, pp. 47–52.

[42] M. Pätzold, *Mobile Radio Channels*, 2nd ed. Chichester: John Wiley & Sons, 2011.

[43] W. C. Jakes, Ed., *Microwave Mobile Communications*. Piscataway, NJ: IEEE Press, 1994.

[44] M. Pätzold and N. Youssef, "Modelling and simulation of direction-selective and frequency-selective mobile radio channels," *International Journal of Electronics and Communications*, vol. AEÜ-55, no. 6, pp. 433–442, Nov. 2001.

[45] I. S. Gradshteyn and I. M. Ryshik, *Table of Integrals, Series, and Products*, 7th ed. Elsevier Academic Press, 2007.

[46] A. Papoulis, *Probability, Random Variables, and Stochastic Processes*, 3rd ed. New York: McGraw-Hill, 1991.

[47] S. Primak, V. Kontorovich, and V. Lyandres, *Stochastic Methods and their Applications to Communications – Stochastic Differential Equations Approach*. Chichester: John Wiley & Sons, 2004.

Appendix D

Paper IV

Title:	A Highly Flexible Trajectory Model Based on the Primitives of Brownian Fields—Part I: Fundamental Principles and Implementation Aspects
Authors:	**Alireza Borhani** and Matthias Pätzold
Affiliation:	University of Agder, Faculty of Engineering and Science, P. O. Box 509, NO-4898 Grimstad, Norway
Journal:	*IEEE Transactions on Wireless Communications*, to be appeared.

A Highly Flexible Trajectory Model Based on the Primitives of Brownian Fields—Part I: Fundamental Principles and Implementation Aspects

Alireza Borhani and Matthias Pätzold

***Abstract* — A fundamental drawback of synthetic mobility models is that the spatial configuration of the path is determined by the temporal features of the mobile station (MS), such as its speed. This is, however, not true in reality. This first part of our paper establishes a new approach for generating *fully spatial* random trajectory (mobility) models to which different speed scenarios can be applied. We employ the new approach to propose a highly flexible trajectory model based on the primitives (integrals) of Brownian fields (BFs). We construct a *drifted partial random bridge* from a given starting point to a random terminating point in the two-dimensional (2D) plane. If the bridge is partially established, a target zone with a predefined radius and centre can be reached via random paths. If the bridge is fully established, a certain destination point can be achieved by means of random bridges. For the broken bridge, totally random terminating points are obtained. The smoothness of the path can be controlled by the primitives of the employed BF. The implementation aspects of the path model in simulation environments are discussed. In wireless communications, the model can be used for tracking (estimating) the location of the MS, performance analysis of mobile ad hoc networks, and channel modelling under non-stationary conditions.**

***Index Terms* — Trajectory model, mobility model, Brownian fields, partial random bridge, drift component, bridge component.**

Manuscript received January 18, 2014; revised May 28, 2014. The review of this paper is coordinating by Dr. W. Wang.

A. Borhani and M. Pätzold are with the Faculty of Engineering and Science, University of Agder, 4898 Grimstad, Norway (e-mails: {alireza.borhani, matthias.paetzold}@uia.no).

I. INTRODUCTION

Trajectory models are of great importance in many avenues of science, including communications engineering. The demanding mobility features of cutting-edge communication technologies add to the vitality of these models. Traffic offering, handover management, adaptive routing control, localization, and registration are only a few examples of challenges caused by the mobility of users. The performance of ad hoc network protocols depends heavily on the mobility of nodes as well. Channel modelling is another main task, which is influenced strongly by the mobility features of the MS.

There are two major approaches for modelling the mobility of users: the user tracing approach and the synthetic approach [1–3]. The first approach extracts mobility patterns directly from real-life observations [4–7]. Despite the accuracy of these models, they are fully deterministic and entirely scenario dependent. Therefore, the performance of communications systems cannot easily be judged by these models. Nevertheless, there exist some trustworthy mobility models created by tracing thousands of wireless users over a long period of time [3].

The second approach is to build a synthetic mobility model based on a given velocity distribution [8–10]. The physical location (trajectory) of the user is then determined by mapping given distributions of the speed and angle-of-motion (AOM) on the Euclidian space. The random walk [11, 12], random waypoint [13], Gauss-Markov [14], city section [15], and the pursue [2] mobility models are among the most important models designed by the aforementioned approach. A survey of mobility models proposed in the literature can be found in [8, 9, 16]. Each of these models has some advantages and disadvantages. For instance, sudden changes in the AOM and (or) the speed of the MS are the most important disadvantages that some of these models suffer from. Furthermore, an important lack in the available mobility models is that none of them can provide a random path that leads to a predefined target zone or destination point[1]. Even the perfect simulation model of [17] does not cover random, but targeted, motions of the MS. The only exemption is the temporal mobility model proposed in [18], which allows targeting a predefined destination point (zone) via a recursive algorithm. One of the major drawbacks of the model proposed in [18] is its code-based structure, which needs significant changes if its objective changes from arriving at a predefined destination point to arriving at a predefined destination zone. In addition, the trajectory model in [18] does not

[1]Notice that the pursue mobility model emulates scenarios, in which pursuing nodes attempt to capture a moving pursued node ahead, which is substantially different from arriving at a predefined target zone via random paths.

support any smoothness control mechanism. Another disadvantage of this model comes in what follows.

A *fundamental drawback* of synthetic mobility models is that the spatial characteristics of the path are forced to be determined by the temporal specifications of the user, such as its speed. A quick question that arises is that why should a physical configuration of a path be a function of the user's speed? This is in contrast to reality, where users try to adapt their speed and AOM to sideways, roads, and highways. Although the physical and temporal characteristics of the user cannot be separated into two concepts, the spatial characteristics of a path are *totally separated* from the temporal behaviour of the users. This issue can also be extracted from [3], where the empirical user tracings reveal that the spatial characteristics of the mobility models are determined by the features of typical roads and walkways, but not by the temporal behaviour of road users. Notice that in reality, one often tries to find a destination point (zone) via possible trajectories heading to that destination. In such a scenario, the chosen path and speed vary from user to user.

Motivated by the discussion above, this first part of our paper proposes a third approach to design *fully spatial* trajectory models to which different speed scenarios can be applied. The main idea is to model the trajectory in position, but not in time. We employ the new approach to propose a novel random trajectory model using the primitives of BFs. To this end, we expand the standard temporal Brownian motion (BM) process to the standard unitless BF, which later actuates the *random component* of the path model. The standard BF is almost surely nowhere differentiable, which results in infrequently seen trajectories with sudden changes of direction. Therefore, we introduce and utilize the differentiable primitives of the standard BFs, which then allows us to generate trajectories with different levels of smoothness. By adding a *drift component* to the random components, we are about to provide a random trajectory model with a bias causing the user to move in a preferred direction. Moreover, we add to the novelty of the model by establishing a *partial random bridge* from a given starting point to a predefined target zone. The proposed spatial trajectory model is thus ready to allow: 1) arriving at a predefined destination point if the bridge is fully established, 2) arriving at a circular boundary (target zone) with a predefined radius and centre if the bridge is partially established, 3) a totally random point in the 2D plane if the bridge is broken, and finally 4) bridging back (closed loop) to the starting point if the bridge is fully established, but the drift component does not exist. Various other configurations are also possible, which will be discussed in the paper. Depending on the chosen primitive of the standard BF, the smoothness level of the entire configuration of paths can also

be controlled. This means that a given path configuration can be obtained in a quite erratic, relatively smooth, or very smooth manner. The proposed path is a 2D local vector with components along the *x*- and *y*-axis over which different speed scenarios can be tested. It is shown that the random walk trajectory model can be obtained as a special case of the proposed model. In another special case, the path configuration becomes very similar to that of the Gauss-Markov mobility model with a tuning parameter close to one.

In this first part of our paper, we also discuss the implementation of the path model in simulation environments, such as MATLAB®. A brief MATLAB® code for simulating the trajectory model is provided. Furthermore, the parametrization of the model is discussed and a practical scheme for determining the model parameters is provided. The results are illustrated and potential applications are discussed. The results demonstrate the high flexibility of the proposed path model in terms of its large configuration range and smoothness control mechanism. In the second part of our paper, we study the statistical properties of the proposed path model, showing that they are in line with those of real-world user tracings [3].

The proposed trajectory model has the potential to attract the interest of researchers from different branches of science, including communications engineering. Researchers focusing on ad hoc networks, cellular networks, localization, tracking, and mobile radio channel modelling[2] are among the potential enthusiasts of the proposed trajectory model. The model can also be used in traffic engineering, risk engineering, crime control, and social science. We will show that the trajectory model proposed in this paper is useful to model many daily life activities, such as possible trajectories from the police department to a crime scene, possible trajectories started from the tourist information office to a historical zone, and possible trajectories of vehicles trying to perform U-turn, only to name a few.

The remainder of this paper is organized as follows. Section II introduces the concept of the new approach, while Section III employs the new approach to prepare the random and deterministic components of the path model in position. The components are then combined to develop the spatial trajectory model in Section IV. The implementation aspects of the proposed path model are addressed in Section V, and the simulation results are discussed in Section VI. Finally, Section VII draws the conclusions.

[2]In the area of mobile radio channel modelling, the authors of [19] and [20] utilize very elementary Brownian mobility models for the development of non-stationary channel models.

II. THE CONCEPT OF THE NEW APPROACH

The common approach for generating synthetic mobility models is to start from given distributions of the speed and the AOM [8–10]. The speed and AOM are then combined to determine the heading destination point of the MS. Accordingly, the MS trajectory is determined by its temporal characteristics. This is in contrast to real-life scenarios, where road users adapt their speed and AOM to the course of the road [3].

To cope with this issue, we propose a new approach in which the starting point is a local random vector multiplied by a measurable parameter in metre, while its final outcome is a spatial trajectory in the 2D Euclidian space. Virtual drivers and pedestrians can then travel along the designed trajectory with different speeds. To achieve this, we need to expand the concept of stochastic processes to random fields in their very general form (see, e.g., [21]). We recall that stochastic processes are essentially mathematical models of random phenomena in time. On the other hand, random fields are generalized stochastic processes defined over a countable parameter, *which is not necessarily time*. The outcomes of random fields fall into some manifolds, multidimensional vectors, or points, which are also not necessarily measurable. Such a concept allows us to generate the random components (random vectors) of the path model *in position, but not necessarily in time*. The components of the random vectors are considered as unitless random gains, which can be multiplied by measurable parameters that control the physical length of the trajectory in metre. The outcome then falls into the Euclidian space. The random vectors can also be added to some deterministic drift components to construct spatial trajectory models. This approach is very useful if the random components are generated by BM processes. Notice that measurability of non-synthetic processes both in their arguments and outcomes restricts their utilization in other domains. However, the concept of random fields allows mapping the argument and outcome of non-synthetic processes into desired manifolds and (or) vectors, *while keeping* the statistical characteristics of the original processes. An important property of our approach is that the argument of the process, namely the position index, is inherently discrete. We divide the new approach in the following five steps:

1. Choosing a stochastic process with desired statistical properties, which then determines the statistical properties of the random components of the path model.

2. Expanding the chosen stochastic process to the corresponding random field defined in position.

3. Adding physical features to the random field, if needed.

4. Preparing the random components, as well as the drift and bridge components, if required.

5. Combining the components and generating the trajectory model in the 2D Euclidian space.

The steps above can be divided into two major parts, where Steps 1–4 comprise the preparation part and Step 5 the generation part. Both parts will be described separately in the two following sections.

III. PREPARATION OF THE TRAJECTORY COMPONENTS

Let us assume that the desired properties are the statistical properties of temporal BM processes. We prepare the components of the trajectory model by means of Steps 1–4 of the new approach. The reason for choosing BM processes as favorable processes is their non-synthetic nature and favorable statistical properties, including their non-differentiability, which will be discussed in what follows in detail. Furthermore, BM processes are quite well-established in proposing mobility models [8, 9, 16].

A. The Temporal BM Process

In 1827, the microscopic observations carried out by the famous botanist, Robert Brown, revealed the chaotic motions of pollen grains in water. The same erratic behavior was also reported from other experimentalists focusing on particle motions in a fluid or gas [22]. In honour of its discoverer, such a motion was then called BM. For the rest of that century, the BM became the centre of many analytical and empirical investigations. In the 1860s, experimentalists realized that the motion originates from suspending molecules. In 1906, Albert Einstein [11] accomplished the basic investigations by providing an exact physical explanation for such motions based on the bombardment of the suspended particles by the atoms of the suspending fluid. Two years later, a perfect mathematical representation of the BM was offered by Langevin [23]. Owing to its importance, Langevin's explanation was later translated into English [24].

The utilization of BM processes in modelling of sophisticated phenomena has been a hot topic from the late 19th century until now. Modelling of stock market fluctuations is one of the earliest applications of such processes in daily life. Medical imaging and fractal theory (see [25] and [26]) are also two more recent

examples, which benefit from BM processes in practice. Modelling the roughness of electromagnetic surfaces and signal processing are further applications (see, e.g., [27] and [28]). In mobile ad hoc networks, 2D BM processes (random walk) are employed to model irregular motions of mobile nodes [8], which are then used to perform network layer analysis. Moreover, 3D BM processes have been used to model fully random motions of mobile users [29].

A stochastic process $\{B(t) : t \in [0,T]\}$ is said to be a standard temporal BM process if the following three conditions are satisfied:

1. $B(0) = 0$.

2. $\forall\ 0 \leq s < t \leq T$, the random variable given by the increment $B(t) - B(s)$ follows the Gaussian distribution with zero mean and variance $t - s$, i.e., $B(t) - B(s) \sim N(0, t-s)$.

3. $\forall\ 0 \leq s < t < v < w \leq T$, the increments $B(t) - B(s)$ and $B(w) - B(v)$ are statistically independent.

From the conditions above, it can be concluded that $B(t)$ is a Wiener process with independent and normally distributed increments. It can be shown that the standard BM process is a continuous-type stochastic process in time, but almost surely *nowhere differentiable* (see, e.g., [30]).

B. The Proposed Brownian Field

We recall that a random field is defined over a countable parameter with outcomes in some manifolds, multidimensional vectors, or points. Herein, the idea is to consider the position variable $l \in [0,L]$ as the countable parameter of the standard BF and a 2D vector space as the corresponding sample space. Subsequently, we define the standard BF over the position variable $l \in [0,L]$, satisfying the following three conditions:

1. $B(0) = 0$.

2. $\forall\ 0 \leq l_i < l \leq L$, the random variable given by the increment $B(l) - B(l_i)$ follows the Gaussian distribution with zero mean and variance $l - l_i$, i.e., $B(l) - B(l_i) \sim N(0, l - l_i)$.

3. $\forall\ 0 \leq l_i < l < l_j < l_q \leq L$, the increments $B(l) - B(l_i)$ and $B(l_q) - B(l_j)$ are statistically independent.

We denote the standard BFs along the *x*- and *y*-axis by $B_x(l)$ and $B_y(l)$, respectively. The outcomes of these two processes are then multiplied by a measurable quantity in metre, enabling to locate the corresponding points in the 2D plane.

C. Featuring (Filtration)

In accordance with the standard BM process, the standard BF is almost surely nowhere differentiable. As a result, with probability approaching 1, any 2D trajectory model based on the *direct* combination of $B_x(l)$ and $B_y(l)$ experiences sudden changes of direction (see Section VI). This results in an erratic path, which can of course be observed in nature. An obvious example of such a trajectory is the BM itself, in which sudden variations in the AOM of suspended particles can be seen in fluids. Nevertheless, due to physical restrictions of man-made applications, the phenomenon of sudden changes in the AOM can rarely be observed in daily life. To cope with this issue, we employ Step 3 of the new approach, in which physical features are added to the utilized BF. Accordingly, we expand the *p*th ($p \geq 1$) primitive of the BM process [31] to that of the BF ${}_pB(l)$ by defining the *p*-fold integrated (filtered) standard BF $B(l)$ as follows

$$ {}_pB(l) = \int_0^l {}_{p-1}B(l')\,dl' \quad \forall p = 1,2,... \tag{D.1}$$

where ${}_0B(l) = B(l)$. Accordingly, the first condition $B(0) = 0$ of the standard BF (see Section III-B) is extended to ${}_pB(0) = 0$. By the fundamental theorem of calculus, the *p*-fold integrated BF ${}_pB(l)$ in (D.1) is p times differentiable and its *q*th derivative equals ${}_{p-q}B(l)$.

The case $p = 1$ is often called Kolmogrov diffusion [32], provided that l takes a temporal dimension and that the outcomes fall into the 3D Euclidian space. Similar to the *p*th primitive of the temporal BM process [31], the *p*th primitive of the BF ${}_pB(l)$ in (D.1) also follows the Gaussian distribution of the form $N(0, \sigma^2_{{}_pB}(l))$, where

$$ \sigma^2_{{}_pB}(l) = \frac{l^{2p+1}}{(p!)^2(2p+1)}. \tag{D.2}$$

In general, the autocovariance function $r^c_{{}_pB_pB}(l_i,l_j)$ of ${}_pB(l)$ is given by the following expression[3]

$$r^c_{{}_pB_pB}(l_i,l_j)=\frac{1}{(p!)^2}\int_0^{\min(l_i,l_j)}(l_i-l')^p(l_j-l')^p\,dl'. \tag{D.3}$$

The special case $l_i=l_j=l$ simplifies $r^c_{{}_pB_pB}(l,l)$ in (D.3) to the variance $\sigma^2_{{}_pB}(l)$ in (D.2). These quantities will play important roles in the analysis of the statistical properties of the trajectory model proposed in Section IV.

D. Components

The aim is to model a path which starts from (x_s,y_s) and terminates *at or about* a given destination point (x_d,y_d). To reach this aim, we define the deterministic increments $\delta_x=(x_d-x_s)/L$ and $\delta_y=(y_d-y_s)/L$ for some positive integer L. These increments act as the drift component of the path. Moreover, let ${}_pB_x(l)$ and ${}_pB_y(l)$ represent the pth primitive of the BF along the x- and y-axis, respectively. We manipulate the random field ${}_pB_x(l)$ to build a partial random bridge of the following form

$${}_pW_x(l,k_b)={}_pB_x(l)-\frac{k_b\,l}{L}\,{}_pB_x(L) \tag{D.4}$$

where the bridge parameter $k_b\in[0,1]$ controls the partial availability of the bridge[4]. The term *partial bridge* has been coined due to the fact that ${}_pW_x(0,k_b)=0$, whereas the value of ${}_pW_x(L,k_b)$ depends on the bridge parameter k_b. If k_b tends to 1, then ${}_pW_x(L,k_b)$ tends to 0. If k_b tends to 0, then ${}_pW_x(L,k_b)$ can be any random value generated by ${}_pB_x(L)$. For $l\neq 0,L$, the process ${}_pW_x(l,k_b)$ can also take any random value. As a result, we address the cases: $k_b=1$, $0<k_b<1$, and $k_b=0$ by the following terms: full bridge, partial bridge, and broken bridge, respectively. This terminology becomes much more meaningful if ${}_pW_x(l,k_b)$ is utilized as a component of the proposed trajectory model (see Section IV). In the same way, the partial bridge ${}_pW_y(l,k_b)$ associated with the y-axis can be constructed. The designed bridges are considered as the random components of the path model.

[3]The proof is similar to the one provided for the pth primitive of the temporal BM process (see, e.g., [33]).

[4]The partial random bridge in (D.4) has never been proposed before in the literature.

IV. THE PROPOSED TRAJECTORY MODEL

We combine the deterministic drift component discussed in Section III-D and random component in (D.4) to construct the proposed trajectory model, which allows us to generate trajectory ${}_p\mathscr{T}$ of the following form

$$ {}_p\mathscr{T} : \left\{ ({}_px(l), {}_py(l)) \;\middle|\; \begin{array}{l} {}_px(l) = x_s + k_d\, l\delta_x + \sigma_x\, {}_pW_x(l,k_b) \\ {}_py(l) = y_s + k_d\, l\delta_y + \sigma_y\, {}_pW_y(l,k_b) \end{array} \right\} \tag{D.5} $$

where the parameter σ_x (σ_y) in metre enables the superposition of the unitless bridge component ${}_pW_x(l,k_b)$ (${}_pW_y(l,k_b)$) and the drift component $k_d\, l\delta_x$ ($k_d\, l\delta_y$) along the x-axis (y-axis)[5]. The *drift parameter* $k_d = 0$ or 1 provides the option to include a drift component. Notice that the starting point $({}_px(0), {}_py(0))$ of the path is always (x_s, y_s). In what follows, we discuss the model parameters and their influence on the configuration of the trajectory ${}_p\mathscr{T}$.

A. Standard Deviation σ_x

The standard deviation σ_x in metre maps the random increments generated by ${}_pW_x(l,k_b)$ to the x-axis. This parameter directly controls the variance of the process ${}_px(l)$ associated with the path ${}_p\mathscr{T}$ along the x-axis[6]. Indeed, σ_x provides an additional degree of freedom to control the randomness of the process ${}_px(l)$ along the x-axis. For instance, by setting $\sigma_x = \sigma_y = 0$, any point on the straight line represented by $y(l) = ax(l) + b$ can be reached, in which the slope a equals $\arctan(\delta_y/\delta_x)$ and the constant shift b is given by $y_s - ax_s$. A comprehensive discussion about adjusting the model parameters, including the standard deviation σ_x, is provided in Section V-B.

B. Bridge Parameter k_b

The effect of the parameter k_b on the random bridge ${}_pW_x(l,k_b)$ has been discussed in Section III-D. To clarify its role in the trajectory model, let us first fix the drift parameter k_d to 1. For the full bridge scenario, i.e., $k_b = 1$, the terminating point $({}_px(L), {}_py(L))$ of the path ${}_p\mathscr{T}$ in (D.5) is nothing else than the planned destination point (x_d, y_d). At any other position between the starting and terminating points determined by $0 < l < L$, the term ${}_pW_x(l,1)$ contributes effectively to the

[5]Owing to fluency reasons, henceforth, we avoid repeating the similarity between the essential properties of the path along the x- and y-axis. Due to the symmetry of the trajectory model, the statistical properties of ${}_px(l)$ and ${}_py(l)$ are the same.

[6]The statistical properties of the path model, including the variance of the process ${}_px(l)$, are studied in Part II of our paper.

randomness of the path. Accordingly, each realization of the path ${}_p\mathscr{T}$ results in an almost surely unique path in the sense that all path realizations have the same starting and terminating points.

If the bridge is partially established, i.e., $0 < k_b < 1$, the path ${}_p\mathscr{T}$ has a tendency to approach the destination point (x_d, y_d). The rule of thumb is that the closer k_b is to 1, the closer is the terminating point $({}_px(L), {}_py(L))$ to the destination point (x_d, y_d). In this regard, the broken bridge, i.e., $k_b = 0$, results in a completely random terminating point $({}_px(L), {}_py(L))$ in the 2D plane. The following theorem provides a sound understanding of the bridge parameter k_b.

Theorem 1. Let D_d denote the distance between the terminating point $({}_px(L), {}_py(L))$ and the destination point (x_d, y_d). If the drift exists, i.e., $k_d = 1$, and the variances along both axes are equal, i.e., $\sigma_x^2 = \sigma_y^2$, then we have

$$\mathrm{P}\left\{ D_d \leq \frac{c\,\sigma_x(1-k_b)}{p!}\sqrt{\frac{L^{2p+1}}{2p+1}} \right\} = 1 - e^{-\frac{c^2}{2}} \tag{D.6}$$

where c is a positive constant.

Proof: See Appendix A. ■

Corollary 1. If the conditions of Theorem 1 are fulfilled, then the terminating point $({}_px(L), {}_py(L))$ falls with probability $1 - e^{-c^2/2}$ into a circular boundary of radius $r_b = c\,\sigma_x(1-k_b)\sqrt{L^{2p+1}/(2p+1)}/p!$ centred on the destination point (x_d, y_d). In other words, the random trajectories lead us to a vicinity of (x_d, y_d), but not necessarily to (x_d, y_d).

Accordingly, if $k_b = 1$, the radius of the circular boundary becomes 0, which means that arriving at (x_d, y_d) is guaranteed with probability $1 - e^{-c^2/2}$. Notice that the constant parameter c is to control the tightness of the circular boundary. In Section VI, we show this boundary is quite tight for any values of k_b and proper choices of c.

C. Drift Parameter k_d

The drift parameter k_d acts as a switch to control the presence of the drift to the destination point (x_d, y_d). If the drift exists, i.e., $k_d = 1$, then the path configuration is as discussed in Section IV-B. Therefore, we only need to discuss the case in which the drift does not exist, i.e., $k_d = 0$. In this case, the presence of a destination point (x_d, y_d) is meaningless. Depending on the partial availability of the bridge, which is controlled by the value of k_b, distinctive path configurations are possible.

For the broken bridge scenario, i.e., $k_b = 0$, the terminating point $({}_px(L), {}_py(L))$ is a fully random point in the 2D plane. Given this case, the primitive $p = 0$ sim-

plifies ${}_p\mathscr{T}$ in (D.5) to the random walk trajectory model in [11, 12]. For $p \geq 1$, the path ${}_p\mathscr{T}$ behaves very similar to the Gauss-Markov trajectory model in [14] with the tuning parameter close to 1.

For the full bridge scenario, i.e., $k_b = 1$, the path ${}_p\mathscr{T}$ describes a random closed-loop walk starting from and terminating at (x_s, y_s).

For the partial bridge scenario, i.e., $0 < k_b < 1$, the path ${}_p\mathscr{T}$ forms semi-circular configurations between those obtained by setting $k_b = 0$ and $k_b = 1$. In Section VI, we show that a proper choice of $0 < k_b < 1$ allows the path ${}_p\mathscr{T}$ to bridge circularly to random points in the 2D plane.

Theorem 2. Let D_s denote the distance between the terminating point $({}_px(L), {}_py(L))$ and the starting point (x_s, y_s). If the drift does not exist, i.e., $k_d = 0$, and the variances along both axes are equal, i.e., $\sigma_x^2 = \sigma_y^2$, then we have

$$\mathrm{P}\left\{ D_s \leq \frac{c\,\sigma_x(1-k_b)}{p!}\sqrt{\frac{L^{2p+1}}{2p+1}} \right\} = 1 - e^{-\frac{c^2}{2}} \tag{D.7}$$

where c is a positive constant.

Proof: Similar to the proof of Theorem 1. ■

Corollary 2. If the conditions of Theorem 2 are fulfilled, then the terminating point $({}_px(L), {}_py(L))$ falls with probability $1 - e^{-c^2/2}$ into a circular boundary of radius $r_b = c\,\sigma_x(1-k_b)\sqrt{L^{2p+1}/(2p+1)}/p!$ centred on the starting point (x_s, y_s). In other words, ${}_p\mathscr{T}$ forms random radial trajectories within a circle of given radius.

Accordingly, if $k_b = 1$, the radius of the circular boundary equals 0, with the consequence that the path bridges back (closed loop) to the starting point (x_s, y_s).

D. Primitive p

To discuss the role of the primitive p, it is beneficial to assume that L tends to infinity. If so, the path ${}_p\mathscr{T}$ is continuous. Referring to Section III-C, the pth primitive of the BF ${}_pB(l)$ in (D.1) is p times differentiable. Therefore, the partial random bridge ${}_pW_x(l, k_b)$ is also p times differentiable. This means that for $p = 0$, the path ${}_0\mathscr{T}$ is not differentiable, as it experiences sudden changes of direction. These sudden changes are due to the low correlation between the random components of the path ${}_0\mathscr{T}$ (see Part II). The higher primitives, however, allow a differentiable path ${}_p\mathscr{T}$, as the integral in (D.1) adds greatly to the correlation of the random components. Therefore, one might conclude that the primitive p determines the smoothness level of the path. Depending on the primitive p, the entire configurations of the path ${}_p\mathscr{T}$ can be obtained in a totally erratic, relatively smooth, or very smooth manner.

Notice that the need to a smoothness control mechanism is due to the fact that the smoothness level of our daily life trajectories varies from activity to activity. For instance, the trajectory of our motion when we are looking for an address is not as smooth as that when we perfectly know how to reach that address. Even the age of mobile users may affect the smoothness of their trajectories. For example, the trajectory of a child that is asked to go to a certain place is normally not as smooth as that of an adult person. The smoothness level also depends on the application. As an example, the erratic motions of a car roof antenna, which is of great importance in the area of channel modelling, should be modelled by an erratic trajectory, rather than a smooth one. Therefore, it is very beneficial to have smoothness control mechanisms to capture different levels of smoothness.

The effect of the model parameters on the configuration of every single realization of the path is listed in Table D.1. For simplicity reasons, we consider the special case of $\sigma_x = \sigma_y$. The table does not cover the effect of the primitive p, as this effect is substantially different from those of the other parameters. Furthermore, the figures listed in Table D.1 are to provide a quick preview of the path ${}_p\mathscr{T}$. An extensive description of the figures is given later in Section VI.

Notice that the substantial difference between the proposed trajectory model in this paper and the one in [18] is that we propose a solid mathematical trajectory model based on the concept of partial random bridges, which allows arriving at a destination point or zone, whereas the model in [18] is a code-based approach. The authors of [17] also use a simulation approach to design a class of path models in NS2, which differs substantially from our new analytical approach. Furthermore, to distinguish between arriving at a certain destination point or destination zone, we just need to tune the bridge parameter. For doing the same regarding the model in [18], the major parts of the code have to be updated. In addition, the mobility model in [18] is a temporal-spatial model, whereas our proposed trajectory model is a fully spatial model. Finally, our proposed model has a smoothness control mechanism, while the one in [18] has not.

Table D.1: The effect of the Model parameters on the configuration of the Path ${}_p\mathscr{T}$.

Model parameters			**Terminating point**	**Property of the path and/or the terminating point**	**Corresponding figure(s)**
$\sigma_x = \sigma_y$	k_d	k_b	$({}_px(L), {}_py(L))$		
0	0	$\in [0,1]$	(x_s, y_s)	Remaining at the starting point	-
0	1	$\in [0,1]$	(x_d, y_d)	Straight line to the destination point	-
$\forall \sigma_x \neq 0$	1	1	(x_d, y_d)	Bridging randomly to the destination point	Figs. D.1–D.3
$\forall \sigma_x \neq 0$	1	$\in (0,1)$	$({}_px(L), {}_py(L))$	Bridging to a random point inside the circular boundary of radius r_b and centred on (x_d, y_d)	Figs. D.4–D.6
$\forall \sigma_x \neq 0$	0	0	$({}_px(L), {}_py(L))$	A random point inside the circular boundary of radius r_b and centred on (x_s, y_s) (random walk trajectory model if $p = 0$)	Figs. D.7–D.9
$\forall \sigma_x \neq 0$	0	1	(x_s, y_s)	Closed loops (bridging back to the starting point)	Fig. D.10
$\forall \sigma_x \neq 0$	0	$\in (0,1)$	$({}_px(L), {}_py(L))$	Bridging circularly to a random point inside the plane	Fig. D.11

To clarify the speed adaptivity of the proposed trajectory model, let us consider the path obtained by connecting the $L+1$ points, i.e., $({}_px(l), {}_py(l))$ $(l = 0,1,...,L)$, generated by (D.5). There exist L sub-trajectories that connect pairs of consecutive points. An arbitrary speed s_l can then be assigned to the lth sub-trajectory. Accordingly, an arbitrary speed vector $(s_1, s_2, ..., s_L)$ of size L explains the speed records of the mobile user along the trajectory ${}_p\mathscr{T}$. The corresponding mobility model can then be used for the design of non-stationary channel models, handover management in cellular networks, and performance analysis of ad hoc networks, only to name a few. We stress that investigating suitable choices of the speed vector is outside of the scopes of this paper.

We finish this section by remarking that the flexibility of the path ${}_p\mathscr{T}$ is threefold: 1) its numerous configurations, 2) its smoothness control possibility, and 3) its adaptivity to different speed scenarios.

V. IMPLEMENTATION OF THE TRAJECTORY ${}_p\mathscr{T}$

In this section, we discuss the implementation aspects of the proposed trajectory ${}_p\mathscr{T}$ in (D.5). We provide a simplified MATLAB® code for simulating ${}_p\mathscr{T}$ as well as a practical scheme for the parametrization of the proposed trajectory model.

A. Implementation of the Path ${}_p\mathscr{T}$

One of the important advantages of the trajectory model in (D.5) is that it can easily be implemented in simulation environments, such as MATLAB®, NS2, and OPNET. The corresponding code is straightforward to develop. In this regard, Table D.2 describes the five main steps to simulate the process ${}_px(l)$ in (D.5) in MATLAB®[7]. Before Step 1, the model parameters, p, L, σ_x, x_s, x_d, k_d, and k_b need to be set (see Section V-B). The code provided in Table D.2 is written under the assumption of $p = 1$, meaning that we integrate over the standard BF $B_x(l)$ only once. For higher values of p, Step 3 needs to be repeated. However, this step must be skipped if $p = 0$ is the assumption. The same approach can be used to generate the process ${}_py(l)$ associated with the path along the y-axis. Plotting $({}_px(l), {}_py(l))$ for $l = 0,1,...,L$ gives then the trajectories shown in Figs. D.1–D.11, which will be discussed in Section VI. Given the 2D vector of $({}_px(l), {}_py(l))$, one can study the statistical characteristics of the path of his (her) own design by means of simulation results, while the reference statistical properties are provided in Part II. It is also note worthy that the path generation by means of the provided code is very fast. For

[7]For more information about the description of the commands and their functionality, see www.mathworks.com.

instance, generating the twenty paths shown in Fig. D.2 takes only about 0.8 s.[8]

B. Setting the Model Parameters

The path model in (D.5) is very flexible with respect to the configuration of the path. This configuration is determined by the model parameters. Among the model parameters, the primitive p, the drift factor k_d, and the bridge factor k_b are completely application-oriented. Given an application, depending on our knowledge of the smoothness of the path and of the availability of any destination point (zone) of interest, these parameters can readily be set. For instance, if the aim is to model the trajectory of a long antenna installed on a moving car, the lower value of p might be better, as the erratic motions of the antenna are indispensable. However, if the antenna is short enough and the motion is sufficiently smooth, the primitive p can be set to higher values.

In Section VI, we also provide some examples to explain the impact of an application on setting the values of the drift factor k_d and the bridge factor k_b.

Herein, we put our main emphasis on adjusting the parameter σ_x (σ_y), which is of special importance. To provide a practical approach for determining this parameter, we employ the following theorem.

Theorem 3. The variance $\sigma^2_{{}_px}(l)$ of the process ${}_px(l)$ associated with the path ${}_p\mathscr{T}$ along the x-axis is given by

$$\sigma^2_{{}_px}(l) \;=\; \sigma_x^2\left(r^c_{{}_pB_x{}_pB_x}(l,l)-2\frac{k_b l}{L}r^c_{{}_pB_x{}_pB_x}(l,L)+\frac{k_b^2 l^2}{L^2}r^c_{{}_pB_x{}_pB_x}(L,L)\right) \quad \text{(D.8)}$$

where the autocovariance function $r^c_{{}_pB_x{}_pB_x}(l_i,l_j)$ is given by (D.3), in which we replace the superscript ${}_pB$ by ${}_pB_x$.

Proof: See Section III-D of Part II. ■

From the theorem above, it is obvious that the parameter σ_x can directly affect the variance $\sigma^2_{{}_px}(l)$ of the process ${}_px(l)$. We remark that the variance $\sigma^2_{{}_px}(l)$ is in general not a constant value, but varies in the position index l. Given an application, what we normally know about these variations is their maximum value. For instance, for a police officer who is patrolling a main street and its vicinity, the maximum variance from that main street has been predefined by the police department.

[8]We have used a regular PC with a Core i7 Processor 2.67 GHz and 4 GB of RAM.

Table D.2: MATLAB® code (in part) for simulating the process ${}_p x(l)$ in (D.5).

Step	**MATLAB® code**	**Description**
1.	$f_0 = [0; randn(L,1)]$	Zero forcing to the standard Gaussian field $[f_0]$
2.	$f_1 = cumsum(f_0)$	Generating the standard BF ${}_0B_x(l)$ $[f_1]$
3.	$f_2 = cumtrapz(f_1)$	Generating the integrated BF ${}_1B_x(l)$ $[f_2]$
4.	$f_3 = [0; repmat(f_2(L+1,:), L, 1)/L]$ $f_4 = cumsum(f_3)$ $f_5 = \sigma_x(f_1 - k_b f_4)$	Generating the bridge ${}_p W_x(l,k_b)$ in (D.4) $[f_5]$
5.	$f_6 = linspace(x_s, x_d, length(f_0))$ $f_7 = k_d f_6 + \sigma_x f_5^T;$	Generating the process ${}_p x(l)$ ${}_1 x(l)$ in (D.5) $[f_7]$

Motivated by this, let $\sigma^2_{px\max}$ denote the maximum value of $\sigma^2_{px}(l)$ in (D.8), in which the parameter σ_x is unknown. The maximum variance $\sigma^2_{px\max}$ can be obtained by any parametric maximum finding algorithm. As an example, for $p=0$, $k_d=k_b=1$, one can obtain $\sigma^2_{0x\max}=\sigma_x^2 L/4$ (see Section IV-A in Part II). Accordingly, the value of σ_x can be written in terms of $\sigma_{px\max}$ and the other previously set parameters. For instance, to generate an $L=100$ points path ${}_0\mathscr{T}$ with a maximum standard deviation of $\sigma_{px\max}=10\,\mathrm{m}$, one needs to set $\sigma_x=2\,\mathrm{m}$.

According to Theorem 3, the parameter σ_x only controls the variance of the path along the x-axis. This means that σ_x together with σ_y determine the distance of the random trajectories from the shortest path. We finish this section by briefing that the best way to set the value of σ_x is to use a predefined application-oriented standard deviation $\sigma_{px\max}$ and then to follow the aforementioned procedure.

VI. SIMULATION RESULTS

The results have been produced by following the procedure described in Section V. In the entire simulations, the starting point (x_s,y_s) is set to the origin of the Cartesian coordinate system, i.e., $(0\,\mathrm{m},0\,\mathrm{m})$, whereas the destination point (x_d,y_d), if any, is set to $(50\,\mathrm{m},50\,\mathrm{m})$. The number of points L is set to 100. Regardless of the primitive p, the maximum standard deviation $\sigma_{px\max}$ along the x-axis is supposed to be equal to the one along the y-axis, i.e, $\sigma_{px\max}=\sigma_{py\max}=\sigma_{\max}$. If $\sigma_{px\max}>\sigma_{py\max}$ ($\sigma_{px\max}<\sigma_{py\max}$), the random trajectories show larger variations along the x-axis (y-axis), as compared to the y-axis (x-axis). The values of the primitive p, drift parameter k_d, and the bridge parameter k_b are displayed in the figures and/or their captions. The constant c, introduced in (D.7), has also been set to 4. In what follows, we demonstrate the possible configurations of the path ${}_p\mathscr{T}$ in Figs. D.1–D.11, and we discuss their potential applications. In these figures, the starting point (x_s,y_s) of the path is signed by an upward triangle, while the terminating point $({}_px(L),{}_py(L))$ is marked by a square. The statistical properties of the paths designed in Part I of this paper are extensively discussed in Part II.

Figs. D.1–D.3 show different realizations of the path ${}_p\mathscr{T}$ in (D.5) for distinct values of the primitive p. It is assumed that the bridge between the starting point (x_s,y_s) and the destination point (x_d,y_d) is fully established, i.e., $k_b=1$. Accordingly, setting $k_d=1$ guarantees terminating at $({}_px(L),{}_py(L))=(x_d,y_d)$, namely the destination point. In this regard, Fig. D.1 shows different realizations of the path ${}_0\mathscr{T}$, where sudden changes in the AOM are expectable. Figs. D.2 and D.3 demonstrate different realizations of the paths ${}_1\mathscr{T}$ and ${}_2\mathscr{T}$, respectively. These paths do not experience unexpected changes of direction. In this connection, the paths in

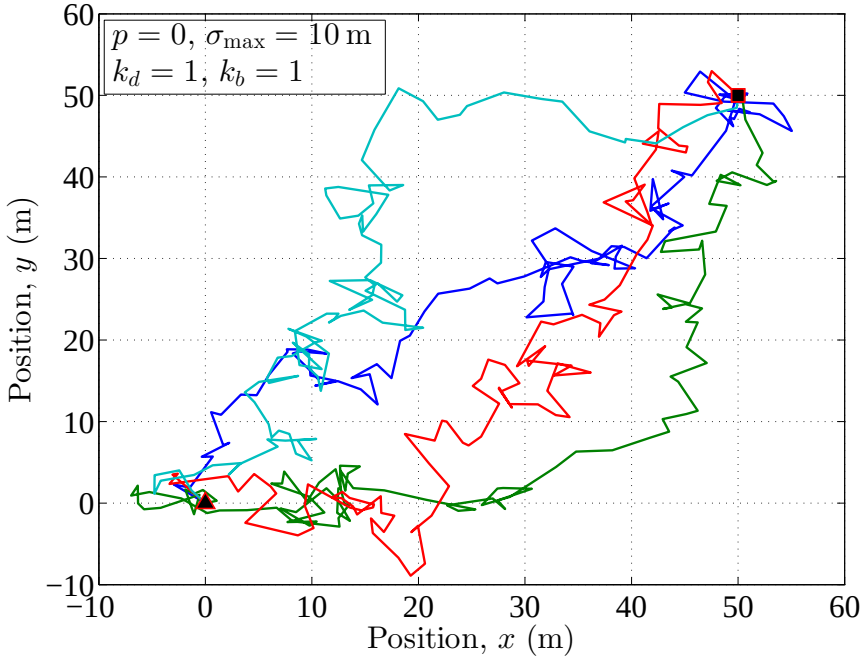

Figure D.1: Different realizations of the path ${}_0\mathscr{T}$ in (D.5) with $k_d = 1$ and $k_b = 1$ (full bridge scenario).

Fig. D.3 are smoother than those in Fig. D.2, which show the impact of the primitive p on the trajectory ${}_p\mathscr{T}$. Notice that the length of the paths in Fig. D.3 are in probability smaller than those of the other two figures. This can also be confirmed by simulating the overall travelling length PDF, which comes in Part II. It is also noteworthy that by increasing (decreasing) $\sigma_{\max}$, the distance of the random trajectories from the shortest path increases (decreases), thus the total travelling distance increases (decreases). We stress that changing the value of $\sigma_{\max}$ does not change the general trend of the trajectory in arriving at a certain destination point (zone). Notice that the primitive p might also be related to the level of knowledge about finding a path to a known destination. If the knowledge is relatively low, one needs to travel a larger distance before arriving at the destination, which corresponds to a high number of changes of direction. If the knowledge is relatively high, a shorter travelling distance might allow one to reach the destination in a smoother way. Such paths can often be seen in daily life, such as potential trajectories to reach a tourist information office. Indeed, the starting and terminating point of many of our daily life activities are perfectly known to us. However, the way that we travel to reach the target point is not unique. Notice that none of the mobility models in [8], allows to generate such targeted, but random, trajectories.

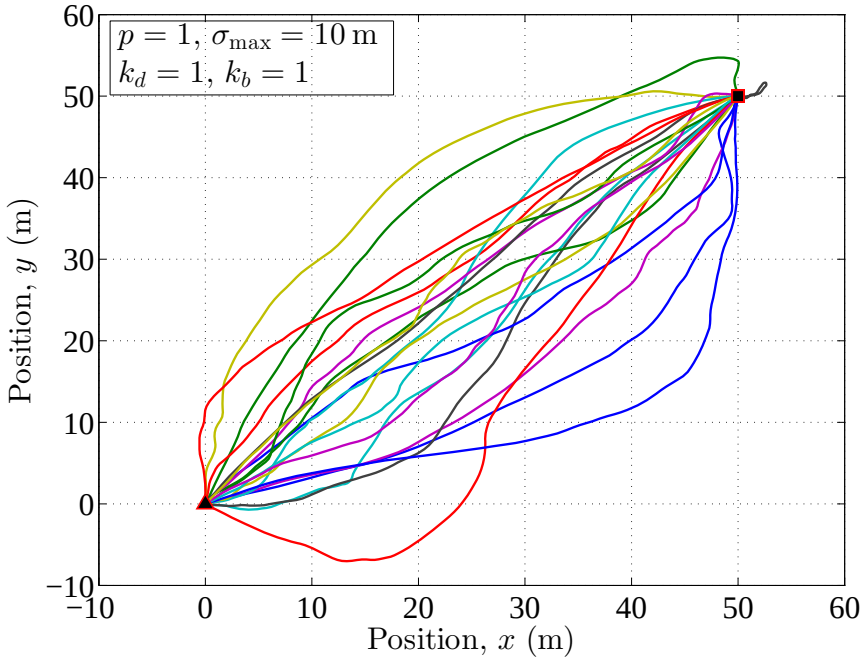

Figure D.2: Different realizations of the path ${}_1\mathscr{T}$ in (D.5) with $k_d = 1$ and $k_b = 1$ (full bridge scenario).

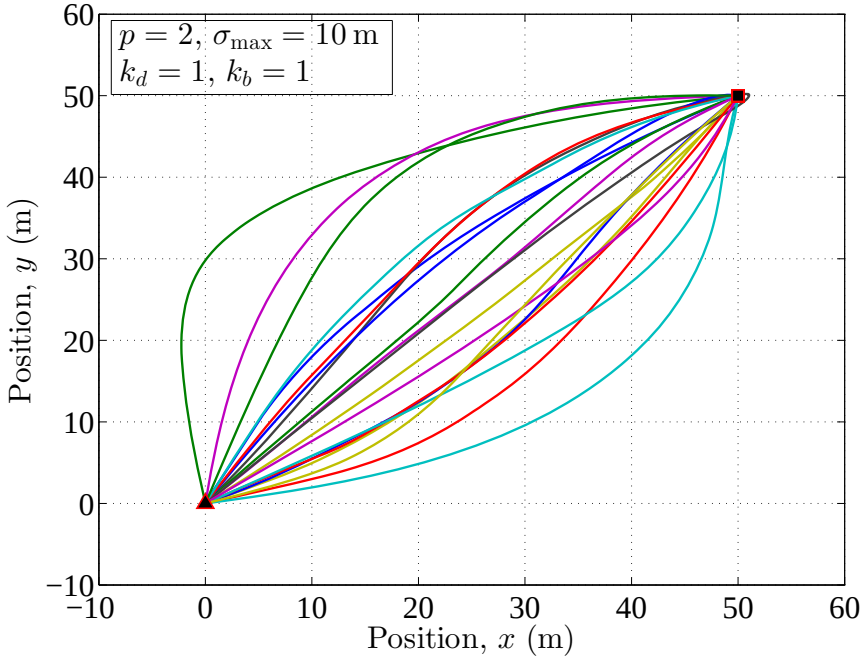

Figure D.3: Different realizations of the path ${}_2\mathscr{T}$ in (D.5) with $k_d = 1$ and $k_b = 1$ (full bridge scenario).

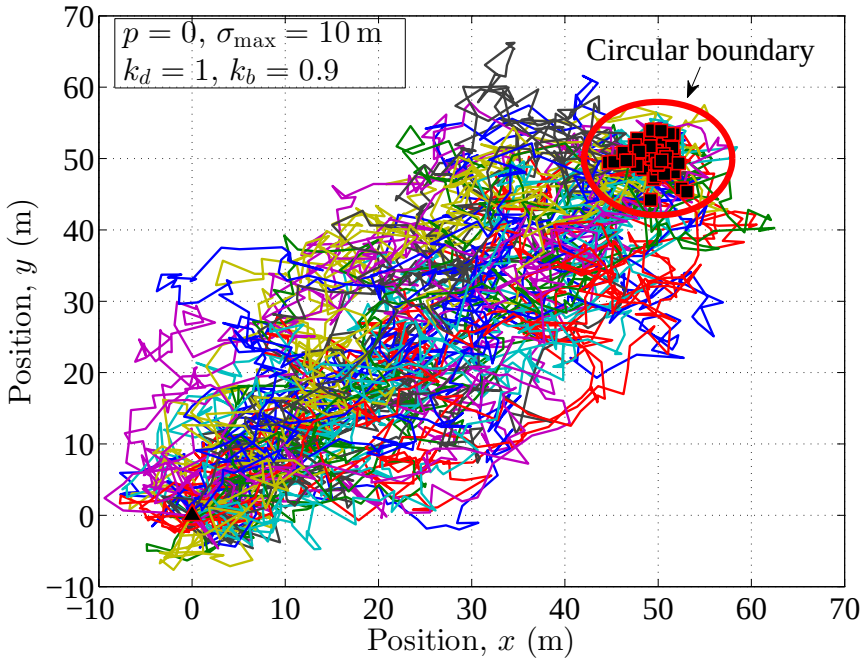

Figure D.4: Different realizations of the path ${}_0\mathscr{T}$ in (D.5) with $k_d = 1$ and $k_b = 0.9$ (partial bridge scenario).

Figs. D.4–D.6 demonstrate numerous realizations of the path ${}_p\mathscr{T}$ in (D.5) for different values of the primitive p, in which the bridge is partially ($k_b = 0.9$) established. For $k_d = 1$, the terminating point $({}_px(L), {}_py(L))$ falls into the circular boundary of Corollary 1 as shown in Figs. D.4–D.6. In these three figures, we have increased the number of realizations to show the tightness of the circular boundary. However, we have avoided a very high number of realizations to keep the visibility of the paths[9]. The effect of the primitive p is the same as what has been discussed in the first set of the figures. This scenario has again many real-life applications. The path started from the tourist information office to the historical zone of the city is one of the handy examples. The possible trajectories from the police department to a crime zone is another example.

The random walk trajectories and its filtered (integrated) versions are illustrated in Figs. D.7–D.9. In this set of figures, there is neither drift, nor bridge to a predefined point, i.e., $k_d = k_b = 0$. Given a position index l, the heading destination point $({}_px(l+1), {}_py(l+1))$ is totally random and is not subject to any drift. Nevertheless, for $p \geq 1$, the high correlation between the points does not allow sudden changes of direction (see Figs. D.8 and D.9). Herein, the angular tendency of the path is

[9]By increasing the number of realizations, it can easily be shown that the circular boundary is quite tight.

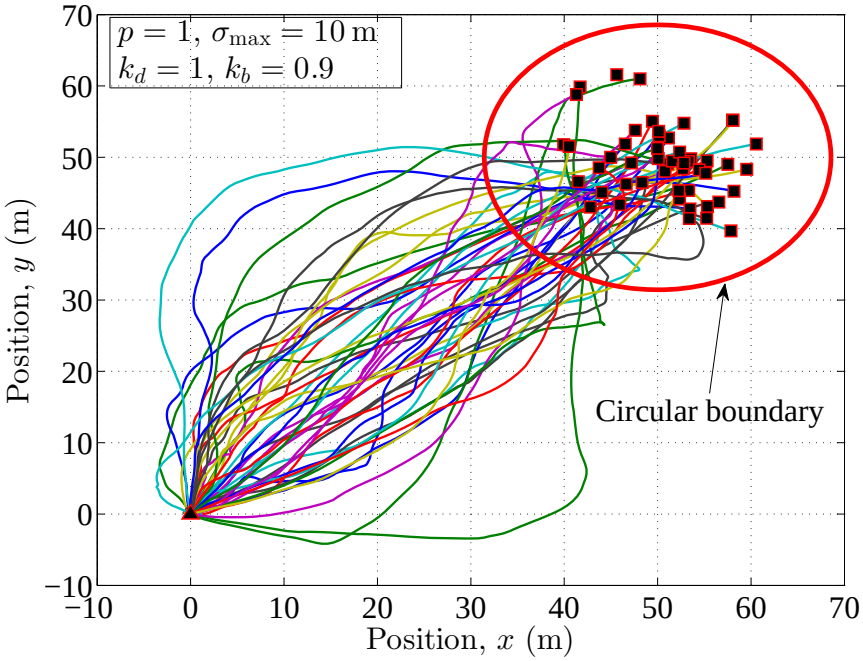

Figure D.5: Different realizations of the path ${}_1\mathscr{T}$ in (D.5) with $k_d = 1$ and $k_b = 0.9$ (partial bridge scenario).

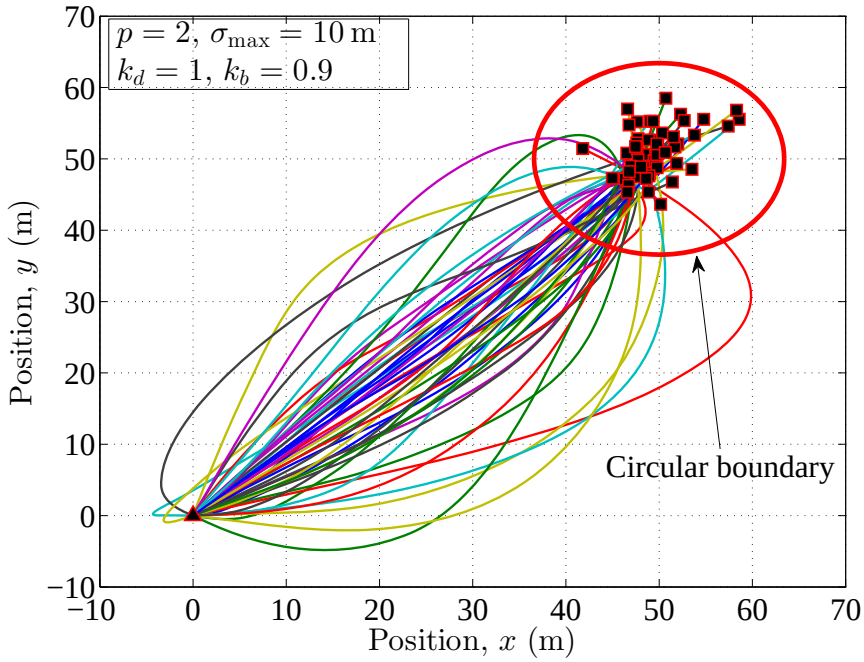

Figure D.6: Different realizations of the path ${}_2\mathscr{T}$ in (D.5) with $k_d = 1$ and $k_b = 0.9$ (partial bridge scenario).

mainly determined by the point next to the starting point, i.e., $({}_px(1), {}_py(1))$. Owing to the randomness of this point, the location of the terminating point $({}_px(L), {}_py(L))$ is completely random. For a predefined $\sigma_{\max}$, a circular boundary (see Corollary 2) centred on the starting point, however, can fence the possible locations of the terminating point. Again, if we increase the number of realizations, it can be verified that the bounds shown in Figs. D.7–D.9 are quite tight. However, to keep the visibility of the paths, we have not increased this number. Fig. D.7 shows the original random walk trajectories, while Figs. D.8 and D.9 display their once and twice integrated versions, respectively. It is worth mentioning that the paths shown in Figs. D.8 and D.9 are very similar to the ones obtained from the Gauss-Markov mobility model with a tuning parameter close to 1. Nonetheless, the superiority of our proposed model is that herein, different speed scenarios can be applied to a given trajectory. We remind that the position $({}_px(l), {}_py(l))$ corresponding to the Gauss-Markov model is a function of the velocity of the motion. The applications of the random walk trajectory model have been studied in the literature (see, e.g, [8, 9]). However, its integrated versions are totally new. From the application perspective, the paths shown in Figs. D.8 and D.9 can represent radial distancing from a starting point in random directions.

A very novel trajectory model is obtained if we set the drift parameter k_d to 0 and the bridge parameter k_b to 1. This allows the distance between $({}_px(l), {}_py(l))$ and the starting point to first increase and then decrease, enabling the trajectory ${}_p\mathscr{T}$ to bridge back to the starting point. In this way, the configuration of the path ${}_p\mathscr{T}$ is determined by random closed loops. Fig. D.10 shows different realizations of such a scenario, in which the maximum standard deviation $\sigma_{\max}$ along each axis has been set to 10 m. The closed loops can also be obtained by choosing other values of p, which only affects the smoothness level of the path. Such trajectories can also be seen in real life. Assume a main hall (as the starting point) that connects different sections of a museum. The trajectories of visitors might then be modelled by the paths shown in Fig. D.10.

Fig. D.11 illustrates another set of trajectories obtained under the assumption of $k_d = 0$ and $k_b = 0.5$. The resulting paths first show a sort of circular behavior near the starting point. By increasing l, these circular shapes, however, are opened to straight lines. The reason of this special configuration is that for $0 < k_b < 1$, the variance of the path along each axis is a combination of a concave and a convex function (see Fig. 5 of Part II). Such paths can be very useful to model vehicle trajectories in roundabouts and U-turns.

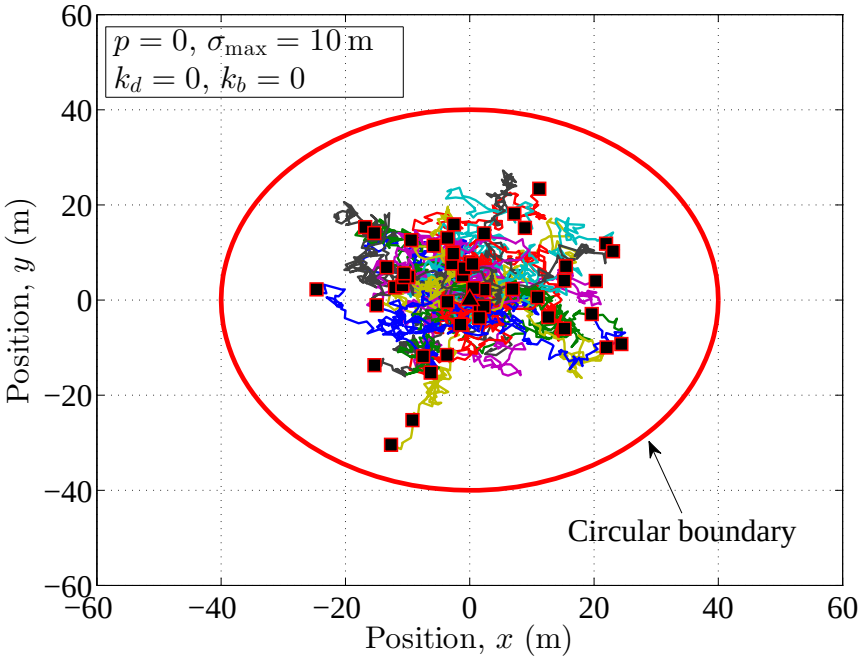

Figure D.7: Different realizations of the path ${}_0\mathscr{T}$ in (D.5) with $k_d = 0$ and $k_b = 0$ (broken bridge scenario).

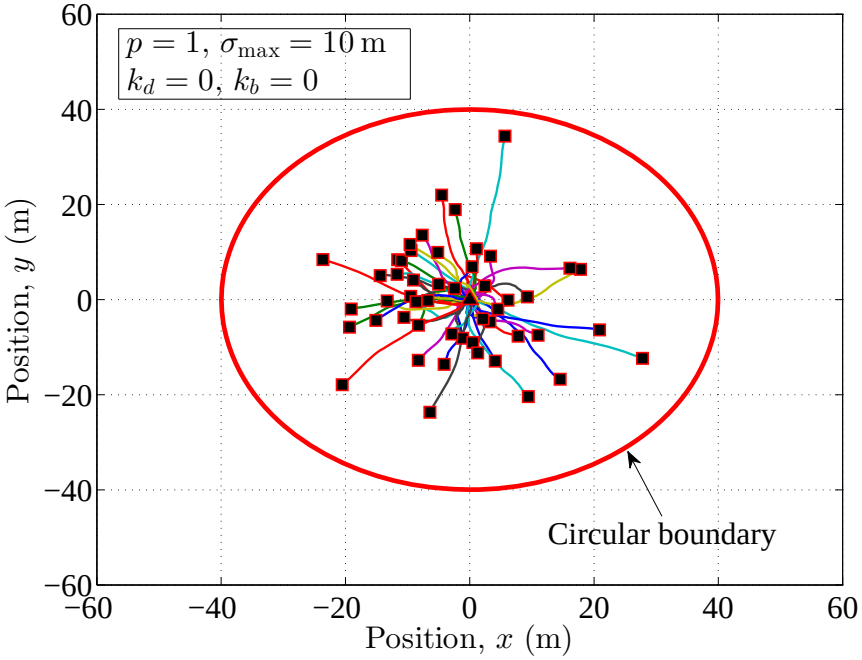

Figure D.8: Different realizations of the path ${}_1\mathscr{T}$ in (D.5) with $k_d = 0$ and $k_b = 0$ (broken bridge scenario).

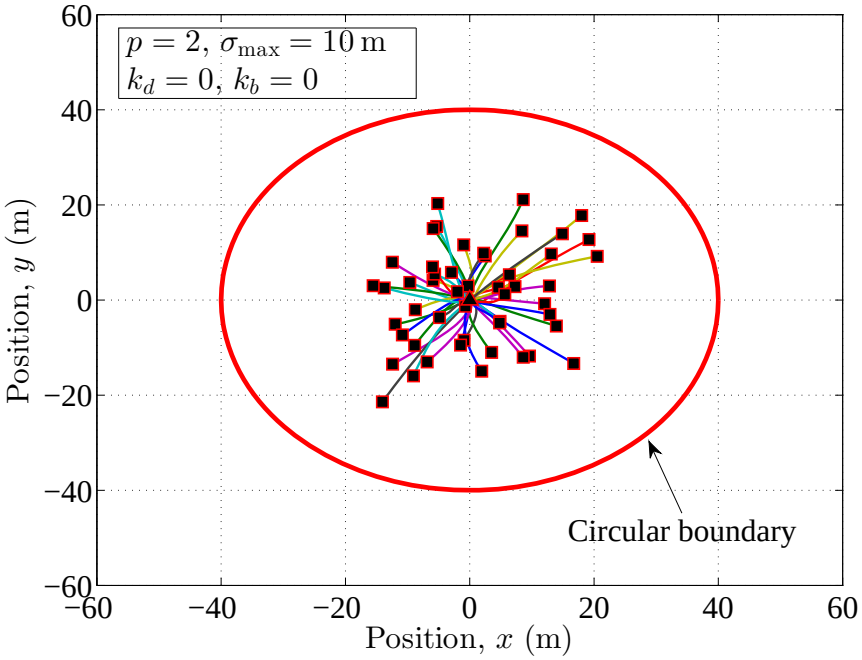

Figure D.9: Different realizations of the path ${}_2\mathscr{T}$ in (D.5) with $k_d = 0$ and $k_b = 0$ (broken bridge scenario).

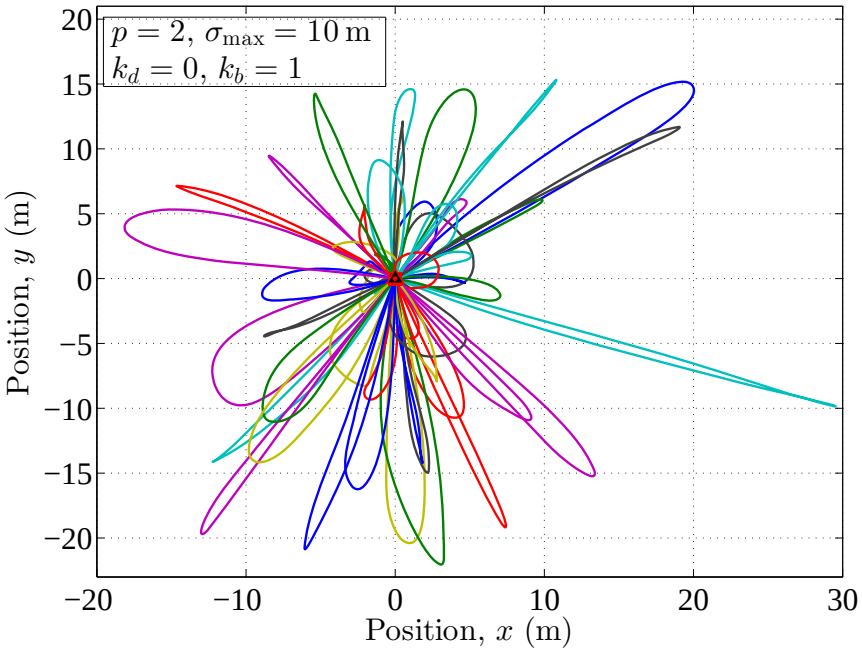

Figure D.10: Different realizations of the path ${}_2\mathscr{T}$ in (D.5) with $k_d = 0$ and $k_b = 1$ (full bridge scenario).

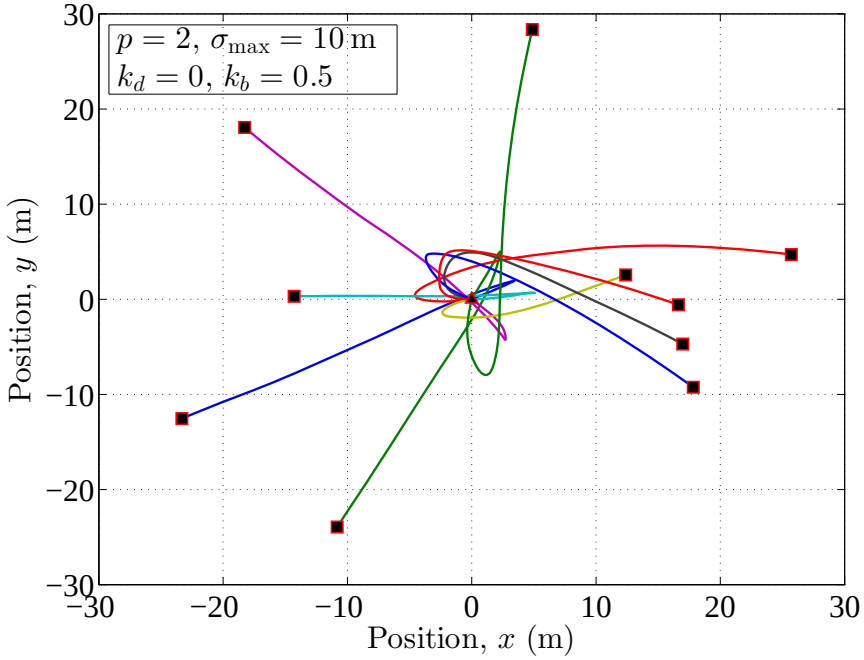

Figure D.11: Different realizations of the path ${}_2\mathscr{T}$ in (D.5) with $k_d = 0$ and $k_b = 0.5$ (partial bridge scenario).

We finish the discussion about the possible configurations of the path by remarking that the above-mentioned configurations are not the only ones that the proposed trajectory model in (D.5) can render.

VII. CONCLUSION

In the first part of our paper, we have introduced a third approach to trajectory modelling, through which fully spatial trajectory models can be obtained. We have proposed a highly flexible trajectory model based on the primitives of BFs. We have shown that the proposed path model renders a great number of configurations, while the smoothness level of each path configuration can be controlled by the primitives of BFs. We have demonstrated that the proposed trajectory model can describe both targeted and non-targeted dynamics of users in motion. In addition, random closed-loop trajectories can be obtained as a special case of the proposed model. The resulting trajectories can be travelled with different speeds without influencing the path configuration. The potential applications of the path configurations have been discussed, showing that the proposed path model can explain many of our daily-life activities. Furthermore, we have provided a MATLAB® code for simulating paths generated by the proposed trajectory model. It has been shown that the code is fast

and easy to implement. A practical scheme for the parametrization of the model has also been provided.

In the second part of our paper, we study the statistical prosperities of the proposed trajectory model. Other possible path configurations can be studied in future works. For example, combinational trajectories to reach a target point via one or several predefined mid-points might be another potential research line. In the future, the proposed approach of this paper can be followed to design other spatial trajectory models, which are not necessarily based on BFs. The new approach can also be extended to generate three-dimensional trajectory models. The smoothness control mechanism proposed in this paper is not flexible in the sense of generating multiple smoothness levels along a single trajectory. This also calls for further investigations on smoothness control mechanisms with applications in trajectory modelling.

APPENDIX D.A

PROOF OF THEOREM 1

Setting $k_d = 1$, $\sigma_x = \sigma_y$, and computing the terminating point $({}_px(L), {}_py(L))$ of the path ${}_p\mathscr{T}$ in (D.5) allows us to write

$$ {}_px(L) = x_d + \sigma_x\, {}_pW_x(L,k_b) \tag{D.9}$$

$$ {}_py(L) = y_d + \sigma_y\, {}_pW_y(L,k_b) \tag{D.10}$$

in which ${}_pW_x(L,k_b) = (1-k_b)\,{}_pB_x(L)$ and ${}_pW_y(L,k_b) = (1-k_b)\,{}_pB_y(L)$ (see (D.4)). The distance D_d from the terminating point $({}_px(L), {}_py(L))$ to the destination point (x_d, y_d) is then given by

$$\begin{aligned} D_d &= \sqrt{({}_px(L)-x_d)^2 + ({}_py(L)-y_d)^2} \\ &= \sigma_x(1-k_b)\sqrt{{}_pB_x^2(L) + {}_pB_y^2(L)}. \end{aligned} \tag{D.11}$$

In the equation above, ${}_pB_x(L)$ is a normally distributed random variable (see Section III-C) of the form $N\left(0, \sigma^2_{{}_pB_x}(L)\right)$, where

$$\sigma^2_{{}_pB_x}(L) = \frac{L^{2p+1}}{(p!)^2(2p+1)}. \tag{D.12}$$

The same distribution holds for ${}_pB_y(L)$. Owing to the independency of ${}_pB_x(L)$ and ${}_pB_y(L)$, the distance D_d in (D.11) follows the Rayleigh distribution with the

parameter (not variance) $\sigma^2_{D_d} = \sigma^2_x(1-k_b)^2\sigma^2_{pB_x}(L)$. Therefore, the probability

$$\mathrm{P}\left\{ D_d \leq \frac{c\,\sigma_x(1-k_b)}{p!}\sqrt{\frac{L^{2p+1}}{2p+1}} \right\} \tag{D.13}$$

is determined by the cumulative distribution function $F_{D_d}(d)$ of the distance D_d (see, e.g., [34, p. 168]). It follows,

$$\begin{aligned} F_{D_d} & \left(\frac{c\,\sigma_x(1-k_b)}{p!}\sqrt{\frac{L^{2p+1}}{2p+1}} \right) \\ &= \mathrm{P}\left\{ D_d \leq \frac{c\,\sigma_x(1-k_b)}{p!}\sqrt{\frac{L^{2p+1}}{2p+1}} \right\} \\ &= 1-\exp\left\{ -\frac{\frac{c^2\sigma_x^2(1-k_b)^2L^{2p+1}}{(p!)^2(2p+1)}}{2\sigma^2_{D_d}} \right\} \\ &= 1-e^{-\frac{c^2}{2}}. \end{aligned} \tag{D.14}$$

REFERENCES

[1] R. R. Roy, *Handbook of Mobile Ad Hoc Networks for Mobility Models*. Springer, 2011.

[2] M. Sánchez and P. Manzoni, "ANEJOS: a Java based simulator for ad hoc networks," *Future Generation Computer Systems*, vol. 17, no. 5, pp. 573 – 583, 2001.

[3] M. Kim, D. Kotz, and S. Kim, "Extracting a mobility model from real user traces," in *Proc. 25th IEEE International Conference on Computer Communications (INFOCOM'06)*, 2006, pp. 1–13.

[4] T. Henderson, D. Kotz, and I. Abyzov, "The changing usage of a mature campus-wide wireless network," in *Proc. The 10th Annual International Conference on Mobile Computing and Networking (MobiCom'04)*. Philadelphia, PA, USA, Feb. 2004, pp. 187–201.

[5] D. Kotz and K. Essien, "Analysis of a campus-wide wireless network," *Wireless Networks*, vol. 11, no. 1-2, pp. 115–133, Jan. 2005.

[6] A. Chaintreau, P. Hui, J. Crowcroft, C. Diot, R. Gass, and J. Scott, "Pocket switched networks: Real-world mobility and its consequences for opportunistic forwarding," in *University of Cambridge Computer Laboratory, Tech. Rep. UCAM-CL-TR-617, Feb.*, 2005.

[7] M. McNett and G. M. Voelker, "Access and mobility of wireless PDA users," in *Department of Computer Science and Engineering, University of California, San Diego, Tech. Rep. CS2004-0780, Feb.*, 2004.

[8] T. Camp, J. Boleng, and V. Davies, "A survey of mobility models for ad hoc network research," *Wireless Communications and Mobile Computing*, vol. 2, no. 5, pp. 483–502, Sep. 2002.

[9] F. Bai and A. Helmy, *A Survey of Mobility Modeling and Analysis in Wireless Adhoc Networks*. Book chapter in: Wireless Ad Hoc and Sensor Networks, Kluwer academic Publishers, 2004.

[10] F. Bai, N. Sadagopan, and A. Helmy, "The IMPORTANT framework for analyzing the impact of mobility on performance of routing protocols for adhoc networks," *Ad Hoc Networks*, vol. 1, no. 4, pp. 383 – 403, 2003.

[11] A. Einstein, "Über die von der molekularkinetischen Theorie der Wärme geforderte Bewegung von in ruhenden Flüssigkeiten suspendierten Teilchen," *Annalen der Physik*, no. 17, pp. 549–560, May 1905.

[12] K. Pearson, "The problem of the random walk," *Nature*, vol. 72, no. 1865, p. 294, 1905.

[13] D. B. Johnson and D. A. Maltz, *Dynamic Source Routing in Ad Hoc Wireless Networks*. The Kluwer International Series in Engineering and Computer Science, 1996, vol. 353.

[14] B. Liang and Z. J. Haas, "Predictive distance-based mobility management for PCS networks," in *Proc. 18th Annual Joint Conference of the IEEE Computer and Communications Societies (INFOCOM'99)*, vol. 3, 1999, pp. 1377–1384.

[15] V. A. Davis, "Evaluating mobility models within an ad hoc network," in *MS thesis, Colorado School of Mines*, 2000.

[16] J. Härri, F. Filali, and C. Bonnet, "Mobility models for vehicular ad hoc networks: a survey and taxonomy," *Communications Surveys Tutorials, IEEE*, vol. 11, no. 4, pp. 19–41, 2009.

[17] J.-Y. Le Boudec and M. Vojnovic, "Perfect simulation and stationarity of a class of mobility models," in *INFOCOM 2005. 24th Annual Joint Conference of the IEEE Computer and Communications Societies. Proceedings IEEE*, vol. 4, 2005, pp. 2743–2754 vol. 4.

[18] J.-M. Chung and D.-C. Go, "Stochastic vector mobility model for mobile and vehicular ad hoc network simulation," *Mobile Computing, IEEE Transactions on*, vol. 11, no. 10, pp. 1494–1507, 2012.

[19] A. Borhani and M. Pätzold, "Modelling of non-stationary mobile radio channels using two-dimensional Brownian motion processes," in *Proc. 6th International Conference on Advanced Technologies for Communications, ATC'13*. Ho Chi Minh City, Vietnam, Oct. 2013.

[20] ——, "Modelling of non-stationary mobile radio channels incorporating the Brownian mobility model with drift," in *Proc. World Congress on Engineering and Computer Science, WCECS13*. San Francisco, USA, Oct. 2013.

[21] E. Vanmarcke, *Random Fields*. Princeton Univ. Press, 2011.

[22] P. Pearle, B. Collett, K. Bart, D. Bilderback, D. Newman, and S. Samuels, "What Brown saw and you can too," *Am. J. Phys.*, vol. 78, no. 12, pp. 1278–1289, Dec. 2010.

[23] P. Langevin, "Sur la théorie du mouvement brownien," *C. R. Acad. Sci. Paris*, no. 146, pp. 530–533, 1908.

[24] D. S. Lemons and A. Gythiel, "On the theory of Brownian motion," *Am. J. Phys.*, vol. 65, no. 11, pp. 530–533, Nov. 1979.

[25] R. C. Earnshaw and E. M. Riley, *Brownian Motion: Theory, Modelling and Applications*. Nova Science Pub Inc, 2011.

[26] R. M. Mazd, *Brownian Motion: Fluctuations, Dynamics, and Applications*. Oxford Science Publication, 2009.

[27] S. Yousefi, J. Jaldén, and T. Eriksson, "Linear prediction of discrete-time $1/f$ processes," *IEEE Signal Proc. Lett.*, vol. 17, no. 11, pp. 901–904, Nov. 2010.

[28] G. Franceschetti, A. Iodice, M. Migliaccio, and D. Riccio, "Scattering from natural rough surfaces modeled by fractional Brownian motion two-dimensional processes," *IEEE Trans. Antennas Propag.*, vol. 47, pp. 1405–1415, 1999.

[29] B. H. Fleury and D. Dahlhaus, "Investigations on the time variations of the wide-band radio channel for random receiver movements," in *Proc. IEEE International Symposium on Spread Spectrum Techniques and Applications (ISSSTA '94)*, vol. 2. Finland, Oulu, pp. 631–636.

[30] P. Mörters and Y. Peres, *Brownian Motion*. Cambridge Series in Statistical and Probabilistic Mathematics, 2010.

[31] L. A. Shepp, "Radon-Nikodym derivatives of Gaussian measures," *The Annals of Mathematical Statistics*, vol. 37, no. 2, pp. 321–354, Dec. 1966.

[32] A. Kolmogorov, "Zufällige Bewegungen," *The Annals of Mathematical Statistics*, vol. 35, no. 2, pp. 116–117, Dec. 1934.

[33] B. X. Chen and W. V. Li, "Quadratic functionals and small ball probabilities for the m-fold integrated Brownian motion," *The Annals of Probability*, vol. 31, no. 2, pp. 1052–1077, 2003.

[34] A. Papoulis, *Probability, Random Variables, and Stochastic Processes*, 3rd ed. New York: McGraw-Hill, 1991.

Appendix E

Paper V

Title:	A Highly Flexible Trajectory Model Based on the Primitives of Brownian Fields—Part II: Analysis of the Statistical Properties
Authors:	**Alireza Borhani** and Matthias Pätzold
Affiliation:	University of Agder, Faculty of Engineering and Science, P. O. Box 509, NO-4898 Grimstad, Norway
Journal:	*IEEE Transactions on Wireless Communications*, under review.

A Highly Flexible Trajectory Model Based on the Primitives of Brownian Fields—Part II: Analysis of the Statistical Properties

Alireza Borhani and Matthias Pätzold

***Abstract* — In the first part of our paper, we have proposed a highly flexible trajectory model based on the primitives of Brownian fields (BFs). In this second part, we study the statistical properties of that trajectory model in depth. These properties include the autocorrelation function (ACF), mean, and the variance of the path along each axis. We also derive the distribution of the angle-of-motion (AOM) process, the incremental travelling length process, and the overall travelling length. It is shown that the path process is in general non-stationary. We show that the AOM and the incremental travelling length processes can be modelled by the phase and the envelope of a complex Gaussian process with nonidentical means and variances of the quadrature components. In accordance with empirical studies, we proof that the AOM process does not follow the uniform distribution. As special cases, we show that the incremental travelling length process follows the Rice and Nakagami-q distributions, whereas the overall travelling path can be modelled by a random variable following either the Gaussian or the lognormal distribution. The usefulness of the results is demonstrated and discussed extensively. It is shown that the results are in line with those of real-world user tracings. The results can be used in many areas of wireless communications.**

***Index Terms* — Trajectory model, mobility model, Brownian fields, autocorrelation function, angle-of-motion, travelling length.**

Manuscript received January 18, 2014; The review of this paper is coordinating by Dr. W. Wang.

A. Borhani and M. Pätzold are with the Faculty of Engineering and Science, University of Agder, 4898 Grimstad, Norway (e-mails: {alireza.borhani, matthias.paetzold}@uia.no).

I. INTRODUCTION

To evaluate the usefulness of mobility models for system-level analysis, the statistical properties of these models need to be studied thoroughly. Many spatial features of the models listed, e.g., in [1–3] are revealed by investigating their statistical characteristics. However, a gap in the related literature is that there exist very limited solid mathematical studies on the *spatial* properties of mobility models. These models have often been proposed in form of Java-based simulation models from which obtaining a sound understanding of the statistical characteristics is not an easy task. The path processes' mean, variance, ACF, AOM, and the travelling length are among the most important spatial characteristics that play important roles in the performance analysis of the overall system. These quantities can also be very useful for the parametrization of the mobility model itself.

The random walk [4, 5], random waypoint [6], Gauss-Markov [7], city section [8], and the pursue [9] mobility models are only to name some few of the mobility models for which their spatial (statistical) characteristics have not been perused. Despite the spatial properties of these models, the temporal properties of these models have often been studied in the literature (see, e.g., [10] and [11]). The expected epoch time and the number of states visited at a fixed time are two important temporal properties of a mobility model that have often been investigated [10].

In this second part of our paper, we focus on the statistical properties of the trajectory model that has been introduced in the first part. We recall that the proposed path model belongs to the class of spatial trajectory models that are based on the primitives of BFs. The random components of the path model are derived from Gaussian processes, which are defined in position rather than time. Herein, we derive the spatial mean and variance of the stochastic trajectory model. We also provide a closed-form expression for the ACF of the path process. Moreover, we introduce a complex spatial increment process, from which the AOM and the incremental travelling length processes are derived. The first-order density of these processes is presented in closed form. By summing up the incremental travelling lengths, we compute the overall travelling length and its probability density function (PDF). The results are illustrated and discussed in detail.

We proof that the path process is in general non-stationary. Furthermore, it is shown that the AOM and the incremental travelling length processes are modelled by the phase and the envelope of a complex Gaussian process with nonidentical means and variances of the quadrature components. We show that the AOM and the incremental travelling length are in general non-stationary processes. In this connection, we demonstrate that the AOM process does not follow the uniform dis-

tribution, which agrees with empirical traces reported in [12]. However, the uniform AOM can be obtained as a special case. In addition, we proof that the incremental travelling length process follows the Rice and Nakagami-q distributions as special cases. For the path based on the primitives of the standard BFs, we show that the overall travelling length follows closely the lognormal distribution, which is in line with many real-life tracing records [12–15]. For the path based on the standard BF, we proof that the overall travelling length follows the Gaussian distribution, which has been reported from studies in dense urban environments [16–22].

The statistical properties provided in this second paper are very useful in many areas of science, such as wireless communications and vehicular technologies. The results of this paper can be used by researchers dealing with ad hoc networks, localization (positioning), network mobility protocols, and mobile radio channel modelling under non-stationary conditions[1].

The remainder of this paper is organized as follows. Section II recalls the principles of the trajectory model proposed in the first part of our paper. The statistical properties of the model are investigated in Section III. Section IV studies the spatial characteristics of the proposed model. To provide a sound understanding of the results, two important special cases of the path model are discussed in Section V. The numerical results are presented in Section VI. Eventually, the conclusion is presented in Section VII.

II. A BRIEF REVIEW OF THE TRAJECTORY MODEL

With reference to the first part of out paper, we model a path starting from (x_s, y_s) and terminating at or in the proximity of a given destination point (x_d, y_d) by the trajectory ${}_p\mathscr{T}$ designed by the following pair

$$ {}_p\mathscr{T} : \left\{ ({}_px(l), {}_py(l)) \;\middle|\; \begin{array}{l} {}_px(l) = x_s + k_d\, l\delta_x + \sigma_x\, {}_pW_x(l,k_b) \\ {}_py(l) = y_s + k_d\, l\delta_y + \sigma_y\, {}_pW_y(l,k_b) \end{array} \right\} \tag{E.1} $$

For a positive integer L, the terms $\delta_x = (x_d - x_s)/L$ and $\delta_y = (y_d - y_s)/L$ denote the deterministic increments along each axis. The drift parameter k_d acts as a switch to control the presence of such a deterministic drift that forces the path to evolve towards the destination point (x_d, y_d) (see Section IV-C of Part I). The parameter σ_x (σ_y) is to control the randomness of the path ${}_px(l)$ (${}_py(l)$) along the x-axis (y-axis)[2]

[1] For the application in channel modelling, see [23] and [24].

[2] Due to the symmetry of the trajectory model, the statistical properties of ${}_px(l)$ and ${}_py(l)$ are the same. Therefore, and for fluency reasons, we henceforth avoid repeating the analogy between the essential properties of the path along the x- and y-axis.

(see Section IV-A of Part I). Furthermore, the objective of the partial random bridge, defined as

$$ {}_pW_x(l,k_b) = {}_pB_x(l) - \frac{k_b\, l}{L}\, {}_pB_x(L) \tag{E.2} $$

is to model the randomness of the path along each axis by means of the pth primitive ${}_pB_x(l)$ of the standard BF $B_x(l)$ associated with the x-axis. The parameter k_b is called the bridge parameter, which determines the integration degree of the bridge to the destination point (see Section IV-B of Part I). In addition, the primitive p determines the smoothness level of the path. We remind that the level of smoothness increases by increasing p (see Section IV-D of Part I).

The trajectory ${}_p\mathscr{T}$ in (E.1) has been designed in such a way that allows 1) arriving at a predefined destination point (x_d, y_d) if the bridge is fully established, i.e., $k_b = 1$, 2) arriving at a target zone with a predefined radius and centre (see Theorem 1 and Corollary 1 of Part I) if the bridge is partially established, i.e., $0 < k_b < 1$, 3) a totally random point in the two-dimensional (2D) plane if the bridge is broken, i.e., $k_b = 0$, and finally 4) bridging back (closed loop) to the starting point (x_s, y_s) if the bridge is fully established, i.e., $k_b = 1$, but the drift component does not exist, i.e., $k_d = 0$. The entire configurations above plus several others have been shown and extensively discussed in Part I of our paper.

III. STATISTICAL PROPERTIES OF THE PROCESS ${}_px(l)$ (${}_py(l)$)

In this section, we investigate the statistical properties of the process ${}_px(l)$ ($l = 1, 2, ..., L$). We first derive the first-order density of ${}_px(l)$ and then study the corresponding mean, ACF, and variance. Owing to the statistical equivalence of the path ${}_p\mathscr{T}$ along the x- and y-axis (see (E.1)), the statistical characteristics of the process ${}_py(l)$ can be obtained from those of ${}_px(l)$ by replacing x by y in the respective equations.

A. First-Order Density of ${}_px(l)$

The process ${}_px(l)$ in (E.1) is a shifted version of the bridge process ${}_pW_x(l,k_b)$, which is consist of the pth primitive of the standard BF $B_x(l)$, given by

$$ {}_pB_x(l) = \int_0^l {}_{p-1}B_x(l')\, dl' \quad \forall p = 1, 2, \ldots . \tag{E.3} $$

With reference to Part I of the series of two papers, the process ${}_pB_x(l)$ in (E.3) is a Gaussian process of the form $N(0,\sigma^2_{pB}(l))$, where

$$\sigma^2_{{}_pB_x}(l) = \frac{l^{2p+1}}{(p!)^2(2p+1)}. \tag{E.4}$$

Referring to (E.2), the bridge process ${}_pW_x(l,k_b)$ is a linear combination of two Gaussian processes. This allows us to conclude that the first-order density of ${}_px(l)$ in (E.1) is a normal distribution of the form $N(m_{px}(l),\sigma^2_{px}(l))$, where the mean $m_{px}(l)$ and the variance $\sigma^2_{px}(l)$ are derived in Sections III-B and III-D, respectively.

It is also worth mentioning that the autocovariance function $r^c_{{}_pB_x\,{}_pB_x}(l_i,l_j)$ of ${}_pB_x(l)$ is given by the following expression

$$r^c_{{}_pB_x\,{}_pB_x}(l_i,l_j) = \frac{1}{(p!)^2}\int_0^{\min(l_i,l_j)} (l_i-l')^p(l_j-l')^p\,dl'. \tag{E.5}$$

The variance $\sigma^2_{{}_pB_x}(l)$ and the autocovariance function $r^c_{{}_pB_pB}(l_i,l_j)$ of ${}_pB_x(l)$ play key roles in the analysis of the statistical properties of the trajectory ${}_p\mathscr{T}$ in (E.1).

B. Mean of ${}_px(l)$

The mean $m_{px}(l)$ of the process ${}_px(l)$ in (E.1) can be computed as follows

$$\begin{aligned} m_{px}(l) &= E\left\{x_s + k_d l\delta_x + \sigma_x\,{}_pW_x(l,k_b)\right\} \\ &= x_s + k_d l\delta_x + \sigma_x E\left\{{}_pB_x(l) - \frac{k_b l}{L}\,{}_pB_x(L)\right\} \\ &= x_s + k_d l\delta_x + \sigma_x E\left\{{}_pB_x(l)\right\} - \frac{k_b l}{L}E\left\{{}_pB_x(L)\right\} \\ &= x_s + k_d l\delta_x \end{aligned} \tag{E.6}$$

where we have used $E\{{}_pB_x(l)\}=0$ for $l=0,1,\ldots,L$. For $k_d=1$ and $\delta_x>0$, the mean $m_{px}(l)$ in (E.6) increases linearly with the position index l, which means that the process ${}_px(l)$ is neither strict-sense stationary nor wide-sense stationary. This can be attributed to the drift of the path, which establishes the dependency of the mean $m_{px}(l)$ upon the position index l. If the drift does not exist, i.e., $k_d=0$, then the mean $m_{px}(l)$ equals the starting length x_s.

C. Autocorrelation Function of ${}_px(l)$

The expectation $E\left\{{}_px(l_i)\,{}_px(l_j)\right\}$ equals the ACF $r_{{}_px{}_px}(l_i,l_j)$ of the process ${}_px(l)$ at the position indices l_i and l_j. It can be shown (see Appendix A) that

$$\begin{aligned} r_{{}_px{}_px}(l_i,l_j) &= m_{{}_px}(l_i)m_{{}_px}(l_j)+\sigma_x^2\left(r^c_{{}_pB_x{}_pB_x}(l_i,l_j)\right. \\ &- \frac{k_b l_j}{L}r^c_{{}_pB_x{}_pB_x}(l_i,L)-\frac{k_b l_i}{L}r^c_{{}_pB_x{}_pB_x}(L,l_j) \\ &+ \left.\frac{k_b^2 l_i l_j}{L^2}r^c_{{}_pB_x{}_pB_x}(L,L)\right) \end{aligned} \tag{E.7}$$

where the autocovariance function $r^c_{{}_pB_x{}_pB_x}(l_i,l_j)$ is given by[3] (E.5), in which we replace the superscript ${}_pB$ by ${}_pB_x$. The ACF $r_{{}_px{}_px}(l_i,l_j)$ in (E.7) cannot be written as a function of the difference $l_d=l_i-l_j$, which confirms that ${}_px(l)$ is not wide-sense stationary.

An important special case occurs if we set one of the arguments of the ACF in (E.7) to 0. In this case, (E.7) reduces to the following expression

$$\begin{aligned} r_{{}_px{}_px}(0,l_j) &= m_{{}_px}(0)m_{{}_px}(l_j)+\sigma_x^2\left(r^c_{{}_pB_x{}_pB_x}(0,l_j)-\frac{k_b l_j}{L}r^c_{{}_pB_x{}_pB_x}(0,L)\right) \\ &= m_{{}_px}(0)m_{{}_px}(l_j) \\ &= x_s(x_s+k_d l_j\delta_x) \end{aligned} \tag{E.8}$$

where we have used $r^c_{{}_pB_x{}_pB_x}(0,l_j)=r^c_{{}_pB_x{}_pB_x}(0,L)=0$. The recent reduction originates from the fact that $\min(0,l_j)=0$ in (E.5) forces $r^c_{{}_pB_x{}_pB_x}(0,l_j)$ to 0. With the same token, it can be shown that $r_{{}_py{}_py}(0,l_j)=m_{{}_py}(0)m_{{}_py}(l_j)$, from which it can be concluded that the correlation between the starting point and any heading point is determined by the product of the corresponding mean values. If one of the mean values is zero, no correlation exists. It can also be shown that if the bridge is fully established, i.e., $k_b=1$, then $r_{{}_px{}_px}(L,l_j)=r_{{}_px{}_px}(l_j,L)=m_{{}_px}(L)m_{{}_px}(l_j)$. In this case, the correlation between the terminating point and its posterior points is also determined by the product of the corresponding mean values.

D. Variance of ${}_px(l)$

[3]To cope with the discreteness of the position index l, one may simply use the equivalent Riemann sum of the integral in (E.5).

The variance $\sigma^2_{px}(l)$ of the process ${}_px(l)$ is computed as follows

$$\begin{aligned}\sigma^2_{px}(l) &= r_{px_px}(l,l) - m^2_{px}(l) \\ &= \sigma^2_x \left(r^c_{pB_{xp}B_x}(l,l) - 2\frac{k_b l}{L} r^c_{pB_{xp}B_x}(l,L) + \frac{k_b^2 l^2}{L^2} r^c_{pB_{xp}B_x}(L,L) \right). \quad \text{(E.9)}\end{aligned}$$

It can be shown that the variance $\sigma^2_{px}(l)$ of the process ${}_px(l)$ in (E.9) is a monotonically increasing function in p. This is intuitively due to the fact that the integration over the standard BF increases the correlation between the random components. Furthermore, it can be verified that $\lim_{l\to 0}\sigma^2_{px}(l) = 0$. Analogously, one can write $\lim_{l\to 0}\sigma^2_{py}(l) = 0$. The two recent limits state that the randomness of the points near the starting point $({}_px(0), {}_py(0))$ (or equivalently (x_s, y_s)) tends to zero. The randomness of the terminating point $({}_px(L), {}_py(L))$ and the points in its close vicinity, however, do not vanish, as the limit

$$\begin{aligned}\lim_{l\to L}\sigma^2_{px}(l) &= \sigma^2_x(1-k_b)^2 r^c_{pB_{xp}B_x}(L,L) \\ &= \sigma^2_x(1-k_b)^2\sigma^2_{pB_x}(L) \quad \text{(E.10)}\end{aligned}$$

is in general not equal to 0. If $k_b \to 1$, then $\lim_{l\to L}\sigma^2_{px}(l) = 0$. It is also worth mentioning that the result in (E.10) is equal to the parameter $\sigma^2_{D_d}$ of the Rayleigh distributed distance D_d between the terminating point $({}_px(L), {}_py(L))$ and the destination point (x_d, y_d), which opens an alternative way to proof Theorem 1 of Part I. We also remark that the variance $\sigma^2_{px}(l)$ of the process ${}_px(l)$ is very useful for adjusting the standard deviation σ_x as one of the important model parameters (see Section V-B of Part I).

IV. SPATIAL CHARACTERISTICS OF THE TRAJECTORY ${}_p\mathscr{T}$

This section deals with the spatial processes, which consist of the elements ${}_px(l)$ and ${}_py(l)$ of the trajectory ${}_p\mathscr{T}$ along the x- and y-axis.

A. Spatial Increment Process

Let the complex process ${}_ps(l) = {}_ps_x(l) + j\,{}_ps_y(l)$ $(l = 1,2,\ldots,L)$ define the spatial increment process of the trajectory ${}_p\mathscr{T}$, where ${}_ps_x(l) = {}_px(l) - {}_px(l-1)$ and ${}_ps_y(l) = {}_py(l) - {}_py(l-1)$ are the increments along the x- and y-axis, respectively.

Theorem 1. The spatial increment ${}_ps(l)$ follows the complex Gaussian distribution of the form $CN\left(m_{ps}, C_{ps}\right)$, where $m_{ps} = [k_d\delta_x,\ k_d\delta_y]^T$,

$$C_{ps} = \begin{pmatrix} \sigma^2_{ps_x}(l) & 0 \\ 0 & \sigma^2_{ps_y}(l) \end{pmatrix} \tag{E.11}$$

$$\begin{aligned} \sigma^2_{ps_x}(l) = \sigma^2_x \Big(& r^c_{pB_{xp}B_x}(l,l) + r^c_{pB_{xp}B_x}(l-1,l-1) \\ & + \frac{k_b^2}{L^2} r^c_{pB_{xp}B_x}(L,L) - 2r^c_{pB_{xp}B_x}(l,l-1) \\ & - \frac{2k_b}{L} r^c_{pB_{xp}B_x}(l,L) + \frac{2k_b}{L} r^c_{pB_{xp}B_x}(l-1,L) \Big) \end{aligned} \tag{E.12}$$

and $\sigma^2_{ps_y}(l)$ can be obtained from (E.12) by replacing the superscript x by y.

Proof: See Appendix B. ■

From Theorem 1, it can be concluded that the spatial increment process ${}_ps(l)$ is not strict-sense stationary, as its first-order density $CN\left(m_{ps}, C_{ps}\right)$ varies in l. The spatial increment process ${}_ps(l)$ is very useful for deriving the AOM process and the incremental travelling length process of the path ${}_p\mathscr{T}$, as will be shown in the next two subsections.

B. AOM Process

The AOM ${}_p\alpha^v(l)$ process, defined as

$$\begin{aligned} {}_p\alpha^v(l) &= \arctan\left(\frac{{}_py(l) - {}_py(l-1)}{{}_px(l) - {}_px(l-1)}\right) \\ &= \arctan\left(\frac{{}_ps_y(l)}{{}_ps_x(l)}\right) \end{aligned} \tag{E.13}$$

can be considered as the phase of the spatial increment process ${}_ps(l)$.

Corollary 1. The first-order density $p_{{}_p\alpha^v}(\alpha^v; l)$ of the AOM process ${}_p\alpha^v(l)$ in (E.13) is given by the following expression

$$\begin{aligned} p_{{}_p\alpha^v}(\alpha^v; l) &= \frac{1}{4\pi g_1(\alpha^v; l)\sigma_{ps_x}(l)\sigma_{ps_y}(l)} \\ &\times \exp\left\{-\frac{1}{2}\left(\frac{k_d^2\delta_x^2}{\sigma^2_{ps_x}(l)} + \frac{k_d^2\delta_y^2}{\sigma^2_{ps_y}(l)}\right)\right\} \\ &\times \left(1 + \frac{\sqrt{\pi} g_2(\alpha^v; l)}{2\sqrt{g_1(\alpha^v; l)}} \operatorname{erfc}\left(\frac{-g_2(\alpha^v; l)}{2\sqrt{g_1(\alpha^v; l)}}\right)\right. \end{aligned}$$

$$\times \quad \exp\left\{\frac{g_2^2(\alpha^v;l)}{4g_1(\alpha^v;l)}\right\}\Bigg) \tag{E.14}$$

where

$$g_1(\alpha^v;l) = \frac{1}{2}\left(\frac{\cos^2(\alpha^v)}{\sigma^2_{{}_ps_x}(l)} + \frac{\sin^2(\alpha^v)}{\sigma^2_{{}_ps_y}(l)}\right) \tag{E.15}$$

$$g_2(\alpha^v;l) = k_d\left(\frac{\delta_x\cos(\alpha^v)}{\sigma^2_{{}_ps_x}(l)} + \frac{\delta_y\sin(\alpha^v)}{\sigma^2_{{}_ps_x}(l)}\right) \tag{E.16}$$

and $\mathrm{erfc}(\cdot)$ stands for the complementary error function [25, p. 887].

Proof: With reference to Theorem 1, the spatial increment ${}_ps(l)$ follows the complex Gaussian distribution of the form $CN\left(m_{ps}, C_{ps}\right)$. The phase and the envelope of complex Gaussian processes with correlated quadratures and non-identical means (variances) have been studied in [26] and [27]. Herein, the correlation ρ between the inphase and quadrature components of the spatial increment process ${}_ps(l)$ is zero, i.e., $\rho = C_{12} = C_{21} = 0$. Starting from the phase distribution of a complex Gaussian distribution with uncorrelated quadratures in [27, Eq. (2)], setting $\rho = 0$, and performing some straightforward mathematical manipulations results in (E.14). ■

In accordance with the spatial increment process ${}_ps(l)$, the AOM process ${}_p\alpha^v(l)$ in (E.13) is not first-order stationary, as its first-order density $p_{{}_p\alpha^v}(\alpha^v;l)$ in (E.14) depends on position index l. The special case of $p = 0$, however, results in a stationary AOM process ${}_p\alpha^v(l)$. In this case, it is straightforward to show by means of (E.5) that the variance $\sigma^2_{{}_ps_x}(l)$ in (E.12) reduces to

$$\sigma^2_{{}_0s_x} = \sigma_x^2\left(1 + \frac{k_b^2}{L} - 2\frac{k_b}{L}\right) \tag{E.17}$$

which does not change in l, stopping the variations of $p_{{}_p\alpha^v}(\alpha^v;l)$ in l as well (see (E.14)–(E.16)). Another stationary case occurs if we decrease the variances σ_x^2 and σ_y^2 towards zero. In this case, $p_{{}_p\alpha_l^v}(\alpha^v;l)$ in (E.14) tends to the delta function located at $\alpha^v = \arctan(\delta_y/\delta_x)$, which is independent of l. Notice that $\arctan(\delta_y/\delta_x)$ indicates the general drift of the path ${}_p\mathscr{T}$ in (E.1).

An important property of the AOM ${}_p\alpha^v(l)$ of the proposed trajectory model is that ${}_p\alpha^v(l)$ is in general not uniformly distributed. This is in agreement with the results obtained from real-world tracings [12]. Nonetheless, under special conditions, the first-order density $p_{{}_p\alpha^v}(\alpha^v;l)$ in (E.14) can be simplified to a constant value,

indicating that the AOM ${}_p\alpha^v(l)$ is uniformly distributed. Notice that the uniform distribution of the AOM is one of the widely made assumptions in the synthetic mobility models proposed in the literature, which is, however, not necessarily true.

C. Incremental Travelling Length Process

The incremental travelling length process ${}_pd(l)$ is defined by the following expression

$$\begin{aligned} {}_pd(l) &= \sqrt{\left({}_px(l)-{}_px(l-1)\right)^2+\left({}_py(l)-{}_py(l-1)\right)^2} \\ &= \sqrt{{}_ps_x^2(l)+{}_ps_y^2(l)} \end{aligned} \tag{E.18}$$

which is the envelope of the spatial increment process ${}_ps(l)$.

Corollary 2. The first-order density $p_{{}_pd}(d;l)$ of the incremental travelling length process ${}_pd(l)$ equals

$$\begin{aligned} p_{{}_pd}(d;l) &= \frac{d}{\sigma_{{}_ps_x}(l)\sigma_{{}_ps_y}(l)}\exp\left\{-\frac{\sigma^2_{{}_ps_x}(l)+\sigma^2_{{}_ps_y}(l)}{4\sigma^2_{{}_ps_x}(l)\sigma^2_{{}_ps_y}(l)}d^2\right. \\ &- \left.\frac{k_d^2\left(\delta_x^2\sigma^2_{{}_ps_y}(l)+\delta_y^2\sigma^2_{{}_ps_x}(l)\right)}{2\sigma^2_{{}_ps_x}(l)\sigma^2_{{}_ps_y}(l)}\right\} \\ &\times \sum_{n=0}^{\infty}\varepsilon_n\cos\left(ng_3(l)\right)I_n\left(\frac{\sigma^2_{{}_ps_x}(l)-\sigma^2_{{}_ps_y}(l)}{4\sigma^2_{{}_ps_x}(l)\sigma^2_{{}_ps_y}(l)}d^2\right) \\ &\times I_{2n}\left(\frac{k_d\sqrt{\delta_x^2\sigma^4_{{}_ps_y}(l)+\delta_y^2\sigma^4_{{}_ps_x}(l)}}{\sigma^2_{{}_ps_x}(l)\sigma^2_{{}_ps_y}(l)}d\right) \end{aligned} \tag{E.19}$$

where

$$g_3(l)=2\arccos\left(\frac{\delta_x\sigma^2_{{}_ps_y}(l)}{\sqrt{\delta_x^2\sigma^4_{{}_ps_y}(l)+\delta_y^2\sigma^4_{{}_ps_x}(l)}}\right) \tag{E.20}$$

and $I_n(\cdot)$ denotes the nth order modified Bessel function of the first kind [25, p. 629]. The parameter ε_n stands for the Neumann factor [28], which equals 1 for $n=0$, and 2 for $n=1,2,....$

Proof: Following the discussion provided in the proof of Corollary 3, setting $\rho=0$ in the envelope distribution in [27, Eq. (1)], and applying simple mathematical manipulations give the PDF in (E.19). ■

It has been shown in [27] that the infinite series in (E.19) is convergent. It is also not difficult to verify that $\forall p, \lim_{d\to\infty} p_{_pd(l)}(d;l) \to 0$. This means that the probability of *jumping far* from $({}_px(l-1), {}_py(l-1))$ to $({}_px(l), {}_py(l))$ tends to zero for all $p = 0, 1, ...$, which is a prerequisite for a realistic path model. An important property of the PDF $p_{_pd}(d;l)$ in (E.19) is its dependency on l, which allows us to conclude that the incremental travelling length process ${}_pd(l)$ in (E.18) is in general non-stationary in the strict sense. Analogously to the discussion in Section IV-B, this dependency can be relaxed by setting $p = 0$. In this case, $\sigma^2_{_{pS_x}}(l)$ is given by (E.17), which makes $p_{_pd}(d;l)$ in (E.19) independent of l.

Another important special case is attained if $\sigma_x = \sigma_y = \sigma_0$ and $\delta_x = \delta_y = \delta_0$. In this case, the PDF $p_{_pd}(d;l)$ in (E.19) reduces to the Rice distribution of the following form

$$p_{_pd}(d;l) \;=\; \frac{d}{\sigma^2_{_{pS_x}}(l)} \exp\left\{-\frac{2k_d^2\delta_0^2 + d^2}{2\sigma^2_{_{pS_x}}(l)}\right\} I_0\left(\frac{k_d\delta_0\sqrt{2}}{\sigma^2_{_{pS_x}}(l)}d\right). \tag{E.21}$$

It is worth mentioning that the Rice distribution above is not a function of l if $p = 0$. Given this special case, the mean $m_{_0d}$ and the variance $\sigma^2_{_0d}$ of the Rician distributed incremental travelling length ${}_0d(l)$ is obtained by (see, e.g., [29, p. 28])

$$m_{_0d} = \sigma^2_{_{0S_x}} \sqrt{\frac{\pi}{2}}\, {}_1F_1\left(-\frac{1}{2}; 1; -\frac{k_d^2\delta_0^2}{\sigma^2_{_{0S_x}}}\right) \tag{E.22}$$

and

$$\sigma^2_{_0d} = 2\sigma^2_{_{0S_x}} + 2k_d^2\delta_0^2 - m^2_{_0d} \tag{E.23}$$

respectively, where the function ${}_pF_q(a_1, ..., a_p; b_1, ..., b_q; x)$ stands for the generalized hypergeometric function [25, p. 1010].

If the drift component does not exist, i.e., $k_d = 0$, the PDF $p_{_pd}(d;l)$ in (E.19) is simplified to the Nakagami-q distribution of the form

$$\begin{aligned} p_{_pd}(d;l) \;=\; & \frac{d}{\sigma_{_{pS_x}}(l)\sigma_{_{pS_y}}(l)} \exp\left\{-\frac{\sigma^2_{_{pS_x}}(l) + \sigma^2_{_{pS_y}}(l)}{4\sigma^2_{_{pS_x}}(l)\sigma^2_{_{pS_y}}(l)} d^2\right\} \\ \times \;\; & I_0\left(\frac{\sigma^2_{_{pS_x}}(l) - \sigma^2_{_{pS_y}}(l)}{4\sigma^2_{_{pS_x}}(l)\sigma^2_{_{pS_y}}(l)}\, d^2\right) \end{aligned} \tag{E.24}$$

which has been reported, e.g., in [29–31].

D. Overall Travelling Length

The overall travelling length ${}_pD$ can be obtained by the sum of all incremental lengths ${}_pd(l)$, i.e., ${}_pD = \sum_{l=1}^{L} {}_pd(l)$. Even if $L \to \infty$, none of the central limit theorems (CLT) of Lindeberg-Lévy and Lyapunov can be applied, as the incremental lengths ${}_pd(l)$ are neither identically distributed, nor independently. The correlation between the components is also not low enough to be neglected. However, the case $p = 0$ results in identically distributed incremental lengths ${}_0d(l)$ (see Section IV-C). For such a special case, the CLT for correlated random variables [32] can be invoked. To provide a closed-form solution for the overall travelling length ${}_pD$, we focus on the special case discussed in Section IV-C, where the first-order density $p_{0d}(d;l) = p_{0d}(d)$ follows the Rice distribution. Consequently, the CLT for correlated random variables permits us to conclude that the travelling length ${}_0D$ is a normally distributed random variable of the form $N\left(Lm_{0d}, L\sigma_{0d}^2\right)$, where the mean m_{0d} and the variance σ_{0d}^2 are given by (E.22) and (E.23), respectively. This distribution can often be seen in dense and crowded areas, such as shopping centres and airports [16–22][4]. In Section VI, the simulation results show that for $p \geq 1$, the travelling length ${}_pD$ follows closely the log-normal distribution, which has been widely addressed in the literature [12–15].

V. SPECIAL CASES

As discussed in the first part of our paper, the primitive $p = 0$ allows erratic paths with sudden changes of direction. However, the higher primitives $p > 0$ result in relatively smooth paths. The level of smoothness increases by increasing p. From these two major categories, we choose $p = 0$ and $p = 1$ to further simplify some of the statistical properties of the process ${}_px(l)$. We also assume the full bridge scenario, i.e., $k_b = 1$, in the presence of a drift component, i.e., $k_d = 1$. This allows us to get a better understanding of the behaviour of ${}_px(l)$.

A. The Zeroth Primitive $p = 0$

The mean $m_{0x}(l)$ in (E.6) is independent of p and remains equal to $x_s + l\delta_x$. The autocovariance function $r^c_{{}_0B_{x0}B_x}(l_i, l_j)$ in (E.5) of the standard BF simplifies to $\min(l_i, l_j)$, which complies with the result, e.g., in [33]. Subsequently, the ACF

[4]Notice that most of the related empirical studies concern the speed distribution of mobile users, but not their travelling length. Nevertheless, the time-distance transformation allows us to extend their obtained distribution to that of the travelling length.

$r_{0x_0x}(l_i,l_j)$ in (E.7) reduces to

$$r_{0x_0x}(l_i,l_j) \;=\; m_{0x}(l_i)m_{0x}(l_j)+\sigma_x^2\left(\min(l_i,l_j)-\frac{l_il_j}{L}\right). \tag{E.25}$$

By setting $l_i=l_j=l$ and subtracting the means' product, one can obtain the variance $\sigma^2_{0x}(l)$ of the process ${}_0x(l)$ by means of the following equation

$$\sigma^2_{0x}(l)=\sigma_x^2 l\left(1-\frac{l}{L}\right). \tag{E.26}$$

The function above has a concave shape with a peak at[5] $l=L/2$ and two zeros at $l=0$ and $l=L$. The value $\sigma^2_{0x\max}$ of the peak then becomes $\sigma^2_{0x\max}=\sigma^2_{0x}(L/2)=\sigma_x^2L/4$. Furthermore, the spatial increment ${}_0s_x(l)$ follows the Gaussian distribution of the form $N(\delta_x,\sigma^2_{0s_x}(l))$, where

$$\sigma^2_{0s_x}(l)=\sigma_x^2\left(1-\frac{1}{L}\right) \tag{E.27}$$

is the simplified version of (E.12) after setting $p=0$ and $k_b=1$. The variance $\sigma^2_{0s_x}(l)$ in (E.27) can also be considered as the special case, $k_b=1$, of its more general form in (E.17).

B. The First Primitive $p=1$

In this case, the path can be attained by substituting the outcomes of the integrated (once) BF in (E.1). The mean $m_{1x}(l)$ remains equal to $x_s+l\delta_x$. The auto-covariance function $r^c_{1B_{x1}B_x}(l_i,l_j)$ in (E.5) of the integrated BF reduces to

$$r^c_{1B_{x1}B_x}(l_i,l_j)\;=\;l_il_j\min(l_i,l_j)-\frac{l_i+l_j}{2}(\min(l_i,l_j))^2+\frac{1}{3}(\min(l_i,l_j))^3. \tag{E.28}$$

For the special case of $l_i=l_j$, the auto-covariance function above becomes $l^3/3$, which agrees with the variance $\sigma^2_{1B}(l)$ in (E.4) and that of reported, e.g., in [33]. The simplification of the variance $\sigma^2_{1x}(l)$ in (E.9) to

$$\sigma^2_{1x}(l)=\sigma_x^2\frac{l^2L}{3}\left(1-\frac{l}{L}\right)^2 \tag{E.29}$$

is also very helpful to confirm its concave shape in l. The peak of the curve is again at $l=L/2$, whereas the zeros are located at $l=0$ and $l=L$. The value $\sigma^2_{1x\max}$ of

[5]The nearest natural number to $L/2$ is acceptable as the position index l of the peak.

the peak equals $\sigma^2_{1x\max} = \sigma^2_{1x}(L/2) = \sigma^2_x L^3/48$. Notice that for a given value of σ^2_x and for large values of $L \gg 1$, the maximum variance $\sigma^2_{1x\max}$ of the process ${}_1x(l)$ is significantly greater than that of ${}_0x(l)$, i.e., $\sigma^2_{0x\max}$ (see Section V-A). It is worth mentioning that for higher values of p, the peak is not at $L/2$ anymore. For $p \geq 2$, the position of the peak has a mild tendency to the terminating position variable, i.e., $l = L$. Furthermore, despite the apparent similarity between $\sigma^2_{1x}(l)$ in (E.29) and $\sigma^2_{0x}(l)$ in (E.26), a general extension to higher values of p cannot be found. For instance, the variance $\sigma^2_{2x}(l)$ associated with the primitive $p = 2$ becomes

$$\sigma^2_{2x}(l) = \sigma^2_x \frac{l^2 L}{60}\left(1 - \frac{l}{L}\right)^2 (-l^2 + 6Ll + 3L^2) \tag{E.30}$$

which has less similarity to (E.26) and (E.29). Nevertheless, the zeros of $\sigma^2_{2x}(l)$ in (E.30) are still at $l = 0$ and $l = L/2$, while its maximum occurs at the nearest natural number to $0.55L$.

VI. NUMERICAL RESULTS

Herein, we illustrate the statistical properties of the reference (path) model. We have also obtained these properties by means of simulation results. This means that we have generated a large enough number of realizations of the path by following the procedure described in Section V-A of Part I. Then, we have derived the statistical properties of the simulation model. An excellent match between the analytical and simulation results have been observed. Due to the similarity of the statistical properties of the reference model and the simulation model, we, nevertheless, omit to show those of the simulation model herein. In accordance with the simulation results presented in Part I of our paper, the starting point (x_s, y_s) is set to the origin of the Cartesian coordinate system, i.e., $(0\,\mathrm{m}, 0\,\mathrm{m})$, whereas the destination point (x_d, y_d), if any, is set to $(50\,\mathrm{m}, 50\,\mathrm{m})$. The number of points L is 100. The maximum standard deviation $\sigma_{px\max}$ along the x-axis is supposed to be equal to the one along the y-axis, i.e, $\sigma_{px\max} = \sigma_{py\max} = \sigma_{\max}$. The only exception is where we plot the ACF $r_{px_px}(l_i, l_j)$ of the path ${}_0\mathscr{T}$, which will be discussed later. Owing to space restrictions, we focus only on a special case in which the bridge to the destination point is fully established, i.e., $k_b = 1$, and the drift component is available, i.e., $k_d = 1$. The values of the primitive p is displayed in the figures and/or their captions.

Figs. E.1–E.3 depict the ACF $r_{px_px}(l_i, l_j)$ of ${}_px(l)$ in (E.7) for different values of the primitive p. To show the effect of the primitive p on $r_{px_px}(l_i, l_j)$, we have used the same standard deviation $\sigma_x = \sigma_y = 2\,\mathrm{m}$ to plot the three figures. This results

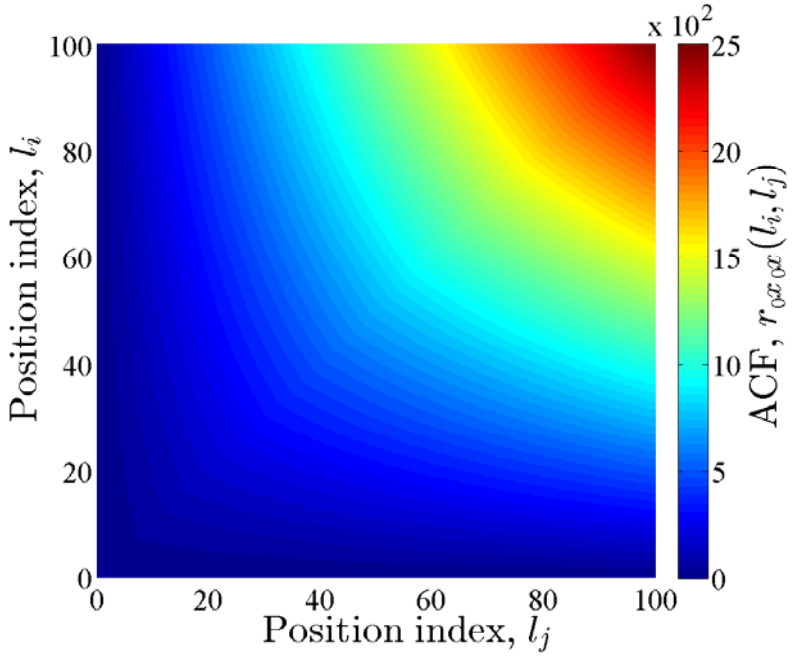

Figure E.1: The ACF $r_{0x_0x}(l_i, l_j)$ in (E.7). The model parameters are $k_d = 1$, $k_b = 1$, and $\sigma_x = \sigma_y = 2$ m.

in completely different maximum standard deviations $\sigma_{px\max}$ of the process ${}_px(l)$ (see Section V-B). The first common observation in the three figures is that the ACF $r_{px_px}(l_i, l_j)$ varies in position index l, which indicates that the process ${}_px(l)$ is non-stationary. The second one is that p, $r_{px_px}(l_i, 0) = r_{px_px}(0, l_j) = 0$, which agrees with the discussion provided in Section III-C. The third observation is that the three figures are symmetric with respect to the line represented by $l_i = l_j$. Fig. E.1 shows that the maximum correlation occurs at $l_i = l_j = L$, i.e., at the terminating point. This can be attributed to the fact that most of the contribution to the correlation between the samples of ${}_0x(l)$ is given by its drift component. As a result, the highest value of the curve occurs at $l_i = l_j = L$, where the mean value of the samples is maximum. Notice that the correlation between the random components of ${}_0x(l)$ is relatively low, as the non-overlapping increments of the standard BF are independent (see Section III of Part I). As opposed to this, integrating over the standard BF ($p > 0$) adds greatly to the correlation between the random components of ${}_0x(l)$. In this case, the contribution of the drift component to the correlation between the samples of ${}_0x(l)$ is in minority. This can be observed in Figs. E.2 and E.3, in which the maximum correlation occurs at (about) $l_i = l_j = L/2$, where the variance $\sigma^2_{px}(l)$ is also maximum (see Section V-B).

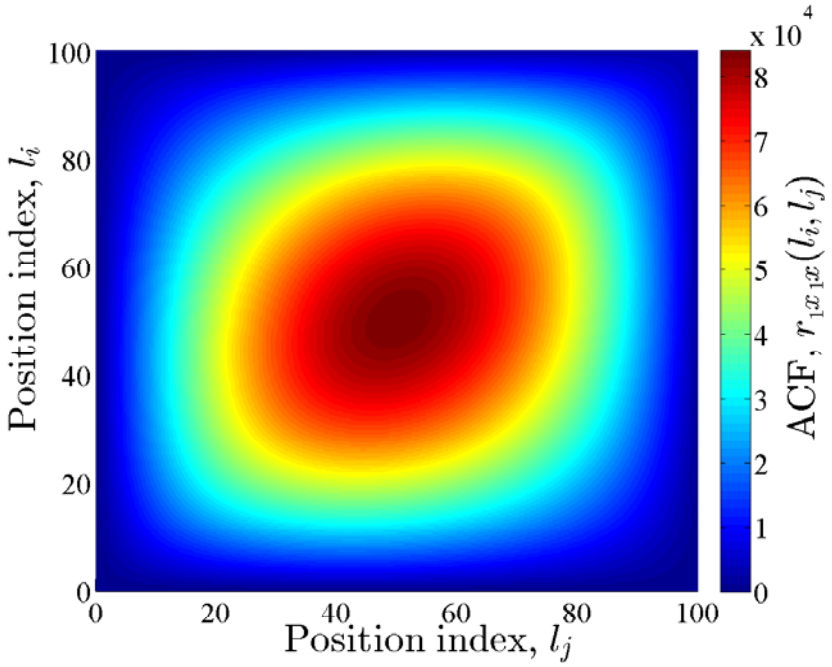

Figure E.2: The ACF $r_{1x_1x}(l_i, l_j)$ in (E.7). The model parameters are $k_d = 1$, $k_b = 1$, and $\sigma_x = \sigma_y = 2$ m.

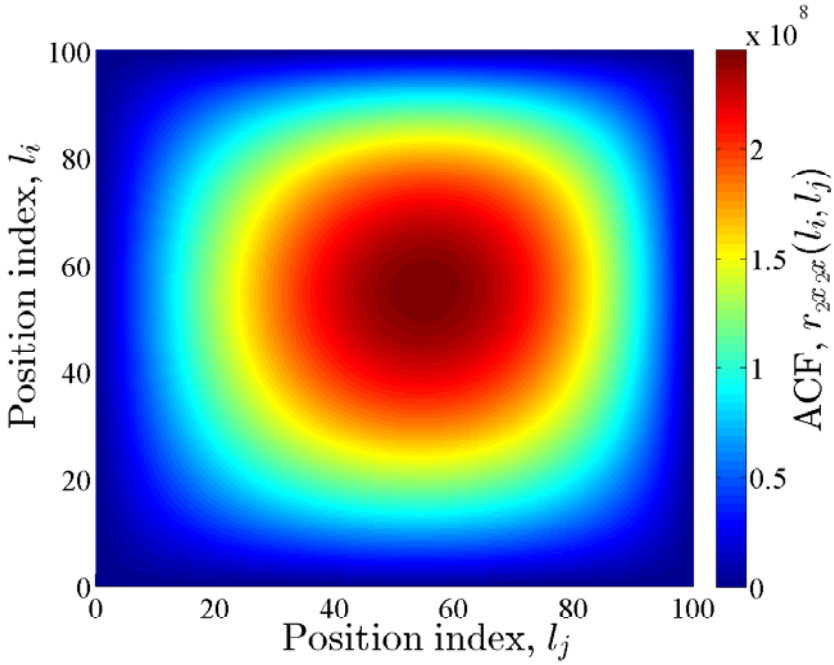

Figure E.3: The ACF $r_{2x_2x}(l_i, l_j)$ in (E.7). The model parameters are $k_d = 1$, $k_b = 1$, and $\sigma_x = \sigma_y = 2$ m.

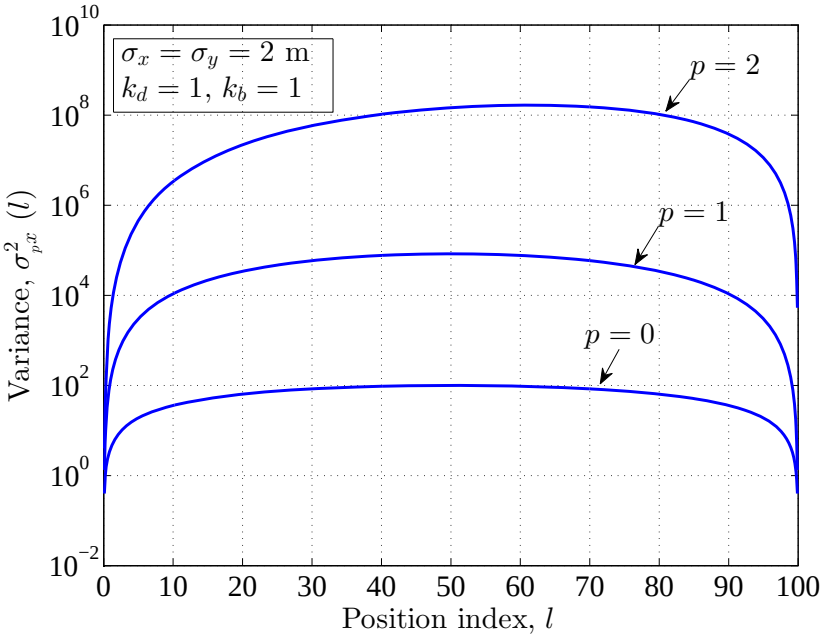

Figure E.4: The variance $\sigma^2_{px}(l)$ in (E.9). The model parameters are $k_d = 1$, $k_b = 1$, and $\sigma_x = \sigma_y = 2\,\text{m}$.

The variance $\sigma^2_{px}(l)$ of the process ${}_px(l)$ in (E.9) is demonstrated in Figs. E.4 and E.5. In accordance with Figs. E.1–E.3, we remain on the assumption of $\sigma_x = \sigma_y = 2\,\text{m}$. Fig. E.4 shows the variance $\sigma^2_{px}(l)$ for different values of p. As discussed in Section III-D, $\sigma_{px\max}$ is a monotonically increasing function in p. The significant increase in $\sigma_{px\max}$ is the result of integrating over the BF. Referring to Fig. E.4, for p equals 0 and 1, the maximum variance $\sigma_{px\max}$ occurs at $l = 50$. For $p = 2$, the peak position, however, moves to $l = 55$, which verifies the mild tendency of the peak position to the terminating point (see Section V-B). Fig. E.5 illustrates the variance $\sigma^2_{2x}(l)$ in (E.9) for different values of the bridge parameter k_b. Herein, we have set the maximum standard deviation to $\sigma_{\max} = \sigma_{2x\max} = 10\,\text{m}$. The importance of the figure is to show the position of the maximum variance. If $k_b = 1$, the variance $\sigma^2_{2x}(l)$ is a concave function given by (E.30) with a peak at $l = 50$. For $k_b = 0$, the variance $\sigma^2_{2x}(l)$ in (E.9) turns to $\sigma^2_{2x}(l) = \sigma^2_x l^5/20$, which is a monotonically increasing function in l. Therefore, the maximum occurs at $l = 100$. Finally, if $0 < k_b < 1$, the variance $\sigma^2_{2x}(l)$ is a combination of a concave and convex function as shown in Fig. E.5. The combined form of $\sigma^2_{2x}(l)$ in the recent case can describe the special configuration of the path shown in Fig. 11 of Part I. Notice that the curves shown in Fig. E.5 show the variances of the paths along the x-axis shown in Figs. 3, 10, and 11 of Part I.

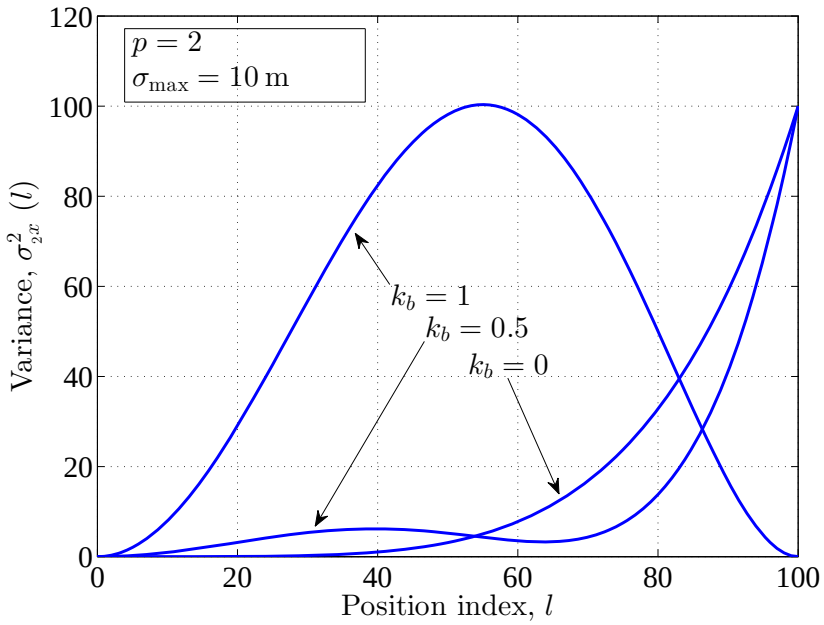

Figure E.5: The variance $\sigma^2_{2x}(l)$ in (E.9). The model parameters are $k_d = 1$, $k_b = 1$ and $\sigma_{\max} = 10\,\mathrm{m}$.

Figs. E.6–E.8 display the AOM PDF $p_{{}_p\alpha^v}(\alpha^v; l)$ in (E.14) for different values of p. The maximum standard deviation $\sigma_{\max}$ has been set to 10 m along both axes. These figures show the AOM PDFs of the paths shown in Figs. 1–3 of Part I. As can be observed in Fig. E.6, the AOM PDF $p_{{}_0\alpha^v}(\alpha^v; l)$ does not vary in position (look at the similarity of the colours along any given value of α^v), which indicates that the AOM process ${}_0\alpha^v$ is stationary in this case (see Section IV-B). The stationarity, however, does not hold for $p = 1$ and $p = 2$, as $p_{{}_p\alpha^v}(\alpha^v; l)$ changes in l (see Figs. E.7 and E.8). A common observation in Figs. E.6–E.8 is that for a given l, the peak of $p_{{}_p\alpha^v}(\alpha^v; l)$ is at $\alpha^v = \arctan(1) = 0.78\,\mathrm{rad}$, which agrees with the slope of the drift shown in Figs. 1–3 of Part I. Moreover, by increasing p, the variance of the AOM process decreases, which is in line with the observations in Figs. 1–3 of Part I. Furthermore, for $\alpha^v = 0.78\,\mathrm{rad}$, the maximum of $p_{{}_p\alpha^v}(\alpha^v; l)$ occurs at $l = 50$ and $l = 55$ if $p = 1$ and $p = 2$, respectively. Finally, as opposed to many proposed mobility models in the literature, herein, the AOM is in general not uniformly distributed, which complies with real-life user tracings reported in [12].

Figs. E.9 and E.10 exhibit the incremental travelling length PDF $p_{{}_pd}(d; l)$ given in (E.19) for p equals 1 and 2, respectively. The model parameters are $k_d = 1$, $k_b = 1$, and $\sigma_{\max} = 10\,\mathrm{m}$. The case $p = 0$ simplifies $p_{{}_pd}(d; l)$ in (E.19) to the Rice distribution (see Section IV-D), which is trivial to be presented here. It is noteworthy that Figs. E.9 and E.10 show the incremental travelling length PDF $p_{{}_1d}(d; l)$ of the

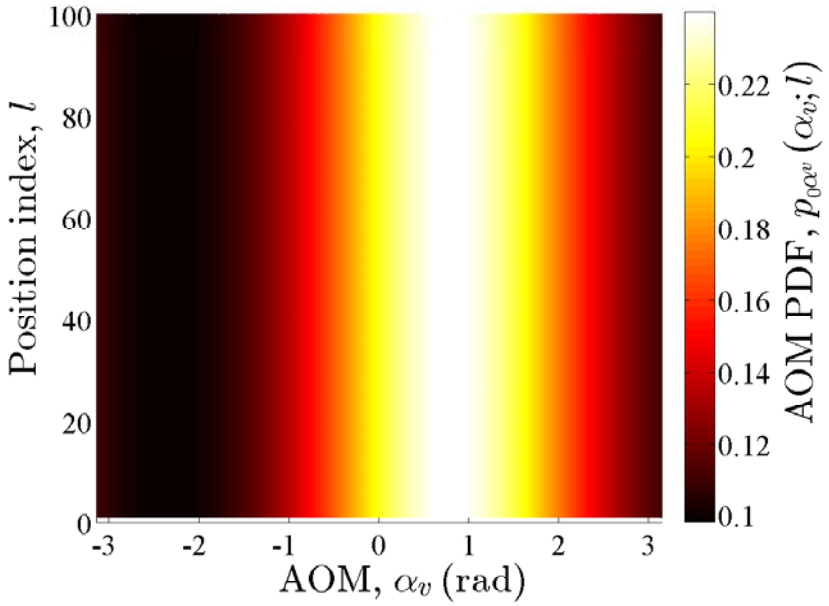

Figure E.6: The AOM PDF $p_{0\alpha^v}(\alpha^v; l)$ in (E.14). The model parameters are $k_d = 1$, $k_b = 1$, and $\sigma_{\max} = 10\,\text{m}$.

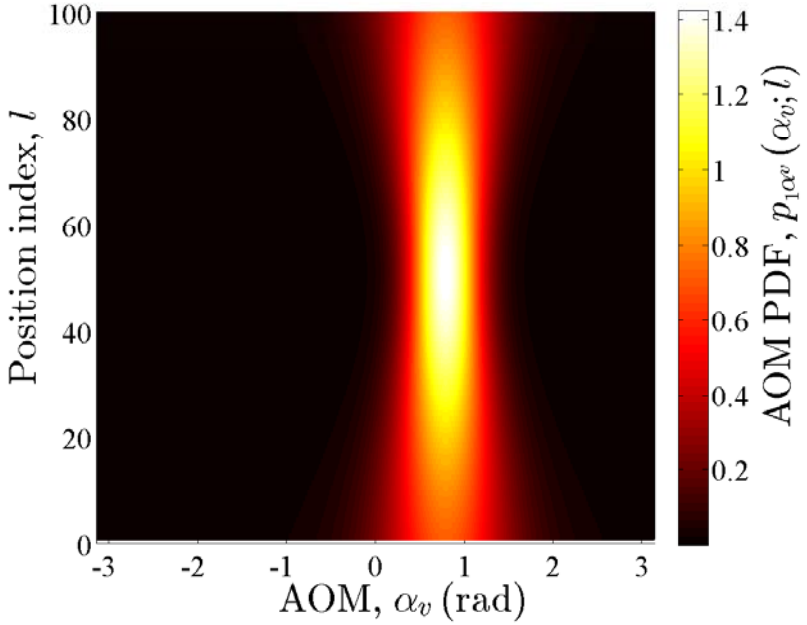

Figure E.7: The AOM PDF $p_{1\alpha^v}(\alpha^v; l)$ in (E.14). The model parameters are $k_d = 1$, $k_b = 1$, and $\sigma_{\max} = 10\,\text{m}$.

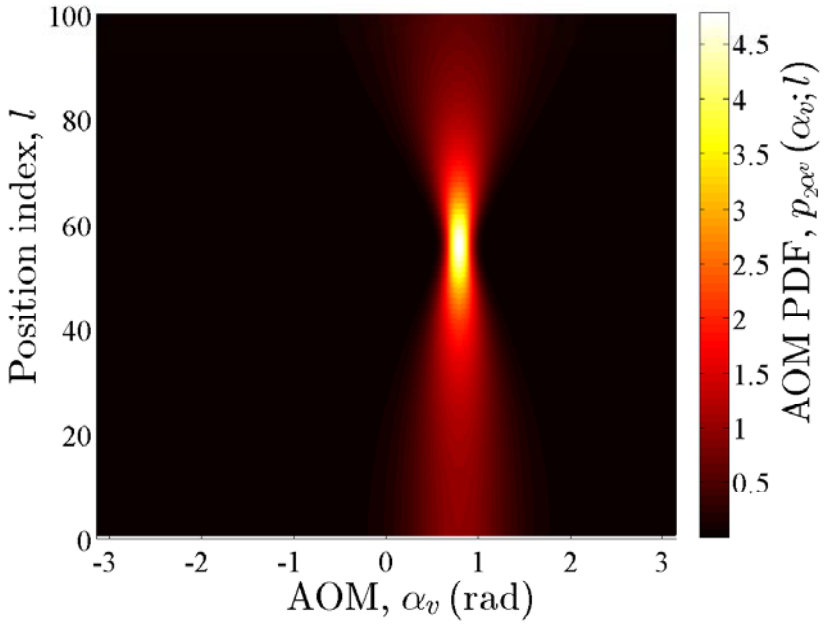

Figure E.8: The AOM PDF $p_{2\alpha^v}(\alpha^v; l)$ in (E.14). The model parameters are $k_d = 1$, $k_b = 1$, and $\sigma_{\max} = 10\,\text{m}$.

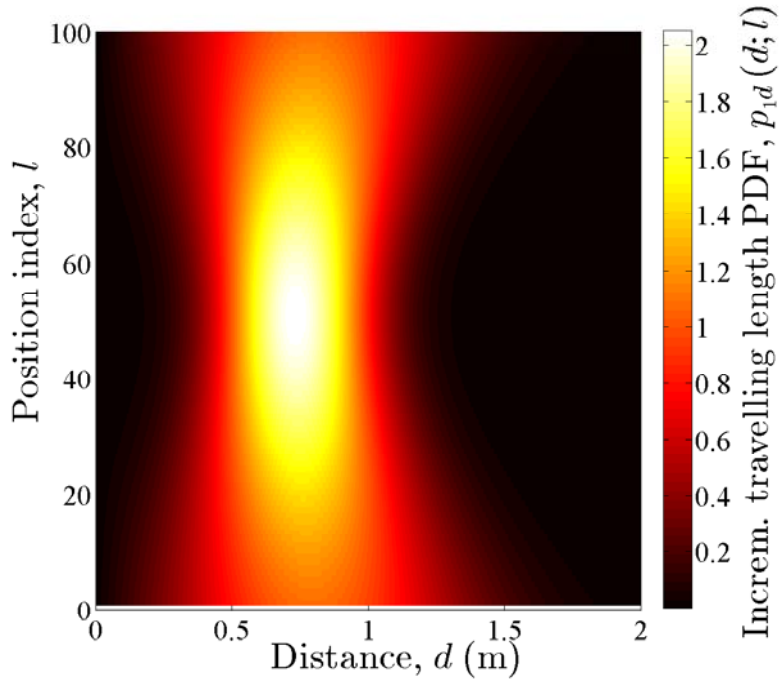

Figure E.9: The incremental travelling length PDF $p_{1d}(d; l)$ in (E.19). The model parameters are $k_d = 1$, $k_b = 1$, and $\sigma_{\max} = 10\,\text{m}$.

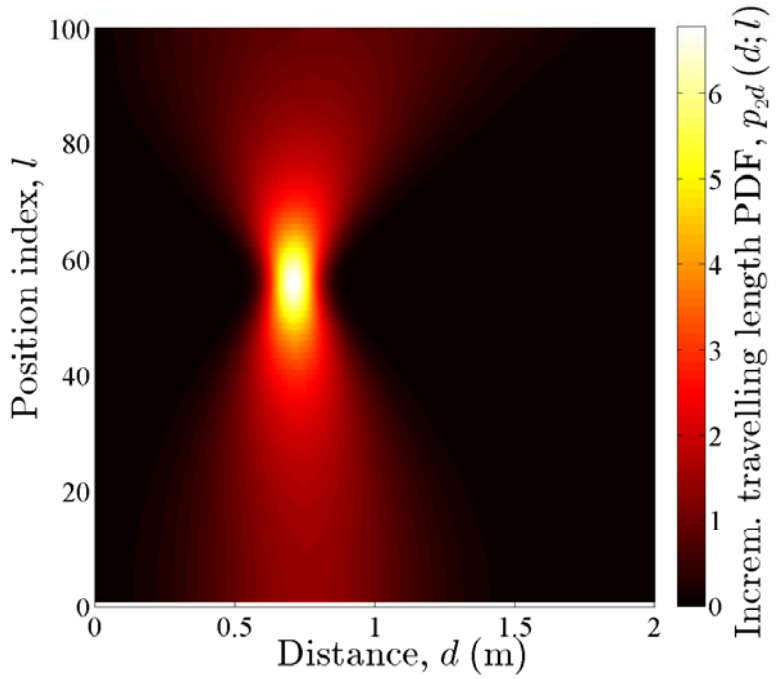

Figure E.10: The incremental travelling length PDF $p_{_2d}(d;l)$ in (E.19). The model parameters are $k_d = 1$, $k_b = 1$, and $\sigma_{\max} = 10\,\text{m}$.

paths shown in Figs. 2 and 3 of Part I, respectively. As can be observed from both Figs. E.9 and E.10, $\lim_{d\to\infty} p_{_pd(l)}(d;l) = 0$, which is in agreement with the discussion in Section IV-C. Indeed, as a prerequisite for a realistic path, the proposed path model does not allow far jumps from (x_{l-1}, y_{l-1}) to (x_l, y_l). Furthermore, the variance of the incremental travelling lengths ${}_pd$ decreases by increasing the primitive p, which can also be confirmed by the paths shown in Figs. 2 and 3 of Part I. An important observation is that for a given l, the maximum $p_{_pd}(d;l)$ occurs slightly after $d = 0.5\,\text{m}$. This value can be compared with the contribution of the drift component to (E.1), which equals $(x_d - x_s)/L = 0.5\,\text{m}$. Adding the contribution of the random component in (E.1) to this value, the recent observation in Figs. E.9 and E.10 can be verified. Eventually, the variations of $p_{_pd}(d;l)$ in l indicate that the incremental travelling length process in (E.18) is non-stationary in the strict sense.

Figs. E.11 and E.12 demonstrate the simulated overall travelling length PDF $p_{_pD}(d)$ discussed in Section IV-D. The simulation results have been obtained by computing the sum ${}_pD = \sum_{l=1}^{L} {}_pd(l)$ for 50000 realizations of the path ${}_p\mathscr{T}$ and then creating the corresponding histogram by means of 100 equally spaced bins. The model parameters are $k_d = 1$, $k_b = 1$, and $\sigma_{\max} = 10\,\text{m}$. For $p = 0$, $p_{_0D}(d)$ follows the Gaussian distribution of the form $N\left(Lm_{_0d}, L\sigma^2_{_0d}\right)$ (see Section IV-D). In this

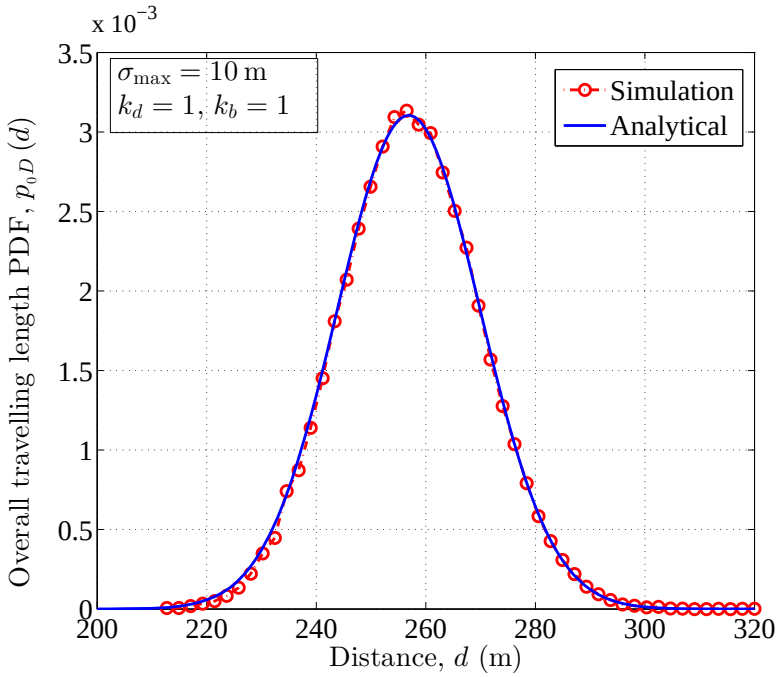

Figure E.11: The overall travelling length PDF $p_{_0D}(d)$ discussed in Section IV-D. The model parameters are $k_d = 1$, $k_b = 1$, and $\sigma_{\max} = 10\,\mathrm{m}$.

regard, Fig. E.11 shows the aforementioned Gaussian distribution, which matches excellently the simulation results. As mentioned before, the Gaussian distribution of the travelling length has been reported in empirical studies such as [16–22]. It is also worth mentioning that Fig. E.11 represents $p_{_0D}(d)$ associated with the paths shown in Fig. 1 of Part I. For $p \geq 1$, the overall travelling length PDF $p_{_pD}(d)$ does not result in an analytical closed-form solution. The simulation results, however, can be obtained by the aforementioned procedure. The results shown in Fig. E.12, are pertinent to the paths shown in Figs. 2 and 3 of Part I. An important observation from Fig. E.12 is that the travelling length PDF $p_{_pD}(d)$ ($p \geq 1$) follows closely the lognormal distribution, which complies with the results from real-world tracings [12–15]. With reference to Fig. E.12, by increasing the primitive p, both the variance and the mean of the travelling length ${}_pD$ decrease. However, the mean value cannot be less than the travelling length of the straight path. For the considered scenario, the length of the straight path equals $50\sqrt{2} = 70.7\,\mathrm{m}$, for which the corresponding overall travelling length PDF $p_{_pD}(d)$ is given by the delta Dirac function of the form $\delta(d - 70.7)$. From Fig. E.12, it can be confirmed that by increasing p, the travelling length PDF $p_{_pD}(d)$ tends to that of the straight path, i.e., $\delta(d - 70.7)$.

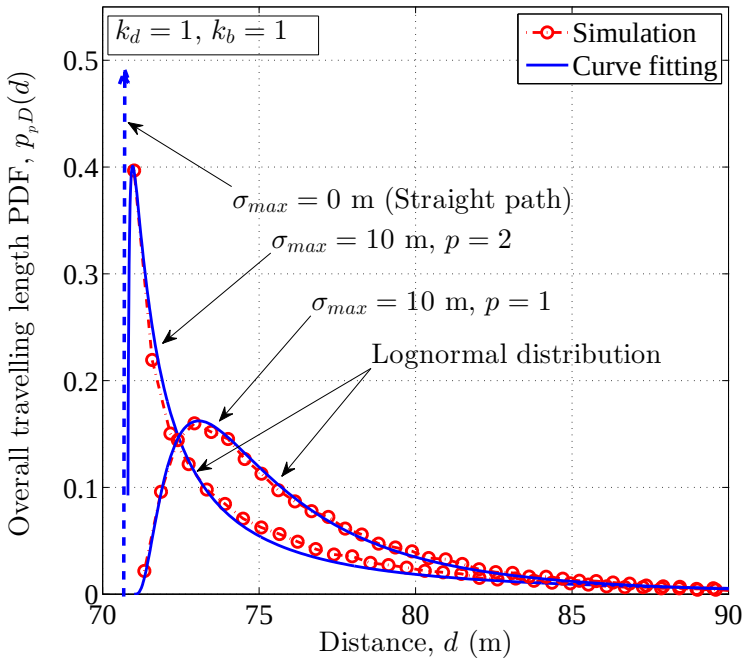

Figure E.12: The overall travelling length PDF $p_{pD}(d)$ discussed in Section IV-D. The model parameters are $k_d = 1$, $k_b = 1$, and $\sigma_{\max} = 10\,\text{m}$.

VII. CONCLUSION

This second part of our paper has investigated the statistical properties of the trajectory model proposed in the first part. We have studied the spatial mean, variance, and the ACF of the path model. We have also introduced a new process that is called the spatial increment process, for which we have shown that it follows the complex Gaussian distribution with nonidentical means and variances of the quadrature components. From this process, the AOM and the incremental travelling length processes of the path have been derived. We have computed the first-order density of these processes in closed form, showing that the AOM is not uniformly distributed, which agrees with real-life traces reported in the literature. We have also proved that the incremental travelling length includes the Rice and Nakagami-q distributions as special cases. Furthermore, we have computed the overall travelling length by summing up the incremental travelling lengths. Simulation results have shown that depending on the primitive order, the length of the travelling path follows either the Gaussian distribution, or the lognormal distribution, which both have been widely reported in empirical studies.

APPENDIX E.A

DERIVATION OF THE ACF $r_{{}_p x {}_p x}(l_i, l_j)$ IN (E.7)

To compute $E\left\{{}_p x(l_i)\,{}_p x(l_j)\right\}$, let us recall from (E.1) that ${}_p x(l_i) = m_{{}_p x}(l_i) + \sigma_x W_x(l_i, k_b) = m_{{}_p x}(l_i) + \sigma_x({}_p B_x(l_i) - \frac{k_b l_i}{L}\,{}_p B_x(L))$, where we have replaced $x_s + k_d l_i \delta_x$ by the mean $m_{{}_p x}(l_i)$ (see (E.6)). This allows us to compute the ACF $r_{{}_p x {}_p x}(l_i, l_j)$ as follows

$$
\begin{aligned}
r_{{}_p x {}_p x}(l_i, l_j) &= E\left\{{}_p x(l_i)\,{}_p x(l_j)\right\} \\
&= E\left\{\left(m_{{}_p x}(l_i) + \sigma_x\left({}_p B_x(l_i) - \frac{k_b l_i}{L}\,{}_p B_x(L)\right)\right)\right. \\
&\times \left.\left(m_{{}_p x}(l_j) + \sigma_x\left({}_p B_x(l_j) - \frac{k_b l_j}{L}\,{}_p B_x(L)\right)\right)\right\} \\
&= E\left\{m_{{}_p x}(l_i) m_{{}_p x}(l_j)\right. \\
&+ \quad \sigma_x m_{{}_p x}(l_i)\left({}_p B_x(l_j) - \frac{k_b l_j}{L}\,{}_p B_x(L)\right) \\
&+ \quad \sigma_x m_{{}_p x}(l_j)\left({}_p B_x(l_i) - \frac{k_b l_i}{L}\,{}_p B_x(L)\right) \\
&+ \quad \sigma_x^2\left({}_p B_x(l_i) - \frac{k_b l_i}{L}\,{}_p B_x(L)\right) \\
&\times \quad \left.\left({}_p B_x(l_j) - \frac{k_b l_j}{L}\,{}_p B_x(L)\right)\right\} \\
&= m_{{}_p x}(l_i) m_{{}_p x}(l_j) \\
&+ \quad \sigma_x m_{{}_p x}(l_i) E\left\{{}_p B_x(l_j) - \frac{k_b l_j}{L}\,{}_p B_x(L)\right\} \\
&+ \quad \sigma_x m_{{}_p x}(l_j) E\left\{{}_p B_x(l_i) - \frac{k_b l_i}{L}\,{}_p B_x(L)\right\} \\
&+ \sigma_x^2 E\left\{\left({}_p B_x(l_i) - \frac{k_b l_i}{L}\,{}_p B_x(L)\right)\right. \\
&\times \quad \left.\left({}_p B_x(l_j) - \frac{k_b l_j}{L}\,{}_p B_x(L)\right)\right\} \\
&= m_{{}_p x}(l_i) m_{{}_p x}(l_j) \\
&+ \sigma_x^2 E\left\{\left({}_p B_x(l_i) - \frac{k_b l_i}{L}\,{}_p B_x(L)\right)\right. \\
&\times \quad \left.\left({}_p B_x(l_j) - \frac{k_b l_j}{L}\,{}_p B_x(L)\right)\right\} \\
&= m_{{}_p x}(l_i) m_{{}_p x}(l_j) + \sigma_x^2\left(E\left\{{}_p B_x(l_i)\,{}_p B_x(l_j)\right\}\right. \\
&- \quad \left.\frac{k_b l_j}{L} E\left\{{}_p B_x(l_i)\,{}_p B_x(L)\right\}\right.
\end{aligned}
$$

$$
\begin{aligned}
&- \quad \frac{k_b l_i}{L} E\left\{ {}_pB_x(L)\, {}_pB_x(l_j) \right\} \\
&+ \quad \frac{k_b^2 l_i l_j}{L^2} E\left\{ B_x^2(L) \right\} \Bigg). \qquad \text{(E.31)}
\end{aligned}
$$

Finally, using $r^c_{{}_pB_{x\,p}B_x}(\cdot,\cdot) = E\left\{ {}_pB_x(\cdot)\, {}_pB_x(\cdot) \right\}$ gives the result in (E.7).

APPENDIX E.B

PROOF OF THEOREM 1

With reference to the path ${}_p\mathscr{T}$ in (E.1), the increment process ${}_ps_x(l) = {}_px(l) - {}_px(l-1)$ along the x-axis can be written as

$$
\begin{aligned}
{}_ps_x(l) &= x_s + k_d\, l\, \delta_x + \sigma_x({}_pB_x(l) - \frac{k_b l}{L}\, {}_pB_x(L)) \\
&- \; x_s - k_d(l-1)\delta_x - \sigma_x({}_pB_x(l-1) + \frac{k_b(l-1)}{L}\, {}_pB_x(L)) \\
&= \; k_d\, \delta_x + \sigma_x({}_pB_x(l) - {}_pB_x(l-1) - \frac{k_b}{L}\, {}_pB_x(L)). \qquad \text{(E.32)}
\end{aligned}
$$

The equation above represents a linear combination of zero-mean Gaussian processes plus the constant shift $k_d\delta_x$. Accordingly, the increment process ${}_ps_x(l)$ follows the Gaussian distribution of the form $N\left(k_d\delta_x, \sigma^2_{{}_ps_x}(l)\right)$, where

$$
\begin{aligned}
\sigma^2_{{}_ps_x}(l) &= E\left\{ (\sigma_x)^2 \left({}_pB_x(l) - {}_pB_x(l-1) - \frac{k_b}{L}\, {}_pB_x(L) \right)^2 \right\} \\
&= \; \sigma_x^2\, E\Bigg\{ {}_pB_x^2(l) + {}_pB_x^2(l-1) + \frac{k_b^2}{L^2}\, {}_pB_x^2(L) \\
&- \; 2\, {}_pB_x(l)\, {}_pB_x(l-1) - \frac{2k_b}{L}\, {}_pB_x(l)\, {}_pB_x(L) \\
&+ \; \frac{2k_b}{L}\, {}_pB_x(l-1)\, {}_pB_x(L) \Bigg\} \\
&= \; \sigma_x^2 \Big(r^c_{{}_pB_{x\,p}B_x}(l,l) + r^c_{{}_pB_{x\,p}B_x}(l-1,l-1) \\
&+ \; \frac{k_b^2}{L^2} r^c_{{}_pB_{x\,p}B_x}(L,L) - 2r^c_{{}_pB_{x\,p}B_x}(l,l-1) \\
&- \; \frac{2k_b}{L} r^c_{{}_pB_{x\,p}B_x}(l,L) + \frac{2k_b}{L} r^c_{{}_pB_{x\,p}B_x}(l-1,L) \Big). \qquad \text{(E.33)}
\end{aligned}
$$

With the same token, the increment process ${}_ps_y(l) = {}_py(l) - {}_py(l-1)$ along the y-axis follows the Gaussian distribution of the form $N\left(k_d\delta_y, \sigma^2_{{}_ps_y}(l)\right)$, where $\sigma^2_{{}_ps_y}(l)$

is obtained from (E.33) by replacing the superscript x by y. Furthermore, the correlation between the increment processes ${}_p s_x(l)$ and ${}_p s_y(l)$ is zero, as their structural elements ${}_p B_x(l)$ and ${}_p B_y(l)$ are statistically independent. Therefore, the spatial increment process ${}_p s(l) = {}_p s_x(l) + i\,{}_p s_y(l)$ follows the complex Gaussian distribution of the form provided in Theorem 1.

REFERENCES

[1] T. Camp, J. Boleng, and V. Davies, "A survey of mobility models for ad hoc network research," *Wireless Communications and Mobile Computing*, vol. 2, no. 5, pp. 483–502, Sep. 2002.

[2] F. Bai and A. Helmy, *A Survey of Mobility Modeling and Analysis in Wireless Adhoc Networks*. Book chapter in: Wireless Ad Hoc and Sensor Networks, Kluwer academic Publishers, 2004.

[3] J. Härri, F. Filali, and C. Bonnet, "Mobility models for vehicular ad hoc networks: a survey and taxonomy," *Communications Surveys Tutorials, IEEE*, vol. 11, no. 4, pp. 19–41, 2009.

[4] A. Einstein, "Über die von der molekularkinetischen Theorie der Wärme geforderte Bewegung von in ruhenden Flüssigkeiten suspendierten Teilchen," *Annalen der Physik*, no. 17, pp. 549–560, May 1905.

[5] K. Pearson, "The problem of the random walk," *Nature*, vol. 72, no. 1865, p. 294, 1905.

[6] D. B. Johnson and D. A. Maltz, *Dynamic Source Routing in Ad Hoc Wireless Networks*. The Kluwer International Series in Engineering and Computer Science, 1996, vol. 353.

[7] B. Liang and Z. J. Haas, "Predictive distance-based mobility management for PCS networks," in *Proc. 18th Annual Joint Conference of the IEEE Computer and Communications Societies (INFOCOM'99)*, vol. 3, 1999, pp. 1377–1384.

[8] V. A. Davis, "Evaluating mobility models within an ad hoc network," in *MS thesis, Colorado School of Mines*, 2000.

[9] M. Sánchez and P. Manzoni, "ANEJOS: a Java based simulator for ad hoc networks," *Future Generation Computer Systems*, vol. 17, no. 5, pp. 573 – 583, 2001.

[10] M. Hossain and M. Atiquzzaman, "Stochastic properties and application of city section mobility model," in *Global Telecommunications Conference, 2009. GLOBECOM 2009. IEEE*, 2009, pp. 1–6.

[11] S. Bandyopadhyay, E. Coyle, and T. Falck, "Stochastic properties of mobility models in mobile ad hoc networks," *Mobile Computing, IEEE Transactions on*, vol. 6, no. 11, pp. 1218–1229, 2007.

[12] M. Kim, D. Kotz, and S. Kim, "Extracting a mobility model from real user traces," in *Proc. 25th IEEE International Conference on Computer Communications (INFOCOM'06)*, 2006, pp. 1–13.

[13] B. C. Csáji, A. Browet, V. A. Traag, J. Delvenne, E. Huens, P. V. Dooren, Z. Smoreda, and V. D. Blondel, "Exploring the mobility of mobile phone users," *Physica A: Statistical Mechanics and its Applications*, vol. 392, no. 6, pp. 1459 – 1473, 2013.

[14] T. Garske, H. Yu, Z. Peng, M. Ye, H. Zhou, X. Cheng, J. Wu, and N. Ferguson, "Travel patterns in China," *PLOS ONE*, vol. 6, no. 2, pp. 1–9, Feb. 2011.

[15] M. A. P. Taylor and Susilawati, "Modelling travel time reliability with the Burr distribution," *Procedia - Social and Behavioral Sciences*, vol. 54, pp. 75–83, 2012.

[16] S. B. Young, "Evaluation of pedestrian walking speeds in airport terminals," *Journal of the Transportation Research Board*, vol. 1674, no. 2, pp. 20–26, 1999.

[17] P. P. Dey, S. Chandra, and S. Gangopadhaya, "Speed distribution curves under mixed traffic conditions," *Journal of Transportation Engineering*, vol. 132, no. 6, pp. 475–481, Jun. 2006.

[18] T. Hastie, R. Tibshirani, and J. Friedman, *The Elements of Statistical Learning: Data Mining, Inference, and Prediction*. Springer, 2001.

[19] J. Jun, "Understanding the variability of speed distributions under mixed traffic conditions caused by holiday traffic," *Transportation Research Part C: Emerging Technologies*, vol. 18, no. 4, pp. 599–610, Jun. 2010.

[20] C.-M. Hsu and F.-L. Lian, "A case study on highway flow model using 2-D Gaussian mixture modeling," in *Proc. Intelligent Transportation Systems Conference, ITSC07*. Seattle, WA, USA, Sep. 2007, pp. 790–794.

[21] N. Ueda, R. Nakano, Z. Ghahramani, and G. E. Hinton, "SMEM algorithm for mixture models," *Neural Computation*, vol. 12, no. 9, pp. 2109–2128, Sep. 2000.

[22] W. Zhu, K. Boriboonsomsin, and M. Barth, "Microscopic traffic flow quality of service from the drivers point of view," in *Proc. Intelligent Transportation Systems Conference, ITSC'07*. Seattle, WA, USA, Sep. 2007, pp. 47–52.

[23] A. Borhani and M. Pätzold, "Modelling of non-stationary mobile radio channels using two-dimensional Brownian motion processes," in *Proc. 6th International Conference on Advanced Technologies for Communications, ATC'13*. Ho Chi Minh City, Vietnam, Oct. 2013.

[24] ——, "Modelling of non-stationary mobile radio channels incorporating the Brownian mobility model with drift," in *Proc. World Congress on Engineering and Computer Science, WCECS13*. San Francisco, USA, Oct. 2013.

[25] I. S. Gradshteyn and I. M. Ryshik, *Table of Integrals, Series, and Products*, 7th ed. Elsevier Academic Press, 2007.

[26] V. A. Aalo, G. P. Efthymoglou, and C. Chayawan, "On the envelope and phase distributions for correlated Gaussian quadratures," *IEEE Communications Letters*, vol. 11, no. 12, pp. 985–987, 2007.

[27] P. Dharmawansa, N. Rajatheva, and C. Tellambura, "Envelope and phase distribution of two correlated Gaussian variables," *IEEE Transactions on Communications*, vol. 57, no. 4, pp. 915–921, 2009.

[28] G. N. Watson, *A Treatise on the Theory of Bessel Functions*. Cambridge Univ. Press, 1944.

[29] M. Pätzold, *Mobile Radio Channels*, 2nd ed. Chichester: John Wiley & Sons, 2011.

[30] R. S. Hoyt, "Probability functions for the modulus and angle of the normal complex variate," *Bell Syst. Tech. J.*, vol. 26, no. 4, pp. 318–359, 1947.

[31] N. Youssef, C.-X. Wang, and M. Patzold, "A study on the second order statistics of Nakagami-Hoyt mobile fading channels," *Vehicular Technology, IEEE Transactions on*, vol. 54, no. 4, pp. 1259–1265, 2005.

[32] H. J. Hilhorst, "Central limit theorems for correlated variables: some critical remarks," *Brazilian Journal of Physics*, vol. 39, no. 2A, pp. 371–379, 2009.

[33] L. A. Shepp, "Radon-Nikodym derivatives of Gaussian measures," *The Annals of Mathematical Statistics*, vol. 37, no. 2, pp. 321–354, Dec. 1966.

Appendix F

Paper VI

Title:	A Random Trajectory Approach for the Development of Non-Stationary Channel Models Capturing Different Scales of Fading
Authors:	**Alireza Borhani**[†], Gordon L. Stüber[‡], and Matthias Pätzold[†]
Affiliations:	[†] University of Agder, Faculty of Engineering and Science, P. O. Box 509, NO-4898 Grimstad, Norway [‡] Georgia Institute of Technology, Faculty of Electrical and Computer Engineering, 30332 Atlanta, GA, United States
Journal:	*IEEE Transactions on Wireless Communications*, under review.

A Random Trajectory Approach for the Development of Non-Stationary Channel Models Capturing Different Scales of Fading

Alireza Borhani, Gordon L. Stüber, and Matthias Pätzold

***Abstract* — This paper introduces a new approach to develop stochastic non-stationary channel models, the randomness of which originates from a random trajectory of the mobile station (MS), rather than from the scattering area. We employ the new approach by utilizing a random trajectory model based on the primitives of Brownian fields (BFs), while the position of scatterers can be generated from an arbitrarily two-dimensional (2D) distribution function. The employed trajectory model generates random paths, along which the MS travels from a given starting point to a fixed predefined destination point. To capture the path loss, we model the gain of each multipath component by a negative power law applied to the travelling distance of the corresponding plane wave, while the randomness of the path travelled results in large-scale fading. It is shown that the local received power is well approximated by a Gaussian process in logarithmic scale even for a very limited number of scatterers. We also show that the envelope of the complex channel gain follows closely a Suzuki process, indicating that the proposed channel model superimposes small-scale fading and large-scale fading. We also derive and analyze the local power delay profile (PDP) and the local power spectral density (PSD) of the channel model.**

***Index Terms* — Non-stationary channels, random trajectory models, small-scale fading, large-scale fading, path loss, envelope of the complex channel gain, received power.**

Manuscript received April 4, 2014; The review of this paper is coordinating by Dr. T. Zemen.

A. Borhani and M. Pätzold are with the Faculty of Engineering and Science, University of Agder, 4898 Grimstad, Norway (e-mails: {alireza.borhani, matthias.paetzold}@uia.no).

G. L. Stüber is with the Faculty of Electrical and Computer Engineering, Georgia Institute of Technology, 30332 Atlanta, GA, United States (e-mail: stuber@ece.gatech.edu).

I. INTRODUCTION

The demanding mobility features of communication technologies call for the need to advance channel models (among other needs), in which non-stationary aspects of the channel are carefully taken into account. In this connection, many empirical and analytical investigations, e.g., [1–3] show that the stationary assumption for the channel is only valid for extremely short travelling distances [4]. Nevertheless, the number of non-stationary channel models [5–9] proposed in the literature is still very limited.

One of the approaches to the development of non-stationary channel models is to update the channel characteristics along the travelling path of the MS, which is surrounded by randomly distributed scatterers. For instance, the authors in [9, 10] provide a non-stationary one-ring channel model under the assumption that the MS is moving along a *fixed* trajectory surrounded by a ring of *randomly* distributed scatterers. In this paper, we expanded this approach by allowing the trajectory of the MS to be random, while the scattering area can in principle be generated by any 2D distribution function. This expansion adds considerably to the robustness of the channel model with respect to the number of scatterers, such that the desired statistical properties can be obtained even if the propagation area is sparsely seeded with scatterers.

This paper utilizes a recently proposed [11, 12] random trajectory based on the primitives of BFs, along which the MS is assumed to move. The proposed trajectory model in [12] is able to generate many different configurations of the path with different smoothness levels. In this paper, we focus on one important path configuration by which the arrival at a fixed predefined destination point is assured. To cope with the scattering effect of the propagation area, we employ a 2D Gaussian probability density function (PDF), by means of which the positions of the scatterers are generated. We keep the position of the scatterers fixed, while we allow the MS to travel along random paths heading to a fixed destination point. Accordingly, the randomness of the channel model originates from the randomness of the trajectory, rather than that of the scattering area. We consider a fixed-to-mobile (F2M) frequency-nonselective communication scenario, in which the waves emitted from the base station (BS) antenna arrive at the MS antenna after a single bounce from every scatterer.

We provide an additive complex channel gain model for the aforementioned propagation scenario, in which not only the Doppler frequencies, but also the propagation path delays and the propagation path gains are stochastic processes that vary in position. In our model, the path gains are determined by a negative power law ap-

plied to the total travelling distance of the plane waves, which is in line with the basic idea of any path loss model. We also provide the angle-of-arrival (AOA) process and the angle-of-motion (AOM) process, from which the Doppler frequency process is derived. The corresponding first-order densities are computed. Accordingly, we fully characterize the complex channel gain of the proposed non-stationary channel model. We then step further by deriving the first-order density of the channel gain envelope, the first-order density of the total received power, as well as the local PDP and the local PSD processes.

The simulation results confirm that the proposed channel model is non-stationary. Given a sparse scattering area, we show that the power of each incoming wave, the so-called received path power, follows closely the lognormal distribution. We also prove that the sum of the received path powers, i.e., the total received power, is well approximated by a Gaussian process in logarithmic scale, indicating that the proposed channel model captures the effect of shadowing. The normality of the total received power complies with the result reported in [13], where a groundbreaking additive model was considered as a physical basis for modelling shadow fading. Furthermore, it is shown that the envelope of the channel gain is well approximated by a Suzuki process, confirming that the proposed channel superimposes large-scale fading and small-scale fading. We note that many measurement campaigns have reported that multi-scale fading channels under non-line-of-sight propagation conditions are best modelled by a Suzuki process [14, 15]. Moreover, we show that the proposed channel model has two degrees of freedom to control the spread of the shadowing. It has been demonstrated that the spread of the shadowing is approximately independent of the position of the BS. This also agrees with the empirical results reported, e.g., in [16–20]. In addition, it is shown that the mean received power decreases by increasing the BS-to-MS distance, affirming that the model captures the path loss effect as well. Finally, we show that the time-varying effect of each scatterer on the local PDP and the local PSD can perfectly be tracked if the channel is sufficiently sparse.

The novelty of the paper arises from the following features. The paper introduces a new approach to channel modelling under non-stationary conditions. This approach is also useful for the simulation/interpretation of measurement campaigns, in which a certain propagation area (fixed scattering area) undergoes several measurement trials (random trajectories). The proposed non-stationary channel model superimposes different levels of fading via a physically explainable multipath fading model, rather than a multiplicative one. The proposed channel model provides a physical (geometrical) insight to the theoretical studies in [13, 21]. The

results provided in this paper are very useful for the development of mobile communication systems, e.g., for the design of Rake receivers [22], power control and handoff algorithms.

The remainder of this paper is organized as follows. Section II introduces the concept of the new approach, while Sections III and IV employ the new approach to model the propagation area and the trajectory of the MS, respectively. The complex channel gain of the proposed non-stationary channel model is developed and characterized in Section V. The statistical properties of the channel model are analysed in Section VI, whereas the simulation results are provided in Section VII. Finally, Section VIII draws the conclusions.

II. THE NEW APPROACH

The traditional approach in geometrical (statistical) channel modelling is to start from a geometric pattern filled by randomly distributed scatterers. A list of such models can be found in [23, 24]. The randomness of the position of scatterers is then injected to the characteristics of the channel model, such as its envelope, PDP, PSD, and correlation properties. One of the key factors influencing the characteristics of the channel models designed by this approach is obviously the number of scatterers. To provide a so-called reference model, this number is assumed to tend to infinity. We call this *the infinity assumption*. The infinity assumption then allows designers to apply some limit theorems, such as the central limit theorem (CLT) of Lindeberg-Lévy, to conclude that the proposed channel model behaves like a Rayleigh, Rice, or lognormal (CLT for products) fading channel. The obvious shortcoming of these reference models is that the infinity assumption does not hold in real-world propagation scenarios. Even if such a dense scattering area exists, moving through this area would not be possible. Therefore, proposing any *mobile* radio channel model with dense scattering scenarios is mathematically convenient but physically meaningless. Another issue is the restriction of computer-based simulation environments, where applying the infinity assumption is not possible. Accordingly, designers provide a so-called simulation model, in which the infinity assumption is relaxed by reducing the number of scatterers. However, this reduction degrades the characteristics of the channel model somewhat from those of reference models.

In this paper, we introduce a new approach in which the randomness of the channel model originates from the randomness of the trajectory of the MS, while the scattering area remains fixed. The positions of the scatterers are determined either by realizing any desired 2D distribution function, or by setting them manually. The new approach assumes a random trajectory, along which the MS is in motion

through a fixed scattering area. Surveys of random trajectory models can be found in [25–27]. Very recently, we have also proposed a highly flexible random trajectory model based on the primitives of BFs [11, 12]. Let us assume that the MS is moving along a random trajectory generated by a mobility model. For a fixed scattering area, each realization of the trajectory results in different AOMs of the MS, different AOAs at the MS, as well as different travelling distances of the plane wave emitted from the transmitter. Therefore, the randomness of the trajectory model is injected to the characteristics of the corresponding channel model. In this paper, we will show that the main statistical properties of the non-stationary channel model developed by applying the new approach are very robust with respect to the number of scatterers. For instance, we will show that the envelope of the complex channel gain closely follows a Suzuki process, even if the number of scatterers is only four. For the same number of scatterers, we will show that the local received power follows the lognormal distribution, indicating that the channel model captures the shadow fading even for a very limited number of scatterers. The merit of the new approach is not only its robustness with respect to the number of scatterers, but also its capability to take non-stationary aspects of the channel into account. Different scales of fading can also be captured if the channel model is developed properly. In what follows, we show that with the new approach, a wide range of measurement campaigns may be simulated.

Let us first remark that the random mobility models in the literature can be divided into two major categories [12]: 1) models that generate targeted trajectories, where each trajectory realization is unique, but subject to a predefined drift (destination point) and 2) models that generate non-targeted trajectories, where each trajectory realization results in a substantially different trajectory. Now recall the principles of the new approach based on tracking the MS and measuring the channel for different realizations of the trajectory surrounded by a fixed scattering area. If the random trajectories are targeted, we somewhat simulate different travelling scenarios in a fixed propagation area. A clear example is when the aim is to characterize an F2M channel along a street. If we repeat this experiment, minor changes of the travelling path are unavoidable, whereas the scattering area is fixed for all trials. These minor changes are modelled by the targeted random trajectory. If the random trajectories are non-targeted, we somewhat simulate measurement campaigns carried out in distinct propagation areas. Notice that although, the new approach assumes that the scattering area is fixed, choosing totally different travelling routs (non-targeted trajectories) is almost similar to encountering different propagation areas.

It is noteworthy that with this approach, we may need a relatively large number of trials (random trajectories) to find the average channel characteristics, such as those reported empirically. In this regard, we stress that a large number of trials is in contrast neither with the potentials of any physical channel, nor with the capabilities of computer-based simulation tools, such as MATLAB®.

III. THE PROPAGATION SCENARIO

Fig. F.1 demonstrates a typical F2M propagation scenario, where the MS is travelling through a scattering area, in which the BS is fixed and located at the distance D_0 from the origin of the Cartesian coordinate system. We assume that at a reference point in time t_0, the MS starts its motion from $(x(0),y(0))$ (or equivalently (x_s,y_s)) and moves along a random trajectory (see Section IV) to reach the terminating point $(x(L),y(L))$ at time t_L. Subsequently, the position of the MS along a random trajectory at time $t_l \in [t_0,t_L]$ is represented by Cartesian coordinates $(x(l),y(l))$, in which l denotes the corresponding position index. For a single realization of the trajectory (see Fig. F.1), the position of the MS at t_l is shown by $(x(l),y(l))$. It is also assumed that a plane wave emitted from the BS arrives at the MS with the AOA $\alpha_n^R(l)$ after only one bounce due to the nth scatterer S_n $(n = 1,2,...,N)$ located at (x_n^S,y_n^S). The MS is in motion with a constant speed of v_R in the direction indicated by the AOM $\alpha_v(l)$. We assume that both the BS and the MS are equipped with a single omnidirectional antenna.

To obtain the position (x_n^S,y_n^S) of the scatterers, in principle,any 2D distribution function can be used. Herein, we use a 2D zero-mean Gaussian distribution with the standard deviation σ_s of 500 m to generate a sparse scattering area with only $N = 4$ scatterers[1]. Fig. F.2 demonstrates the results, where each scatterer has been marked by a different colour. We have placed the BS at $(-500\,\text{m}, 0\,\text{m})$, meaning that the distance D_0 from the BS to the starting point of the MS is 500 m. Notice that owing to the sparsity of the channel, the position of the scatterers in Fig. F.2 does not indicate a Gaussian distribution. Accordingly, these positions could be obtained by any other 2D distribution function. Therefore, we can conclude that the results provided in this paper are not affected by changing the type of scatterer distribution function, provided that the channel is sufficiently sparse. The interpretation of the plotted random trajectories in Fig. F.2 follows in the next section.

[1]Notice that the number of scatterers can be set to higher values, as it may be expected in real-world propagation environments. Nevertheless, to show the robustness of the proposed channel model with respect to the number of scatterers, as well as for enabling visual inspections, we analyze the channel under sparse scattering conditions.

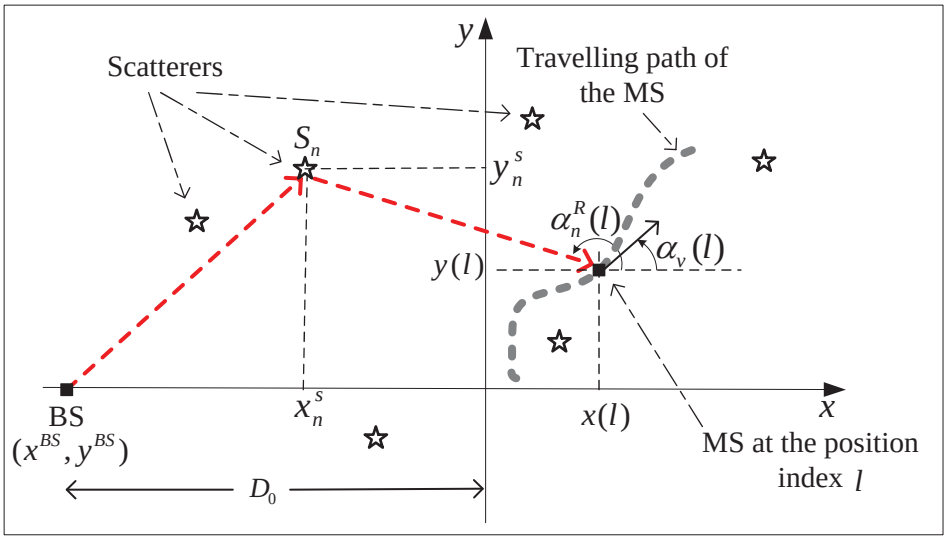

Figure F.1: A typical F2M propagation scenario assuming single-bounce scattering.

IV. THE TRAJECTORY MODEL

To run the new approach, we employ a recently proposed trajectory model based on the primitives of BFs [11]. According to this model, a path starting from (x_s, y_s) and terminating at or in the proximity of a predefined destination point (x_d, y_d) is modelled by the random trajectory ${}_p\mathscr{T}$ given by the following set of pairs

$$ {}_p\mathscr{T}: \left\{ ({}_px(l), {}_py(l)) \;\middle|\; \begin{array}{l} {}_px(l) = x_s + k_d\, l\, \delta_x + \sigma_x\, {}_pW_x(l,k_b) \\ {}_py(l) = y_s + k_d\, l\, \delta_y + \sigma_y\, {}_pW_y(l,k_b) \end{array} \right\} \tag{F.1} $$

for $l = 1, 2, ..., L$, where L is a positive integer. The terms $\delta_x = (x_d - x_s)/L$ and $\delta_y = (y_d - y_s)/L$ denote the deterministic increments along the x- and y-axis, respectively. The drift parameter k_d acts as a switch to control the presence of such a deterministic drift that forces the trajectory to evolve towards the destination point (x_d, y_d). The parameter σ_x (σ_y) controls the randomness of the trajectory process ${}_px(l)$ (${}_py(l)$) along the x-axis (y-axis).[2] Furthermore, the objective of the partial random bridge, defined as

$$ {}_pW_x(l,k_b) = {}_pB_x(l) - \frac{k_b\, l}{L}\, {}_pB_x(L) \tag{F.2} $$

[2]Note that owing to the symmetry of the trajectory model, the statistical properties of ${}_px(l)$ and ${}_py(l)$ are the same.

models the randomness of the trajectory along each axis by means of the pth primitive ${}_pB_x(l)$ of the standard BF $B_x(l)$ associated with the x-axis. The parameter k_b is called the bridge parameter, which determines the integration degree of the bridge to the destination point. In addition, the primitive p determines the smoothness level of the trajectory, which increases as p grows [11].

The trajectory ${}_p\mathscr{T}$ in (F.1) has been designed in such a way that it allows: 1) arriving at a predefined destination point (x_d, y_d) if the bridge is fully established, i.e., $k_b = 1$; 2) arriving at a target zone with a predefined radius and centre if the bridge is partially established, i.e., $0 < k_b < 1$; 3) a totally random point in the 2D plane if the bridge is broken, i.e., $k_b = 0$; and finally 4) bridging back (closed loop) to the starting point (x_s, y_s) if the bridge is fully established, i.e., $k_b = 1$, but the drift component does not exist, i.e., $k_d = 0$. The entire set of configurations above plus several others have been shown and discussed in [11]. From the configurations above, it can be concluded that ${}_p\mathscr{T}$ in (F.1) allows for the generation of both targeted and non-targeted random trajectories (see Section II). One of the novel features of ${}_p\mathscr{T}$ in (F.1) is its representation in position, rather than time. This allows us to test different speed scenarios without influencing the trajectory configuration (see [11]).

In this paper, *we focus* on a special case of the random trajectory in (F.1), where the *first primitive* of BFs is employed, i.e., $p = 1$, and the random bridge to the destination point (x_d, y_d) is *fully established*, i.e., $k_b = k_d = 1$. This means that we choose the model parameters such that the trajectory model generates targeted random travelling paths. For such a special case, it has been shown in [12] that if $\sigma_x = \sigma_y$, the random trajectory takes its maximum distance from the shortest trajectory (straight line from the starting point to the destination point) at the position index $l = L/2$. In this paper, we denote this maximum distance by $\sigma_{\max}$, which equals $\sigma_x \sqrt{L^3/48}$. Since investigating the effect of the primitive p is outside of the scope of this paper, we henceforth drop the index p from the notations.

Fig. F.2 displays several realizations of the random trajectory $\mathscr{T}$ in (F.1) for two different values of $\sigma_{\max}$. It is assumed that the origin $(0\,\mathrm{m}, 0\,\mathrm{m})$ of the Cartesian coordinates is the starting point of the travelling path, whereas the point located at $(500\,\mathrm{m}, 500\,\mathrm{m})$ is the destination point.

V. THE COMPLEX CHANNEL GAIN PROCESS

To model the complex channel gain of the propagation scenario (see Figs. F.1 and F.2), we expand that of a frequency-nonselective channel given in [28, pp. 45–48]. This expansion allows the Doppler frequencies[3] $f_n(l)$, propagation path delays

[3]The frequency shift caused by the Doppler effect is given by $f = f_{\max}\cos(\alpha)$, where $f_{\max} = f_0 v/c_0$ is the maximum Doppler frequency, f_0 denotes the carrier frequency, c_0 stands for the speed

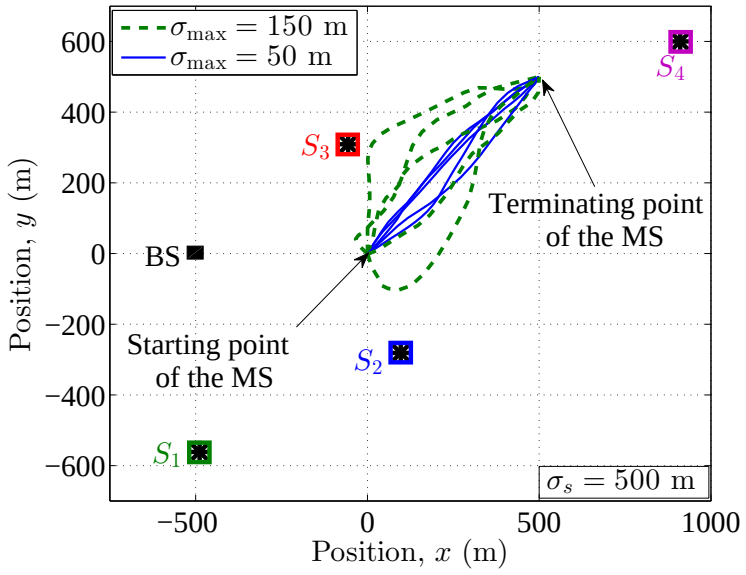

Figure F.2: A simulated sparse scattering area ($N = 4$), illustrating several realizations of the random trajectory $\mathscr{T}$ in (F.1), where $L = 20$.

$D_n(l)$, and the propagation path gains $c_n(l)$ to vary in the position index l. Accordingly, we model the complex channel gain $\mu(t_l)$ by means of the following expression

$$\mu(t_l) = \sum_{n=1}^{N} c_n(l) e^{j(2\pi f_n(l) t_l - k_0 D_n(l) + \phi_n)} \tag{F.3}$$

representing the sum of all scattered components in time. In this equation, the random variable ϕ_n represents the phase shift of the nth propagation path caused by the physical interaction of the transmitted signal with the nth scatterer S_n. It is often assumed that the phases ϕ_n are independently and identically distributed random variables, each of which is uniformly distributed between $-\pi$ and π (see, e.g., [28, p. 47] and [30, p. 59]).

Recall the trajectory model provided in Section IV. It is assumed that the position of the MS is given by the pair of stochastic processes $(x(l), y(l))$ in (F.1). Furthermore, suppose that one realization of the Gaussian scattering area is given (see Fig. F.2), which allows us to determine the position (x_n^S, y_n^S) of all N scatterers. Thus, we can represent the model parameters $f_n(l)$, $D_n(l)$, and $c_n(l)$ as stochastic processes that vary in the position index l. As a special case, these parameters

of light, and α equals the difference between the AOA and the AOM [29].

become deterministic values if we consider only one realization of the trajectory $\mathscr{T}$. Nevertheless, we still may have a stochastic complex channel gain $\mu(t_l)$ if the phase shifts ϕ_n are random. Another option to obtain a stochastic complex channel gain $\mu(t_l)$ is to focus on a single trajectory realization, while the scattering area is assumed to be random [9]. In what follows, we study the parameters of the complex channel gain $\mu(t_l)$ in (F.3).

A. Propagation Path Length Process $D_n(l)$

Referring to Fig. F.1, the total travelling distance $D_n(l)$ of the nth plane wave is the sum of a constant distance D_n^{BS-S} from the BS to the position (x_n^S, y_n^S) of the nth scatterer S_n and a random distance $D_n^{S-MS}(l)$ from S_n to the position $(x(l), y(l))$ of the MS, i.e.,

$$\begin{aligned} D_n(l) &= D_n^{BS-S} + D_n^{S-MS}(l) \\ &= \sqrt{(y^{BS}-y_n^S)^2+(x^{BS}-x_n^S)^2} + \sqrt{(y_n^S-y(l))^2+(x_n^S-x(l))^2}. \end{aligned} \quad \text{(F.4)}$$

Theorem 1. Let $m_x(l)$ ($m_y(l)$) and $\sigma_x(l)$ ($\sigma_y(l)$) denote the mean and the standard deviation of the process $x(l)$ ($y(l)$) in (F.1), respectively. The first-order density $p_{D_n}(d_n;l)$ of the total travelling distance process $D_n(l)$ in (F.4) is given by

$$\begin{aligned} p_{D_n}(d_n;l) = \frac{d_n - D_n^{BS-S}}{\sigma_x^2(l)} \exp\left\{ -\frac{(x_n^S - m_x(l))^2}{2\sigma_x^2(l)} - \frac{(y_n^S - m_y(l))^2 + (d_n - D_n^{BS-S})^2}{2\sigma_x^2(l)} \right\} \\ \times I_0\left(\frac{\sqrt{(x_n^S - m_x(l))^2 + (y_n^S - m_y(l))^2}}{\sigma_x^2(l)} (d_n - D_n^{BS-S}) \right) \end{aligned} \quad \text{(F.5)}$$

where $\sigma_x(l) = \sigma_y(l)$.

Proof: See Appendix A. ■

From Theorem 1, the first-order density $p_{\tau'_n}(\tau'_n;l)$ of the propagation delay process $\tau'_n(l) = c_0^{-1} D_n(l)$ can be derived. It is straightforward to show that $p_{\tau'_n}(\tau'_n;l)$ is given by $p_{\tau'_n}(\tau'_n;l) = c_0\, p_{D_n}(c_0\tau'_n;l)$.

B. Propagation Path Gain Process $c_n(l)$

With the objective to model Rayleigh and Rice processes, one of the widely made assumptions in the literature (see, e.g., [30, p. 85]) is that the path gains[4] $c_n(l)$ are equal, deterministic, and independent of the propagation path length $D_n(l)$. We relax these assumptions by allowing the path gains to be determined by $c_n(l) =$

[4]Notice that $c_n(l)$ is indeed not unitless. However, for consistency reasons we use the term path *gain* to address this quantity.

$CD_n^{-\gamma/2}(l)$, where $D_n(l)$ is the total travelling distance of the nth path given in (F.4). The idea of this formulation originates from the fundamental concept of any path loss model, according to which the received power (herein, the received path power $c_n^2(l)$) reduces by a negative power law (controlled by γ) if the travelling distance (herein, $D_n(l)$) of the corresponding plane wave increases. This formulation also captures the definition of the path magnitude provided in [28, p. 47]. The power law γ is often called the path loss exponent, which has been reported to be $\gamma = 2$ in the free space, while it ranges from 3 to 5 in rural and urban areas. Moreover, the constant C accounts for the total transmission power, antenna(s) gain, wave length, number of scatterers N, and a few more physical parameters (see [31, 32]).

The propagation path gain process $c_n(l)$ is a non-linear transformation of the path length process $D_n(l)$. Therefore, its first-order density $p_{c_n}(y_n;l)$ can be obtained by applying the concept of transformation of random variables [33, p. 130]. It follows

$$p_{c_n}(y_n;l) = \frac{2}{\gamma}\left(C^2 y_n^{-(\gamma+2)}\right)^{\frac{1}{\gamma}} \times p_{D_n}((C^2 y_n^{-2})^{\frac{1}{\gamma}};l) \tag{F.6}$$

where $p_{D_n}(\cdot;l)$ is the first-order density of $D_n(l)$ given in Theorem 1.

Of great interest is also the first-order density $p_{c_n^2}(y_n;l)$ of $c_n^2(l)$, namely the received path power associated with the nth plane wave. It can be shown that $p_{c_n^2}(y_n;l)$ can be presented in the following form

$$p_{c_n^2}(y_n;l) = \frac{1}{\gamma}\left(C^2 y_n^{-(\gamma+1)}\right)^{\frac{1}{\gamma}} \times p_{D_n}((C^2 y_n^{-1})^{\frac{1}{\gamma}};l). \tag{F.7}$$

We will show in Section VII that $p_{c_n^2}(y_n;l)$ follows closely the first-order density of a lognormal process.

C. Doppler Frequency Process $f_n(l)$

The local Doppler frequency $f_n(l)$ is defined by a non-linear transformation of the local AOA $\alpha_n^R(l)$ and the local AOM $\alpha_v(l)$ of the MS. It follows

$$f_n(l) = f_{\max}\cos\left(\alpha_n^R(l) - \alpha_v(l)\right) \tag{F.8}$$

where $\alpha_n^R(l)$ and $\alpha_v(l)$ are given by (see Fig. F.1)

$$\alpha_n^R(l) = \arctan\left(\frac{y_n^S - y(l)}{x_n^S - x(l)}\right) \tag{F.9}$$

and

$$\alpha_v(l) = \arctan\left(\frac{y(l+1)-y(l)}{x(l+1)-x(l)}\right) \tag{F.10}$$

for $l = 0, 1, ..., L-1$, respectively.

Theorem 2. The first-order density $p_{\alpha_n^R}(\alpha_n; l)$ of the AOA process $\alpha_n^R(l)$ in (F.9) is given by

$$p_{\alpha_n^R}(\alpha_n; l) = \frac{1}{2\pi}\exp\left\{-\frac{(x_n^S - m_x(l))^2 + (y_n^S - m_y(l))^2}{2\sigma_x^2(l)}\right\} \times \left(1+\sqrt{2\pi}g(\alpha_n; l)\,\mathrm{erfc}\left(-\sqrt{2}g(\alpha_n; l)\right)\exp\left\{2g^2(\alpha_n; l)\right\}\right) \tag{F.11}$$

where

$$g(\alpha_n; l) = \frac{1}{2\sigma_x(l)}\left((x_n^S - m_x(l))\cos(\alpha_n) + (y_n^S - m_y(l))\sin(\alpha_n)\right) \tag{F.12}$$

and $\mathrm{erfc}(\cdot)$ stands for the complementary error function [34, p. 887].

Proof: Following the discussion in the proof of Theorem 1, the AOA process $\alpha_n^R(l)$ in (F.9) can be considered as the phase of a complex Gaussian process with $(x_n^S - x(l))$ and $(y_n^S - y(l))$ as the inphase and quadrature component, respectively. The phase of complex Gaussian processes with correlated components and non-identical means (variances) has been studied in [35] and [36]. Setting $\rho = 0$ in [36, Eq. (2)] and performing some mathematical manipulations result in (F.11). ■

The first-order density $p_{\alpha_v}(\alpha_n; l)$ of the AOM process $\alpha_v(l)$ in (F.10) has been derived in [12]. Accordingly, the elements $\alpha_n^R(l)$ and $\alpha_v(l)$ of the local Doppler frequency process $f_n(l)$ in (F.8) are completely determined. Nonetheless, deriving an analytical expression for the first-order density $p_{f_n}(f_n; l)$ of the Doppler frequency $f_n(l)$ is cumbersome, particularly because $\alpha_n^R(l)$ and $\alpha_v(l)$ are not statistically independent processes. Therefore, we study the behaviour of $f_n(l)$ by means of simulations (see Section VII).

VI. CHANNEL CHARACTERISTICS

In this section, we step further toward investigating other important characteristics of the channel, such as the envelope (of the complex channel gain) process, local received power process, local PDP process, as well as the local PSD (of the Doppler frequencies) process.

A. Envelope Process

Let $\zeta(t_l)$ denote the envelope of the complex channel gain $\mu(t_l)$ in (F.3), i.e., $\zeta(t_l) = |\mu(t_l)|$. By fixing the position index l and using the result in [37, Eq. (18)], it follows that the first-order density $p_\zeta(z;l)$ of the envelope process $\zeta(t_l)$ is given by

$$p_\zeta(z;l) = (2\pi)^2 z \int_0^\infty \left[\prod_{n=1}^{N} \int_0^\infty p_{c_n}(y_n;l) J_0(2\pi y_n x)\, dy_n \right] J_0(2\pi z x) x\, dx \quad \text{(F.13)}$$

where $p_{c_n}(y_n;l)$ is the first-order density of the propagation path gain $c_n(l)$ provided in (F.6), and $J_0(\cdot)$ stands for the zeroth-order Bessel function of the first kind [34, Eq. (8.411.1)]. In agreement with [30, p. 131], the Doppler frequency $f_n(l)$, propagation path delay $D_n(l)$, and the phase shift ϕ_n have no influence on $p_\zeta(z;l)$. Moreover, referring to (F.13), $p_\zeta(z;l)$ varies in the position index l, indicating that the envelope process $\zeta(t_l)$ is non-stationary in the strict sense. In Section VII, we show that depending on l, $p_\zeta(z;l)$ can be approximated by the first-order density of different standard processes, including the Rayleigh, lognormal, Weibull, and the Suzuki process. However, the goodness-of-fit is not always acceptable. In this context, we will show that among the aforementioned candidates, the Suzuki process always gives the best fit to $p_\zeta(z;l)$ in (F.13). This agrees completely with many empirical studies, reporting that physical channels with both small-scale and large-scale fading are best modelled by the Suzuki process [14, 15]. Notice that the Suzuki process is a product process of a Rayleigh process and a lognormal process. We stress that the aim of this paper is not to decompose the envelope $\zeta(t_l)$ into Rayleigh and lognormal processes, but to show that $\zeta(t_l)$ superimposes small-scale fading and large-scale fading (see [15]).

B. Local Received Power

It has been shown in [38] that the total received power Ω spatially averaged around the MS is given by the sum $\sum_{n=1}^{N} c_n^2$, in which c_n denotes the gain of the nth path. We extend this formulation by considering the non-stationarity of the total received power $\Omega(l)$ at the position index l. It follows

$$\Omega(l) = \sum_{n=1}^{N} c_n^2(l) \quad \text{(F.14)}$$

where $c_n^2(l) = C^2 D_n^{-\gamma}(l)$ in Watts is the position-dependent received path power associated with the nth incoming plane wave (see Section V-B). The first-order density $p_\Omega(\omega;l)$ of the total received power $\Omega(l)$ can be obtained by the following expression

$$p_\Omega(\omega;l) = \int_{-\infty}^{+\infty} \Psi_\Omega(\nu;l) e^{j2\pi\nu\omega}\, d\nu \tag{F.15}$$

in which $\Psi_\Omega(\nu;l)$ represents the characteristic function of the total received power $\Omega(l)$. This function is the result of the product

$$\Psi_\Omega(\nu;l) = \prod_{n=1}^{N} \Psi_{c_n^2}(\nu;l) \tag{F.16}$$

where $\Psi_{c_n^2}(\nu;l)$ denotes the characteristic function of the received path power $c_n^2(l)$. The function $\Psi_{c_n^2}(\nu;l)$ is attained by taking the complex conjugate of the Fourier transform of the first-order density $p_{c_n^2}(y_n;l)$ of $c_n^2(l)$ in (F.7), i.e.,

$$\Psi_{c_n^2}(\nu;l) = \int_{-\infty}^{+\infty} p_{c_n^2}(y_n;l) e^{j2\pi\nu y_n}\, dy_n. \tag{F.17}$$

Providing a closed-form expression for the integral above is not possible. Nevertheless, this does not affect our understanding of the distribution of the total received power $\Omega(l)$. Recall that the received path power $c_n^2(l)$ can be well approximated by a lognormal process (see Sections V-B and VII). It has been shown theoretically that not only a sum of a few lognormal processes, but also that of a large number of lognormal processes can be approximated by a lognormal process [13, 21, 39]. Therefore, we conclude that the total received power $\Omega(l)$ in (F.14) follows approximately a lognormal process both in sparse and rich scattering areas. In Section VII, we show that for the considered sparse scattering area ($N = 4$), the local received power $\Omega(l)$ follows closely the normal distribution in logarithmic scale.

We remark that the additive model proposed in [13] provides a physical basis for shadow fading, whereas the traditional multiplicative approach is hard to be explained physically. In [13], different distributions of $c_n^2(l)$, including the lognormal, gamma, chi-square, and the Weibull distribution, have been employed to show that the sum in (F.14) follows the Gaussian distribution in logarithmic scale. However, the reason for these choices was never discussed. In this paper, we provide a geometrical insight to the additive shadow fading model presented in [13], in which

the distribution of $c_n^2(l)$ is determined by a physical measure, namely the travelling distance $D_n(l)$ of the nth plane wave (see Section V-B). Nonetheless, the objective of our paper is not to give a physical explanation for the shadow fading.

C. Local Power Delay Profile

The PDP of stationary channel models is obtained by the product of the time-invariant received power and the PDF of the propagation delays. In reality, however, both the received power and the propagation delay process vary in time (position). The non-stationary channel model proposed in this paper takes these variations into account. Accordingly, we expand the definition of the PDP to the following local PDP

$$S_{\tau'}(\tau';l) = \sum_{n=1}^{N} m_{c_n^2}(l)\, p_{\tau'_n}(\tau'_n;l) \tag{F.18}$$

where

$$m_{c_n^2}(l) = \int_{-\infty}^{\infty} y_n\, p_{c_n^2}(y_n;l)\, dy_n \tag{F.19}$$

is the mean received power of the nth path and $p_{\tau'_n}(\tau'_n;l)$ is the first-order density of the delay $\tau'_n(l)$ (see Section V-A). Furthermore, $p_{c_n^2}(y_n;l)$ is the first-order density of the received path power associated with the nth incoming plane wave (see (F.7)).

D. Local Power Spectral Density

The PSD of stationary channel models is the product of the time-invariant received power and the PDF of the Doppler frequencies. These quantities are, however, time-variant in practice. Toward the aims of this paper, we model the local PSD as follows

$$S_{\mu\mu}(f;l) = \sum_{n=1}^{N} m_{c_n^2}(l)\, p_{f_n}(f;l) \tag{F.20}$$

in which $p_{f_n}(f_n;l)$ denotes the first-order density of the Doppler frequency $f_n(l)$. As discussed in Section V-C, presenting $p_{f_n}(f_n;l)$ in a closed form is cumbersome. Nonetheless, numerical techniques assist us to illustrate and analyze the local PSD $S_{\mu\mu}(f;l)$ in (F.20). Thus, we defer the illustration of the local PSD to Section VII.

VII. SIMULATION RESULTS

A. Parameter Settings and Procedures

We consider the propagation area shown in Fig. F.2, in which the $N = 4$ scatterers are distinguished in four different colours. We again emphasize that the number of scatterers can be set to a higher value. Nonetheless, to demonstrate the robustness of the proposed channel model with respect to the number of scatterers, as well as for enabling visual inspections, we perform the simulations under sparse scattering conditions. We recall from Fig. F.2 that the MS starts its motion from the origin $(0\,\mathrm{m}, 0\,\mathrm{m})$ of the Cartesian coordinates and travels toward the destination point located at $(500\,\mathrm{m}, 500\,\mathrm{m})$. In addition, it is assumed that the BS is located at $(-500\,\mathrm{m}, 0\,\mathrm{m})$. We use the operating frequency $f_0 = 2.1\,\mathrm{GHz}$ of the universal mobile telecommunications system (UMTS) in our numerical computations. The speed of the MS is supposed to be 30 km/h, which allows a maximum Doppler frequency $f_{\max}$ of about 60 Hz. Furthermore, we consider the free space path loss exponent, i.e., $\gamma = 2$, as we believe that it suits more to our lossless single-bounce scattering scenario. Nevertheless, the effect of increasing γ will also be illustrated and discussed. The constant C is assumed to be 0.05 $\mathrm{W}^{1/2}$ m (see Section V-B). As stated before, the parameters of the path model have been set such that arriving at the destination point $(500\,\mathrm{m}, 500\,\mathrm{m})$ via a relatively smooth trajectory is assured (see Section IV). The trajectory consists of 21 points indexed by $l = 0$ (starting point) until $l = L = 20$ (terminating/destination point). We also assume that the time t_l associated with each position index l does not vary in the realization.

The simulation results have been produced by taking the following steps: 1) We have first generated $N = 4$ scatterers by means of a 2D Gaussian distribution with zero mean and variance $\sigma_s = 500\,\mathrm{m}$. 2) We have realized the trajectory $\mathscr{T}$ in (F.1) for about 5000 times. 3) Each time, we have measured the total travelling distance $D_n(l)$ (see F.4), the local AOA $\alpha_n^R(l)$ (see F.9), and the local AOM $\alpha_v(l)$ (see F.10). From the measured quantities, 4) we have then computed the characteristics of interests, including the channel envelope, local received power, local PDP, and the local PSD. As an example, for a given position index l, we have transformed the measured $D_n(l)$ via $c_n(l) = CD_n^{-\gamma/2}(l)$ to obtain the received path power. The entire $N = 4$ path powers have then been summed up to attain the total received power $\Omega(l)$. This has been done for 5000 realizations of the trajectory. 5) The corresponding normalized histograms containing a proper number of equally spaced bins have been generated and the results have been shown in the form of a PDF.

In what follows, the simulation results are demonstrated and discussed extensively. For fluency reasons, we do not necessarily represent the results in the same order as they have been derived.

B. Results

Fig. F.3 illustrates the PDF $p_\zeta(z;l)$ of the envelope $\zeta(t_l)$ in (F.13) for two different values of l. The best standard curves to each $p_\zeta(z;l)$ have also been fitted. At $l=4$ (almost the first quarter of the travelling path), the envelope $\zeta(t_4)$ can be well approximated by all of the standard candidates, excluding the lognormal distribution. For $l=10$ (almost in the middle of the travelling path), $\zeta(t_{10})$ follows closely the Suzuki distribution, but neither the lognormal nor the Rayleigh distribution. Notice that $p_\zeta(z;10)$ is almost bounded by the PDFs of the lognormal and the Rayleigh distribution, indicating that the proposed channel behaves as a lognormal-Rayleigh fading channel, which is often called a Suzuki fading channel. We have used the loglikelihood [40] as the goodness-of-fit metric, concluding that the Suzuki process gives *always the best* fit to the envelope of the proposed multi-scale fading non-stationary channel model. Since assessing the goodness-of-fit by visual inspections is straightforward for most of the position indices ls, we omit the results of the loglikelihood test herein. Notice that by increasing l, the mean of the envelope $\zeta(t_l)$ decreases. This can be attributed to the fact that, by increasing the distance between the BS and the MS, the attenuation effect of the scattering area on the plane waves increases.

Fig. F.4 depicts the PDF $p_{c_2^2}(y_2;10)$ of the received path power $c_2^2(10)$ associated with the incoming wave from S_2 (see Fig. F.2). In this figure, we have shown the simulation result, the analytical result (see (F.7)), as well as the best lognormal curve fitting result. An excellent match between them can be seen, confirming that the $p_{c_2^2}(y_2;10)$ in (F.7) is correct and well approximated by the PDF of the lognormal distribution. In other words, the received path power $c_2^2(10)$ follows the Gaussian distribution in logarithmic scale. The same conclusion holds for $p_{c_n^2}(y_n;l)$ of $c_n^2(l)$ associated with the other incoming waves $n=1,2,...,4$, as well as the other position indices $l=0,1,...,20$. Nevertheless, it should be mentioned that $p_{c_n^2}(y_n;l)$ tends to a delta function as l tends to 0 and/or $L=20$. This is due to that fact that the starting and terminating points of $\mathscr{T}$ in (F.1) are fixed (realization-independent). Notice that this does not limit the applicability of the proposed non-stationary channel model, as by changing the parameters of the trajectory model in (F.1), we are able to generate random trajectories that do not necessarily terminate at a fixed destination point. In this case, the received path power $c_n^2(L)$ becomes a random variable, rather than a fixed value.

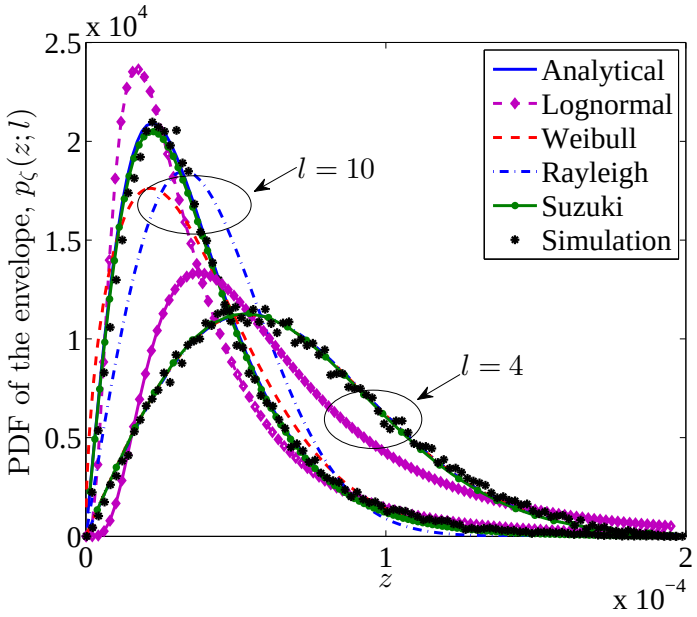

Figure F.3: The PDF $p_\zeta(z;l)$ (see (F.13)) of the envelope $\zeta(t_l)$ associated with the position index l.

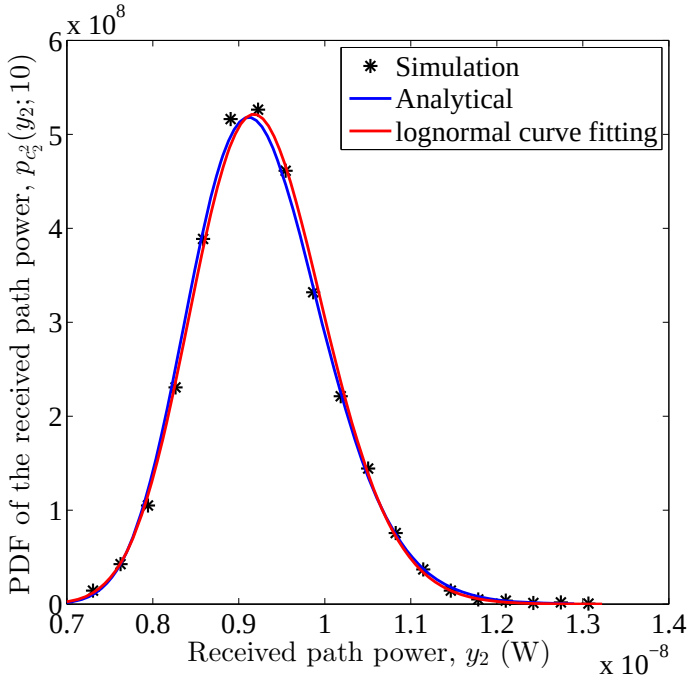

Figure F.4: The PDF $p_{c_2^2}(y_2;10)$ (see (F.7)) of the received path power $c_2^2(10)$ associated with the incoming wave from S_2.

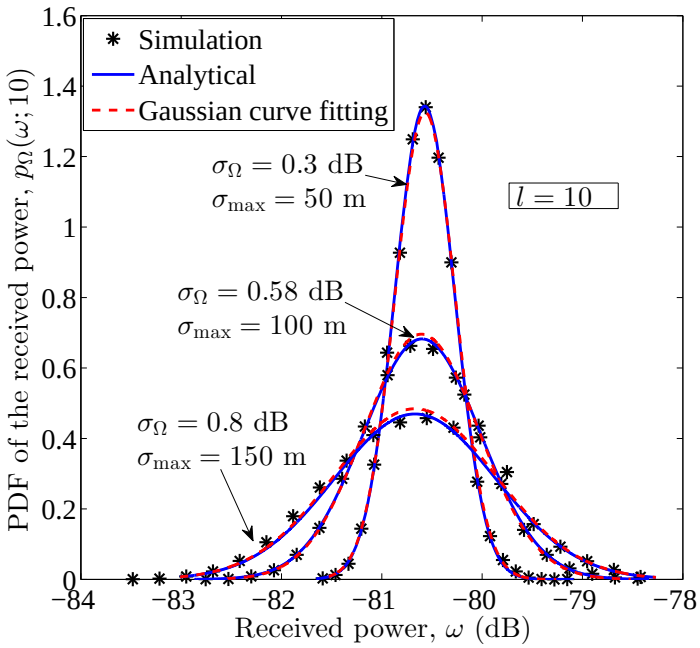

Figure F.5: The PDF $p_\Omega(\omega;10)$ (see (F.15)) of the local received power $\Omega(10)$ in logarithmic scale for different values of $\sigma_{\max}$.

Fig. F.5 demonstrates the PDF $p_\Omega(\omega;10)$ (see (F.15)) of the total received power $\Omega(10)$ in logarithmic scale, where the position index l has been set to 10 (almost in the middle of the travelling path). Notice that according to (F.15), $p_\Omega(\omega;l)$ varies in l (see Fig. F.8). To keep the visibility of the figure, we display only $p_\Omega(\omega;10)$, but for different values of $\sigma_{\max}$. The excellent match between the simulation results and the analytical ones confirms the correctness of (F.15). The best Gaussian fit to each plot has also been displayed. As can be observed, for different values of $\sigma_{\max}$, the total received power $\Omega(10)$ follows closely the normal distribution, which allows us to conclude that the proposed channel model captures the so-called shadow fading. It is also important to mention that by increasing $\sigma_{\max}$, the spread of the received power increases. This is supported by Fig. F.2, where increasing $\sigma_{\max}$ results in increasing the variations of the total travelling distance $D_n(l)$ of each trajectory. Notice that $D_n(l)$ is directly proportional to the local received power $\Omega(l)$ (see Section V-B) and that the standard deviation $\sigma_\Omega(10)$ of the local received power can be controlled by the variance of the random trajectory.

Fig. F.6 shows the effect of the path loss exponent γ on the standard deviation $\sigma_\Omega(10)$ of the local received power at the position index $l = 10$. We remark that $\sigma_\Omega(l)$ is obtained by computing the square root of the second central moment of

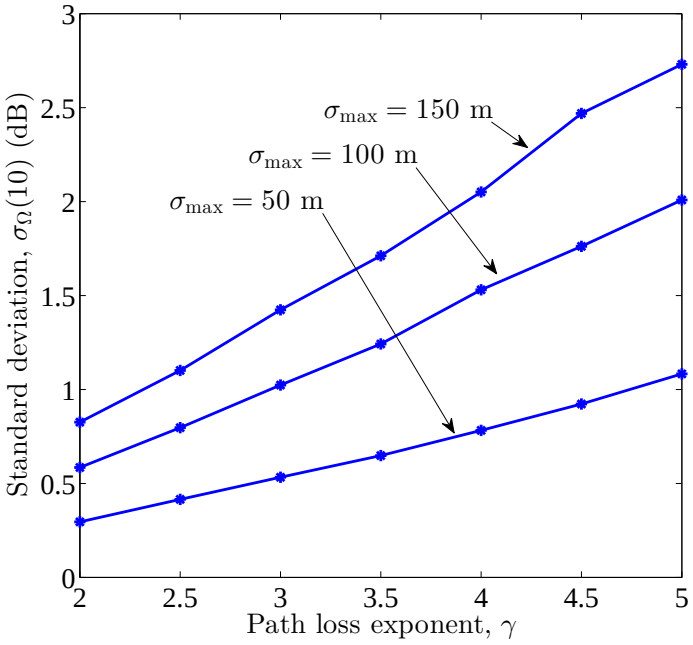

Figure F.6: The standard deviation $\sigma_\Omega(10)$ of the local received power in logarithmic scale for different values of $\sigma_{\max}$ versus the path loss exponent γ.

$\Omega(l)$. Referring to this figure, for a given $\sigma_{\max}$, the value of $\sigma_\Omega(10)$ increases by growing γ. This can also be supported by the path gain model proposed in Section V-B, where increasing γ magnifies the variations of the total travelling distance $D_n(10)$. This figure allows us to conclude that the standard deviation $\sigma_\Omega(10)$ of the local received power can be controlled not only by $\sigma_{\max}$, but also by γ. Therefore, the proposed channel model provides two degrees of freedom for controlling the spread of the shadow fading. In addition, according to Fig. F.6, the proposed channel model is able to generate large-scale fading with a spread between 0.25 dB and 2.75 dB. This range covers the empirically reported range from 0.85 dB to 2 dB measured in outdoor environments [41]. Furthermore, changing the two degrees of freedom allows us to obtain even higher spreads such as those reported in [22].

The standard deviation $\sigma_\Omega(10)$ of the local received power versus the distance D_0 of the BS from the origin is depicted in Fig. F.7. As can be observed, by increasing D_0, the value of $\sigma_\Omega(10)$ remains approximately constant. This is in line with the results of many measurement campaigns, such as those reported in [13, 16–20]. It is worth mentioning that by increasing the value of $\sigma_{\max}$, $\sigma_\Omega(10)$ cannot be well approximated by a constant value.

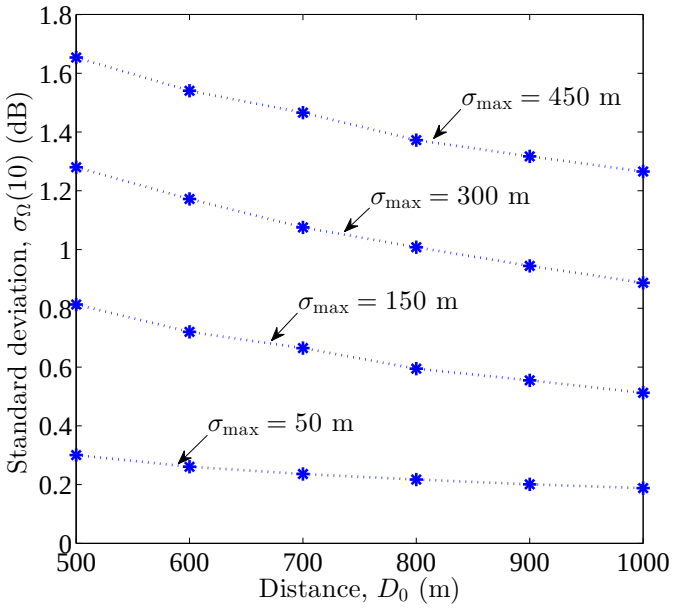

Figure F.7: The standard deviation $\sigma_\Omega(10)$ of the local received power in logarithmic scale for different values of $\sigma_{\max}$ versus the distance D_0 of the BS from the origin.

Fig. F.8 displays the mean $m_\Omega(l)$ and the spread $\sigma_\Omega(l)$ of the local received power by the decreasing dashed-line and the solid vertical bars, respectively. The minimum and the maximum of the local received power (see Fig. F.5) obtained by the simulation results have also been merged into this figure. We note that $m_\Omega(l)$ shows the time-varying path loss, whereas $\sigma_\Omega(l)$ depicts the time-varying shadow fading. The variations of these two in l confirm that the proposed channel model is non-stationary. From this figure, it can be concluded that the spread $\sigma_\Omega(l)$ of the local received power is a concave function in l with a maximum at $l = 10$ and two zeros at $l = 0$ and $l = 20$. This is in line with the illustration in Fig. F.2, where the starting and the terminating points of each trajectory are fixed (independent of the realization), while the maximum variations of the trajectory $\mathscr{T}$ occur at $l = L/2 = 10$ (almost in the middle of the travelling path)[5].

Fig. F.9 exhibits the local PDP $S_{\tau'}(\tau';l)$ (see (F.18)) in the position index l, where $\sigma_{\max} = 50\,\text{m}$. The variations of $S_{\tau'}(\tau';l)$ in l once again verify that the proposed channel model is non-stationary. In this figure, we have used different colours to distinguish the contribution of each scatterer to the PDP $S_{\tau'}(\tau';l)$. These colours are the same as those chosen in Fig. F.2. As an example, the scatterer S_4 (located

[5]This has been proved mathematically in [12].

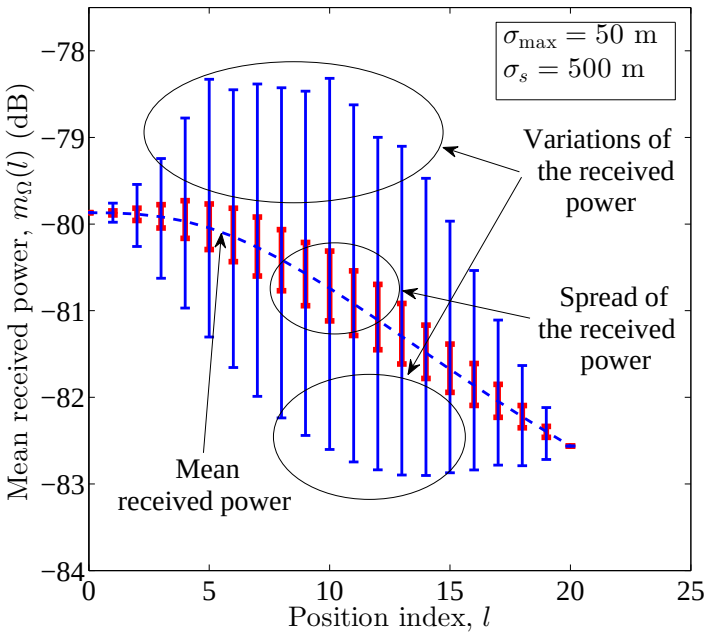

Figure F.8: The mean received power (path loss) $m_\Omega(l)$ as well as the spread $\sigma_\Omega(l)$ of the local received power (shadow fading) in the position index l.

at the north east of the MS) is shown in purple (see Fig. F.2). At $l = 0$, this scatterer has the greatest distance to the MS (the origin), thus the wave retransmitted from S_4 results in the largest delay $\tau_4'(0)$ component as shown in Fig. F.9. Referring to Fig. F.2, the total travelling distance of the 4th plane wave ($\tau_4'(l)$), however, decreases when the MS moves toward the destination point, which is located in a close vicinity of S_4. This can also be observed in Fig. F.9, where the purple part (associated with $\tau_4'(l)$) of the plot tends to smaller delays as l increases. The contribution of the other scatterers can also be tracked in Fig. F.9. This is, however, difficult if the number of scatterers increases. It is also noteworthy that for a given l, the farthest (nearest) scatterer to the MS results in the lowest (highest) PDP $S_{\tau'}(\tau';l)$ as shown in Fig. F.9. This can be confirmed by the fact that the power of each plane wave decreases by increasing its travelling distance, which has been modelled by $c_n(l) = CD_n^{-\gamma/2}(l)$ in this paper. Another important observation in Fig. F.9 is the variation of the delay spread in l. As can be observed, the delay spread first increases and then decreases (look at each colour and follow its spread when l increases). The reason is similar to what has been discussed in the interpretation of Fig. F.4. Since the starting and the terminating point of the trajectory are always fixed, the PDFs $p_{\tau'_n}(\tau';0)$ and $p_{\tau'_n}(\tau';L)$ tend to the delta function located at $\tau'_n(0)$

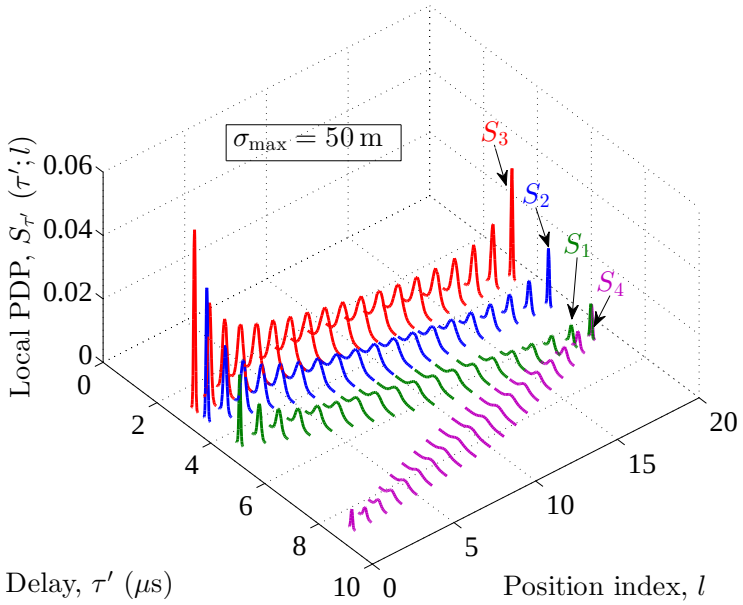

Figure F.9: The local PDP $S_{\tau'}(\tau';l)$ (see (F.18)) in the position index l, illustrating the contribution of each scatterer.

and $\tau'_n(L)$, respectively. For visual reasons, however, we omit these delta functions (associated with each scatterer). The observed maximum delay spread at $l = 10$ can be attributed to the fact that the maximum variations of $\mathscr{T}$ happen almost in the middle of the travelling path (see Section IV).

Fig. F.9 represents the local PSD $S_{\mu\mu}(f;l)$ (see (F.20)) in the position index l, where $\sigma_{\max}$ has been set to 50 m. The interpretation of this figure is very similar to that of the previous one, but in the frequency domain. Referring to Fig. F.2, for all values of l, the wave emitted from S_1 arrives at the MS with the AOA $\alpha_n^R(l)$ almost equal to the AOM $\alpha_v(l)$ of the MS. Therefore, this scatterer causes the maximum negative Doppler shift of about -60 Hz (see the green part of the plot). On the contrary, the scatterer located almost always in the front of the MS, i.e., S_4 results in the maximum positive Doppler shift of about 60 Hz (see the purple part of the plot). Nevertheless, the PSD $S_{\mu\mu}(f;l)$ associated with S_4 is much smaller than that pertinent to S_1. The reason is that the travelling distance of the 4th plane wave is much longer than that of the first scatterer S_1, thus the attenuation effect is much higher. Worth mentioning is also the red part (associated with S_3) of the PSD $S_{\mu\mu}(f;l)$. This part starts with a positive mean Doppler shift and ends with a negative one. This variation can be tracked in Fig. F.2, where the wave retransmitted from S_3, first

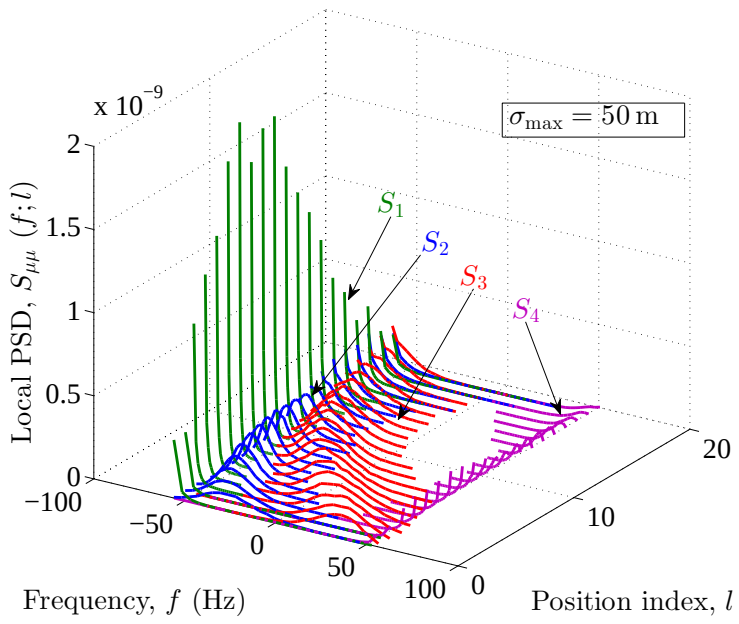

Figure F.10: The local PSD $S_{\mu\mu}(f;l)$ (see (F.20)) in the position index l, illustrating the contribution of each scatterer.

arrives at the front of the MS and then at its back. The variations of the Doppler spread along l can be explained in the same way as for the delay spread. An important difference, however, is that the PSD $S_{\mu\mu}(f;l)$ does not tend to the delta function at $l = 0$ ($l = 19$), as the AOM $\alpha_v(0)$ ($\alpha_v(19)$) of the MS varies from realization to realization.

VIII. CONCLUSION

In this paper, we have introduced a new approach for modelling non-stationary mobile fading channels. The new approach is based on random trajectories of the MS, rather than random distributions of scatterers. The new approach enables us to obtain required channel characteristics even if the number of scatterers is very limited. We have used a random trajectory model based on the primitives of BFs to develop a non-stationary channel model that captures multi-scale fading. The new model is physically explainable, as it is based on the additive multipath fading propagation mechanism. To model the path loss, we have allowed the path gains to be determined by the travelling distance of the corresponding plane waves, while the randomness of each distance generates large-scale fading. In this connection, we have shown that the local received power follows closely a Gaussian process in

logarithmic scale, while the envelope of the channel can be well-approximated by a Suzuki process. The Suzuki process is reported to be the best for the modelling of real-life channels showing different scales of fading. It has been demonstrated that the proposed model enables two degrees of freedom to control the spread of shadow fading, while this spread is weakly affected by the position of the BS. We have also derived and displayed the local PDP process and the local PSD process. It has been shown that these quantities vary in position, confirming that the proposed channel is non-stationary. We have shown that if the channel is sparse enough, the contribution of each scatterer to these quantities can be tracked, individually.

In future works, the new approach can be applied to develop new channel models with other objectives than capturing multi-scale fading. In addition, the utilized random trajectory model in this paper can be substituted by other trajectory models to see whether the same performance can be obtained or not.

APPENDIX F.A

PROOF OF THEOREM 1

It has been shown in [12] that the first-order density of $x(l)$ in (F.1) is a normal distribution of the form $N(m_x(l), \sigma_x^2(l))$, where the mean $m_x(l)$ and the variance $\sigma_x^2(l)$ are given by $x_s + l\delta_x$ and

$$\sigma_x^2(l) = \sigma_x^2 \frac{l^2 L}{3} \left(1 - \frac{l}{L}\right)^2 \tag{F.21}$$

respectively. The same statement holds for the first-order density of $y(l)$, provided that we replace the index x by y. This allows us to conclude that $(x_n^S - x(l))$ and $(y_n^S - y(l))$ are also normal processes of the form $N(x_n^S - m_x(l), \sigma_x^2(l))$ and $N(y_n^S - m_y(l), \sigma_y^2(l))$, respectively. The process $D_n^{S-MS}(l)$ can then be considered as the envelope of a complex Gaussian distribution with $(x_n^S - x(l))$ and $(y_n^S - y(l))$ as its inphase and quadrature component. The phase and the envelope of complex Gaussian processes with correlated quadratures and non-identical means (variances) have been studied in [35] and [36]. Herein, the correlation ρ between the inphase and quadrature components is zero, as $x(l)$ and $y(l)$ are independent processes (see [12]). Setting $\rho = 0$ in the envelope distribution in [36, Eq. (1)], and

assuming $\sigma_x = \sigma_y$ gives

$$p_{D_n^{S-MS}}(d'_n;l) = \frac{d'_n}{\sigma_x^2(l)} \exp\left\{ -\frac{(x_n^S - m_x(l))^2}{2\sigma_x^2(l)} - \frac{(y_n^S - m_y(l))^2 + d'^2_n}{2\sigma_x^2(l)} \right\} \times I_0\left(\frac{\sqrt{(x_n^S - m_x(l))^2 + (y_n^S - m_y(l))^2}}{\sigma_x^2(l)} d'_n \right). \quad \text{(F.22)}$$

With reference to (F.4), the total distance process $D_n(l) = D_n^{BS-S} + D_n^{S-MS}(l)$ is a linear function of $D_n^{S-MS}(l)$. Considering the first-order density $p_{D_n^{S-MS}}(d'_n;l)$ of $D_n^{S-MS}(l)$ in (F.22) and applying the concept of transformation of random variables give the PDF in (F.5).

REFERENCES

[1] A. Ispas, G. Ascheid, C. Schneider, and R. Thomä, "Analysis of local quasi-stationarity regions in an urban macrocell scenario," in *Proc. 71th IEEE Vehicular Technology Conference, VTC 2010-Spring*. Taipei, Taiwan, May 2010.

[2] A. Gehring, M. Steinbauer, I. Gaspard, and M. Grigat, "Empirical channel stationarity in urban environments," in *Proc. 4th European Personal Mobile Communications Conference*. Vienna, Austria, Feb. 2001.

[3] D. Umansky and M. Pätzold, "Stationarity test for wireless communication channels," in *Proc. IEEE Global Communications Conference, IEEE GLOBECOM 2009*. Honolulu, Hawaii, USA, Nov./Dec. 2009.

[4] A. Paier, J. Karedal, N. Czink, C. Dumard, T. Zemen, F. Tufvesson, A. F. Molisch, and C. F. Mecklenbräucker, "Characterization of vehicle-to-vehicle radio channels from measurements at 5.2 GHz," *Wireless Personal Communications (WPC)*, vol. 50, no. 1, pp. 19–32, Jul. 2009.

[5] G. Matz, "On non-WSSUS wireless fading channels," *IEEE Trans. Wireless Commun.*, vol. 4, no. 5, pp. 2465–2478, Sep. 2005.

[6] A. Ghazal, C.-H. Wang, H. Haas, M. Beach, X. Lu, D. Yuan, and X. Ge, "A non-stationary MIMO channel model for high-speed train communication systems," in *Vehicular Technology Conference (VTC Spring), 2012 IEEE 75th*, May 2012, pp. 1–5.

[7] A. Chelli and M. Pätzold, "A non-stationary MIMO vehicle-to-vehicle channel model based on the geometrical T-junction model," in *Proc. International*

Conference on Wireless Communications and Signal Processing, WCSP 2009. Nanjing, China, Nov. 2009.

[8] J. Karedal, F. Tufvesson, N. Czink, A. Paier, C. Dumard, T. Zemen, C. F. Mecklenbräuker, and A. F. Molisch, "A geometry-based stochastic MIMO model for vehicle-to-vehicle communications," *IEEE Trans. Wireless Commun.*, vol. 8, no. 7, pp. 3646–3657, Jul. 2009.

[9] A. Borhani and M. Pätzold, "A novel non-stationary channel model utilizing Brownian random paths," *In press, REV Journal on Electronics and Communications, 2014*.

[10] ——, "A non-stationary one-ring scattering model," in *Proc. IEEE Wireless Commun. and Net. Conf. (WCNC'13)*. Shanghai, China, Apr. 2013.

[11] ——, "A highly flexible trajectory model based on the primitives of Brownian fields—part I: Fundamental principles and implementation aspects," *Under review, IEEE Trans. Wireless Commun.*

[12] ——, "A highly flexible trajectory model based on the primitives of Brownian fields—part II: Analysis of the statistical properties," *Under review, IEEE Trans. Wireless Commun.*

[13] J. Salo, L. Vuokko, H. M. El-Sallabi, and P. Vainikainen, "An additive model as a physical basis for shadow fading," *IEEE Trans. Veh. Technol.*, vol. 56, no. 1, pp. 13–26, Jan 2007.

[14] H. Suzuki, "A statistical model for urban radio propagation," *IEEE Trans. Commun.*, vol. 25, no. 7, pp. 673–680, Jul. 1977.

[15] F. Hansen and F. I. Meno, "Mobile fading—Rayleigh and lognormal superimposed," *IEEE Trans. Veh. Technol.*, vol. 26, no. 4, pp. 332–335, Nov. 1977.

[16] M. J. Marsan, G. C. Hess, and S. S. Gilbert, "Shadowing variability in an urban land mobile environment at 900 MHz," *Electronics Letters*, vol. 26, no. 10, pp. 646–648, May 1990.

[17] J. E. Berg, R. Bownds, and F. Lotse, "Path loss and fading models for microcells at 900 MHz," in *42nd IEEE Vehicular Technology Conference*, May 1992, pp. 666–671.

[18] S. Mockford, A. M. D. Turkmani, and J. D. Parsons, "Local mean signal variability in rural areas at 900 MHz," in *40th IEEE Vehicular Technology Conference*, May 1990, pp. 610–615.

[19] A. Mawira, "Models for the spatial correlation functions of the (log)-normal component of the variability of VHF/UHF field strength in urban environment," in *Third IEEE Int. Symp. on Personal, Indoor and Mobile Radio Communications, PIMRC '92.*, Oct. 1992, pp. 436–440.

[20] S. Kozono and K. Watanabe, "Influence of environmental buildings on UHF land mobile radio propagation," *IEEE Trans. Commun.*, vol. 25, no. 10, pp. 1133–1143, Oct. 1977.

[21] N. B. Mehta, J. Wu, A. F. Molisch, and J. Zhang, "Approximating a sum of random variables with a lognormal," *IEEE Trans. Wireless Commun.*, vol. 6, no. 7, pp. 2690–2699, Jul. 2007.

[22] A. F. Molisch, "Ultrawideband propagation channels—theory, measurement, and modeling," *IEEE Trans. Veh. Technol.*, vol. 54, no. 5, Sep. 2005.

[23] K. T. Wong, Y. I. Wu, and M. Abdulla, "Landmobile radiowave multipaths' DOA-distribution: Assessing geometric models by the open literature's empirical datasets," *IEEE Trans. Antennas Propag.*, vol. 58, no. 3, pp. 946–958, Mar. 2010.

[24] A. Borhani and M. Pätzold, "A unified disk scattering model and its angle-of-departure and time-of-arrival statistics," *IEEE Trans. Veh. Technol.*, vol. 62, no. 2, pp. 473–485, Feb. 2013.

[25] T. Camp, J. Boleng, and V. Davies, "A survey of mobility models for ad hoc network research," *Wireless Communications and Mobile Computing*, vol. 2, no. 5, pp. 483–502, Sep. 2002.

[26] F. Bai and A. Helmy, *A Survey of Mobility Modeling and Analysis in Wireless Adhoc Networks*. Book chapter in: Wireless Ad Hoc and Sensor Networks, Kluwer academic Publishers, 2004.

[27] J. Härri, F. Filali, and C. Bonnet, "Mobility models for vehicular ad hoc networks: a survey and taxonomy," *IEEE Communications Surveys & Tutorials*, vol. 11, no. 4, pp. 19–41, 2009.

[28] G. Stüber, *Principles of Mobile Communications*, 3rd ed. Springer, 2011.

[29] W. C. Jakes, Ed., *Microwave Mobile Communications*. Piscataway, NJ: IEEE Press, 1994.

[30] M. Pätzold, *Mobile Fading Channels*, 2nd ed. Chichester: John Wiley & Sons, 2011.

[31] T. K. Sarkar, Z. Ji, K. Kim, A. Medouri, and M. Salazar-Palma, "A survey of various propagation models for mobile communication," *Antennas and Propagation Magazine, IEEE*, vol. 45, no. 3, pp. 51–82, Jun. 2003.

[32] C. Phillips, D. Sicker, and D. Grunwald, "A survey of wireless path loss prediction and coverage mapping methods," *Communications Surveys Tutorials, IEEE*, vol. 15, no. 1, pp. 255–270, 2013.

[33] A. Papoulis, *Probability, Random Variables, and Stochastic Processes*, 3rd ed. New York: McGraw-Hill, 1991.

[34] I. S. Gradshteyn and I. M. Ryzhik, *Table of Integrals, Series, and Products*, 7th ed. Elsevier Academic Press, 2007.

[35] V. A. Aalo, G. P. Efthymoglou, and C. Chayawan, "On the envelope and phase distributions for correlated Gaussian quadratures," *IEEE Communications Letters*, vol. 11, no. 12, pp. 985–987, 2007.

[36] P. Dharmawansa, N. Rajatheva, and C. Tellambura, "Envelope and phase distribution of two correlated Gaussian variables," *IEEE Transactions on Communications*, vol. 57, no. 4, pp. 915–921, 2009.

[37] M. Pätzold and G. Rafiq, "Sparse multipath channels: Modelling, analysis, and simulation," in *Personal Indoor and Mobile Radio Communications (PIMRC), 2013 IEEE 24th International Symposium on*, Sept 2013, pp. 30–35.

[38] G. D. Durgin, *Space-Time Wireless Channels*. NJ: Prentice-Hall, 2003.

[39] G. C. Hess, *Handbook of Land-Mobile Radio System Coverage*. Norwood, MA: Artech House, 1997.

[40] A. W. F. Edwards, *Likelihood*. Cambridge University Press, 1992.

[41] B. K. et al., "UWB channel characterization in outdoor environments," *IEEE, Tech. Rep. Document IEEE P802.15-15-04-0440-00-004a*, pp. 1–6, Aug. 2004.

Appendix G

Paper VII

Title:	A Novel Non-Stationary Channel Model Utilizing Brownian Random Paths
Authors:	**Alireza Borhani** and Matthias Pätzold
Affiliation:	University of Agder, Faculty of Engineering and Science, P. O. Box 509, NO-4898 Grimstad, Norway
Journal:	*REV Journal on Electronics and Communications (JEC)*, in press.

A Novel Non-Stationary Channel Model Utilizing Brownian Random Paths

Alireza Borhani and Matthias Pätzold

***Abstract* — This paper proposes a non-stationary channel model in which real-time dynamics of the mobile station (MS) are taken into account. We utilize Brownian motion (BM) processes to model targeted and non-targeted dynamics of the MS. The proposed trajectory model consists of both drift and random components to capture both targeted and non-targeted motions of the MS. The Brownian trajectory model is then employed to provide a non-stationary channel model, in which the scattering effects of the propagation area are modelled by a non-centred one-ring geometric scattering model. The starting point of the motion is a fixed point in the propagation environment, whereas its terminating point is a random point along a predetermined drift. The drift component can be controlled by a so-called drift parameter. Tracking the MS on the proposed Brownian path allows us to derive the local angles-of-arrival (AOAs) and local angles-of-motion (AOMs), which are expressed by stochastic processes rather than random variables. We compute the first-order densities of the AOA and AOM processes in closed form. The local power spectral density (PSD) of the Doppler frequencies and the autocorrelation function (ACF) of the complex channel gain are also provided. Given a walking speed scenario, the analytical results are demonstrated and explained in depth. It turns out that the proposed Brownian path model results in a non-stationary non-isotropic channel model. The proposed geometry-based channel model is very useful for the performance analysis of mobile communication systems under non-stationary conditions.**

***Index terms* — Brownian motion processes, non-stationary channels, targeted motions, non-targeted motions, non-centred one-ring scattering model.**

The material in this paper was presented in part at the 6th International Conference on Advanced Technologies for Communications (ATC'13), Ho Chi Minh City, Vietnam, Oct. 2013, and the World Congress on Engineering and Computer Science (WCECS'13), UC Berkeley, USA, Oct. 2013. The corresponding conference papers received the Best Paper Award from ATC'13 and the Certificate of Merit from WCECS'13.

A. Borhani and M. Pätzold are with the Faculty of Engineering and Science, University of Agder, 4898 Grimstad, Norway (e-mails: {alireza.borhani, matthias.paetzold}@uia.no).

I. INTRODUCTION

Channel modelling is recognized as one of the fundamental tasks in the advancement of communication systems. There exist three major approaches to channel modeling: deterministic, stochastic, and geometry-based [1]. Among them, geometric channel models have been found very suitable for modelling non-stationary environments [1–3]. However, most of the geometric channel models proposed in the literature have been simplified under the assumption that the stochastic radio channel is stationary in time. By considering a very short observation time instant, the AOM and AOA at the MS can be assumed as random variables such that the stationarity assumption holds. The one-ring scattering model [4–6] and the unified disk scattering model (UDSM) [7] are two examples chosen from the list of stationary channel models in [8] and [7].

Many empirical and analytical investigations, e.g., [9–11], however, reveal that the stationarity of the channel is only valid for extremely short travelling distances [12]. The potential suitability of geometric channel models for explaining non-stationary environments [1–3] on the one hand, and the results of real-life measurement campaigns [9–11] on the other hand, encourage us to study geometric channel models under non-stationary conditions.

The number of analytical investigations [13–16] with the focus on the statistical properties of non-stationary channels is very limited. For instance, none of the established geometric scattering models listed in [7, 8] has been studied under non-stationary conditions. The only exception is the non-stationary one-ring scattering model studied in [17–19], in which it is assumed that the MS travels along either a straight line [17], or a semi-random path with drift [18], or a totally random path [19]. Accordingly, considering the proposed paths in a ring of scatterers allowed us to propose a non-stationary channel model. A disadvantage of the model in [18] is that the path model has been equipped with a Brownian random component only along one of the axes of the Cartesian coordinate system. This randomness is then mapped to the other axis via the slope of the drift. Therefore, the randomness might disappear if the slope is too high (low).

In this paper, we allay the aforementioned drawback by proposing a path model in which two independent BM processes are assigned to model the random components of the path along each axis. In this regard, the strength of the random components can be controlled by a simple parameter. We also extend the path model of [18] by equipping the model with a so-called drift parameter. This parameter controls the presence of the deterministic drift components along the axes. Accordingly, the straight (line) path model in [17] is obtained from the proposed model if

only the drift components exist, but not the random components; the targeted path model (modified and generalized version of the one in [18]) is attained if both the random and drift components exist; the non-targeted path model in [19] is achieved if the random components exist, but the drift components do not. To capture the scattering effects of the propagation environment, the proposed path is supposed to be surrounded by a ring of uniformly distributed scatterers.

By tracking the MS along the proposed Brownian path, we are able to derive the local AOAs and the local AOMs. These quantities are modelled by stochastic processes instead of random variables. We provide the first-order density of the AOA and AOM processes in closed form. In addition, the local PSD of the Doppler frequencies and ACF of the complex channel gain are computed. Considering the operating frequency of the universal mobile telecommunications system (UMTS), we perform numerical computations for a walking speed scenario. The analytical results are displayed to confirm the non-stationarity of the channel model. It is proved that non-stationarity in time is not in line with the common isotropic propagation assumption on the channel. Furthermore, it is shown that the stationary one-ring scattering model [4–6] can be obtained as a special case of the proposed channel model.

The rest of this paper is organized as follows. BM processes are reviewed briefly in Section II, whereas Section III employs BM processes to provide the Brownian path model. Section IV presents the propagation scenario by means of the non-centred one-ring scattering model. Section V derives the complex channel gain of the proposed channel model. Its statistical properties are investigated in Section VI. Numerical results are provided in Section VII. Eventually, the summary of our findings and the conclusions are drawn in Section VIII.

II. REVIEW OF BROWNIAN MOTION PROCESSES

A standard BM process $\{B(t) : t \in [0,T]\}$ is a Wiener process with normally and independently distributed increments, satisfying the following conditions:

1. $B(0) = 0$.

2. $\forall\ 0 \leq s < t \leq T$, the increment $B(t) - B(s)$ is a normally distributed random variable with zero mean and variance $t - s$, i.e., $B(t) - B(s) \sim N(0, t-s)$.

3. $\forall\ 0 \leq s < t < u < v \leq T$, the non-overlapping increments $B(t) - B(s)$ and $B(v) - B(u)$ are statistically independent.

BM processes have a broad range of applications in different branches of science, such as in economy, medical science, and engineering. Stock market analysis, diagnosis imaging, and fractal theory [20] are some examples, which benefit from BM processes in practice. In mobile ad hoc networks, 2D BM processes known as the random walk mobility model, are also used to model atypical motions of mobile nodes [21]. The mobility model is then used to perform network layer analysis. In addition, three-dimensional BM processes have been used to model fully random motions of mobile users in the Euclidian space [22].

III. PATH MODELLING

In what follows, we utilize the spatial representation of the BM process provided in [18]. This representation enables us to introduce a spatial path model rather than a temporal one. Notice that the spatial representation of the path allows us to consider numerous speed scenarios for the MS.

A. Spatial Representation of Brownian Motion Processes

We assume that the MS starts its motion from a predefined point with Cartesian coordinates (x_s, y_s) in the two-dimensional (2D) plane. Moreover, let the point (x_d, y_d) denote a reference point (the potential destination point) along the drift of the path. Following the procedure described in [18], we introduce the spatial stochastic process $B(x)$ over the range $[x_s, x_d]$, satisfying the following conditions:

1. $B(x_s) = 0$.
2. $\forall\ x_s \leq x_p < x \leq x_d$, the increment $B(x) - B(x_p)$ is a normally distributed random variable with zero mean and variance $x - x_p$, i.e., $B(x) - B(x_p) \sim N(0, x - x_p)$.
3. $\forall\ x_s \leq x_p < x < x_q < x_m \leq x_d$, the non-overlapping increments $B(x) - B(x_p)$ and $B(x_m) - B(x_q)$ are statistically independent.

Computational reasons encourage us to consider the spatial BM process at discrete values of x. Accordingly, we define $\Delta x = (x_d - x_s)/L$ for some positive integer L. We also let $B_l^{(x)}$ denote the BM process at $x_l = x_s + l\Delta x$ $(l = 0, 1, ..., L)$. Referring to the last two conditions of the spatial stochastic process $B(x)$, one can conclude that $B_l^{(x)} = B_{l-1}^{(x)} + \Delta B_l^{(x)}$, where the increment $\Delta B_l^{(x)}$ is a normally distributed random variable of the form $N(0, \Delta x)$.

The same procedure can be followed to obtain the spatial stochastic process $B(y)$ over the range $[y_s, y_d]$. Analogously, let $\Delta y = (y_d - y_s)/L$ stand for the deterministic

increment along the y-axis. In addition, let the spatial stochastic process $B_l^{(y)}$ denote the BM process at $y_l = y_s + l\Delta y$. A direct consequence is the equality $B_l^{(y)} = B_{l-1}^{(y)} + \Delta B_l^{(y)}$ in which $\Delta B_l^{(y)}$ follows the Gaussian distribution of the form $N(0, \Delta y)$.

B. The Brownian Path Model

To model motions of the MS in the 2D plane, we propose a path with deterministic drift components along each axis. The fluctuations of the path are modeled by two independent spatial BM processes $B_l^{(x)}$ and $B_l^{(y)}$ associated with the $x-$ and $y-$axis, respectively. Accordingly, the path $\mathscr{P}$ of the MS is modelled by means of

$$\mathscr{P}: \left\{ (x_l, y_l) \;\middle|\; \begin{array}{l} x_l = x_s + k_d l\Delta x + \sigma_x B_l^{(x)} \\ y_l = y_s + k_d l\Delta y + \sigma_y B_l^{(y)} \end{array} \right\} \tag{G.1}$$

where $l = 0, 1, ..., L$ is the position index, and the drift parameter k_d is to manage the behaviour of the deterministic drift components along each axis. Furthermore, the variable σ_x (σ_y) controls the randomness of the path along the $x-$axis ($y-$axis). Notice that the randomness of the path $\mathscr{P}$ originates inherently from the randomness of the BM process B_l. Therefore, the parameters σ_x and σ_y provide additional degrees of freedom to magnify (attenuate) the randomness.

In what follows, we study several important special cases, which simplify the model in (G.1) to the path models proposed in [17–19]. We also remark some potential applications of the proposed path model.

C. Special Cases

A very simple path model can be obtained from (G.1) if we set $\sigma_x = \sigma_y = 0$, which ignores the random components of the path. In this case, if the drift components exist, i.e., $k_d = 1$, then the straight-line path model proposed in [17] can be attained as a special case. This model is useful to explain very smooth paths, beginning from a starting point and ending at a terminating point in the 2D plane.

The path model of [18] can also be obtained as a special case of the model in (G.1) if we set $\sigma_x = 0$ and $k_d = 1$. In this case, the only random component of the path is along the $y-$axis. The drawback of such a model is that by increasing the slope of the drift, the random component will be faded. Nevertheless, the targeted Brownian path model in (G.1) has been equipped with two independent random components, i.e., $B_l^{(x)}$ and $B_l^{(y)}$, describing the fluctuations of the path along each axis. In mobile communications, the proposed path model can be used to explain typical dynamics of users in motion, such as pedestrians walking along a street, but not necessarily along a very smooth path. In vehicular communications, the model

can be utilized to describe jittery motions of the vehicle antenna, while the vehicle is moving along a road.

Another important special case is obtained by ignoring the drift components, i.e., $k_d = 0$. By doing so, the path model in (G.1) reduces to the non-targeted Brownian path model proposed in [19]. This model is known as the random walk mobility model, which is very useful to explain irregular dynamics of mobile users.

IV. THE PROPAGATION SCENARIO

We use the non-centred one-ring scattering model [18] to capture the scattering effect caused by randomly distributed scatterers in a propagation area. Fig. G.1 presents the considered model with the uniform distribution of the local scatterers S_n $(n = 1, 2, ..., N)$ on a ring of radius R centered on the origin, but not necessarily on the MS. Referring to this figure, α_n^S denotes the angle-of-scatterer (AOS) pertinent to the nth scatterer S_n. At a reference point in time t_0, the MS starts its motion from (x_0, y_0) and moves along the path $\mathscr{P}$ to reach the terminating point (x_L, y_L) at time t_L. Subsequently, the position of the MS at time $t_l \in [t_0, t_L]$ is represented by Cartesian coordinates (x_l, y_l). We assume single-bounce scattering, meaning that a wave emitted from the BS arrives at the MS with the AOA $\alpha_n^R(l)$ after only one bounce due to the nth scatterer S_n. Concerning the velocity scenario, we assume that the MS is in motion with a constant speed of v_R in the direction indicated by the AOM $\alpha_v(l)$, which is determined by the Brownian path $\mathscr{P}$.

Two realizations of the proposed Brownian path $\mathscr{P}$ in such a geometric scattering model are shown in Figs. G.2 and G.3. It is assumed that the starting point of the path is the origin of the Cartesian system, while the destination point (x_d, y_d) is located at (100,100). The radius of the ring has also been set to $R = 300$ m. Fig. G.2 displays a realization of the targeted Brownian path in (G.1) with the parameters $k_d = 1$, $L = 100$, and $\sigma_x = \sigma_y = 3$. The drift of the path has also been shown by the dotted line. The illustrated path $\mathscr{P}$ varies from realization to realization. However, the general drift of the path does not change. Notice that averaging over different realizations of the targeted path results in a straight line (drift line) from (0,0) to (100,100). Fig. G.3 exhibits a realization of the non-targeted path $\mathscr{P}$ in (G.1), where $k_d = 0$, $L = 100$, and $\sigma_x = \sigma_y = 6$. As it can be observed from this figure, the path exhibits random walk behaviour.

The illustrated propagation scenarios in Figs. G.1–G.3 differ completely from the stationary one-ring channel model [4–6], in which the MS is located at the center of the ring of scatterers, while the AOM is a fixed value. Therein, assuming a very short observation time interval justifies a stationary and isotropic channel model,

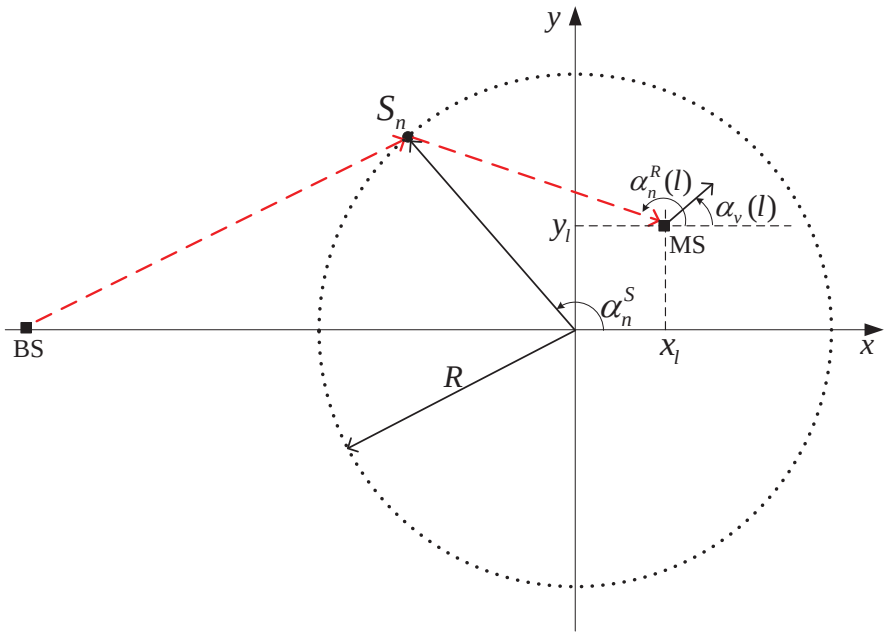

Figure G.1: The non-centred one-ring scattering model for a single-bounce scattering scenario.

while herein, the proposed path $\mathscr{P}$ results in a non-stationary non-isotropic channel model.

In what follows, we first provide an expression for the complex channel gain, and then we study the statistical characteristics of the proposed non-stationary channel model.

V. THE COMPLEX CHANNEL GAIN

For a typical fixed-to-mobile (F2M) scenario, the complex channel gain $\mu(t_l)$ of frequency-nonselective F2M channels is modeled by a complex stochastic process, representing the sum of all scattered components as follows [18]

$$\mu(t_l) = \lim_{N\to\infty} \sum_{n=1}^{N} c_n e^{j(2\pi f_n(t_l)t_l + \theta_n)}. \tag{G.2}$$

Note that $\mu(t_l)$ accounts for the effect of non-stationarity by the time-variant Doppler frequencies[1] $f_n(t_l)$ rather than the time-invariant one, i.e., f_n (see [24, p. 59]). In this equation, c_n stands for the attenuation factor caused by the physical interaction of the emitted wave with the nth scatterer S_n. In addition, the random

[1]The frequency shift caused by the Doppler effect is given by $f = f_{\max}\cos(\alpha)$, where $f_{\max} = f_0 v/c_0$ is the maximum Doppler frequency, f_0 denotes the carrier frequency, c_0 stands for the speed of light, and α equals the difference between the AOA and the AOM [23].

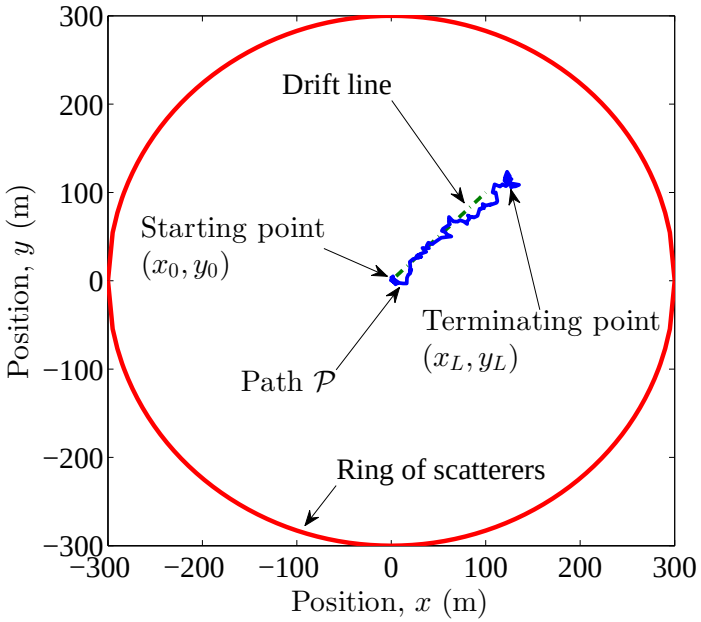

Figure G.2: Realization of a targeted Brownian path $\mathscr{P}$ in the ring of scatterers. The model parameters are $k_d = 1$, $L = 100$, $\sigma_x = \sigma_y = 3$, and $R = 300\,\text{m}$.

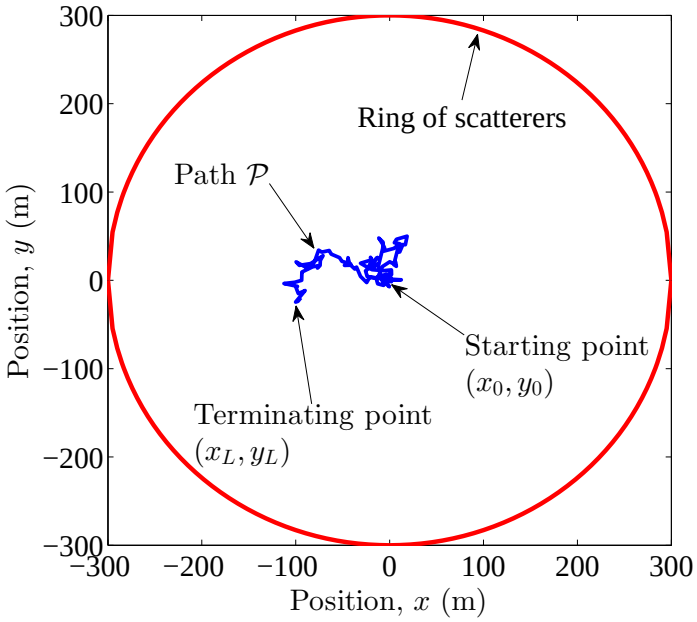

Figure G.3: Realization of a non-targeted Brownian path $\mathscr{P}$ in the ring of scatterers. The model parameters are $k_d = 0$, $L = 100$, $\sigma_x = \sigma_y = 6$, and $R = 300\,\text{m}$.

variable θ_n represents the phase shift of the nth path. It is assumed that θ_ns are independently and identically distributed random variables, each of which is uniformly distributed between $-\pi$ and π [24, p. 59].

VI. STATISTICAL CHARACTERISTICS OF THE CHANNEL MODEL

We start investigating the statistical properties of the complex channel gain in (G.2) by deriving the local AOA at the MS, which affects strongly other statistical quantities. In addition, we study the AOM process in detail. The AOA and AOM processes will then be used to extract the PSD of the Doppler frequencies. Finally, the ACF of the complex channel gain is derived from the provided PSD. We remark that the illustration of the analytical results is deferred to Section VII.

A. The Local Angles-of-Arrival

According to Fig. G.1, the AOA $\alpha_n^R(l)$ at the point (x_l, y_l) is computed as

$$\alpha_n^R(l) = \arctan\left(\frac{R\sin(\alpha_n^S) - y_l}{R\cos(\alpha_n^S) - x_l}\right). \tag{G.3}$$

For a given position index l, the only random variable on the right-hand side of (G.3) is the AOS α_n^S, which is assumed to be uniformly distributed between $-\pi$ and π (see Section IV). As the number N of local scatterers tends to infinity in the reference model, it is mathematically convenient to assume that the discrete AOS α_n^S is a continues random variable denoted by α^S. Referring to [18, 19], the first-order density $p_{\alpha^R}(\alpha^R; l)$ of the stochastic process $\alpha^R(l)$ in (G.3) is given by the following expression

$$p_{\alpha^R}(\alpha^R; l) = \frac{1}{2\pi}\left(1 - \frac{x_l\cos(\alpha^R) + y_l\sin(\alpha^R)}{\sqrt{R^2 - (x_l\sin(\alpha^R) - y_l\cos(\alpha^R))^2}}\right) \tag{G.4}$$

where $-\pi \leq \alpha^R < \pi$. It is worth mentioning that $p_{\alpha^R}(\alpha^R; l)$ in (G.4) depends heavily on the position (x_l, y_l) of the MS. This means that the AOA $\alpha^R(l)$ is first-order non-stationary. As a special case, if the path $\mathscr{P}$ crosses the ring's center $(0,0)$, then $p_{\alpha^R}(\alpha^R; l)$ in (G.4) reduces to $1/(2\pi)$, which is the AOA probability density function (PDF) of the stationary one-ring scattering model [4–6].

B. The Local Angles-of-Motion

The path $\mathscr{P}$ can be changed to a continues and piecewise differentiable path after applying simple linear interpolation techniques. Accordingly, the AOM $\alpha_v(l)$

at the point (x_l, y_l) can be written in the following form

$$\begin{aligned} \alpha_v(l) &= \arctan\left(\frac{y_{l+1}-y_l}{x_{l+1}-x_l}\right) \\ &= \arctan\left(\frac{k_d\Delta y+\sigma_y(B_{l+1}^{(y)}-B_l^{(y)})}{k_d\Delta x+\sigma_x(B_{l+1}^{(x)}-B_l^{(x)})}\right) \end{aligned} \tag{G.5}$$

where the terms $B_{l+1}^{(x)}-B_l^{(x)}$ and $B_{l+1}^{(y)}-B_l^{(y)}$ are two independent random variables of the forms $N(0,\Delta x)$ and $N(0,\Delta y)$, respectively (see Section III-A). Therefore, the AOM $\alpha_v(l)$ process can be considered as the phase of a complex Gaussian process given by $s_l=(x_{l+1}-x_l)+j(y_{l+1}-y_l)$, in which $x_{l+1}-x_l \sim N(k_d\Delta x,\sigma_x^2\Delta x)$ and $y_{l+1}-y_l \sim N(k_d\Delta y,\sigma_y^2\Delta y)$. The phase of the complex Gaussian distribution with non-identical means and variances has been studied in [25] and [26]. Herein, we avoid representing the first-order density of the AOM (the phase distribution), as it can readily be obtained by substituting the means and the variances of the underlying complex Gaussian process in [26, Eq. (2)]. As a special case, if the drift component does not exist, i.e., $k_d=0$, and $\sigma_x^2\Delta x=\sigma_y^2\Delta y$, then the AOM follows the uniform distribution defined over the range $(-\pi,\pi]$ (see [19]). For this special case, the AOM is first-order stationary.

C. The Local Power Spectral Density

The local Doppler frequency $f(l)$ is defined by a non-linear transformation of the local AOA $\alpha^R(l)$ and the local AOM $\alpha_v(l)$ of the MS. It follows

$$f(l)=f_{\max}\cos\left(\alpha^R(l)-\alpha_v(l)\right) \tag{G.6}$$

where $\alpha^R(l)$ is described statistically by the first-order density $p_{\alpha^R}(\alpha^R;l)$ in (G.4). Furthermore, $\alpha_v(l)$ describes the AOM at the point (x_l,y_l) after realizing the path $\mathscr{P}$ (see (G.5)). Therefore, the only random variable on the right-hand side of (G.6) is the AOA. This is in contrast with the procedure used in [18], where the AOM is also assumed to be a random variable. To obtain the first-order density $p_f(f;l)$ of the Doppler frequencies $f(l)$, we fix the position index l, and then we apply the concept of transformation of random variables. The result is shown in (G.7) [see the top of the next page], where

$$A_{\pm}(f;l)=\arctan\left(\frac{y_{l+1}-y_l}{x_{l+1}-x_l}\right)\pm\arccos\left(\frac{f}{f_{\max}}\right) \tag{G.8}$$

for $-f_{\max}\le f\le f_{\max}$.

$$p_f(f;l) = \frac{1}{2\pi f_{\max}\sqrt{1-(f/f_{\max})^2}} \times \left(2 - \frac{x_l \cos(A_+(f;l)) + y_l \sin(A_+(f;l))}{\sqrt{R^2 - (x_l \sin(A_+(f;l)) - y_l \cos(A_+(f;l)))^2}} - \frac{x_l \cos(A_-(f;l)) + y_l \sin(A_-(f;l))}{\sqrt{R^2 - (x_l \sin(A_-(f;l)) - y_l \cos(A_-(f;l)))^2}} \right) \tag{G.7}$$

With reference to [24, p. 85], the first-order density $p_f(f;l)$ of the Doppler frequencies is proportional to the local PSD $S_{\mu\mu}(f;l)$ of the complex channel gain $\mu(t_l)$. This allows us to present $S_{\mu\mu}(f;l)$ by the following expression

$$S_{\mu\mu}(f;l) = 2\sigma_0^2 p_f(f;l). \tag{G.9}$$

In the equation above, $2\sigma_0^2$ is the mean power of $\mu(t_l)$, and $p_f(f;l)$ is given by (G.7). For the special case that the path $\mathscr{P}$ crosses the ring's center $(0,0)$, the first-order density $p_f(f;l)$ in (G.7) reduces to

$$p_f(f;l) = \frac{1}{\pi f_{\max}\sqrt{1-(f/f_{\max})^2}} \tag{G.10}$$

which, after its multiplication by the mean power $2\sigma_0^2$, results in the Jakes PSD [23]. Notice that the Jakes PSD is not only associated with the stationary one-ring scattering model [4–6], but also with any other scattering model that is circularly symmetric with respect to the MS [7].

D. The Local Autocorrelation Function

The local ACF $r_{\mu\mu}(\tau;l)$ of the non-stationary complex channel gain $\mu(t_l)$ is obtained by taking the inverse Fourier transform of the local PSD $S_{\mu\mu}(f;l)$ in (G.9) (see [27, pp. 282-285]). Accordingly, one can write

$$r_{\mu\mu}(\tau;l) = \int_{-f_{\max}}^{f_{\max}} S_{\mu\mu}(f;l) e^{j2\pi f\tau} df. \tag{G.11}$$

For the special case that the path $\mathscr{P}$ goes across the ring's center, the local PSD $S_{\mu\mu}(f;l)$ in (G.10) can be employed to compute the inverse Fourier transform in (G.11). In this case, the local ACF $r_{\mu\mu}(\tau;l)$ in (G.11) reduces to $2\sigma_0^2 J_0(2\pi f_{\max}\tau)$,

where $J_0(\cdot)$ stands for the zeroth-order Bessel function of the first kind [28, Eq. (8.411.1)].

VII. NUMERICAL RESULTS

We use the operating frequency $f_0 = 2.1\,\text{GHz}$ of UMTS in our numerical computations. To study the effect of targeted and non-targeted travelling paths of the MS, the paths $\mathscr{P}$ shown in Figs. G.2 and G.3 have been used, respectively. Besides these two, we consider the path represented by a straight line from the starting point (0,0) to the terminating point (100,100). This path can be obtained either by averaging over different realizations of the targeted path shown in Fig. G.2, or by setting $\sigma_x = \sigma_y = 0$ in (G.1). Given these three different paths, we illustrate the statistical properties of the channel model in terms of the AOA at the MS, PSD of the Doppler frequencies, and the ACF of the complex channel gain. It is also assumed that the MS is moving with a speed v_R of 5 km/h, which equals an average walking speed. For the considered operating frequency, this speed allows a maximum Doppler frequency $f_{\max}$ of about 10 Hz. The mean power $2\sigma_0^2$ has been set to unity.

Figs. G.4–G.6 depict the first-order density $p_{\alpha^R}(\alpha^R;l)$ of the AOA process $\alpha^R(l)$ given in (G.4). In this regard, Fig. G.4 shows $p_{\alpha^R}(\alpha^R;l)$ of the AOA at the MS travelling along the targeted path $\mathscr{P}$ shown in Fig. G.2, while Fig. G.5 demonstrates that along the straight path. Furthermore, the non-targeted path shown in Fig. G.3 is used to display $p_{\alpha^R}(\alpha^R;l)$ in Fig. G.6. A common observation in the three figures is the uniform distribution of the AOA at $l = 0$, which can be attributed to the circularly symmetric starting point of the three paths. For the two targeted paths, the probability of receiving signals from the scatterers ahead (behind) decreases (increases) if the MS continues its motion along the path $\mathscr{P}$. However, this behaviour does not hold for the non-targeted path, in which the heading destination point is not subject to any drift. The irregular behaviour of $p_{\alpha^R}(\alpha^R;l)$ shown in Fig. G.6 is indeed due to the irregular behaviour of the path shown in Fig. G.3. In addition, as can be observed in Figs. G.4 and G.5, the lowest probability of receiving signals belongs to the average direction of the motion, i.e., the angle corresponds to the slope of the drift.

Figs. G.7–G.9 exhibit the local PSD $S_{\mu\mu}(f;l)$ presented in (G.9). The classical Jakes PSD (resembling a U-shape) can be observed for the stationary case ($l = 0$) in all these three figures. This is again due to the circularly symmetric position of the MS at the beginning of the motion. At this position, $S_{\mu\mu}(f,0)$ is a symmetric function with respect to f, justifying that the channel is isotropic at the origin. This property, however, does not hold if the MS moves along any of the paths $\mathscr{P}$. The

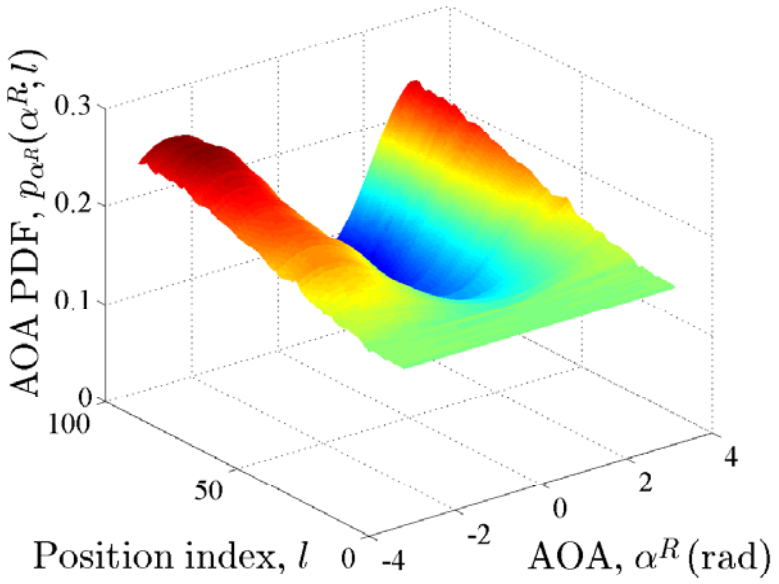

Figure G.4: The behavior of the first-order density $p_{\alpha^R}(\alpha^R; l)$ in (G.4) for the targeted path illustrated in Fig. G.2.

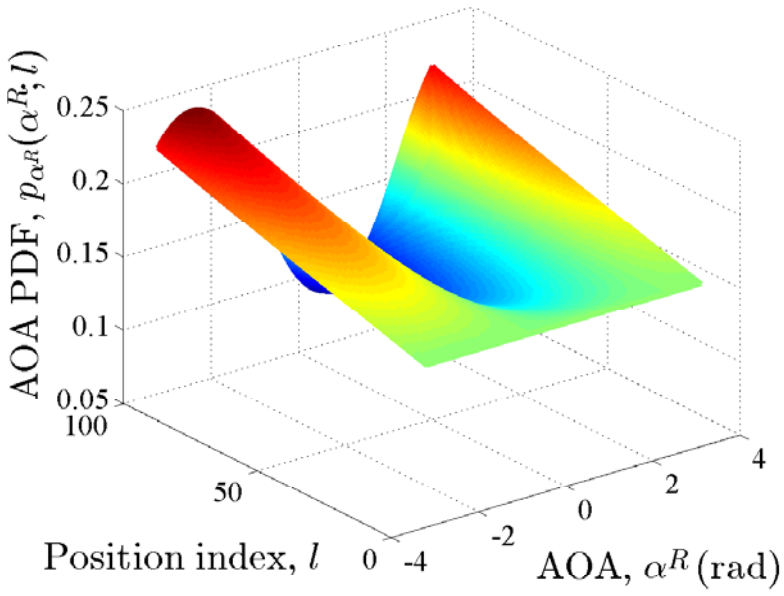

Figure G.5: The behavior of the first-order density $p_{\alpha^R}(\alpha^R; l)$ in (G.4) for the straight path (averaged targeted path).

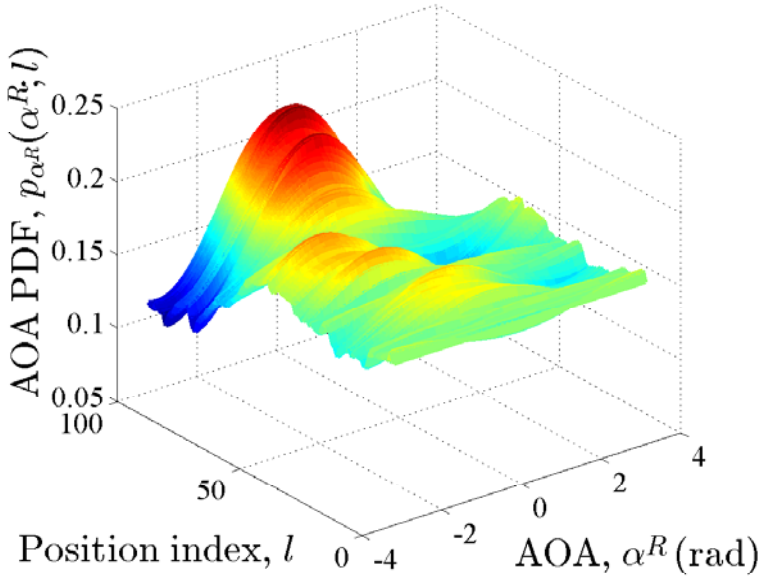

Figure G.6: The behavior of the first-order density $p_{\alpha^R}(\alpha^R; l)$ in (G.4) for the non-targeted path illustrated in Fig. G.3.

variations of the PSD in the three figures can be explained as follows. If the MS faces a lower number of scatterers ahead and a higher number of them behind, a higher probability of negative Doppler shifts can be expected. Otherwise, positive Doppler shifts occur with a higher probability. Given the two targeted paths, a higher and a lower probability of negative and positive Doppler shifts in Figs. G.7 and G.8 can be explained by the radial drift of these paths. Nevertheless, owing to the randomness of the path, some exceptions might be observed (see Fig. G.7).

Figs. G.10–G.12 demonstrate the absolute value of the local ACF $r_{\mu\mu}(\tau; l)$ provided in (G.11). Recalling that the PSD $S_{\mu\mu}(f; l)$ is in general asymmetric (see Figs. G.7–G.9), its inverse Fourier transform, i.e., the ACF $r_{\mu\mu}(\tau; l)$ in (G.11), is in general complex. Nonetheless, at the starting point $l = 0$, the three figures display ACFs $|r_{\mu\mu}(\tau; l)|$ of the form $2\sigma_0^2 |J_0(2\pi f_{\max}\tau)|$. With reference to Figs. G.10–G.12, the ACF varies in position (time), justifying that the proposed channel model is non-stationary. Referring to Figs. G.10 and G.11, the correlation grows by increasing l for a given value of $\tau \neq 0$. This growth, however, occurs with some fluctuations (see Fig. G.10), which are due to the randomness of the corresponding path (see Fig G.2). We finish this part by remarking that herein, the effect of changing motion patterns (path models) can better be observed (described) by plotting the PSD rather than the ACF.

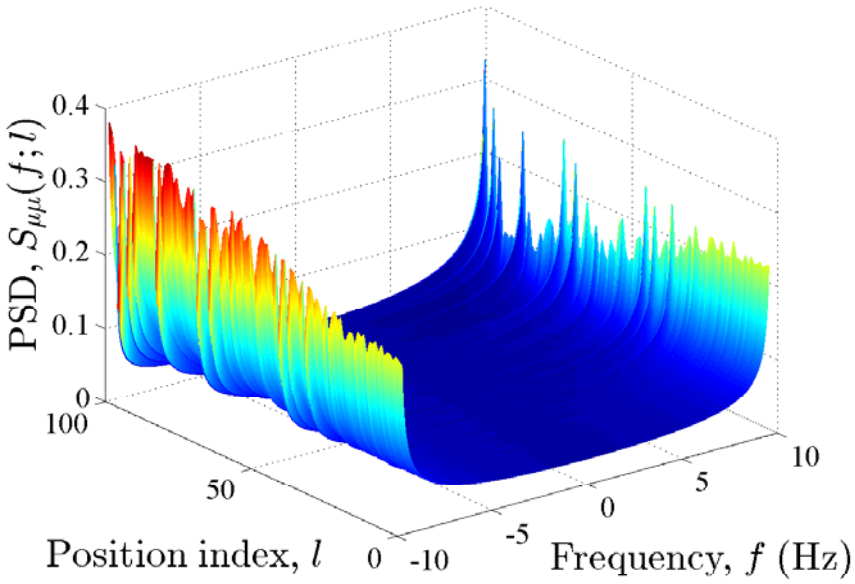

Figure G.7: The behavior of the local PSD $S_{\mu\mu}(f;l)$ in (G.9) for the targeted path illustrated in Fig. G.2.

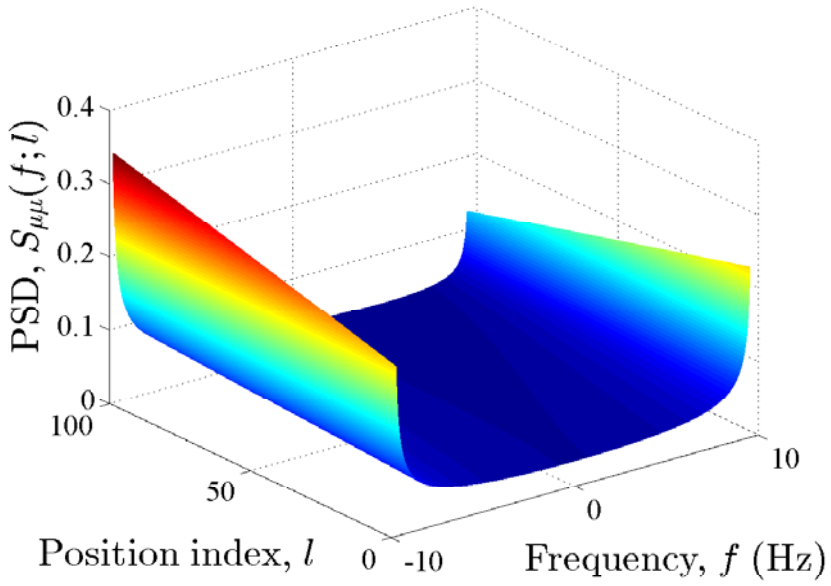

Figure G.8: The behavior of the local PSD $S_{\mu\mu}(f;l)$ in (G.9) for straight path (averaged targeted path).

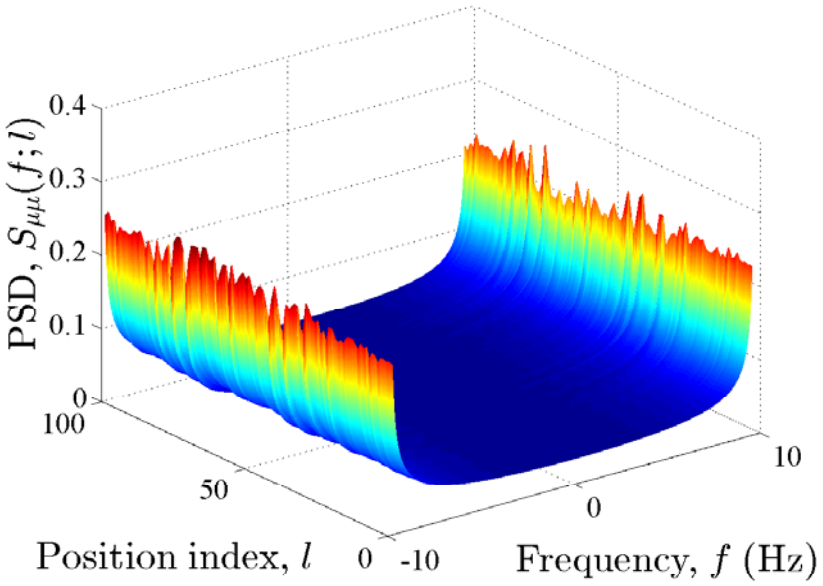

Figure G.9: The behavior of the local PSD $S_{\mu\mu}(f;l)$ in (G.9) for the non-targeted path illustrated in Fig. G.3.

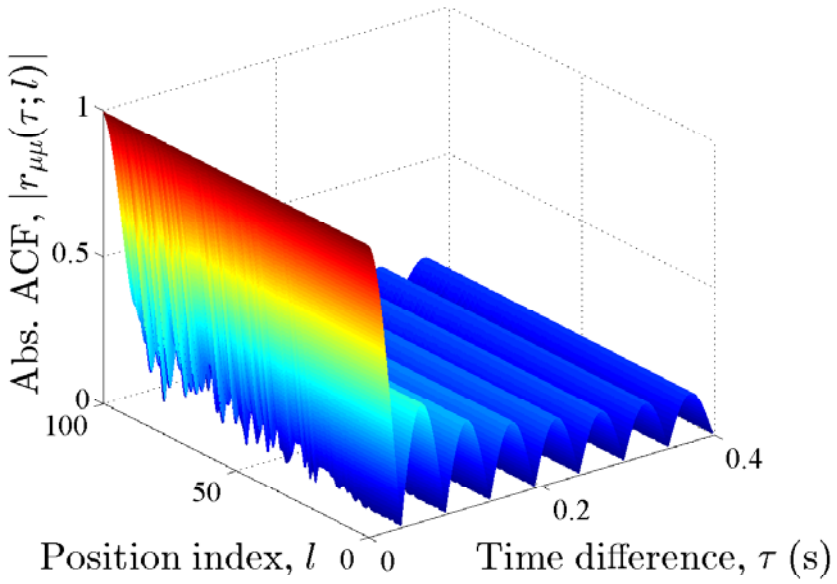

Figure G.10: The behavior of the absolute value of the local ACF $|r_{\mu\mu}(\tau;l)|$ (see (G.11)) for the targeted path illustrated in Fig. G.2.

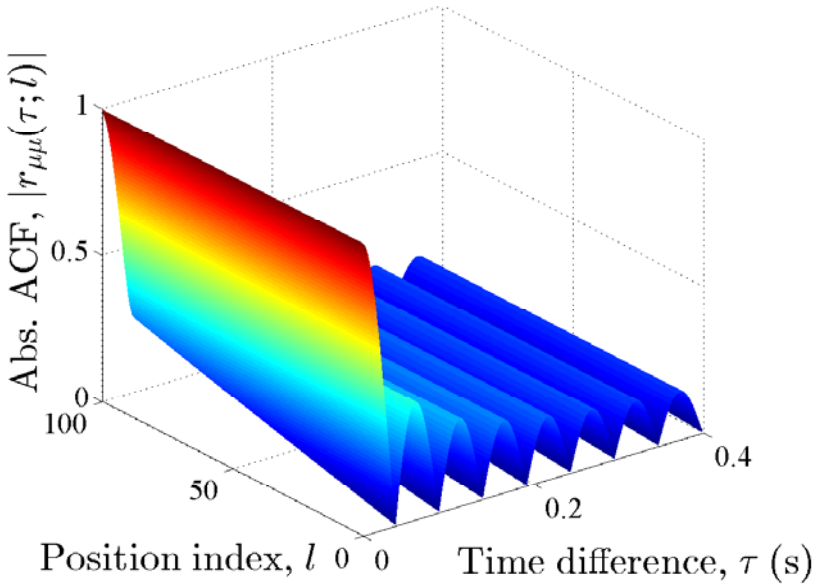

Figure G.11: The behavior of the absolute value of the local ACF $|r_{\mu\mu}(\tau;l)|$ (see (G.11)) for the straight path (averaged targeted path).

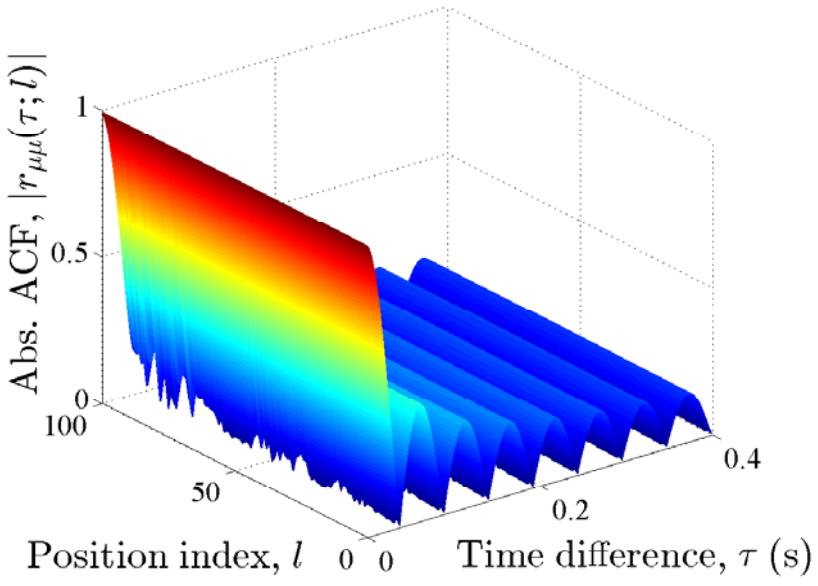

Figure G.12: The behavior of the absolute value of the local ACF $|r_{\mu\mu}(\tau;l)|$ (see (G.11)) for the non-targeted path illustrated in Fig. G.3.

VIII. CONCLUSION

This paper has proposed a Brownian path model to generate realistic trajectories of the MS. Particularity, the proposed path model unifies both targeted and non-targeted motions of the MS. We have employed the proposed path model to provide a non-stationary channel model. To cope with the scattering effect, we have utilized the non-centred one-ring scattering model, in which the MS is surrounded by a ring of scatterers centred not necessarily on the MS. By tracking the MS on the proposed Brownian path, we have derived analytical expressions for the time-varying AOA and AOM. The first-order densities of AOA and AOM processes have been computed. These processes have then been used to compute the PSD of the Doppler frequencies and the ACF of the complex channel gain. It has been shown that the proposed path model results in a non-stationary non-isotropic channel model. Nevertheless, the stationary isotropic one-ring scattering model can be obtained as a special case. Considering a walking speed scenario, we have illustrated the statistical characteristics of the proposed channel model. It has been shown that the AOA and AOM processes are in general first-order non-stationary, which implies that the PSD and ACF depend on time. We have also shown that the effect of changing mobility pattern can better be seen in the PSD as compared to the ACF of the complex channel gain. In future works, the analytical results will be verified by means of empirical data.

REFERENCES

[1] J. Karedal, F. Tufvesson, N. Czink, A. Paier, C. Dumard, T. Zemen, C. Mecklenbräuker, and A. Molisch, "A geometry-based stochastic MIMO model for vehicle-to-vehicle communications," *IEEE Trans. Wireless Commun.*, vol. 8, no. 7, pp. 3646–3657, Jul. 2009.

[2] A. F. Molisch, A. Kuchar, J. Laurila, K. Hugl, and R. Schmalenberger, "Geometry-based directional model for mobile radio channels—principles and implementation," *European Transactions on Telecommunications*, vol. 14, no. 4, pp. 351–359, Jul./Aug. 2003.

[3] A. F. Molisch, "A generic model for MIMO wireless propagation channels in macro- and microcells," *Signal Processing, IEEE Transactions on*, vol. 52, no. 1, pp. 61–71, 2004.

[4] D.-S. Shiu, G. J. Foschini, M. J. Gans, and J. M. Kahn, "Fading correlation and its effect on the capacity of multielement antenna systems," *IEEE Trans. Commun.*, vol. 48, no. 3, pp. 502–513, Mar. 2000.

[5] A. Abdi and M. Kaveh, "A space-time correlation model for multielement antenna systems in mobile fading channels," *IEEE J. Select. Areas Commun.*, vol. 20, no. 3, pp. 550–560, Apr. 2002.

[6] M. Pätzold and B. O. Hogstad, "A space-time channel simulator for MIMO channels based on the geometrical one-ring scattering model," in *Proc. 60th IEEE Semiannual Veh. Technol. Conf., VTC 2004-Fall*, vol. 1. Los Angeles, CA, USA, Sep. 2004, pp. 144–149.

[7] A. Borhani and M. Pätzold, "A unified disk scattering model and its angle-of-departure and time-of-arrival statistics," *IEEE Trans. Veh. Technol.*, vol. 62, no. 2, pp. 473–485, Feb. 2013.

[8] K. T. Wong, Y. I. Wu, and M. Abdulla, "Landmobile radiowave multipaths' DOA-distribution: Assessing geometric models by the open literature's empirical datasets," *IEEE Trans. Antennas Propag.*, vol. 58, no. 3, pp. 946–958, Mar. 2010.

[9] A. Ispas, G. Ascheid, C. Schneider, and R. Thomä, "Analysis of local quasi-stationarity regions in an urban macrocell scenario," in *Proc. 71th IEEE Vehicular Technology Conference, VTC 2010-Spring*. Taipei, Taiwan, May 2010.

[10] A. Gehring, M. Steinbauer, I. Gaspard, and M. Grigat, "Empirical channel stationarity in urban environments," in *Proc. 4th European Personal Mobile Communications Conference*. Vienna, Austria, Feb. 2001.

[11] D. Umansky and M. Pätzold, "Stationarity test for wireless communication channels," in *Proc. IEEE Global Communications Conference, IEEE GLOBECOM 2009*. Honolulu, Hawaii, USA, Nov./Dec. 2009.

[12] A. Paier, J. Karedal, N. Czink, C. Dumard, T. Zemen, F. Tufvesson, A. F. Molisch, and C. F. Mecklenbräucker, "Characterization of vehicle-to-vehicle radio channels from measurements at 5.2 GHz," *Wireless Personal Communications (WPC)*, vol. 50, no. 1, pp. 19–32, Jul. 2009.

[13] G. Matz, "On non-WSSUS wireless fading channels," *IEEE Trans. Wireless Commun.*, pp. 2465–2478, Sep. 2005.

[14] A. Ghazal, C.-H. Wang, H. Haas, M. Beach, X. Lu, D. Yuan, and X. Ge, "A non-stationary MIMO channel model for high-speed train communication systems," in *Proc. 75th IEEE Vehicular Technology Conference, VTC 2012-Spring*. Yokohama, Japan, May 2012.

[15] A. Chelli and M. Pätzold, "A non-stationary MIMO vehicle-to-vehicle channel model based on the geometrical T-junction model," in *Proc. International Conference on Wireless Communications and Signal Processing, WCSP 2009*. Nanjing, China, Nov. 2009.

[16] J. Karedal, F. Tufvesson, N. Czink, A. Paier, C. Dumard, T. Zemen, C. F. Mecklenbräuker, and A. F. Molisch, "A geometry-based stochastic MIMO model for vehicle-to-vehicle communications," *IEEE Trans. Wireless Commun.*, vol. 8, no. 7, pp. 3646–3657, Jul. 2009.

[17] A. Borhani and M. Pätzold, "A non-stationary one-ring scattering model," in *Proc. IEEE Wireless Commun. and Net. Conf. (WCNC'13)*. Shanghai, China, Apr. 2013.

[18] ——, "Modelling of non-stationary mobile radio channels incorporating the Brownian mobility model with drift," in *Lecture Notes in Engineering and Computer Science: World Congress on Engineering and Computer Science, WCECS'13*, vol. 2. San Francisco, USA, Oct. 2013, pp. 695–700.

[19] ——, "Modelling of non-stationary mobile radio channels using two-dimensional Brownian motion processes," in *Proc. 6th International Conference on Advanced Technologies for Communications, ATC'13*. Ho Chi Minh City, Vietnam, Oct. 2013, pp. 241–246.

[20] R. C. Earnshaw and E. M. Riley, *Brownian Motion: Theory, Modelling and Applications*. Nova Science Pub Inc, 2011.

[21] T. Camp, J. Boleng, and V. Davies, "A survey of mobility models for ad hoc network research," *Wireless Communications and Mobile Computing*, vol. 2, no. 5, pp. 483–502, Sep. 2002.

[22] B. H. Fleury and D. Dahlhaus, "Investigations on the time variations of the wide-band radio channel for random receiver movements," in *Proc. IEEE International Symposium on Spread Spectrum Techniques and Applications (ISSSTA'94)*, vol. 2. Finland, Oulu, pp. 631–636.

[23] W. C. Jakes, Ed., *Microwave Mobile Communications*. Piscataway, NJ: IEEE Press, 1994.

[24] M. Pätzold, *Mobile Fading Channels*, 2nd ed. Chichester: John Wiley & Sons, 2011.

[25] V. A. Aalo, G. P. Efthymoglou, and C. Chayawan, "On the envelope and phase distributions for correlated Gaussian quadratures," *IEEE Communications Letters*, vol. 11, no. 12, pp. 985–987, 2007.

[26] P. Dharmawansa, N. Rajatheva, and C. Tellambura, "Envelope and phase distribution of two correlated Gaussian variables," *IEEE Transactions on Communications*, vol. 57, no. 4, pp. 915–921, 2009.

[27] F. Hlawatsch and F. Auger, *Time-Frequency Analysis: Concepts and Methods*. London (UK): ISTE and Wiley, 2008.

[28] I. S. Gradshteyn and I. M. Ryzhik, *Table of Integrals, Series, and Products*, 7th ed. Elsevier Academic Press, 2007.

Appendix H

Paper VIII

Title:	A New Non-Stationary Channel Model Based on Drifted Brownian Random Paths
Authors:	**Alireza Borhani** and Matthias Pätzold
Affiliation:	University of Agder, Faculty of Engineering and Science, P. O. Box 509, NO-4898 Grimstad, Norway
Book Chapter:	*Springer, Transactions on Engineering Technologies*, in press.

A New Non-Stationary Channel Model Based on Drifted Brownian Random Paths

Alireza Borhani and Matthias Pätzold

***Abstract* — This paper utilizes Brownian motion (BM) processes with drift to model mobile radio channels under non-stationary conditions. It is assumed that the mobile station (MS) starts moving in a semi-random way, but subject to follow a given direction. This moving scenario is modelled by a BM process with drift (BMD). The starting point of the movement is a fixed point in the two-dimensional (2D) propagation area, while its destination is a random point along a predetermined drift. To model the propagation area, we propose a non-centred one-ring scattering model in which the local scatterers are uniformly distributed on a ring that is *not* necessarily centred on the MS. The semi-random movement of the MS results in local angles-of-arrival (AOAs) and local angles-of-motion (AOMs), which are stochastic processes instead of random variables. We present the first-order density of the AOA and AOM processes in closed form. Subsequently, the local power spectral density (PSD) and autocorrelation function (ACF) of the complex channel gain are provided. The analytical results are simulated, illustrated, and physically explained. It turns out that the targeted Brownian path model results in a statistically non-stationary channel model. The interdisciplinary idea of the paper opens a new perspective on the modelling of non-stationary channels under realistic propagation conditions.**

Index Terms — Brownian motion processes, channel modelling, local autocorrelation function, local power spectral density, non-centred one-ring scattering model, non-stationary channels, targeted motions.

A. Borhani and M. Pätzold are with the Faculty of Engineering and Science, University of Agder, 4898 Grimstad, Norway (e-mails: {alireza.borhani, matthias.paetzold}@uia.no).

I. INTRODUCTION

To develop mobile communication systems, geometric channel models are recognized as one of the most effective candidates, which allow a fairly accurate system performance analysis. As an example, the one-ring scattering model [1–3], in which the local scatterers are uniformly distributed on a ring centered on the MS, is an appropriate model capturing the propagation effects in rural and sub-urban propagation areas. The unified disk scattering model (UDSM) [4] is also one of the most general geometric channel models, which covers numerous circularly-symmetric scattering models as special cases, including the one-ring model. In this regard, an overview of the most important geometric channel models can be found in [5].

Geometric channel models often profit from a common simplification, namely the stationarity assumption of the stochastic channel in time. Considering a very short observation time instant justifies a time-invariant AOA at the MS, which then results in a statistically stationary channel model. Many empirical and analytical investigations, e.g., [6–8], however, show that this property is only valid for *very* short travelling distances [9]. This calls for the need to develop and analyze stochastic channel models under non-stationary conditions.

Despite the drastic number of investigations on stationary geometric channel models, the literature lacks studies on non-stationary geometric channel models. Only a small number of analytical studies, e.g., [10–13], cope with the statistical properties of non-stationary channels. To the best knowledge of the authors, except the non-stationary one-ring scattering model studied in [14], none of the established geometric scattering models listed in [5] has been analyzed under non-stationary conditions. In [14], a non-stationary one-ring channel model has been derived by assuming that the MS moves from the center of the ring to the ring's border on a straight line. In this paper, we further expand the idea of [14] by allowing the MS to randomly fluctuate around a straight line, where its starting point is not necessarily the ring's center. It can be any point inside the ring of scatterers. To this end, we let the MS move in a semi-random way, but subject to follow a given preferred direction. By establishing an analogy between such a motion and the chaotic movement of particles suspended in fluids discovered by Robert Brown (see [15]), we model the travelling path of the MS by a BMD. We coin the term *targeted Brownian path model* to address the proposed path model of the MS. For a given BM process, the randomness of the path can be controlled by a single parameter. By eliminating the randomness of the path, the MS arrives at a fixed destination point via a straight path. Accordingly, the path model of [14] can be obtained as a special case of the proposed targeted Brownian path model.

Moving along a targeted Brownian path results in local AOAs and local AOMs, which are modelled by stochastic processes rather than random variables. We present the first-order density of the AOA and AOM processes in closed form. Expressions for the local PSD of the Doppler frequencies and ACF of the complex channel gain are also provided. These expressions are different from those presented in [16]. Numerical computations at 2.1 GHz illustrate the analytical results and verify the non-stationarity of the channel model. It is shown that non-stationarity in time contradicts the common isotropic propagation assumption on the channel. It is also proved that the one-ring scattering model can be obtained as a special case of the proposed channel model of this paper.

It is worth mentioning that 3D BM processes have been used to model fully random motions of mobile users [17]. However, 1D BM processes with drift have never been used to model semi-random motions of mobile users. Several other mobility models have also been employed in mobile ad hoc networks [18], but not in the area of channel modelling. In a nutshell, the novelty of this paper arises from the pioneering utilization of the BMD process as a path model for the modelling of non-stationary mobile fading channels.

The remainder of this paper is organized as follows. Section II gives a brief introduction to BM processes as a physical phenomenon, while Section III utilizes the BM process for developing the targeted Brownian path model. Section IV describes the propagation scenario by means of the non-centred one-ring scattering model. The complex channel gain of the proposed channel model is then described in Section V. Section VI investigates the statistical properties of the channel model. Numerical results are provided in Section VII. Finally, Section VIII summarizes our main findings and draws the conclusions.

II. PRINCIPLES OF BROWNIAN MOTION PROCESSES

BM was originally discovered in 1827 by the famous botanist, Robert Brown. It describes the chaotic movement of particles suspended in a fluid or gas [15]. In the 1860s, there were experimentalists who clearly recognized that the motion is due to the impact of suspending molecules. Finally, in 1906, Albert Einstein [19] offered an exact physical explanation of such a motion based on the bombardment of the suspended particles by the atoms of the suspending fluid. In 1908, a mathematical explanation of the BM was provided by Langevin [20][1]. BM processes have a wide range of applications, such as modelling of stock market fluctuations, medical

[1] A translation of [20] into English has been provided in [21].

imaging, and fractal theory [22]. In mobile ad hoc networks, 2D BM processes (random walk) are also employed to model irregular motions of mobile nodes [18]. The model is then used for network layer analysis.

A stochastic process $\{B(t) : t \in [0,T]\}$ is said to be a standard BM process if:

1. $B(0) = 0$.

2. $\forall\ 0 \leq s < t \leq T$, the random variable given by the increment $B(t) - B(s)$ follows the Gaussian distribution with zero mean and variance $t - s$, i.e., $B(t) - B(s) \sim N(0, t-s)$.

3. $\forall\ 0 \leq s < t < u < v \leq T$, the increments $B(t) - B(s)$ and $B(v) - B(u)$ are statistically independent.

From the conditions above, it can be concluded that $B(t)$ is a Wiener process with normally and independently distributed increments.

III. PATH MODELLING

In what follows, we first provide an equivalent spatial representation of the temporal BM process. Subsequently, the proposed local BM process is used to model the targeted motion of the MS along a predetermined drift.

A. Spatial Representation of BM Processes

To establish an analogy between the BM process and the MS movement, let us first assume that the MS starts from a given point with Cartesian coordinates (x_s, y_s) in the 2D plane. The aim is to model the random path starting from (x_s, y_s) via the BM process described in Section II. For this purpose, we establish a mapping from the temporal representation of the BM process $B(t)$ to the spatial representation of the BM process $B(x)$ by replacing the temporal variable t by the spatial variable x. Accordingly, the first condition of the BM process, i.e., $B(0) = 0$, changes to $B(x_s) = 0$. By assuming (x_d, y_d) as the terminal point of the movement, we introduce the scalar standard BM process over the range $[x_s, x_d]$ by means of the spatial stochastic process $B(x)$, which satisfies the following three conditions:

1. $B(x_s) = 0$.

2. $\forall\ x_s \leq x_p < x \leq x_d$, the random variable given by the increment $B(x) - B(x_p)$ follows the Gaussian distribution with zero mean and variance $x - x_p$, i.e., $B(x) - B(x_p) \sim N(0, x - x_p)$.

3. $\forall\, x_s \leq x_p < x < x_q < x_m \leq x_d$, the increments $B(x) - B(x_p)$ and $B(x_m) - B(x_q)$ are statistically independent.

For computational reasons, it is useful to consider the BM process at discrete values of x. To this end, we define $\Delta x = (x_d - x_s)/L$ for some positive integer L. Hence, $B_l = B(x_l)$ denotes the BM process at $x_l = x_s + l\Delta x$ $(l = 0, 1, ..., L)$. Now, with reference to Conditions 2 and 3, it can be concluded that $B_l = B_{l-1} + \Delta B_l$, where each ΔB_l is an independent normal distributed random variable of the form $N(0, \Delta x)$.

B. The Targeted Brownian Path Model

To model the targeted motion of the MS in the 2D plane, we propose a path with a controllable drift in a preferred direction, while the fluctuations of the path are modeled by the spatial BM process B_l. Accordingly, the path $\mathscr{P}$ of the MS is modelled as follows

$$\mathscr{P}: \left\{ (x_l, y_l) \;\middle|\; \begin{array}{l} x_l = x_s + l\Delta x, \\ y_l = a x_l + b + \sigma_y B_l, \end{array} \right\} \tag{H.1}$$

where $l = 0, 1, ..., L$ is the position index, the variable a denotes the slope of the drift, b is a constant shift along the y-axis, and σ_y allows to control the randomness of the path. Considering the fact that the randomness of the path $\mathscr{P}$ originates inherently from the randomness of the BM process B_l, the parameter σ_y provides an additional degree of freedom to control the randomness. For instance, by setting σ_y to 0, any point on the line represented by $y_l = a x_l + b$ can be reached. Whereas, increasing the value of σ_y reduces the chance of arriving at that point. However, the mean direction of the path remains unchanged. It is also noteworthy that the path model in (H.1) reduces to that in [14] if $\sigma_y = 0$. The model also enables to incorporate random fluctuations only along a specific line. For instance, by increasing a towards infinity, the fluctuations occur only along the y-axis. The same behaviour can be attained along any other line (axis) if we simply rotate the coordinate system.

In mobile communications, the proposed targeted Brownian path can be a very useful model to describe typical dynamics of users in motion, such as persons walking along a street, but not necessarily along a very smooth path. In vehicular communications, the model can also be used to explain the jittery motion of the vehicle antenna, while the vehicle is moving along a given direction.

IV. THE PROPAGATION SCENARIO

To cope with the scattering effect caused by the propagation area, we propose a non-centred one-ring scattering model, in which the local scatterers are uniformly

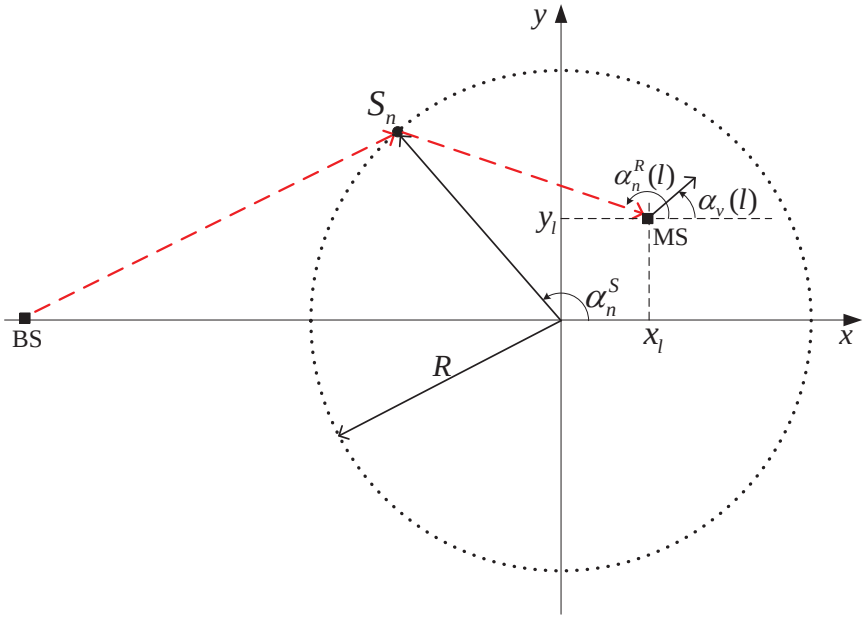

Figure H.1: The non-centred one-ring scattering model for a single-bounce scattering scenario.

distributed on a ring that is not necessarily centred on the MS. The displacement of the MS from the ring's center results in a non-isotropic channel model. This model is an appropriate geometric scattering model to explain environments, in which the base station (BS) antenna is highly elevated to scattering-free levels, while the MS antenna is surrounded by a large number of local scatterers. This situation occurs mostly in rural and sub-urban areas.

Fig. H.1 shows the proposed non-centred one-ring scattering model with the uniform distribution of the local scatterers S_n $(n = 1,2,...,N)$ on a ring of radius R centered on the origin. In this regard, α_n^S denotes the angle-of-scatterer (AOS) associated with the nth scatterer. At a reference point in time t_0, the MS starts its movement from (x_0,y_0) and tracks the path $\mathscr{P}$ to reach (x_L,y_L) at time t_L. The position of the MS at time $t_l \in [t_0,t_L]$ is described by Cartesian coordinates (x_l,y_l). It is also assumed that the MS is moving with a constant velocity v_R in the direction indicated by the AOM $\alpha_v(l)$. Owing to high path loss, we assume that at time t_l, a wave emitted from the BS reaches the MS at the AOA $\alpha_n^R(l)$ after a single bounce by the nth randomly distributed scatterer S_n located on the ring. A realization of the proposed Brownian path $\mathscr{P}$ in such a geometric scattering model is shown in Fig. H.2, in which the starting point (x_0,y_0) of the path is set to the ring's center[2].

[2]We have chosen the ring's center as the starting point of the movement to enable the verification of our numerical results (see Section VII) with the ones from the one-ring scattering model. However, the analytical results provided in the paper are not limited to such a special case.

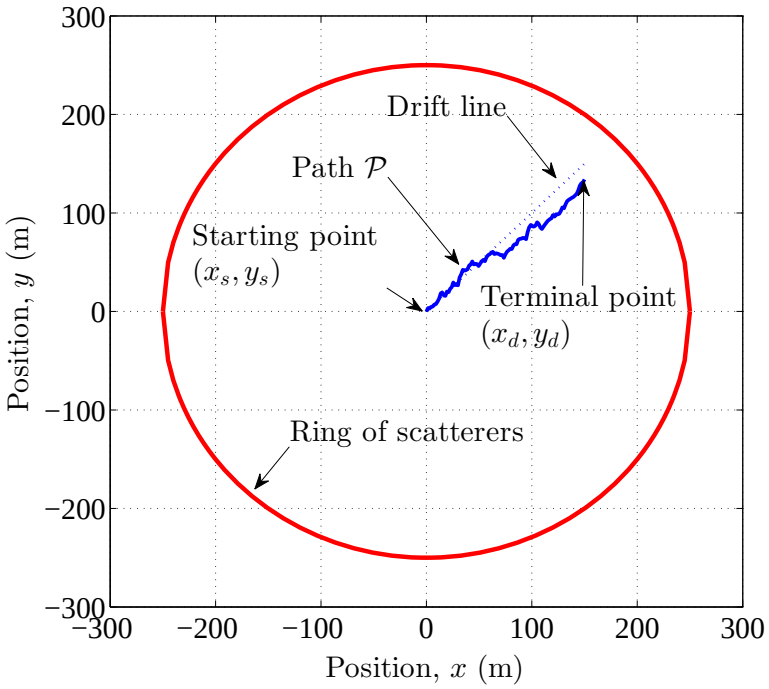

Figure H.2: Realization of a targeted Brownian path $\mathscr{P}$ in the ring of scatterers. The model parameters are $L = 100$, $a = 1$, $b = 0$, $\sigma_y = 2$, $x_s = 0\,\text{m}$, $x_d = 150\,\text{m}$, and $R = 250\,\text{m}$.

The above mentioned propagation scenario is completely different from the one-ring scattering model [1–3], in which the MS is located at the center of the ring, while its AOM is a deterministic variable. Therein, considering a very short observation time results in a stationary and isotropic channel model, while herein, the proposed path $\mathscr{P}$ justifies a non-stationary non-isotropic channel model. The proposed jittery path model $\mathscr{P}$ is also different from the smooth path model of [14]. Indeed, the random behavior of the AOM $\alpha_v(l)$ (see Fig. H.2) allows a much more flexible non-stationary channel model than the one proposed in [14]. In what follows, after providing an expression for the complex channel gain, we study the statistical properties of the proposed non-stationary channel model.

V. THE COMPLEX CHANNEL GAIN

The propagation scenario presented in Section IV is a non-stationary version of the typical fixed-to-mobile (F2M) scenario studied in [23, pp. 56–60]. Therein, the complex channel gain $\mu(t_l)$ of frequency-nonselective F2M channels was modeled by means of a complex stochastic process representing the sum of all scattered

components as follows

$$\mu(t_l) = \lim_{N\to\infty} \sum_{n=1}^{N} c_n e^{j(2\pi f_n t_l + \theta_n)}. \tag{H.2}$$

In the equation above, c_n denotes the attenuation factor caused by the physical interaction of the emitted wave with the nth scatterer S_n, and f_n stands for the Doppler frequency[3] caused by the movement of the MS. In addition, the random variable θ_n represents the phase shift of the nth path, which is often assumed to be uniformly distributed between 0 and 2π [23, p. 59].

The complex channel gain in (H.2) suits the proposed non-stationary one-ring model, if we replace the Doppler frequency f_n by $f_n(t_l)$. This apparently minor change adds a great deal of mathematical computations to the statistical characterization of the channel.

VI. STATISTICAL PROPERTIES OF THE CHANNEL MODEL

To investigate the statistical properties of the complex channel gain described in (H.2), let us start from the local AOA, which plays a key role in other statistical quantities. Notice that we defer the illustration and physical explanation of the analytical results to Section VII.

A. The Local Angles-of-Arrival

Referring to the geometric scattering model in Fig. H.1, the AOA $\alpha_n^R(l)$ at the point (x_l, y_l) is given by

$$\alpha_n^R(l) = \arctan\left(\frac{R\sin(\alpha_n^S) - y_l}{R\cos(\alpha_n^S) - x_l}\right). \tag{H.3}$$

For a given position l, the only random variable in the right side of (H.3) is the AOS α_n^S. Since the number N of local scatterers tends to infinity in the reference model, it is mathematically convenient to assume that the discrete AOS α_n^S is a continues random variable α^S, which is assumed to be uniformly distributed between $-\pi$ and π (see Section IV). By applying the concept of transformation of random variables [25, p. 130] and performing some mathematical manipulations, it can be shown that the first-order density $p_{\alpha^R}(\alpha^R; l)$ of the stochastic process $\alpha^R(l)$ in (H.3)

[3]The frequency shift caused by the Doppler effect is given by $f = f_{\max}\cos(\alpha)$, where $f_{\max} = f_0 v/c_0$ is the maximum Doppler frequency, f_0 denotes the carrier frequency, c_0 stands for the speed of light, and α equals the difference between the AOA and the AOM [24].

becomes

$$p_{\alpha^R}(\alpha^R;l)=\frac{1}{2\pi}\left(1-\frac{x_l\cos(\alpha^R)+y_l\sin(\alpha^R)}{\sqrt{R^2-\left(x_l\sin(\alpha^R)-y_l\cos(\alpha^R)\right)^2}}\right) \tag{H.4}$$

in which $-\pi \leq \alpha^R < \pi$. It is worth mentioning that $p_{\alpha^R}(\alpha^R;l)$ in (H.4) depends strongly on the position (x_l,y_l) of the MS. This means that the AOA $\alpha^R(l)$ is *not* first-order stationary. As a special case, if the path $\mathscr{P}$ crosses the ring's center $(0,0)$, then $p_{\alpha^R}(\alpha^R;l)$ in (H.4) reduces to $1/(2\pi)$, which is the AOA probability density function (PDF) of the one-ring model [1–3].

B. The Local Angles-of-Motion

By performing the linear interpolation scheme, the path $\mathscr{P}$ becomes continues and piecewise differentiable. This allows us to present the AOM $\alpha_v(l)$ at the location point (x_l,y_l) by the following expression

$$\begin{aligned}\alpha_v(l) &= \arctan\left(\frac{y_{l+1}-y_l}{x_{l+1}-x_l}\right)\\ &= \arctan\left(a+\sigma_y\frac{B_{l+1}-B_l}{x_{l+1}-x_l}\right).\end{aligned} \tag{H.5}$$

In the right side of (H.5), $B_{l+1}-B_l$ is the only random variable, which follows the Gaussian distribution of the form $N(0,\Delta x)$ (see Section III-A). Again, by applying the concept of transformation of random variables, the PDF $p_{\alpha_v}(\alpha_v)$ of the AOM $\alpha_v(l)$ in (H.5) is given by

$$p_{\alpha_v}(\alpha_v)=\frac{1}{\sqrt{2\pi}\sigma\cos^2(\alpha_v)}e^{\dfrac{-(\tan(\alpha_v)-a)^2}{2\sigma^2}} \tag{H.6}$$

where $-\pi/2 \leq \alpha_v \leq \pi/2$ and $\sigma=\sigma_y/\sqrt{\Delta x}$. Notice that $p_{\alpha_v}(\alpha_v)$ in (H.6) is independent of the position (x_l,y_l) of the MS, meaning that the AOM α_v is first-order stationary. It can be shown that the mean α_v equals $\arctan(a)$, in which a is the slope of the drift of the path $\mathscr{P}$.

C. The Local Power Spectral Density

The local Doppler frequency $f(l)$ is obtained through a non-linear transformation of the local AOA $\alpha^R(l)$ and the local AOM $\alpha_v(l)$ of the MS. It follows

$$f(l)=f_{\max}\cos\left(\alpha^R(l)-\alpha_v(l)\right) \tag{H.7}$$

where $\alpha^R(l)$ is described by the first-order density $p_{\alpha^R}(\alpha^R;l)$ in (H.4). In addition, the angle $\alpha_v(l)$ denotes the AOM at the point (x_l,y_l) after realizing the path $\mathscr{P}$ (see (H.5)). Accordingly, for a given position index l, the only random variable on the right-hand side of (H.7) is the AOA $\alpha^R(l)$. This is different from the approach used in [16], where the AOM is also assumed to be a random variable. To compute the first-order density $p_f(f;l)$ of the Doppler frequencies $f(l)$, we fix the position index l, and then we apply the concept of transformation of random variables. It follows

$$\begin{aligned} p_f(f;l) &= \frac{1}{2\pi f_{\max}\sqrt{1-(f/f_{\max})^2}} \\ &\times \left(2 - \frac{x_l\cos(A_+(f;l)) + y_l\sin(A_+(f;l))}{\sqrt{R^2-(x_l\sin(A_+(f;l)) - y_l\cos(A_+(f;l)))^2}}\right. \\ &- \left.\frac{x_l\cos(A_-(f;l)) + y_l\sin(A_-(f;l))}{\sqrt{R^2-(x_l\sin(A_-(f;l)) - y_l\cos(A_-(f;l)))^2}}\right) \end{aligned} \tag{H.8}$$

where

$$A_\pm(f;l) = \arctan\left(\frac{y_{l+1}-y_l}{x_{l+1}-x_l}\right) \pm \arccos\left(\frac{f}{f_{\max}}\right) \tag{H.9}$$

for $-f_{\max} \le f \le f_{\max}$.

Referring to [23, p. 85], the first-order density $p_f(f;l)$ of the Doppler frequencies is proportional to the local PSD $S_{\mu\mu}(f;l)$ of the complex channel gain $\mu(t_l)$. This allows us to present $S_{\mu\mu}(f;l)$ by the following expression

$$S_{\mu\mu}(f;l) = 2\sigma_0^2 p_f(f;l). \tag{H.10}$$

In the equation above, $2\sigma_0^2$ is the mean power of $\mu(t_l)$, and $p_f(f;l)$ is given by (H.8). For the special case that the path $\mathscr{P}$ crosses the ring's center $(0,0)$, the first-order density $p_f(f;l)$ in (H.8) reduces to

$$p_f(f;l) = \frac{1}{\pi f_{\max}\sqrt{1-(f/f_{\max})^2}} \tag{H.11}$$

which, after its multiplication by the mean power $2\sigma_0^2$, results in the Jakes PSD [24]. Notice that the Jakes PSD is not only associated with the stationary one-ring scattering model [1–3], but also with any other scattering model that is circularly sym-

metric with respect to the MS [4].

D. The Local Autocorrelation Function

With reference to the generalized Wigner-Ville spectrum [26, pp. 282-285], the local ACF $r_{\mu\mu}(\tau;l)$ of the non-stationary complex channel gain $\mu(t_l)$ can be attained by taking the inverse Fourier transform of the local PSD $S_{\mu\mu}(f;l)$ in (H.10). Accordingly, one can write

$$r_{\mu\mu}(\tau;l) = \int_{-f_{\max}}^{f_{\max}} S_{\mu\mu}(f;l) e^{j2\pi f\tau} df. \tag{H.12}$$

As a special case, if the path $\mathscr{P}$ goes across the ring's center, a scaled version of $p_f(f;l)$ in (H.11) can be employed to compute the inverse Fourier transform in (H.12). In this case, the local ACF $r_{\mu\mu}(\tau;l)$ in (H.12) reduces to $2\sigma_0^2 J_0(2\pi f_{\max}\tau)$, where $J_0(\cdot)$ stands for the zeroth-order Bessel function of the first kind [27, Eq. (8.411.1)].

VII. NUMERICAL RESULTS

Channel modelling at the 2 GHz band is of great importance in mobile communications. With reference to the operating frequency of the universal mobile telecommunications system (UMTS), the carrier frequency $f_0 = 2.1$ GHz has been chosen in our numerical computations. In addition, we consider the path $\mathscr{P}$ shown in Fig. H.2 as the travelling path of the MS. This allows us to have the positions (x_l, y_l) for $l = 0, 1, ..., L$. It is also assumed that the MS is moving with a velocity v_R of 80 km/h, which results in a maximum Doppler frequency $f_{\max}$ of 155.5 Hz. The mean power $2\sigma_0^2$ has been set to unity.

Fig. H.3 illustrates the first-order density $p_{\alpha^R}(\alpha^R;l)$ of the AOA process $\alpha^R(l)$ provided in (H.4). With reference to the path $\mathscr{P}$ shown in Fig. H.2, the MS starts its movement from the center of the ring. This circularly symmetric starting point explains the uniform distribution of the AOA at $l = 0$. By moving along the path $\mathscr{P}$, the probability of receiving signals from the scatterers ahead reduces, whereas the probability of receiving from the scatterers behind increases. This behavior continuous up to $l = 100$, where $p_{\alpha^R}(\alpha^R, 100)$ takes its minimum value at $\alpha^R = \arctan(1) = 0.78$ radian.

Fig. H.4 displays the PDF $p_{\alpha_v}(\alpha_v)$ of the AOM $\alpha_v(l)$ in (H.6). The simulated AOM is also shown in this figure. An excellent match between the simulation and analytical results can be observed. The mean α_v equals $\arctan(1) = 0.78$ radian as shown in the figure. The plot shows explicitly the tendency of the MS to follow the

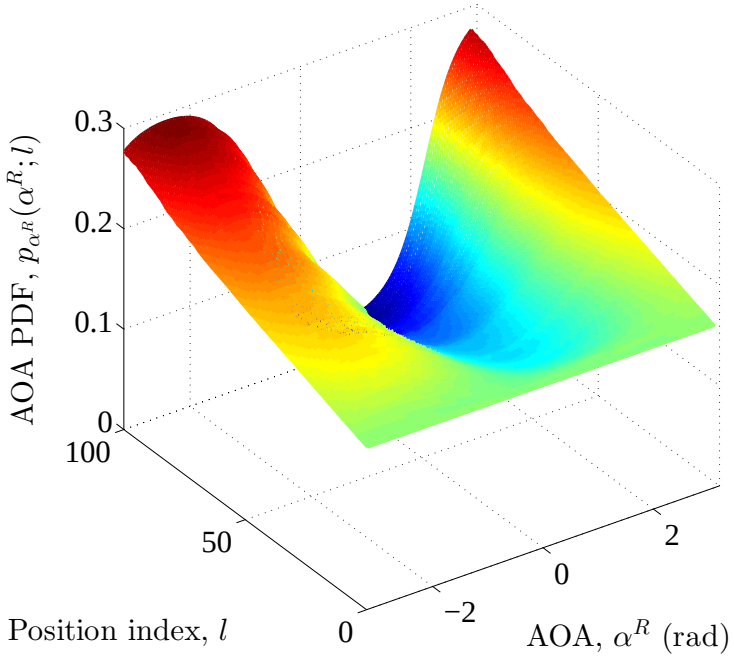

Figure H.3: The behavior of the first-order density $p_{\alpha^R}(\alpha^R; l)$ in (H.4) for the propagation scenario illustrated in Fig. H.2.

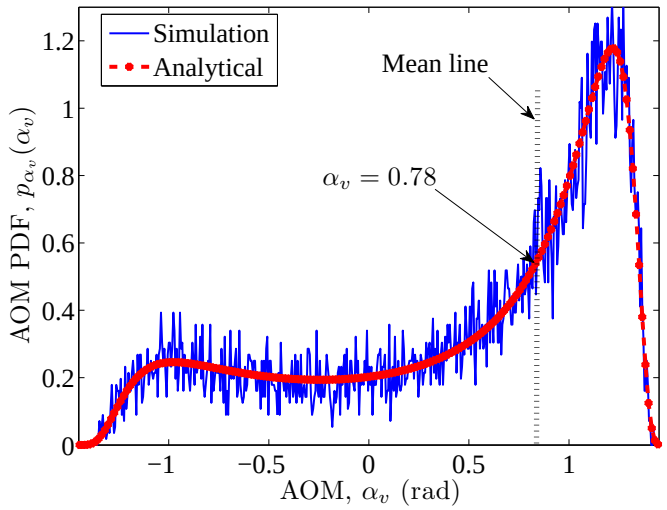

Figure H.4: The behavior of the AOM PDF $p_{\alpha_v}(\alpha_v)$ in (H.6) for the propagation scenario illustrated in Fig. H.2.

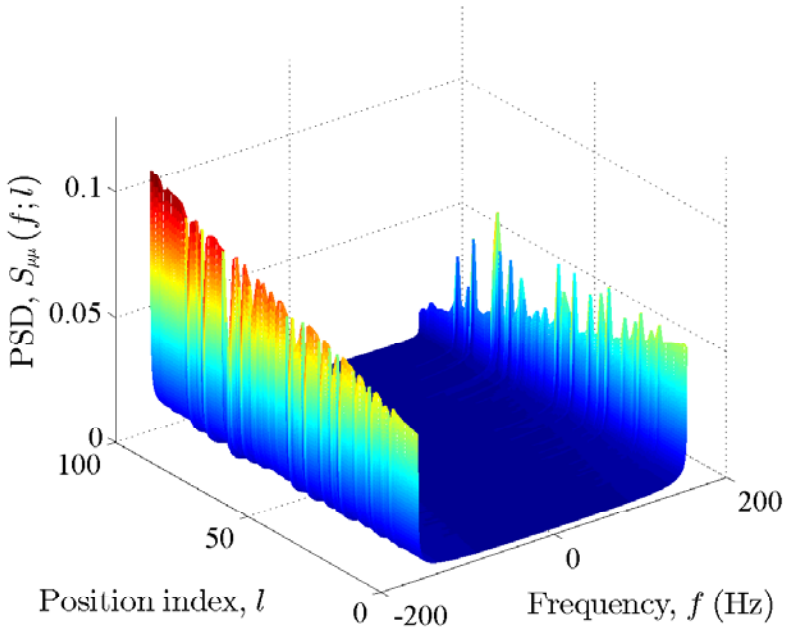

Figure H.5: The behavior of the local PSD $S_{\mu\mu}(f;l)$ in (H.10) for the propagation scenario illustrated in Fig. H.2.

predetermined drift of the path $\mathscr{P}$. This tendency depends solely on the slope a of the drift, which has been set to 1 herein. It is noteworthy that if the randomness σ_y of the path tends to zero, the AOM PDF approaches the delta function at $\alpha_v = 0.78$ radian.

Fig. H.5 depicts the local PSD $S_{\mu\mu}(f;l)$ presented in (H.10). The classical Jakes PSD with a U-shape can be observed in the stationary case ($l = 0$), where the MS is located at the ring's center. At this position, $S_{\mu\mu}(f,0)$ is a symmetric function with respect to f, indicating that the channel is instantaneously isotropic. However, this feature does not hold if the MS continuous its motion along the path $\mathscr{P}$. In this regard, by increasing l, an asymmetric behavior of the local PSD $S_{\mu\mu}(f;l)$ can be observed. Notice that moving along the path $\mathscr{P}$ results in confronting a lower number of scatterers ahead and a higher number of them behind the MS. This allows a higher and a lower probability of negative and positive Doppler shifts as shown in Fig. H.5.

Fig. H.4 displays the PDF $p_{\alpha_v}(\alpha_v)$ of the AOM $\alpha_v(l)$ in (H.6). The simulated AOM is also shown in this figure. An excellent match between the simulation and analytical results can be observed. The mean α_v equals $\arctan(1) = 0.78$ radian as

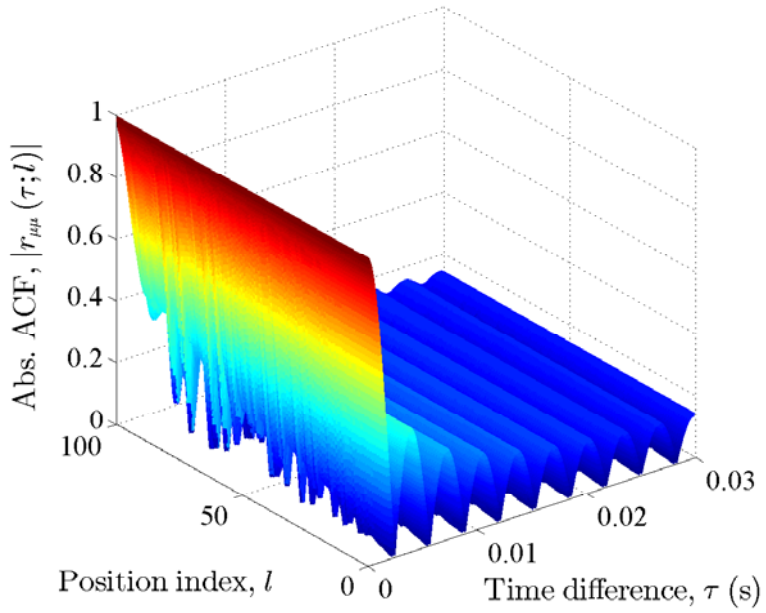

Figure H.6: The behavior of the absolute value of the local ACF $|r_{\mu\mu}(\tau;l)|$ (see (H.12)) for the propagation scenario illustrated in Fig. H.2.

shown in the figure. The plot shows explicitly the tendency of the MS to follow the predetermined drift of the path $\mathscr{P}$. This tendency depends solely on the slope a of the drift, which has been set to 1 herein. It is noteworthy that if the randomness σ_y of the path tends to zero, the AOM PDF approaches the delta function at $\alpha_v = 0.78$ radian.

Fig. H.5 depicts the local PSD $S_{\mu\mu}(f;l)$ presented in (H.10). The classical Jakes PSD with a U-shape can be observed in the stationary case ($l = 0$), where the MS is located at the ring's center. At this position, $S_{\mu\mu}(f,0)$ is a symmetric function with respect to f, indicating that the channel is instantaneously isotropic. However, this feature does not hold if the MS continuous its motion along the path $\mathscr{P}$. In this regard, by increasing l, an asymmetric behavior of the local PSD $S_{\mu\mu}(f;l)$ can be observed. Notice that moving along the path $\mathscr{P}$ results in confronting a lower number of scatterers ahead and a higher number of them behind the MS. This allows a higher and a lower probability of negative and positive Doppler shifts as shown in Fig. H.5.

Fig. H.6 shows the absolute value of the local ACF $r_{\mu\mu}(\tau;l)$ given in (H.12). Notice that due to the asymmetric behavior of the PSD $S_{\mu\mu}(f;l)$ (see Fig. H.5), the ACF $r_{\mu\mu}(\tau;l)$ is in general complex. A quite time-varying behavior of the ACF

can be observed. It is also noteworthy that for a given time difference $\tau \neq 0$, the correlation increases through some fluctuations if l grows.

VIII. CONCLUSION

In this paper, we have proposed a targeted Brownian path model to explain the travelling path of the MS. The proposed path model has a tendency to follow a preferred direction. To describe the propagation area, we have proposed a non-centred one-ring scattering model, in which the MS is not necessarily located at the ring's center. We have assumed that the MS is moving along the proposed targeted Brownian path model in such a geometric scattering model. It has been turned out that the proposed path model results in a non-stationary non-isotropic channel model. As a special case, the stationary isotropic one-ring scattering model can also be obtained from the proposed non-stationary channel model. The statistical properties of the proposed channel model have been derived, illustrated, and discussed extensively. It has been shown that the AOA process is first-order non-stationary, while the PDF of the AOM is stationary. The corresponding PSD of the Doppler frequencies and ACF of the complex channel gain have also been provided, showing that these characteristics are heavily time-dependent. Validating the analytical results by means of empirical data needs to be addressed in future works.

REFERENCES

[1] D.-S. Shiu, G. J. Foschini, M. J. Gans, and J. M. Kahn, "Fading correlation and its effect on the capacity of multielement antenna systems," *IEEE Trans. Commun.*, vol. 48, no. 3, pp. 502–513, Mar. 2000.

[2] A. Abdi and M. Kaveh, "A space-time correlation model for multielement antenna systems in mobile fading channels," *IEEE J. Select. Areas Commun.*, vol. 20, no. 3, pp. 550–560, Apr. 2002.

[3] M. Pätzold and B. O. Hogstad, "A space-time channel simulator for MIMO channels based on the geometrical one-ring scattering model," in *Proc. 60th IEEE Semiannual Veh. Technol. Conf., VTC 2004-Fall*, vol. 1. Los Angeles, CA, USA, Sep. 2004, pp. 144–149.

[4] A. Borhani and M. Pätzold, "A unified disk scattering model and its angle-of-departure and time-of-arrival statistics," *IEEE Trans. Veh. Technol.*, vol. 62, no. 2, pp. 473–485, Feb. 2013.

[5] K. T. Wong, Y. I. Wu, and M. Abdulla, "Landmobile radiowave multipaths' DOA-distribution: Assessing geometric models by the open literature's empirical datasets," *IEEE Trans. Antennas Propag.*, vol. 58, no. 3, pp. 946–958, Mar. 2010.

[6] A. Ispas, G. Ascheid, C. Schneider, and R. Thomä, "Analysis of local quasi-stationarity regions in an urban macrocell scenario," in *Proc. 71th IEEE Vehicular Technology Conference, VTC 2010-Spring*. Taipei, Taiwan, May 2010.

[7] A. Gehring, M. Steinbauer, I. Gaspard, and M. Grigat, "Empirical channel stationarity in urban environments," in *Proc. 4th European Personal Mobile Communications Conference*. Vienna, Austria, Feb. 2001.

[8] D. Umansky and M. Pätzold, "Stationarity test for wireless communication channels," in *Proc. IEEE Global Communications Conference, IEEE GLOBECOM 2009*. Honolulu, Hawaii, USA, Nov./Dec. 2009.

[9] A. Paier, J. Karedal, N. Czink, C. Dumard, T. Zemen, F. Tufvesson, A. F. Molisch, and C. F. Mecklenbräucker, "Characterization of vehicle-to-vehicle radio channels from measurements at 5.2 GHz," *Wireless Personal Communications (WPC)*, vol. 50, no. 1, pp. 19–32, Jul. 2009.

[10] G. Matz, "On non-WSSUS wireless fading channels," *IEEE Trans. Wireless Commun.*, pp. 2465–2478, Sep. 2005.

[11] A. Ghazal, C.-H. Wang, H. Haas, M. Beach, X. Lu, D. Yuan, and X. Ge, "A non-stationary MIMO channel model for high-speed train communication systems," in *Proc. 75th IEEE Vehicular Technology Conference, VTC 2012-Spring*. Yokohama, Japan, May 2012.

[12] A. Chelli and M. Pätzold, "A non-stationary MIMO vehicle-to-vehicle channel model based on the geometrical T-junction model," in *Proc. International Conference on Wireless Communications and Signal Processing, WCSP 2009*. Nanjing, China, Nov. 2009.

[13] J. Karedal, F. Tufvesson, N. Czink, A. Paier, C. Dumard, T. Zemen, C. F. Mecklenbräuker, and A. F. Molisch, "A geometry-based stochastic MIMO model for vehicle-to-vehicle communications," *IEEE Trans. Wireless Commun.*, vol. 8, no. 7, pp. 3646–3657, Jul. 2009.

[14] A. Borhani and M. Pätzold, “A non-stationary one-ring scattering model,” in *Proc. IEEE Wireless Commun. and Net. Conf. (WCNC’13)*. Shanghai, China, Apr. 2013.

[15] P. Pearle, B. Collett, K. Bart, D. Bilderback, D. Newman, and S. Samuels, “What Brown saw and you can too,” *Am. J. Phys.*, vol. 78, no. 12, pp. 1278–1289, Dec. 2010.

[16] A. Borhani and M. Pätzold, “Modelling of non-stationary mobile radio channels incorporating the Brownian mobility model with drift,” in *Lecture Notes in Engineering and Computer Science: Proceedings of The World Congress on Engineering and Computer Science 2013, WCECS 2013*, vol. 2. San Francisco, USA, pp. 695–700.

[17] B. H. Fleury and D. Dahlhaus, “Investigations on the time variations of the wide-band radio channel for random receiver movements,” in *Proc. IEEE International Symposium on Spread Spectrum Techniques and Applications (ISSSTA ’94)*, vol. 2. Finland, Oulu, pp. 631–636.

[18] T. Camp, J. Boleng, and V. Davies, “A survey of mobility models for ad hoc network research,” *Wireless Communications and Mobile Computing*, vol. 2, no. 5, pp. 483–502, Sep. 2002.

[19] A. Einstein, “Über die von der molekularkinetischen Theorie der Wärme geforderte Bewegung von in ruhenden Flüssigkeiten suspendierten Teilchen,” *Annalen der Physik*, no. 17, pp. 549–560, May 1905.

[20] P. Langevin, “Sur la théorie du mouvement brownien,” *C. R. Acad. Sci. Paris*, no. 146, pp. 530–533, 1908.

[21] D. S. Lemons and A. Gythiel, “On the theory of Brownian motion,” *Am. J. Phys.*, vol. 65, no. 11, pp. 530–533, Nov. 1979.

[22] R. C. Earnshaw and E. M. Riley, *Brownian Motion: Theory, Modelling and Applications*. Nova Science Pub Inc, 2011.

[23] M. Pätzold, *Mobile Fading Channels*, 2nd ed. Chichester: John Wiley & Sons, 2011.

[24] W. C. Jakes, Ed., *Microwave Mobile Communications*. Piscataway, NJ: IEEE Press, 1994.

[25] A. Papoulis, *Probability, Random Variables, and Stochastic Processes*, 3rd ed. New York: McGraw-Hill, 1991.

[26] F. Hlawatsch and F. Auger, *Time-Frequency Analysis: Concepts and Methods*. London (UK): ISTE and Wiley, 2008.

[27] I. S. Gradshteyn and I. M. Ryzhik, *Table of Integrals, Series, and Products*, 7th ed. Elsevier Academic Press, 2007.